SYNTHESIS AND DEVELOPMENT OF STIMULI RESPONSIVE SELF-AGGREGATES FOR TASK SPECIFIC APPLICATIONS

Thesis Submitted for the Degree of

Doctor of Philosophy (Science)

to

Jadavpur University

August 2022

by

Deblina Sarkar

School of Biological Sciences

Indian Association for the Cultivation of Science

Jadavpur, Kolkata 700032

India

इंडियन एसोसियेशन फर दि कल्टिवेशन आफ साइंस
ইণ্ডিয়ান এ্যাসোসিয়েশন ফর দি কালটিভেশন অব সায়েন্স
Indian Association for the Cultivation of Science
2A & B Raja S. C. Mullick Road, Jadavpur,
Kolkata - 700032, India

Dr. Prasanta Kumar Das
Senior Professor
School of Biological Sciences

Phone : +91-33-2473-4971
Fax : +91-33-2473-2805
Email : bcpkd@iacs.res.in

To Whom It May Concern

This is to certify that the thesis entitled "**SYNTHESIS AND DEVELOPMENT OF STIMULI RESPONSIVE SELF-AGGREGATES FOR TASK SPECIFIC APPLICATIONS**" submitted by Miss Deblina Sarkar who got her name registered on 20.02.2018 for the award of Ph.D. (Science) Degree of Jadavpur University, is absolutely based upon her own work under the supervision of Prof. Prasanta Kumar Das and that neither this thesis nor any part of it has been submitted for either any degree/diploma or any other academic award anywhere before.

Prasanta Kr. Das 29/08/22
(PRASANTA KUMAR DAS)

Signature of the supervisor
and date with official seal

Dr. Prasanta K. Das
Senior Professor
Chair-School of Biological Sciences
Indian Association for the Cultivation of Science
Jadavpur, Kolkata - 700032

Dedicated to My Beloved

Baba and Maa

DECLARATION

The research work embodied in this thesis entitled "**SYNTHESIS AND DEVELOPMENT OF STIMULI RESPONSIVE SELF-AGGREGATES FOR TASK SPECIFIC APPLICATIONS**" being submitted to Jadavpur University, Kolkata has been carried out at Indian Association for the Cultivation of Science, Jadavpur, under the supervision of Prof. Prasanta Kumar Das, Senior Professor, School of Biological Sciences, Indian Association for the Cultivation of Science. This work is original and has not been submitted in part or in full, for any degree or diploma to this or any other university.

Deblina Sarkar
29/8/22
DEBLINA SARKAR
August 2022

CONTENTS

Preface i

Acknowledgement iv

List of abbreviations vii

Synopsis ix

Introduction 1-39

Stimuli-responsive behaviour found in nature 2

Self-assembly: from chaos to order 2

Beyond amphiphiles: towards self-assembly & inspiration from nature . 3

Non-covalent interactions: bringing the amphiphiles together 6

Various self-aggregates 8-12

- Micelles 9
- Reverse micelles 9
- Supramolecular gels 10
- Low molecular weight hydrogels (LMHG) 11
- Low molecular weight organogels (LMOG) 11
- Ambidextrous gelators (AGs) 11
- Vesicles 12

Stimuli 13

Drug delivery systems (DDS) 14

Smart DDS (stimuli-responsive DDS) 15

Vesicles as stimuli responsive DDS 16

Organic nanoparticles 17

Aggregation induced emission: origin of fluorescent organic nanoparticles (FONPs) 17

Fabrication of fluorescent organic nanoparticles 19-24

Self-assembly method..20

Polymerization method..20

Emulsion method.. 21

Nanoprecipitation method 21

Reprecipitation method..22

Layer-by-layer (LbL) assembly..23

Particle replication in nonwetting templates (PRINT)..23

Electrospraying...24

Microfluidics 24

Applications of organic nanoparticles in cell biology.............................25-26

Self-assembled nanoparticles as a biosensing platform 25

Delivery vehicle.. 25

Present thesis 26-31

Stimuli responsive disintegration of self-assembled vesicles derived from cholesterol-based hydrazone tethered amphiphiles..26

Naphthalimide-based azo-functionalized supramolecular vesicle as hypoxia-responsive drug delivery vehicle.. 27

Naphthalimide based fluorescent organic nanoparticles in selective detection of Fe^{3+} and its application as a diagnostic probe for Fe^{2+}/Fe^{3+} transition..........................29

Naphthalenediimide based various amino acids appended organic nanoparticles with tuneable aggregation-induced emission (AIE)..30

References 32

Chapter 1 40-65

Stimuli responsive disintegration of self-assembled vesicles derived from cholesterol-based hydrazone tethered amphiphiles

1.1. Introduction..40

1.2. Results and discussion 41-55

1.2.1. Hydrazone-tailored amphiphiles and their self-assemblies **41**

1.2.2. Microscopic investigations and DLS study of the self-assembly.............................. **43**

1.2.3. Spectroscopic studies of **CBH-1** and **CBH-2** vesicles **45**

1.2.3.1. Steady-state fluorescence anisotropy **45**

1.2.3.2. UV-visible study and aggregation pattern **46**

1.2.4. XRD study.. **47**

1.2.5. Participation of intermolecular non-covalent interactions in self-assembly **47**

1.2.6. pH-responsive cleavage of hydrazone bond: dissipation of self-assembly **49**

1.2.7. Doxorubicin loading and release studies **54**

1.3. Conclusion **55**

1.4. Experimental section **56-62**

1.4.1. Materials and methods **56**

1.4.2. Synthesis of hydrazone-tailored amphiphiles (**CBH-1-3**) **56**

1.4.3. Preparation of vesicles **58**

1.4.4. Transmission electron microscopy (TEM) study **58**

1.4.5. Field-emission scanning electron microscopy (FESEM) **59**

1.4.6. Atomic force microscopy (AFM) study **59**

1.4.7. Fluorescence microscopy study... **59**

1.4.8. Dynamic light scattering (DLS) and zeta (ζ) potential measurements **59**

1.4.9. Fluorescence anisotropy.. **60**

1.4.10. UV-visible study **60**

1.4.11. FTIR study.. **61**

1.4.12. Solvent dependent ^{1}H-NMR study **61**

1.4.13. X-ray diffraction (XRD) study **61**

1.4.14. MALDI-TOF mass spectrometry study **61**

1.4.15. Doxorubicin loading and release **61**

1.5. Characterization data **62**

1.6. References **63**

Chapter 2 .... **66-100**

Naphthalimide-based azo-functionalized supramolecular vesicle as hypoxia-responsive drug delivery vehicle

2.1. Introduction **66**

2.2. Results and discussion **67-87**

2.2.1. Molecular designing of **NI-Azo** **67**

2.2.2. Investigation of microscopic structure and size distribution of the self-assembly of **NI-Azo** **68**

2.2.3. Spectroscopic investigation for self-aggregation of **NI-Azo** **71**

2.2.4. Hypoxia-responsive cleavage of azo bond (-N=N-): obliteration of Self-Aggregates **74**

2.2.5. Curcumin loading and release studies **78**

2.2.6. Cytocompatibility of **NI-Azo** vesicles. **80**

2.2.7. Bioimaging **81**

2.2.8. Killing ability of curcumin loaded **NI-Azo** vesicles via hypoxia-responsive drug release **83**

2.2.9. Cell apoptosis **86**

2.3. Conclusion **87**

2.4. Experimental section **88-95**

2.4.1. Materials and methods **88**

2.4.2. Synthesis of **NI-Azo** **88**

2.4.3. Determination of critical aggregation concentration (CAC) **89**

2.4.4. Preparation of vesicular solution **90**

2.4.5. Transmission electron microscopy (TEM) **90**

2.4.6. Field-emission scanning electron microscopy (FESEM) **90**

2.4.7. Atomic force microscopy (AFM) study **90**

2.4.8. Cryogenic transmission electron microscopy (Cryo-TEM) **90**

2.4.9. Dynamic light scattering (DLS) study and zeta (ζ) potential measurement **91**

2.4.10. Fluorescence microscopy 91
2.4.11. UV-visible study 91
2.4.12. Solvent-dependent ^{1}H-NMR study 92
2.4.13. Solvent-dependent FTIR Study 92
2.4.14. X-ray diffraction 92
2.4.15. MALDI-TOF mass spectrometry 92
2.4.16. Microorganisms and culture conditions 92
2.4.17. Curcumin loading and release 93
2.4.18. Cell culture 93
2.4.19. MTT assay 94
2.4.20. Flow cytometry 94

2.5. Characterization data 95

2.6. Spectra 96-97

2.6.1. ^{1}H-NMR spectrum 96
2.6.2. Mass spectrum 97

2.7. References 98

Chapter 3 101-137

Naphthalimide based fluorescent organic nanoparticles in selective detection of Fe^{3+} and its application as a diagnostic probe for Fe^{2+}/Fe^{3+} transition

3.1. Introduction 101

3.2. Results and discussion 102-124

3.2.1. Molecular designing of **NID** 102
3.2.2. Microscopic investigations and DLS study of the self-assemblies of **NID** 103
3.2.3. Spectroscopic study for self-assembly of **NID** amphiphile 105
3.2.4. Investigation of the emissive nature of organic nanoparticles 106
3.2.5. Fluorimetric sensing of Fe^{3+} 111
3.2.6. Influence of Fe^{3+} on the morphology of self-aggregated **NID** FONPs 117

3.2.7. Circular dichroism (CD) study **118**

3.2.8. Cytocompatibility of **NID** derivative-based FONPs **119**

3.2.9. Bioimaging **120**

3.3. Conclusion **125**

3.4. Experimental section **125-132**

3.4.1. Materials and methods **125**

3.4.2. Synthesis of **NID** **126**

3.4.3. Preparation of organic nanoparticles **127**

3.4.4. Transmission electron microscopy (TEM) study **128**

3.4.5. Field-emission scanning electron microscopy (FESEM) **128**

3.4.6. Atomic force microscopy (AFM) study **128**

3.4.7. Fluorescence microscopy study **128**

3.4.8. Dynamic light scattering (DLS) study **128**

3.4.9. UV-visible study **128**

3.4.10. Solvent dependent ^{1}H-NMR study **129**

3.4.11. Photoluminescence study **129**

3.4.12. Quantum yield (QY) measurement **129**

3.4.13. Time resolved study **130**

3.4.14. Job's plot measurements **130**

3.4.15. Circular dichroism (CD) study **131**

3.4.16. Cell culture **131**

3.4.17. MTT assay **131**

3.4.18. Bioimaging **131**

3.4.19. Co-culture experiment **132**

3.4.20. Flow cytometry **132**

3.5. Characterization data **133**

3.6. Spectra **133-134**

3.6.1. ^{1}H-NMR spectra **133**

3.6.2, ^{13}C-NMR spectra **134**

3.6.3. Mass spectra **134**

3.7. References **135**

Chapter 4 .... **138-178**

Naphthalenediimide based various amino acids appended organic nanoparticles with tuneable aggregation-induced emission (AIE)

4.1. Introduction **138**

4.2. Results and discussion **139-159**

4.2.1. Molecular designing of naphthalenediimides based amphiphiles **NDI-1-9** **139**

4.2.2. Self-aggregation of amphiphiles **140**

4.2.3. Microscopic study and DLS measurements **142**

4.2.4. Photoluminescence property **146**

4.2.5. Spectroscopic investigation of self-aggregation **148**

4.2.6. Fluorescence spectroscopy **151**

4.2.7. Time-resolved study **157**

4.3. Conclusion **159**

4.4. Experimental section **160-165**

4.4.1. Materials **160**

4.4.2. Synthesis of NDI derivatives **160**

4.4.3. Sample preparation for spectroscopic and microscopic investigations **162**

4.4.4. Transmission electron microscopy (TEM) study **163**

4.4.5. Field-emission scanning electron microscopy (FESEM) **163**

4.4.6 Dynamic light-scattering (DLS) **163**

4.4.7. Fluorescence microscopy **163**

4.4.8. UV-visible spectroscopic investigation **163**

4.4.9. ^{1}H-NMR study in varying solvent composition **164**

4.4.10. Fluorescence spectroscopy **164**

4.4.11. Quantum yield (QY) measurement **164**

4.4.12. Time resolved study **164**

4.5. Characterization data **165-168**

4.6. Spectra **168-175**

4.6.1. ^{1}H-NMR spectrum **168**

4.6.2. Mass spectrum **172**

4.7. References **176**

Postlude **179**

List of publications **180**

PREFACE

The research work documented in the current thesis entitled as "**SYNTHESIS AND DEVELOPMENT OF STIMULI RESPONSIVE SELF-AGGREGATES FOR TASK SPECIFIC APPLICATIONS**" demonstrates the design and development of amphiphiles derived functional soft-materials and their judicious application in the various field. It describes membrane mimetic supramolecular self-assemblies and their stimuli responsive applications in bio-medicine. The present thesis also deals with the self-aggregation of luminogenic amphiphiles that exhibit unique photoluminescence properties in their aggregated form and their utility in sensing and bioimaging. Furthermore, the research work can potentially contribute to various applications in interdisciplinary sciences.

The present investigations have been carried out by the author in the School of Biological Sciences, Indian Association for the Cultivation of Science, Jadavpur, Kolkata 700032, India during the period 2017-2022 under the supervision of Prof. Prasanta Kumar Das.

The thesis contains four chapters in addition to general introduction.

The **Introduction** mainly highlights the beauty of self-assemblies. It delivers a brief outline of how mother nature has motivated the scientists to construct bio-inspired soft-materials and replicate their utility. It also provides a concise demonstration of known self-assembled supramolecular systems, nature of interaction and their wide range of applications especially focusing on their stimuli responsive properties in theranostic endeavour. Development of self-assembled fluorescent materials with unique optical properties and their exploration particularly as bio-probes is also emphasized in the introductory part.

Chapter 1 describes the development of cholesterol-based pH-responsive hydrazone-appended amphiphiles varying the carbonyl moieties (that generated the "hydrazone" bond) from aldehyde (benzaldehyde, *p*-dimethylaminobenzaldehyde) to ketone (benzophenone). For the first two, vesicular self-aggregates were formed via *H*-type aggregation in 1:3 v/v, DMSO-water and highly ordered lamellar structure was verified by low angle X-ray diffraction (XRD) patterns. These vesicles got disassembled at acidic pH ($pH < 5.0$) in contrast to showing stability in neutral environment. Cleavage of the hydrazone bond in acidic environment, that lead to destruction of self-assembly, was investigated by UV-visible, FTIR and mass spectrometric studies. In the transmission electron microscopic (TEM) images of the acid treated vesicles, absence of spherical structures established its disintegration. In addition, drug loading inside the vesicles and its pH-sensitive release from the **CBH-1** vesicles were confirmed using doxorubicin.

Chapter 2 demonstrates self-aggregated vesicle in 1:9 (v/v), tetrahydrofuran (THF)-water from naphthalimide-based azo moiety containing amphiphiles through *H*-type of aggregation. Azo (–N=N–) bond is subject to be reduced in the presence of the azoreductase enzyme, which is overexpressed in the hypoxic microenvironment. The optical density of this characteristic azo (–N=N–) moiety of the vesicles at 458 nm got weakened in the presence of both extracellular and intracellular bacterial azoreductase extracted from *Escherichia coli* bacteria as well as sodium dithionite (chemical mimic of azoreductase). This signifies that azoreductase/sodium dithionite induces azo bond cleavage, that was verified from MALDI-TOF spectrometric data. Anticancer drug curcumin was encapsulated within vesicles and that killed cancerous B16F10 cells in $CoCl_2$-induced hypoxic environment because of the azoreductase-sensitive drug release through the early apoptotic pathway, where the cell killing was 2.15-fold higher than that of the normoxic condition and 2.4-fold higher compared to that of native curcumin in the hypoxic environment. Also, cancer cell killing efficacy of curcumin-loaded vesicles was 4.5- and 1.9-fold higher than that of NIH3T3 cells (non-cancerous) in normoxic and hypoxic microenvironments, respectively.

Chapter 3 illustrates development of FONPs from the naphthalimide based histidine appended amphiphile, in 99 vol% water in DMSO through *J*-type aggregation. Aggregation-induced emission (AIE) was observed with excimer formation at 470 nm having bluish green emission. These FONPs were employed in selective sensing of Fe^{3+} and bioimaging of Fe^{3+} inside cells due to their emissive properties and low toxicity. Fluorescence intensity of the FONPs got significantly reduced with addition of Fe^{3+} due to the formation of a 1 : 1 stoichiometric complex with the histidine part. The limit of detection (LOD) of this turn-off sensor was calculated to be 12.5±1.2 μM having high selectivity over other metal ions. In view of the variable oxidative stress within different cells, FONPs were utilized for sensing Fe^{2+} to Fe^{3+} redox state transition selectively in cancer cells (B16F10) compared to non-cancerous ones (NIH3T3). Co-culture experiment and flow cytometry further confirmed selective sensing of cancer cells. Hence, these FONPs can be a selective diagnostic tool for cancerous cells on account of their higher H_2O_2 amount.

Chapter 4 demonstrates development of naphthalenediiimide (NDI) based amphiphiles with varying amino acid substitution from L-alanine to L-phenyl alanine to 3-(2-naphthyl)-L-alanine (increasing π-electrons) with or without alkyl spacer (C-6, C-11). Construction of self-aggregated organic nanoparticles of ~50 nm occurred at 50 vol% water or methyl cyclohexane (MCH) onwards in DMSO/DMF or $CHCl_3$ via *J*-aggregation. Amphiphiles, where amino acids are directly connected to the NDI, self-assembled into FONPs (MCH in $CHCl_3$) and displayed aggregation-induced emission (AIE) through excimer formation at 484 nm to 495 nm, and 590 where red shift was observed with increasing π-electrons donor side. FONPs of 6-amino caproic acid spacer containing NDI derivatives showed AIE at 505 nm and 545 nm (water in DMF/DMSO) and 11-amino undecanoic acid containing analogues showed AIE at 480 nm and 585 nm in $CHCl_3$-MCH and DMF/DMSO-water. The multi colour emission from blue-green to yellow-orange with enhancement of π-electron cloud in the side chain of NDI derivatives was detected probably due to the facilitated electron transfer at a lower energy to the electron deficient NDI core that caused red shifted emission maxima. This was again clarified by controlling the availability of π-electrons of phenyl ring by including electron withdrawing $-NO_2$ and donating -OMe groups at the molecular structure of other two amphiphiles that exhibited blue shifted (475 nm) and red shifted (570 nm) emission maxima compared to the unsubstituted phenyl alanine appended one (495 nm). Nevertheless, increased alkyl spacer length between side chain substitution and NDI core produced relatively lower quantum yield apparently due to the impeded electron transfer.

Each chapter (**Chapter 1** to **4**) begins with a short Introduction followed by Results and Discussion, Conclusion, Experimental section, Characterization Data along with the Spectra (^{1}H- and or ^{13}C-NMR and Mass) of the synthesized amphiphilic molecules and finally the References.

ACKNOWLEDGEMENT

As I have come to the end of my doctoral journey, I feel that I owe my gratitude and sincere acknowledgement to a lot of people, who were always there by my side and who supported me in so many ways that I could ever imagine. This course of doctoral research has been a pleasant journey to me which would have been incomplete without my co-workers, friends and well-wishers. My heartfelt thanks to all of them.

My sincere respect and thanks goes first to my supervisor, Prof. Prasanta Kumar Das for his support, inspiration, guidance and constant encouragement throughout the different stages of my doctoral investigations. His dynamism, vision and sincerity inspired me immensely. He stood by me during all the projects, motivated me even when I failed, and guided me towards the correct path. It would have been impossible for me to achieve this goal without him. It was a great privilege and honour to work under his guidance and I could not have hoped for a better mentor than him for my doctoral studies.

I take the pleasure of acknowledging my research institution, Indian Association for the Cultivation of Science (IACS) for providing me this platform to pursue my doctoral research work and also Council of Scientific and Industrial Research (CSIR) for the fellowship.

I am forever indebted to all my teachers who enlightened my knowledge with care, starting from primary school to Masters in Chemistry course. I am eternally grateful to Miss Gopa Maity madam for her love, support and enthusiasm in the early days of my childhood, all the teachers of Mission Girls' High School for building up my character and off course, Surojit Sir who planted the seeds of interest in chemistry during my school days. I convey my deepest respect to my Jadavpur university teachers especially Prof. G.M. Sir, Prof. A.K.M. Sir, Prof. R.G. Madam, Prof. S.R.R.C. Sir, Prof. S.B. Sir, Prof. U.J. Sir, Prof.

S.C.B. Sir, Prof. B.B. Sir, Prof. S. Bhar Sir, Dr. S.C. Sir, Dr. S.D. Sir, Dr. T.R.B. Madam and many more for broadening the world of Chemistry.

It gives me immense pleasure to offer my sincere thanks to the staffs of IACS, especially Supriyo da, Champa di, Gopal da, Suman da, Sumit da, debopriya di and Sujit da, who helped me a lot in experimental work during the entire period of my Ph.D and Chanchal da whose constant support always helped me during this journey.

Finally, talking about my lab, it's a real pleasure to be a part of this family. The lab in itself is a nice little household; truly, a home away from home. Words are simply not enough to express my cordial gratitude to all my senior and junior labmates, Moumita di, Krishnendu da, Saheli di, Soumik da, Pritam da, Debayan, Monalisa, Anup, Dipak, Sudeshna, Aftab, Kathakoli, Afreen, Madhurima and Aparajita di. I want to convey special thanks to Pritam da for his endless co-operation in my initial research work and Debayan for his constant encouragement.

They rendered me enormous support in every possible way they could. I will cherish all of them for showering me with some wonderful memories and colourful days in IACS both inside and outside the lab.

I also owe my heartful thanks to some of my friends namely Subarna (who was also my roommate), Shantanu, Anas, Writhabrata and Supriyo who not only helped me in my research work but also blessed me with a life of joy in the hours when lab lights were off. I am also thankful to all the seniors and juniors of our department who have helped me in one way or other during this period.

I also pay my homage and express gratitude to my close relatives i.e mani, meso, younger brother Dibyo, elder brother Bile dada, jethu, dadama, dimma, chotodadu, tublu uncle, aaka; childhood friends i.e Ruchira, Payel, Poulomi; college friends i.e Rapti, Arka for their love, support and encouragement.

Last but not the least, I must express my deepest gratitude to my parents (Mr. Arunava Sarkar and Mrs. Suvra Sarkar) although I am not sure if words can even express how much they mean to me. They are my pillars. I am nothing without them. Everything I have done in my life or will do in future is because of them. Thank you for keeping faith in me, standing beside me in all my difficult times. I am forever indebted to you for what I am.

Deblina Sarkar

August 2022

LIST OF ABBREVIATIONS

ACQ : Aggregation caused quenching

AFM : Atomic force microscopy

AG : Ambidextrous gelator

AIE : Aggregation induced emission

ANS : 8-anilino-1-naphthalenesulfonic acid

Boc : *tert*-Butoxycarbonyl

CAC : Critical aggregation concentration

CD : Circular dichroism

CMC : Critical micellar concentration

CTAB : Cetyltrimethylammonium bromide

DCC : *N*, *N*′-dicyclohexylcarbodiimide

DCM : Dichloromethane

DHB : 2,5-Dihydroxybenzoic acid

DLS : Dynamics light scattering

DMAP : 4-*N*, *N*-(dimethylamino)pyridine

DMEM : Dulbecco’s modified eagle’s medium

DMF : *N*, *N*-Dimethylformamide

DMSO : Dimethyl sulfoxide

DPH : 1,6-diphenyl-1,3,5-hexatriene

EDTA : Ethylenediaminetetraacetic acid

EtOAc : Ethyl acetate

FBS : Fetal bovine serum

FEG-TEM : Field-emission gun transmission electron microscopy

FE-SEM : Field-emission scanning electron microscopy

FITC : Fluorescein isothiocyanate

FONP : Fluorescent organic nanoparticles

FTIR : Fourier transform infrared

HLB : Hydrophilic-lipophilic balance

HOBT	:	Hydroxybenzotriazole
HRMS	:	High resolution mass spectrometry
ICT	:	Intramolecular charge transfer
LMHG	:	Low-molecular-weight hydrogel
LMOG	:	Low-molecular-weight organogel
LMWG	:	Low-molecular-weight gel
MALDI	:	Matrix-assisted laser desorption/ionization
MCH	:	Methyl cyclohexane
MeOH	:	Methanol
MTT	:	(3-(4,5-Dimethylthiazol-2-yl)-2,5-diphenyltetrazolium bromide
NDI	:	Naphthalene diimide
NHS	:	N-hydroxy succinimide
NMR	:	Nuclear magnetic resonance
PBS	:	Phosphate-buffered saline
PI	:	Propidium iodide
RIR	:	Restricted intramolecular rotation
ROS	:	Reactive oxygen species
SAFIN	:	Self-assembled fibrillar network
TCSPC	:	Time-correlated single photon count
TEM	:	Transmission electron microscopy
TFA	:	Trifluoroacetic acid
THF	:	Tetrahydrofuran
TOF	:	Time of flight
UV	:	Ultra-violet
XRD	:	X-ray diffraction

SYNOPSIS

Mother Nature runs its very own factory, manufacturing new devices and materials with great precision and flexibility starting at the nanoscale. Drawing inspiration from her has always been beneficial for mankind in numerous ways. Construction of self-assembled novel supramolecular architectures from amphiphilic building blocks by means of several non-covalent interactions (e.g. hydrogen bonding, π-π stacking, van der Waal's interactions, electrostatic forces, hydrophobic forces etc.) is one of those instances of mimicking a natural event. Structural diversity of the amphiphilic molecules and modes of interaction among themselves in varying media give rise to the different morphologies (micelles, reverse micelles, vesicles, microemulsions, gel fibres etc.). Supramolecular self-aggregates are convenient to form and easy to functionalize owing to the ease of modification of amphiphiles that enhances their utility in task specific applications. Moreover, self-assembly or disassembly can be judiciously controlled by tuning the amphiphilic back bone, making them respond to several external triggers like heat, light, magnetic field, sound as well as internal triggers like pH, enzyme, hypoxia, redox state. Stimuli responsive destruction of self-aggregates have huge applications in the domain of "smart" Drug Delivery Systems. Also, organic nanoparticles with unique luminogenic properties have revolutionized the biomedicinal arena. To this end, the present thesis gives an overview on development of amphiphiles derived diverse self-assembled systems for task specific applications with distinctive features of the soft-materials. It deals with fabrication of supramolecular vesicles with stimuli responsive junction that leads to pH sensitive and hypoxia responsive drug release which might have noteworthy influence in cancer cell killing. Also, using metal ions as stimuli in terms of changing the emission properties of self-aggregates, development of fluorescent organic nanoparticles (FONPs) based Fe^{3+} sensor with ability to differentiate between +2 and +3 state of iron is described here. Furthermore, this thesis demonstrates the fabrication of FONPs with tuneable emissions simply by altering the functionalities of the amphiphiles. Overall, this thesis focuses on "smart" supramolecular systems having application in bioimaging, sensing of biologically important entities inside mammalian cells as well as drug delivery.

Chapter 1 describes development of cholesterol-based pH-responsive hydrazone appended amphiphiles (**CBH-1-3**) varying the carbonyl moieties (that generated the "hydrazone" bond) from aldehyde (benzaldehyde (**CBH-1**)), *p*-dimethylaminobenzaldehyde (**CBH-2**)) to ketone (benzophenone (**CBH-3**)) (Figure 1). Among them, **CBH-1** and **CBH-2** formed vesicular self-aggregates via *H*-type aggregation in 1:3 v/v, DMSO-water with diameter of ~50-120 nm and ~150-250 nm for **CBH-1** and **CBH-2**, respectively.

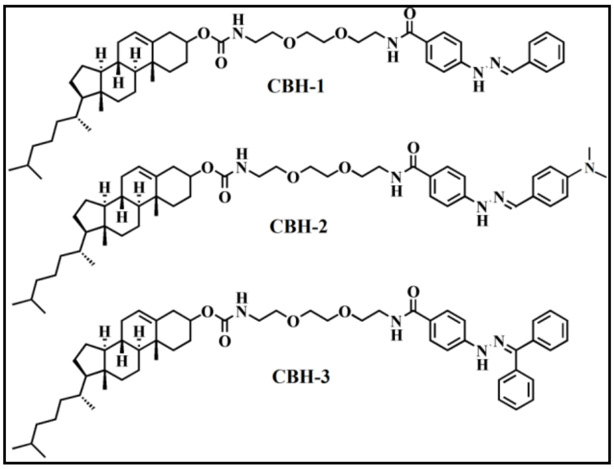

Figure 1. Chemical structures of hydrazone-tailored amphiphiles **CBH-1-3**.

Furthermore, the formation of bilayer vesicles possibly through highly ordered lamellar like structure was validated by low angle X-ray diffraction (XRD) pattern. These vesicles were stable at neutral environment but got disassembled at acidic pH (pH < 5.0) (Figure 2).

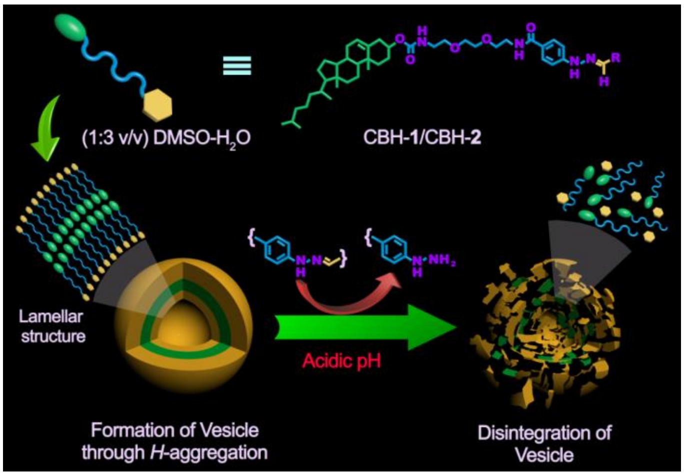

Figure 2. Schematic presentation of formation of self-assembly by hydrazone-tailored amphiphiles through *H*-type of aggregation and pH-responsive disintegration of self-assemblies.

Cleavage of the hydrazone bond in acidic environment leading to destruction of self-assembly was investigated by UV-visible, FTIR and mass spectrometric studies. In the transmission electron microscopic (TEM) images of the acid treated vesicles, absence of spherical structures established its disintegration. In addition, drug loading inside the vesicles and its pH-sensitive release from the **CBH-1** vesicles were confirmed using doxorubicin by means of fluorescence microscopy and fluorescence spectroscopy. (Figure 3).

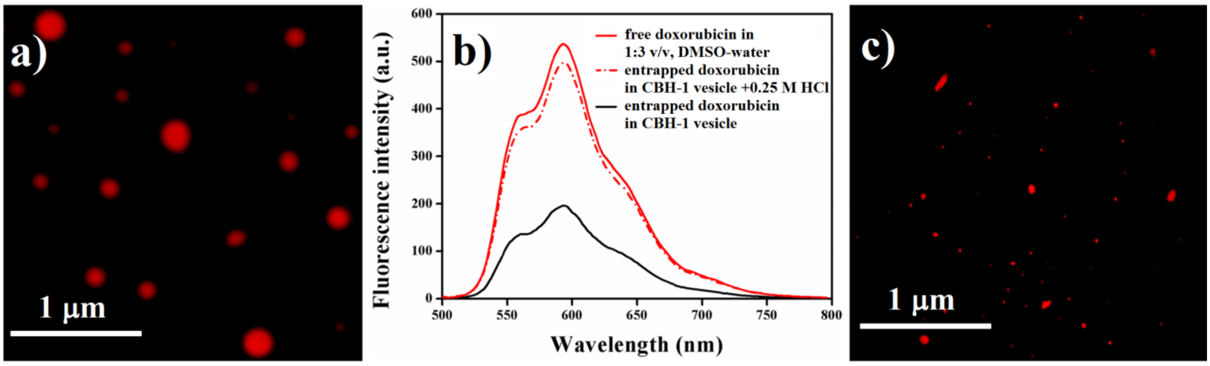

Figure 3. (a) Fluorescence microscopic image (λ_{ex} = 490 nm) of doxorubicin encapsulated CBH-1 vesicles, (b) emission spectra of doxorubicin entrapped within **CBH-1** vesicles, after treating with 0.25 M HCl and free doxorubicin, (c) fluorescence microscopic image of released doxorubicin after treating with 0.25 M HCl.

This finding also triggered our interest to design more hydrophilic segment containing stimuli-responsive amphiphiles, which will have the potential to form vesicular aggregates in greater percentage of water and hence exploit their potentials in diverse biological applications.

Chapter 2 illustrates construction of hypoxia responsive supramolecular vesicles as drug delivery system because it has notable significance particularly at early stage of cancer in the context of tumor specific delivery. Self-aggregated vesicle in 1:9 (v/v), tetrahydrofuran (THF)-water from naphthalimide-based azo moiety containing amphiphile (**NI-Azo**) was formed through *H*-type of aggregation having diameter of 200-250 nm (Figure 4, 5).

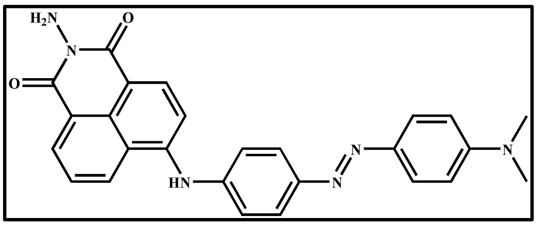

Figure 4. Structure of **NI-Azo** molecule.

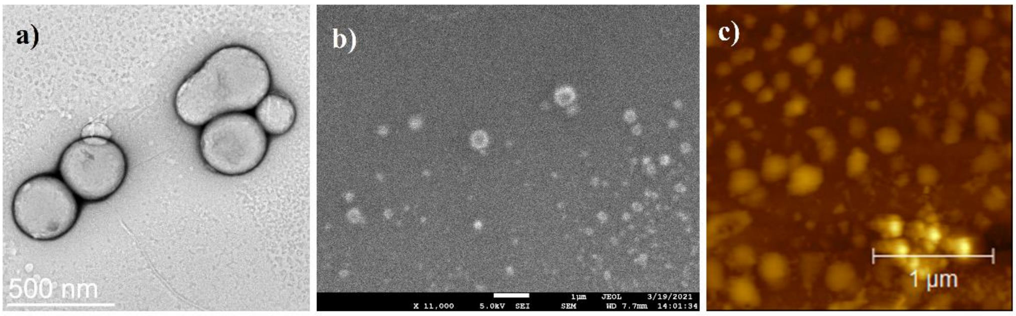

Figure 5. (a) Negatively stained TEM image, (b) FESEM image, (c) AFM image **NI-Azo** in (1:9, v/v) THF-water binary solvent mixture ([**NI-Azo**] = 25 µM).

Azo (−N=N−) bond is subject to be reduced in the presence of the azoreductase enzyme, which is overexpressed in the hypoxic microenvironment. The optical density of this characteristic azo (−N=N−) moiety of **NI-Azo** vesicles at 458 nm got weakened in the presence of both extracellular and intracellular bacterial azoreductase extracted from *Escherichia coli* bacteria as well as sodium dithionite (chemical mimic of azoreductase). This signifies that azoreductase/sodium dithionite induces azo bond cleavage in **NI-Azo**. Formation of aniline (aromatic amine) derivatives through the cleavage of the azo bond by azoreductase and sodium dithionite was confirmed by the UV spectroscopic study of NI-Azo vesicles and MALDI-TOF spectrometric study of fragments obtained after sodium dithionite treatment. Anticancer drug curcumin was encapsulated within **NI-Azo** vesicles that killed cancerous B16F10 cells in CoCl$_2$-induced hypoxic environment because of the azoreductase-sensitive drug release through the early apoptotic pathway. The cell killing efficiency was 2.15-fold higher than that of the normoxic condition and 2.4-fold higher compared to that of native curcumin in the hypoxic environment (Figure 6). Also, cancer cell killing efficacy of curcumin-loaded **NI-Azo** vesicles was 4.5- and 1.9-fold higher than that of NIH3T3 cells (non-cancerous) in normoxic and hypoxic microenvironments, respectively (Figure 6). The half-inhibitory concentration (IC$_{50}$) was found to be 33 μg/mL for **NI-Azo-cur** in case of hypoxic B16F10 cells (Figure 6).

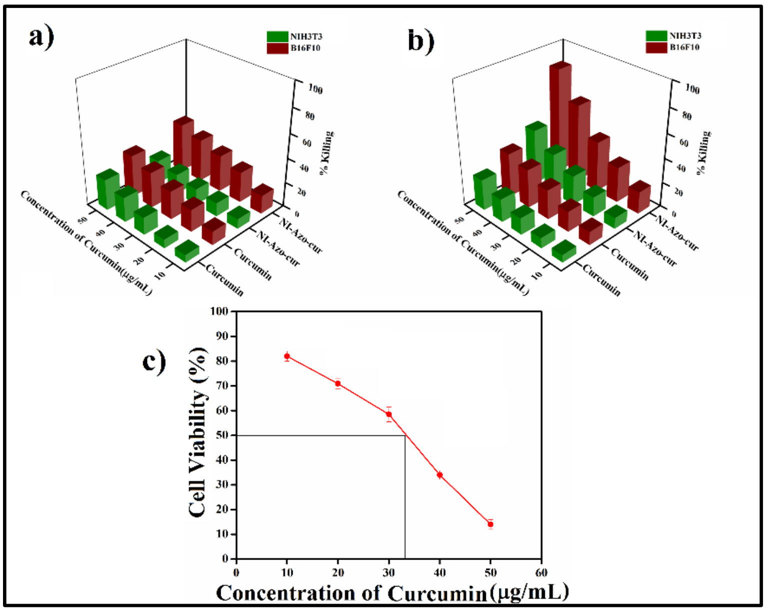

Figure 6. % Killing of cells determined by MTT assay. NIH3T3 and B16F10 cells incubated with varying concentrations of curcumin (10-50 μg/mL) and **NDI-Azo-cur** ([curcumin] = 10-50 μg/mL) (a) normoxic condition (in absence of CoCl$_2$), (b) with CoCl$_2$ induced hypoxia. (c) IC$_{50}$ determination of **NDI-Azo-cur** ([curcumin] = 10-50 μg/mL) after 24 h incubation of B16F10 cells in CoCl$_2$ induced hypoxic environment. The standard deviation and experimental errors were in the range of ~1-3 %, respectively, in triplicate experiments.

In a nutshell, hypoxia responsive destruction of self-assembly lead to curcumin release by means of azo bond breakage paving the path towards new cancer therapeutics by harnessing the properties of complicated tumor microenvironment in theranostic strategies (Figure 7).

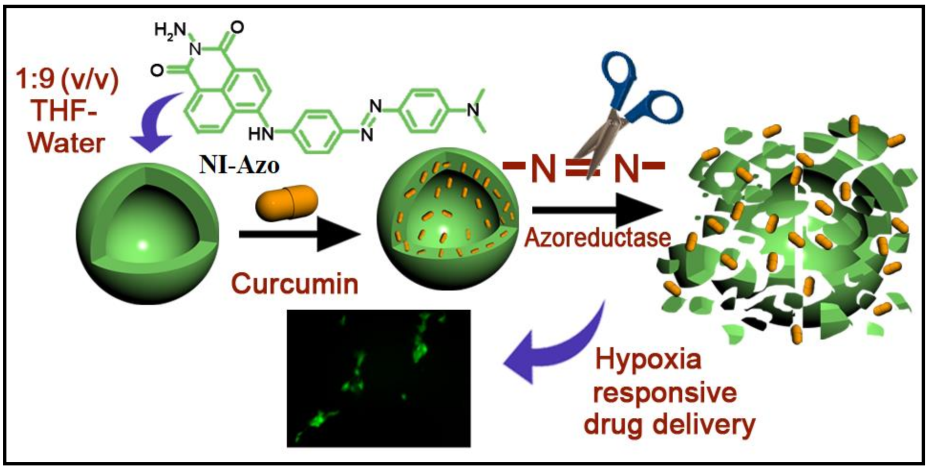

Figure 7. Schematic representation of hypoxia responsive curcumin release from **NI-Azo** vesicles.

Chapter 3 deals with Fluorescent organic nanoparticle (FONP) based bio-probes for selective detection of metal ion where the analyte ion acts as a trigger for quenching fluorescence. In this work, naphthalimide based L-histidine appended amphiphile (**NID**) was synthesized which formed bluish green emitting FONPs in 99% water-DMSO binary solvent system via *J*-type aggregation (Figure 8).

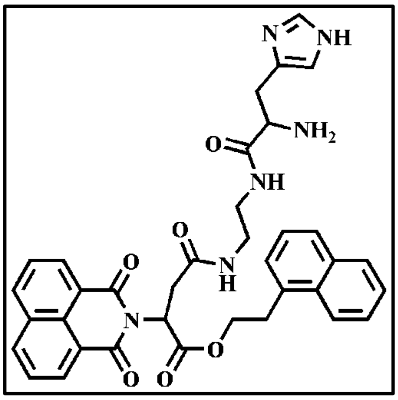

Figure 8. Structure of **NID** molecule.

The amphiphile showed negligible emission in DMSO (non self-assembled state) but became highly emissive at 60% and above water content at the aggregated state. Aggregation-induced emission (AIE) was observed with excimer formation at 470 nm upon excitation at 350 nm. These FONPs were employed in selective sensing of Fe^{3+} and bioimaging of Fe^{3+} inside cells due to their emissive properties and low toxicity (Figure 9).

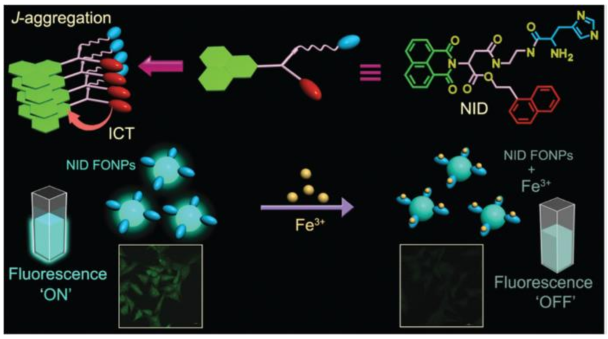

Figure 9. Schematic presentation of **NID** based fluorescent organic nanoparticles in the selective sensing of Fe^{3+} and as a diagnostic probe for Fe^{2+}/Fe^{3+} transition. ICT: intramolecular charge transfer.

Among the various tested metal ions, presence of Fe^{3+} led to the selective quenching of the emission intensity of **NID** FONPs due to 1:1 stoichiometric complex formation with the histidine residue (Figure 10). Consequently, the spherical morphology of the self-aggregated organic particle transformed to spindle shaped particles as confirmed by microscopic techniques. The limit of detection (LOD) of this turn-off sensor was calculated to be 12.5±1.2 μM having high selectivity over other metal ions (Figure 10).

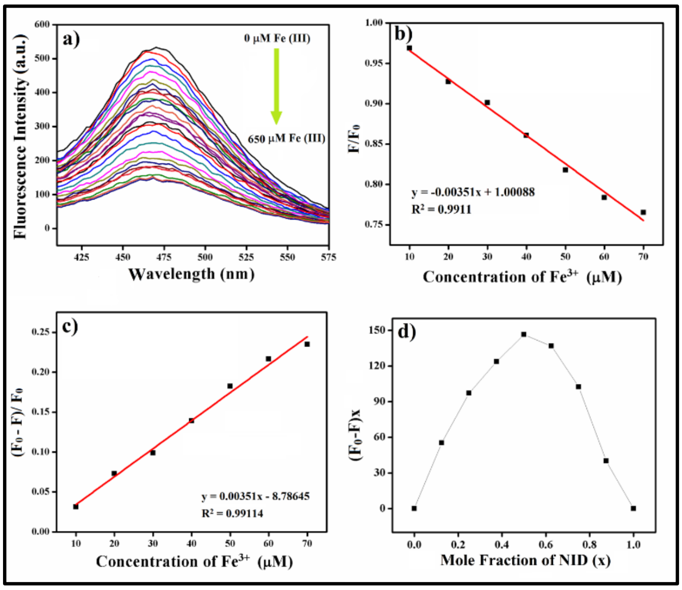

Figure 10. (a) Fluorescence spectra of **NID** FONPs (50 μM) in absence and presence of varying concentration of Fe^{3+} (excitation wavelength = 350 nm), (b) Stern-Volmer plot of Fe^{3+} doped in (1:99, v/v) DMSO-water solution of **NID** (50 μM), (c) Fluorescence response of **NID** FONPs towards Fe^{3+} sensing with varying concentration of Fe^{3+} in (1:99, v/v) DMSO-water ([**NID**] = 50 μM), (d) Job's plot for stoichiometry of metal complex.

Concurrently, **NID** FONP was successfully employed for bioimaging of Fe^{3+} ions via fluorescence quenching within living cells as well as detecting Fe^{2+}/Fe^{3+} transition selectively inside cancer cell due to its high H_2O_2 content. Co-culture experiment and flow cytometry further confirmed selective sensing of cancer cells. Hence, **NID** FONPs can be a selective diagnostic tool for cancerous cells on account of their higher H_2O_2 amount.

Chapter 4 of this present thesis is solely focused on development of self-aggregated FONPs with tuneable emission wavelength by modulating the amphiphilic backbone. Here, naphthalenediiimide (NDI) based amphiphiles (**NDI-1-9**) with varying amino acid substitution from L-alanine to L-phenyl alanine to 3-(2-naphthyl)-L-alanine with or without alkyl spacer (C-6, C-11) were developed (Figure 11).

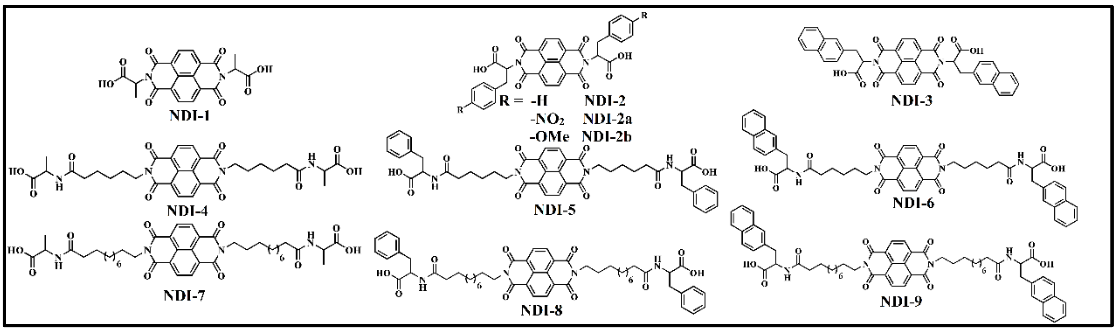

Figure 11. Structures of naphthalenediimide (NDI) derivatives, **NDI-1-9**, **NDI-2a** and **NDI-2b**.

Construction of self-aggregated organic nanoparticles of ~50 nm took place at 50 vol% water or methyl cyclohexane (MCH) onwards in DMSO/DMF or $CHCl_3$ via *J*-aggregation. All the developed organic nanoparticles (except **NDI-4** and **NDI-7**) exhibited aggregation induced emission at varying emission maxima (Figure 12).

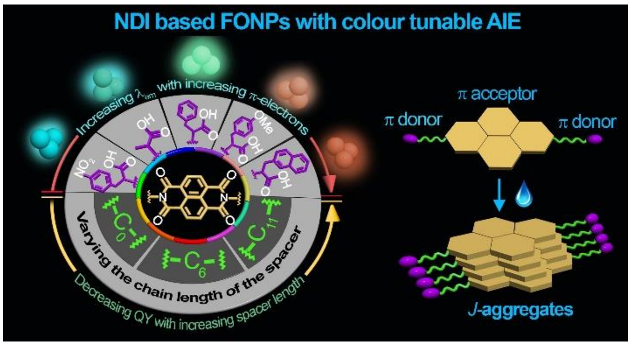

Figure 12. Schematic representation of various amino acid containing NDI based FONPs with tuneable emission.

Red shifted emission maxima were observed (greenish blue to bluish green to orange emissions) from λ_{em} = 484 nm to 495 nm and 590 nm in case of **NDI-1-3** FONPs upon enrichment of π-electron cloud from L-alanine to L-phenylalanine to 3-(2-naphthyl)-L-alanine. FONPs of 6-amino caproic acid spacer containing NDI derivatives (**NDI-5** and **NDI-6**) showed AIE at 505 nm and 545 nm (water in DMF/DMSO) and 11-amino undecanoic acid containing analogues (**NDI-8** and **NDI-9**) showed AIE at 480 nm and 585 nm in $CHCl_3$-MCH and DMF/DMSO-water. The multi colour emission from blue-green to yellow-orange with enhancement of π-electron cloud in the side chain of NDI derivatives was detected probably due to the facilitated electron transfer at a lower energy to the electron deficient NDI core that caused red shifted emission maxima. This was again clarified by controlling the availability of π-electrons of phenyl ring of **NDI-2** by incorporating electron withdrawing $-NO_2$ and donating -OMe groups at the molecular backbone (**NDI-2a**, λ_{em} = 475 nm and **NDI-2b**, λ_{em} = 570 nm**)** that showed blue (20 nm) shifted and red (75 nm) shifted emission maxima compared to that of **NDI-2** (λ_{em} = 495 nm). All these observations further ascertained that fluorescence property due to AIE of organic nanoparticle gets modulated depending on the presence of transferrable π-electron to the NDI core. Overall, this signifies the influence of electronic structure of the substituents in tuning the emission maxima of NDI derivatives causing multi colour luminescence (Figure 13). Nevertheless, increased alkyl spacer length between side chain substitution and NDI core produced relatively lower quantum yield apparently due to the impeded electron transfer (Figure 12).

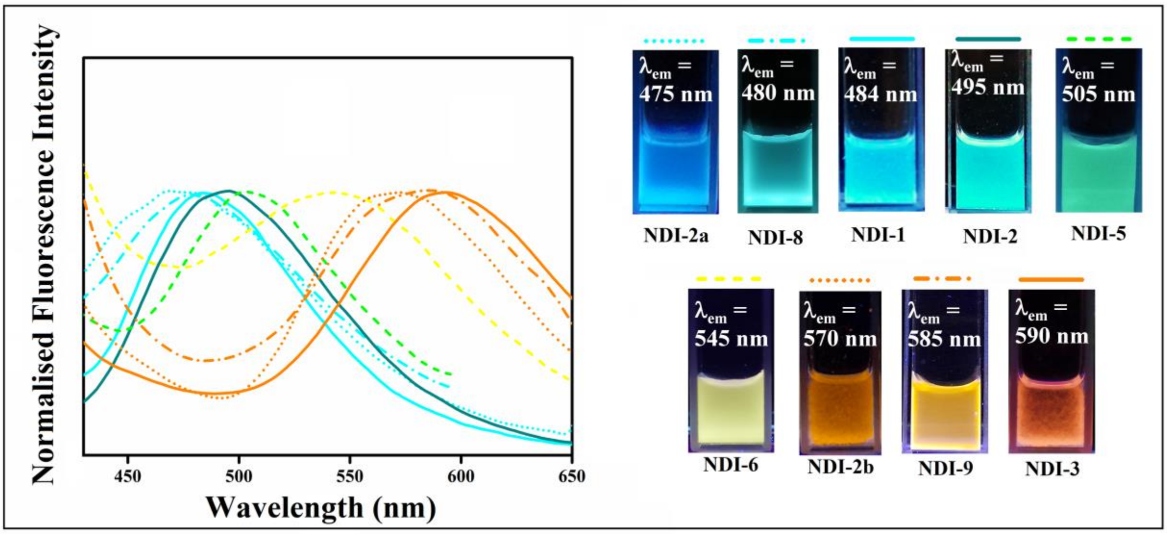

Figure 13. Tuneable emission maxima (with normalised emission intensity) of substituent-modified NDI derivatives (**NDI-1, 2, 2a, 2b, 3, 5, 6, 8** and **9** (λ_{ex} = 350 nm)) along with corresponding photographs of multicolour emission of the NDI derivatives irradiated with a UV-lamp (λ_{ex} = 365 nm).

Introduction

"A scientist in his laboratory is not a mere technician: he is also a child confronting natural phenomena that impress him as though they were fairy tales"

-Marie Curie

"Let Nature be your teacher."

-William Wordsworth

Human beings live in the realm of nature being constantly aware of its influence in his existence in the form of the air he breathes, the food he consumes as well as the water he drinks. Since the beginning, the relationship between man and nature has been uniquely complicated, being beautiful to puzzling to even extremely cruel sometimes. In a desperate attempt to tame the wild nature, humans became more and more interested in getting civilized. Nature has triggered this human civilization by forcing the mankind to face obstacles and find the solution. Nature is designed in a way that controls every step in this living world. Even after billion years of evolution, man could not solve the mysteries of nature and of humanity completely. Science enlightens us to know the acquirement of the "knowledge of the world of nature". It is the very ability of the mankind that observe and recognize all the regularities among the chaos in nature for survival since the emergence of Homo sapiens as a species. Evolution made humans the ultimate learning machines, that requires an oil named "curiosity" for proper functioning. Nature never fails to amaze its beholder sowing the seeds of eagerness to know and to question. Curiosity allows us to look for the reasons behind a natural phenomenon and think about the ways in which it can be applied elsewhere to solve a real-life problem opening the door to discovery and invention. We are blessed to be programmed to leave unbeaten track to explore new ones otherwise we would be doomed (Figure 1).[1]

Figure 1. Man and Nature

STIMULI-RESPONSIVE BEHAVIOUR FOUND IN NATURE

Nature is filled with examples of living systems reacting to external environmental changes (Figure 2).[2] Mimosa pudica plant goes through a change in leaf angles responding to touch whereas, the Venus flytrap quickly closes its leaves to entrap insects. Namaqua chameleons alters their colour by changing the space between guanine crystals under their skin and cephalopods change their skin colour according to their surroundings in self-defence. Inside the cells, charge gradient between the two sides of the membrane makes the ion channels operational. Even muscle contraction regulated by actin filaments are activated when calcium ions interact with troponin. In an attempt of mimicking this naturally occurring responsivity scientists have been keen to develop stimuli responsive "smart" materials and utilize them to understand & solve various problems.

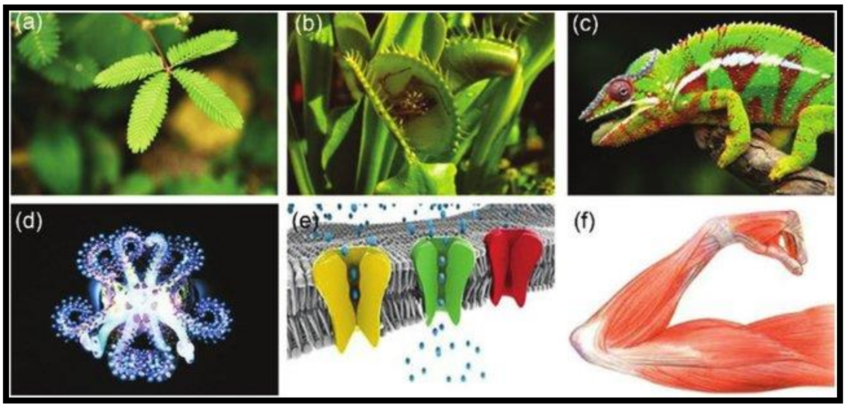

Figure 2. Stimuli-responsive behaviours found in nature. (a) Mimosa pudica, (b) Venus flytrap, (c) chameleons, (d) squid, (e) ion channels of cells membranes and (f) muscles. (taken from reference 2)

SELF-ASSEMBLY: FROM CHAOS TO ORDER

Our universe is an elaborate ordered system where patterns and connectivity are the conduits of energy flow towards achieving order in nature. Everything that is not truly random has some kind of pattern in it. We see patterns everywhere in nature: from symmetry of snowflakes, fractals of fern leaves, the curl of a chameleon's tail, the spiral of a pinecone's scales, natural tessellation in honeycomb to even the ripples created by wind moving in sand dunes (Figure 3).[3-8] "Self-assembly" is a natural event associated with the movement from "chaos to order." From atoms to stars to even galaxies are created from assembly of fundamental particles. The most elementary yet most complicated example of self-assembly found in nature is "cells". The building block of all life forms is a well-ordered system and the progression of life depends on the assembly and disassembly of the biological components going within it. Taking inspiration from all these things, a scientist dreams the wildest dream of creating life artificially.

Figure 3. Order in nature.

BEYOND AMPHIPHILES: TOWARDS SELF-ASSEMBLY & INSPIRATION FROM NATURE

A long time ago in the year of 1937, Karl Lothar Wolf first coined the term “Übermoleküle” (supermolecule or supramolecule) in an attempt to describe hydrogen-bonded acetic acid dimers.[9] Small molecules spontaneously come together by different non covalent interactions like hydrogen bonding, hydrophobic interactions, π-π stacking, coordination interactions, van der Waal’s forces and ion-dipole interactions and give rise to aggregates of different morphologies with dimension ranging from nanoscale to micrometres.[10-12] Colloids, liquid crystals, biomolecular condensates, micelles, reverse micelles, liposomes, gel and organic nanoparticles are examples of such supramolecular assemblies. World’s greatest and most productive factory “Nature” is flooded with examples of Hydrogen bond-assisted supramolecular assembly. For instance, bi-layered cell membrane, DNA double helices as well as α-helices or β-sheet structures in proteins are result of such self-organization. Among them, one of the most amazing models of self-assembly, the cytoplasmic membrane (Figure 4) composed of lipid bilayer with embedded protein, can separate the interior of all cells (organelles) from the extracellular adverse atmosphere and provides suitable environment to perform cellular processes smoothly inside cells.[13]

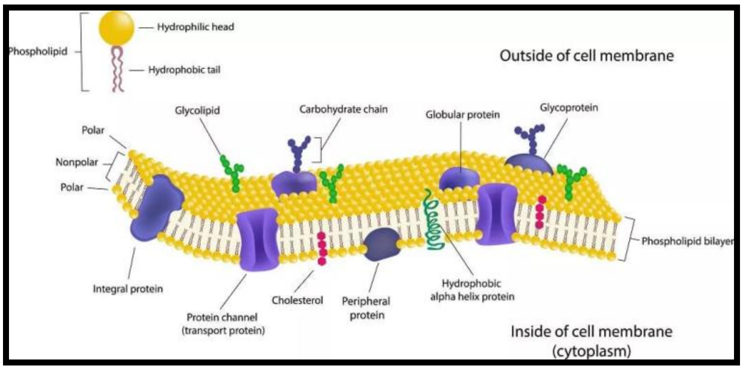

Figure 4. Cross-section of cell-membrane. (taken from Reference 13)

In case of DNA, the carrier of genetic information for the development, advancement and reproduction of all living organisms, the double helix structure is formed by H-bonding between nucleobases: adenine, thymine (two hydrogen bonds) and guanine, cytosine (three hydrogen bonds) (Figure 5).[14]

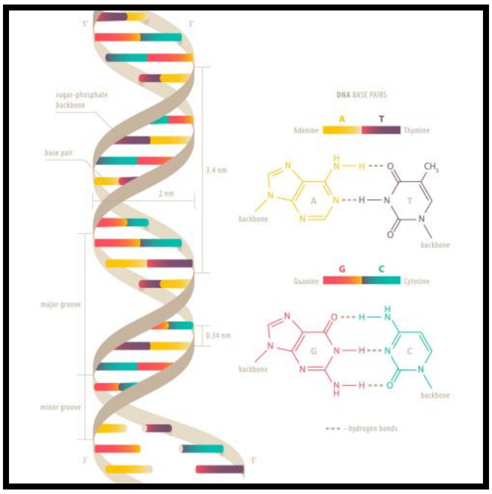

Figure 5. Chemical structure of DNA. (taken from Reference 14)

In another amazing example of nature created supramolecular self-assembly, the primary structure of protein (the amino acid sequence) pre-regulates different segments to achieve well-organized secondary structures (α-helices or β-sheets) by means of hydrogen bonding between -CO group and -NH groups of the peptide bond. These chains are then folded into tertiary structure by H-bonds, electrostatic forces, disulphide linkages, and Vander Waal's forces which determines the overall topographic shape of the macromolecules. Lastly, the folded macromolecules assemble into the bioactive structural protein (quaternary structure). To this end, researchers have aspired to utilize supramolecular self-assembly for (1) mimicking the natural biological membrane, (2) revealing the mechanism for the biological self-organization and (3) creating structures or materials capable of novel biological roles.

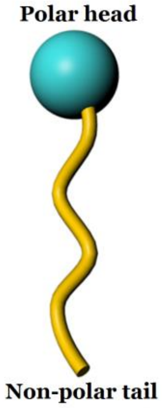

Figure 6. Structure of amphiphile.

Now, if we converge our thoughts to the basic building block of self-aggregates in the diverse world of self-assembly that has been controlling our life ever since in every possible way, we end up with the “amphiphiles” or “surfactants”. Amphiphiles (from the *Greek* words, *amphis*: “both”, *philia*: “love”) are molecules with a hydrophilic “head” group which are ionic, polar or hydrogen-bond (H-bond) forming groups and a hydrophobic “tail” part that are generally saturated or unsaturated hydrocarbon chains (Figure 6).[15-16] Presence of both lipophilic and hydrophilic part renders solubility both in aqueous medium and some organic solvents. ‘Surface active’ property leads to the nomenclature of “surfactant” which is used for lowering the surface tension in interface.[17] Surfactants undergo molecular self- aggregation in solutions and in bulk, generates different architectures.[18-19] By tuning the amphiphilic structures, not only regulation of morphology can be achieved to some extent, but also incorporation of several functionality leads to different task-specific application. These amphiphiles can be categorized roughly in four different classes: anionic, cationic, zwitterionic and nonionic depending on the "head” group functionality (Figure 7).[20] Anionic amphiphiles, with negatively charged head groups and positively charged counterions, are widely used as detergents. Cationic surfactants are composed of positively charged head groups (e.g. quaternary ammonium ion) and an anion such as halide as a counterion. Most common example of cationic amphiphiles are cetyltrimethylammonium bromide (CTAB) and sodium bis(2-ethylhexyl) sulfosuccinate (AOT).[16,18,20] Zwitterionic amphiphiles consists of both positive and negative charge in their backbone (e.g. phospholipid, phosphatidylcholine). It shows amphoteric nature depending on the pH of the environment. At higher pH, it acts as a cation due to protonation while acting as an anion at low pH. The nonionic surfactants, on the other hand, does not contain any charge. In that case, the polar head consists of polyether or polyhydroxyl functionalities.[16] Depending on the topology of the both polar head and non-polar tail, other two classes of macromolecular amphiphiles are introduced: gemini and bola-amphiphiles.[16] For gemini amphiphile, two hydrophilic heads are attached with a spacer and two closer hydrophobic chains, that renders a compact packing.[20] Bola-amphiphiles are macromolecules containing two polar head groups located at both terminals of single or multiple alkyl chain (hydrophobic residue).[20]

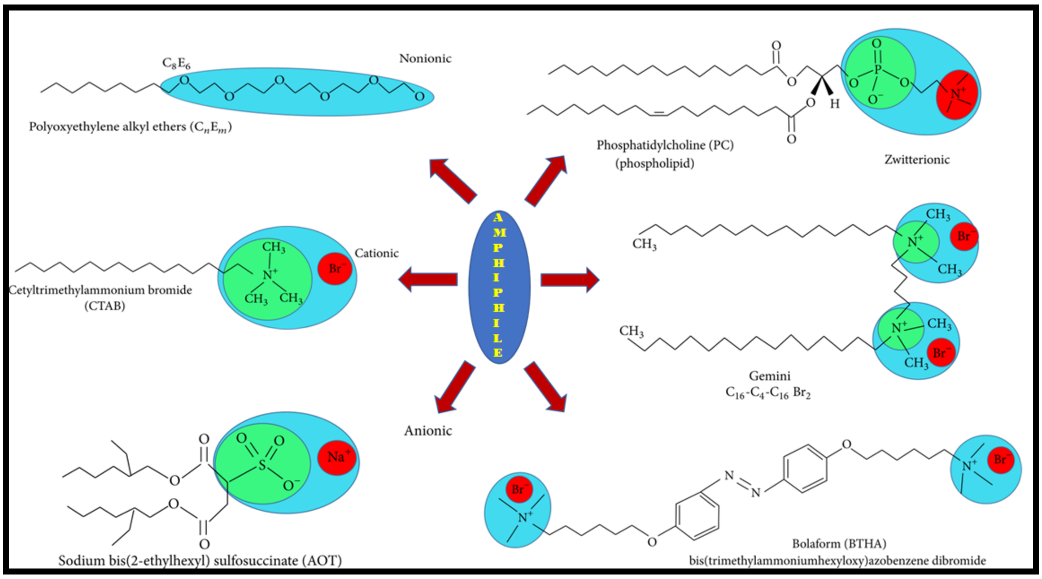

Figure 7. Classification and examples of amphiphiles. (taken from reference 20)

These two unconventional amphiphiles are widely used in dispersing, foaming and drug as well as gene delivery.[20] In addition to formation of the classical spherical or disk like aggregates, Bola amphiphiles are also known to generate helical self-assemblies.[21] In the field of surface chemistry, Hydrophilic and lipophilic balance (HLB) is one of the most significant parameter in developing diverse self-assembled systems ranging from micelles, reverse micelles, vesicles, and liquid crystalline mesomorphic phases to higher order self-assemblies like fibres, ribbons, helices and microtubes. It is fundamentally a ranking of how hydrophilic an amphiphile is; determined by calculating values for the different regions of the molecule, as described by Griffin in 1949 and 1954.[22,23] The effective final morphology is governed by the structural features of the building block as well as by the balance between the hydrophobic hydrophilic segments (HLB) of the supramolecular amphiphiles that leads to several task specific bio-chemical and bio-medicinal application.

NON-COVALENT INTERACTIONS: BRINGING THE AMPHIPHILES TOGETHER

In an amphiphile, the hydrophobic and hydrophilic segments are irreversibly linked by covalent bonds. On the other hand, a supramolecular self-assembly is composed of amphiphiles, who are connected with one another by different non-covalent forces like hydrogen bonding, van der Waal's forces, hydrophobic interaction π-π stacking e.t.c (Figure 8).[24-28]

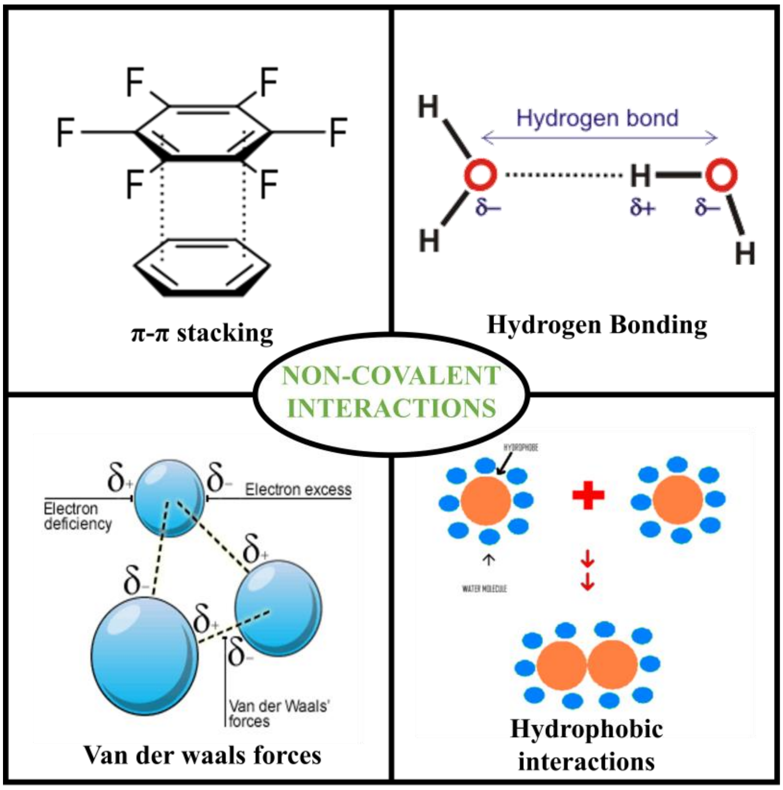

Figure 8. Different types of non-covalent interactions. (taken from reference 24-27)

Although the forces involved in assembly are weak in nature, relevant number of these weak interactions provides an overall effect that is sturdy enough to hold different amphiphiles together.[20] Furthermore, these interactions are weak enough to provide the aggregates the flexibility it requires as well as sturdy enough to endure slight perturbation. As mentioned earlier, these interactions are very weak in nature compared to covalent bonds, metal ligand interaction is the only exception (Table 1). H-bonding is very crucial in most of the biological processes that happen within cell; it combines and breaks apart biomolecules as per requirement. All biomolecules have H-bond acceptors and donors within them. For example, in water molecule (H2O) the non-bonding electrons act as H-bond acceptors while hydrogen atoms are the donors. Consequently, H-bonding plays an important role on the properties of water as well as its relevant functions in biological systems.[29-30] The second principle driving force of self-assembly is hydrophobic effect as it brings non polar (hydrophobic) molecules come together into supramolecular self-aggregation.[31-32] Besides these two, the van der Waal's interaction is another significant weak interaction between atoms or molecules that disappears with increased distance. It is considered to be an amalgamation of London forces between instantaneously induced dipoles and Debye forces between dipoles and induced dipoles, For instance, in biological membranes, the tightly packed arrangement of hydrocarbon chains of phospholipids results in due to van der Waal's interaction.[33-34]

Table 1. Strength of the main noncovalent interaction involved in amphiphiles self-assembly (taken from reference 20).

Bonding and interaction type	Energy in kJ/mol
Covalent bond	100–400
Ion-ion/ion-dipole/dipole-dipole	200–300/50–200/5–50
Hydrogen bond	4-120
Cation-n(π) interaction	5-80
π-π interaction	0–50
van der Waal's interaction	<5
Metal-ligand	0-400

All the self-assembled nanostructures (micelles, reverse micelles, vesicles and supramolecular gels etc) are manifestations of these soft interactions. Notably, the reversible nature of the interactions leads to dynamic self-assembly suitable for task specific applications.[35-38]

VARIOUS SELF-AGGREGATES

Construction of nanoscale materials decorated with functionalities tasked for specific applications have never been easier without the emergence of supramolecular self-assemblies especially with the bottom up approach.[39] From a chemist's point of view, supramolecular aggregate are nothing but the assembled form of "encoded" molecular components, although the chemical and physical pathways are often based on speculation, observing the nature of the interaction the components have with each other along with the environment surrounding them.[39] Control over the geometry of the self-aggregates can be achieved by carefully tuning the molecular design as well as by modifying the solvent systems. Molecular recognition can be done by incorporating precise moieties in the amphiphilic backbone regulating it for task-specific applications. In aqueous solution, surfactants tend to position themselves in a manner so that their hydrophilic head groups remain outside keeping hydrophobic alkyl chain at the centre in order to form micelles.[17] Conversely, in non-polar solvent, these amphiphiles orient in opposite direction generating reverse micelles.[17] Apart from these fundamental supramolecular structures, higher ordered self-assembled systems like vesicles, emulsions, liquid crystals, gels, nano fibers, ribbons etc. have the major emphasis in interdisciplinary subjects in recent times.[40-42]

Micelles

Let us begin with one of the simplest forms of self-assembly: micelles. When the amphiphilic molecules are spread in water, they combine to form micelle, a spherical self-aggregate, after a certain concentration called 'Critical Micellar Concentration' (CMC).[15,43] CMC is an intrinsic property of a surfactant and the morphology and dimension of a micelle depends on surfactant concentration, temperature, pH, and ionic strength etc. Here, the hydrophobic alkyl part stays inwards creating a lipophilic core, at the same time, the hydrophilic groups direct outwards in the water (Figure 9).[12] Below CMC, surfactants remain as monomers completely surrounded by water whereas in the micellar form, their hydrophobic part is hidden inside having less contact with the aqueous phase. This paves the path towards their applicability as detergent. Not only that, the core of the micelle acts as a vessel for multistep chemical reactions providing a "green chemistry" platform.[44]

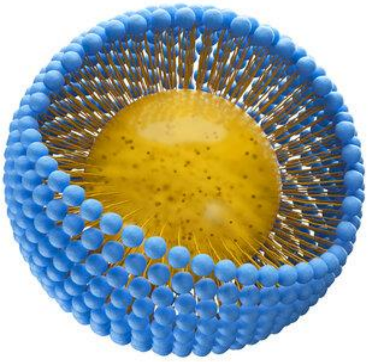

Figure 9. Structure of micelle. (taken from reference 45)

Reverse micelles

As the name suggests, reverse micelles are spherical aggregates formed in apolar medium resulting in water-in-oil system.[29-31] In this case, polar heads are oriented inwards creating a "water pocket" inside themselves whereas lipophilic groups stay at the periphery. (Figure 10).[46-47] The size of the water pool is directly related to molar ratio of water to surfactant ($[H_2O]/[Surfactant]$) termed as W_0.[46-47] The reverse micelles resemble biological membrane in so many ways in terms of compartmentalizing ability that they results in huge applicability in biomimetics.[48-49]. Reverse micelles act as experimental media for the development of several nanomaterials judicially choosing the proper surfactant.

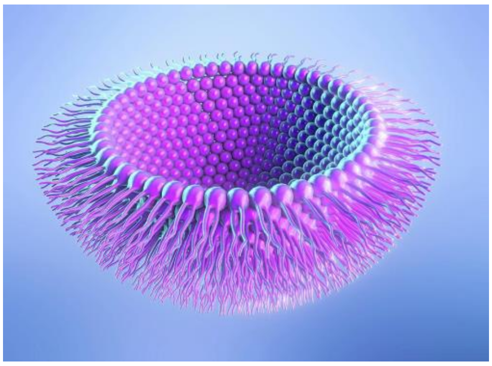

Figure 10. Structure of reverse micelle. (taken from reference 14)

Supramolecular gels

Supramolecular gels are magnificent example of self-assembly that has a tremendous application in wide range of interdisciplinary sciences.[50-54] Gels are macroscopically semisolid materials that do not flow on turning down the vial (Figure 11).[55] Here, a large number of solvent molecules remain entrapped by small amount of gelator molecules. It is kind of an intermediate state in between solubilization and crystallization. Both chemical cross-linking or physical interactions can cause gelation. Generally, gels formed due to chemical bonding, are thermally irreversible (polyester, polyamide, poly(vinyl alcohol), polyethylene etc.).[56]

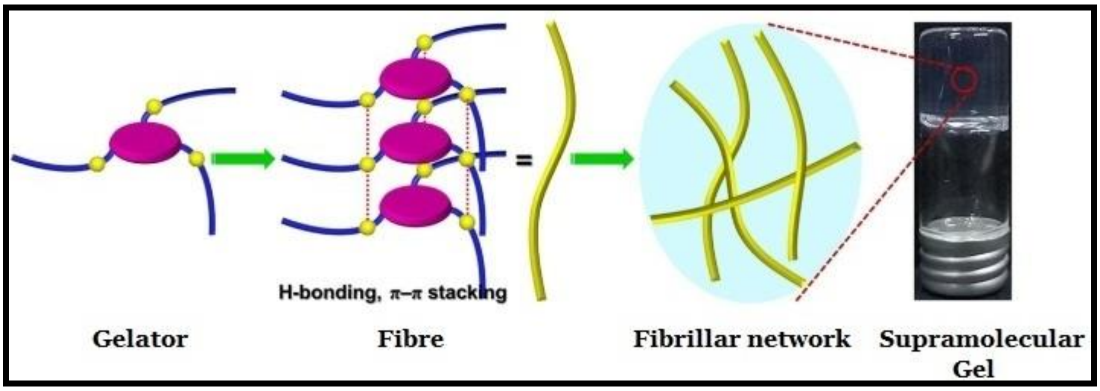

Figure 11. Schematic representation of the formation of self-assembled fibrillar network (SAFIN) and gel. (taken from the reference 55)

On the contrary, gels formed by weak non-covalent forces (crown ethers, cyclodextrins, cucurbiturils etc.) get easily converted to sol by heating. Soft materials derived from low molecular weight gelators (LMWG) (supramolecular or simply molecular gels) is a widely explored research topic nowadays due to their potential applications in controlled drug release, pollutant removal and tissue engineering.[56-59] Self-assembled fibrillar network (SAFIN) is formed via combined influence of H-bonding, π-π stacking, donor-acceptor interactions, metal chelation and van der Waal's force and other soft interactions.[57-59]

LMWGs are categorized into three major classes: (1) hydrogelators (that immobilize water), (2) organogelators (that can gelatinize organic solvents) and (3) ambidextrous gelators (that can restrict the gravitational flow of both water and organic solvent).

Low molecular weight hydrogels (LMHG)

Hydrogelators (small amphiphilic molecules able to immobilize water) are becoming an interesting topic of research due to its application in tissue engineering, vehicles for drug delivery, and pollutant capture and removal.[60-63] As stated earlier, an optimum balance between hydrophobicity and hydrophilicity is crucial to design a hydrogelator molecule as the hydrophobic groups promotes aggregation and hydrophilic groups provide the water solubility amphiphilic. Conventional amphiphiles contain a polar head group and a hydrophobic entity. Incorporation of proper functional motifs within the molecular structure make the hydrogelators respond to external stimuli (pH, light, enzymes) and even enables task specific (delivery vehicle, reduction of metal salts etc.) applications.[64-66]

Low molecular weight organogels (LMOG)

Low molecular weight organogelators (LMOGs) forms gels in a wide variety of organic solvents (e.g. *n*-hexane, *n*-octane, acetonitrile, benzene, toluene, nitrobenzene etc.).[67-68] In case of organogels, the principle forces responsible are mainly dipolar interactions, H-bonding, electrostatic interaction, π-π stacking, metal-coordination etc.[65-66] The vital factors like solvent polarity, conformational flexibility, molecular shape of the gelator, and temperature too impact organogelation. The applicability of organic gelators lie over *in situ* formation of nanoparticles, phase selective gelation, dye removal, development of light harvesting soft materials and enzyme immobilization matrices.[67-69]

Ambidextrous gelators (AGs)

Ambidextrous gelators (AGs) are the small organic molecules that can immobilize both water and organic solvents i.e. a single molecular scaffold forms hydrogel and organogel simultaneously.[70-73] This is more advantageous because these materials can immobilize solvents with extreme polarities (from non-polar organic solvents to highly polar water molecules). The structural motifs of AG enable to gelatinize solvents of extreme polarity by means of non-covalent interactions (both hydrophilic and hydrophobic) in both kind of solvents. AGs are gaining much attention in recent years because of their unique physiological behaviour and multi-tasking ability in the material science and nanotechnology.[70-73]

Vesicle

Another beautiful manifestation supramolecular self-assembly is vesicles or liposomes (Figure 12).[74] British haematologist A. D. Bangham first discovered the lipid vesicle in 1964. Although, at that time the designated terminology was “spherulites”.[75] The commonly used term “vesicle” was originated from the Latin word “vesicula” which means “small bladder” and it is extensively used in biology, chemistry and. Not only phospholipids, but also small amphiphilic molecules with a polar head and double hydrocarbon chains are capable of the forming bilayer vesicles with inner aqueous core and outer bulk water separated by hydrophobic layer making it an appropriate mimic of biological membrane.[76]

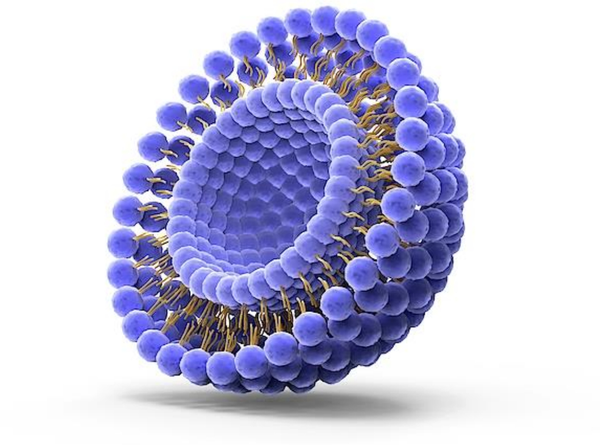

Figure 12. Structure of vesicle (taken from reference 74).

The constituent amphiphiles of these vesicles may be single-/twin-chained polymeric molecules, phospholipids that form of vesicles through apt mechanism.[76-78] Ease of fabrication as well as functionalisation, cytocompatibility, compartmentalizing ability, high encapsulating efficiency and exogenous stimuli responsiveness enhances their utility in task specific applications in the broad arena of biology, chemistry and pharmacology.[76] Vesicles are majorly classified into three categories: i) multilamellar vesicles, ii) unilamellar vesicles and iii) multivesicular liposomes. As the terms suggest, unilamellar vesicles are comprised of only one lamellar lipid bilayer whereas, multilamellar vesicles are made of several lamellar membranes displaying a onion-like morphology and in a multivesicular liposome several vesicles remain inside of a bigger vesicle.[79] Unilamellar vesicles may be small, large or even giant having dimension of 20-100 nm, >100 nm and >1000 nm.[79] Both hydrophobic and hydrophilic cargo can be loaded within vesicles making them an excellent nano-carrier.[80] Designing the amphiphile in such way that it can lead to stimuli responsive drug release when required, is beneficial. Therefore, this membrane mimetic system has huge prospects as a cellular transporter in gene therapy and drug delivery.[78]

STIMULI

A stimulus (plural "stimuli") is anything that can trigger a physical or behavioural change. Soft materials that respond to those stimuli are being leveraged to improve spatiotemporal control of therapeutics. Design and development of these materials that undergo physical or chemical transformations in response to explicit biological signals is a significant area of research not only for improving efficacies of current therapies and imaging tools but also for emerging customised theranostic agents.

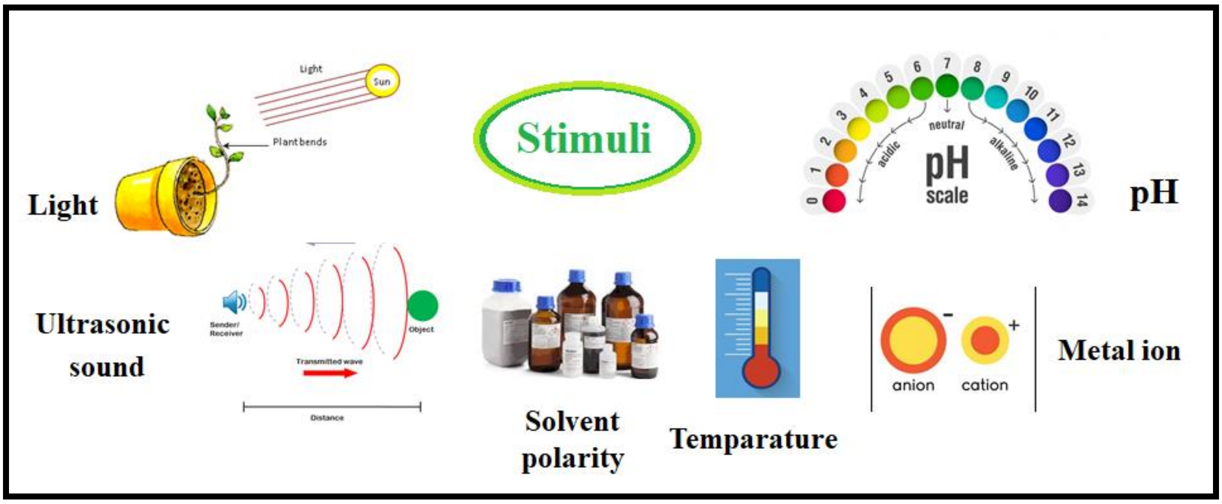

Figure 13. Different types of stimuli (taken from reference 81)

Primarily, stimuli can be classified in two categories: (a) exogenous and (b) endogenous. Some nanomaterials are triggered by external physical stimuli like heat, light, ultraviolet and near Infrared (NIR) radiation, ultrasound as well as magnetic fields, in addition to mechanical forces for instance, shear thinning upon injection.[82-85] Endogenous stimuli include pH, hypoxia, redox or enzymes, as well as temperature variations.[86-90] Even glucose, nucleic acids and other biomolecules, ATP and reactive oxygen species (ROS) can act as innate biological stimuli as they manifest the physiological difference between healthy and diseased cells.[91] Therefore, development of task-specific materials is crucial with the advantages of their stimuli responsive nature that has potential to mimic biological processes.

DRUG DELIVERY SYSTEMS (DDS)

Drugs have been used to improve health and protecting mankind from life threatening diseases for ages now. Development of a new drug is a costly and time-consuming affair owing to discovery, clinical testing and regulatory approval. Also, eliminating the side effects of these drugs still remain a challenge even today especially in case of diseases like cancer, neurodegenerative diseases, and infectious diseases. Three drug delivery paradigms that construct the foundation of contemporary drug delivery are drug modifications, microenvironment alterations and drug delivery systems (DDS).[92] Drug delivery systems can amalgamate these previous two approaches by forming an interface between the drug and its microenvironment. A drug delivery system (DDS) is a formulation or a device that introduces a therapeutic material to the body, advances its efficiency and lowers cytotoxicity by regulating the rate, time and centre of drug release.

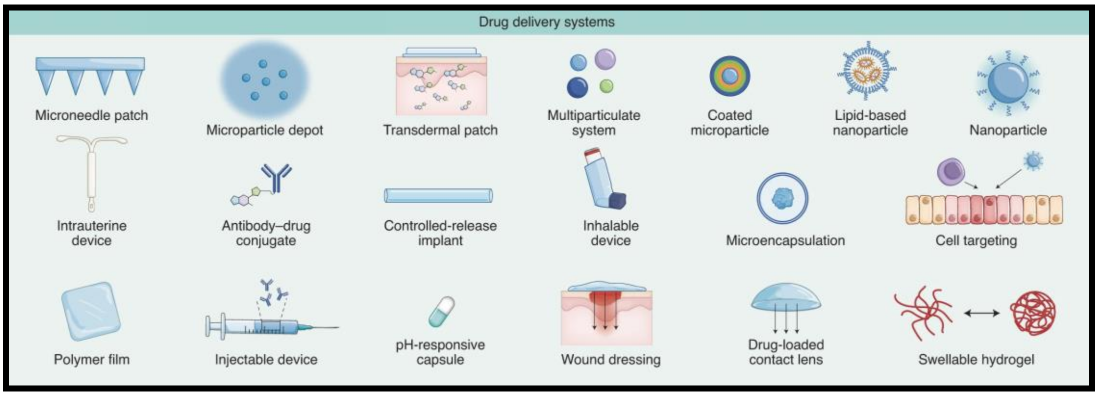

Figure 14. Diverse drug delivery systems (taken from reference 92)

In the initial years of drug delivery, it was determined that varying the rate of drug release can change biodistribution, half-life of the drug, total drug exposure with time as well as its maximum concentration in serum.[93] Even though, altering the dose and the infusion rates can impact these parameters, the emergence of "controlled-release" delivery systems paved the path towards better control.[94,95] Examples of DDS include hydrogels, micelles, vesicles, polymeric materials, micro and nanoparticles, that modify the particle-surface augmenting drug longevity and aiming certain cells via target-specific interactions with the microenvironment.[96] A DDS not only solves the problem of poor drug solubility (as well as toxicity due to the used solubilizer) but also it eliminates the possibility of rapid renal clearance. Therefore, requirement of higher doses can be avoided. Several examples of controlled-release systems can be found in literature, most of them are small molecules. The same delivery strategy is applicable for peptide and protein delivery. The effectiveness of peptide therapeutics was strengthened by "sustained-release" systems which is basically a subclass of controlled-release systems that keeps therapeutic drug concentrations intact for longer time periods. Leuprolide acetate, formulated in microspheres (Lupron Depot) was considered a pioneer of sustained release systems (release for up to 6 months) followed by other peptide therapeutics.[97-98]

SMART DDS (STIMULI-RESPONSIVE DDS)

The concept of "smart" DDSs has emerged from the "controlled release" platforms. In case of smart DDSs, a drug is released only at a target place reducing the side effects in a significant manner. At present, the drug-loaded nanocarriers (polymeric nanoparticle, organic-inorganic hybrid nanoparticle, liposomes, exosomes) accumulate at the targets by active or passive targeting technique and release only there by means of stimuli-responsive characteristics.[99] As discussed earlier, these stimuli can be endogenous and/or exogenous. One of the most common triggers is p^H of the environment. Most DDSs are based on the pH difference of stomach (pH = 2) and intestinal track (pH = 7).[100] Targeting the low pH in the tumor matrix is a well-known way of cancer therapeutics.[101]

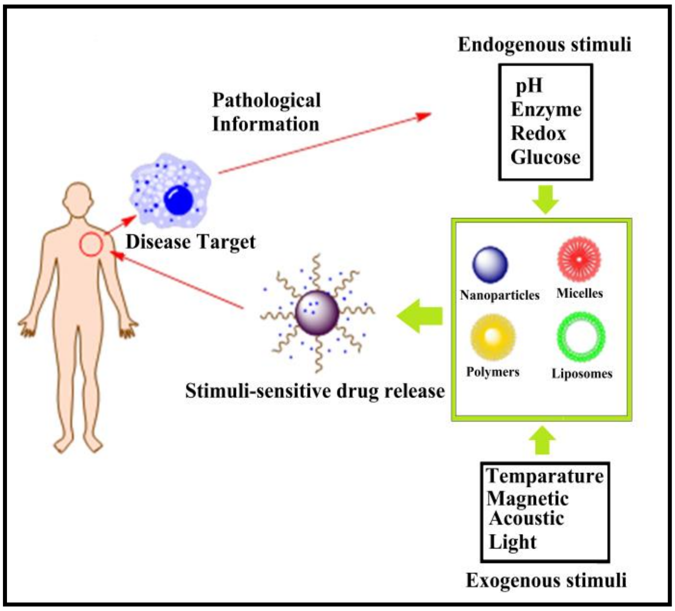

Figure 15. Stimuli responsive DDSs (taken from reference 99)

Utilizing the variation of redox potential in microenvironment, redox responsive DDSs are developed. Among which, Glutathione (GSH) sensitive delivery system is an excellent option for targeting cancer cells owing to significantly high abundance of GSH levels within tumor cell compared to that in normal cells.[102] Enzyme responsive delivery vehicles are drawing much attention nowadays as lipase, glycosidases, proteases or phospoholipases are involved in all kind of metabolic pathway, therefore they can achieve enzyme-facilitated drug release by the bio-catalytic action at the inflammatory as well as cancer cells.[103] Temperature can be another trigger for drug release as inflammation or cancer cells have higher temperature compared to normal cells.[104] In addition to that, tumor cells can be externally heated by triggers like (e.g. ultrasound, magnetic field).[105] These eventually lead to thermos-sensitive DDS development. Photo-sensitive nanocarriers can attain on-off drug release by external light illumination regulating assembly or disassembly.[106] Sometimes a combination of multiple stimuli leads to desired outcome.

VESICLES AS STIMULI RESPONSIVE DDS

In the year of 1971, Gregoriadis et al. utilized liposomes as drug delivery systems for the first time.[107] Since then, vesicles (particularly of diameter up to 100 nm) are widely being used as carrier of anti-cancer, anti-inflammatory drugs and gene medicines. [108], The first FDA approved nanomedicine delivery system is Doxil® which comprises of PEGylated liposomes.[109]

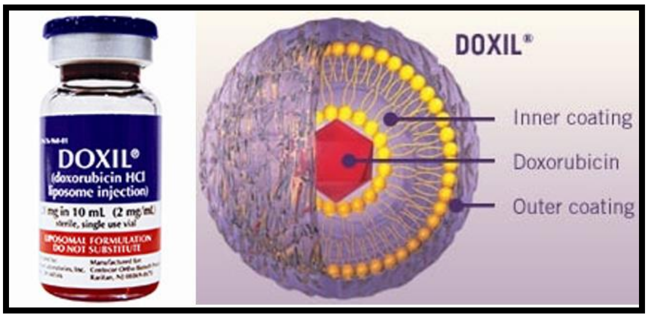

Figure 16. Doxil (taken from reference 110,111)

Among nanocarriers, drug potency is never an issue for vesicles as each of them can entrap thousands of drug molecules.[112] Quite naturally, hydrophilic drugs can be readily encapsulated within the aqueous core, but neutral hydrophobic drugs have a tendency to be quickly unloaded in presence of cell membranes.[113] Luckily, “remote loading” techniques that depend on pH or chemical gradients across the bilayer results in brilliant retention of hydrophobic drugs (such as doxorubicin and vincristine).[114-115] Control over the rate and degree of drug bioavailability mostly rely upon the design of triggered-release systems where the drug release takes place by alteration in pH, temperature, magnetic fields, enzymes, light or radiofrequency.[116-117] Among them, use of temperature sensitive liposomes is most convenient in terms of both safety and capability.[118-119] ThermoDox is a temperature sensitive liposomal Dox that has gone closest to clinical use by clearing phase-I trial.[118] furthermore, loading vesicles with MNPs and exposing them in magnetic field brings about cytocompatibility, efficient targeting, easy recovery and improved efficacy.[120] More often than not, external triggers turn out to be more efficient as well as specific with improved spatial and temporal resolution decoupling the combining effects that generate because of the biological heterogeneity.

ORGANIC NANOPARTICLES

Organic nanoparticles (ONPs) are generally defined as particles comprised of carbon-containing macromolecules (mainly lipids or polymeric) with dimension of 10 nm to 1 µm.[121-122] Their utility lies in various fields ranging from electronic to photonic, conducting materials to sensors, medicine to biotechnology, and so forth.[123-126] Uniquely tailored structure are easily attained for this organic nanoparticles that aids intended applications. For supramolecular self-assembled systems, non-covalent interactions make the organic nanoparticles more labile, susceptible to external environment along with easing their excretion process. Organic nanoparticles can be classified into two groups: nanospheres and nanocapsules (Figure 17).[126-127] Nanospheres are comprised of solid mass entirely and nanocapsules are hollow shell like structures with liquid or empty core enclosed by an organic residue. In general, these ONPs are round but non-spherical shape are also quite natural.

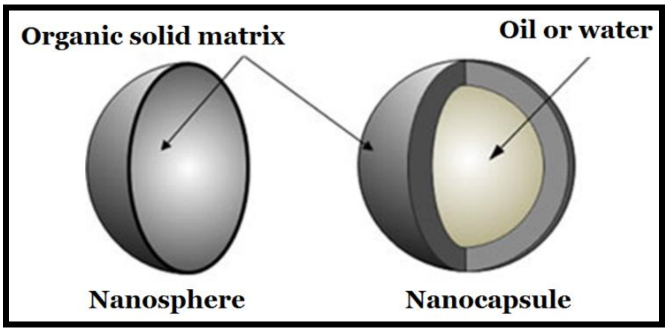

Figure 17. Structure of organic nanoparticles. (taken from reference 126,127)

AGGREGATION INDUCED EMISSION: ORIGIN OF FLUORESCENT ORGANIC NANOPARTICLES (FONPS)

> *"Together We Shine, United We Soar!"*
>
> ...[128]

Since the origin of life, light has been indispensable for survival. Luminophores emit light. To decipher the mystery of light, multiple breakthrough innovation related to light-emitting processes has taken place. Generally, luminescence of individual entities have been widely explored in absence of any kind of chromophoric interactions.[129-131] However, the emission property suffers a lot at higher concentration which is termed as " concentration quenching" phenomenon.[132] "Formation of aggregates" is reason behind this reduction in fluorescence. Therefore, this is commonly denoted as "Aggregation caused quenching" (ACQ) (Figure 18).[128,133,134] As a matter of fact, most conventional fluorophores are comprised of multiple planar aromatic rings that results in strong π-π interaction that eventually quenches the emission as the relaxing pathway of the aggregates from excited to ground state becomes non-radiative.[128,134] This ACQ phenomenon restricts the application of these conventional fluorophore significantly.

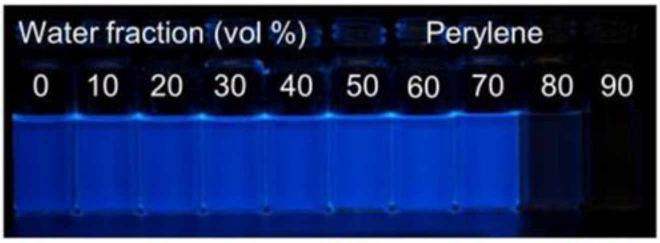

Aggregation-Caused Quenching (ACQ)

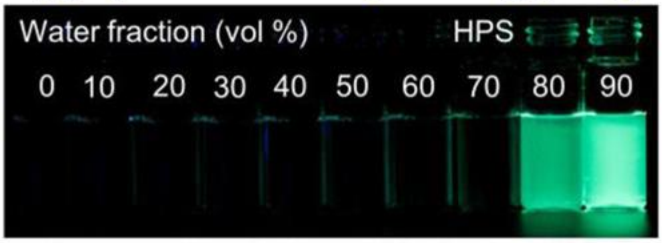

Aggregation-Induced Emission (AIE)

Figure 18. Examples of aggregation-caused quenching and aggregation-induced emission. (taken from reference 128)

To overcome the shortcomings of conventional fluorophores with ACQ, several attempts were made. In the year of 2001, Tang *et al* discovered an extraordinary luminogen system, where the fluorophore shines brightly in aggregated state (Figure 18).[131,135] A series of silole derivatives were reported which were non-emissive in solution state (molecularly dissolved state) but showed intense photoluminescence in their self-aggregated state. This unusual phenomenon was coined as "Aggregation Induced Emission" (AIE). After this discovery, molecular design of the fluorophore was modified again and again for efficient AIE during self-aggregation.[134-135] Further research proceeded with these AIE active aggregates (generally spherical), which were majorly π chromophores. They were called Fluorescent Organic nanoparticles (FONPs). These non-planar or propeller shaped π-conjugated molecules have a potential to restrict their intramolecular rotation by dodging strong π-π interaction in their assembled state. This essentially minimalize the non-radiative pathway that leads to enhancement of emission intensity during self-assembly (Figure

19).[134] Pre-associated excimer formation/*J*-aggregation/*E*-*Z*-isomerization/twisted intramolecular charge transfer (TICT)/ excited-state intramolecular proton transfer (ESIPT) are some other necessary factors that leads to AIE.[134] As the FONPs are very easy to prepare, easy to functionalize and have excellent cytocompatibility compared to its inorganic counterparts, they are being widely used in sensing, bioimaging as well as in optoelectronic devices. [134]

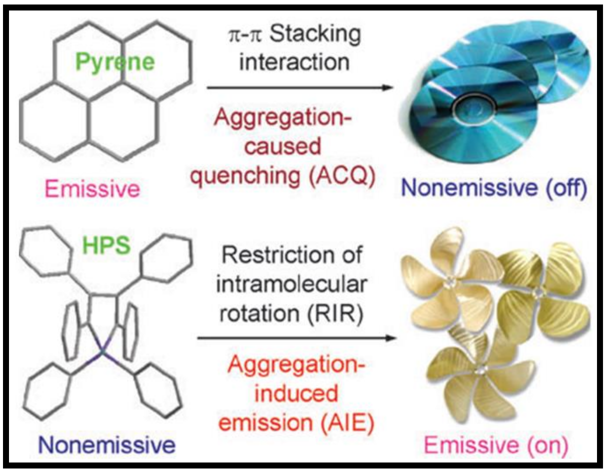

Figure 19. Schematic representation of both ACQ and AIE. (taken from reference 134)

Tetraphenylethene, siloles, cyano-substituted diarylethene, triphenylethene, distyrylanthracene, naphthalene diimide, naphthalimide derivatives are some examples of organic moieties that are being vigorously explored for diverse applications.[134-137]

FABRICATION OF FLUORESCENT ORGANIC NANOPARTICLES

Features of organic nanoparticles relies upon their building blocks, which are judicially optimized according to particular application prerequisites. Based on that, numerous synthetic strategies are developed. Commonly, two widely used approaches are followed in ONP generation: “bottom-up” and “top-down”.[138] The bottom-up strategy involves the construction of nanoparticles by gathering distinct organic molecules into nanoparticles. Self-assembly is one of the most illustrative bottom-up strategies, suitable for achieving intended functionality towards directional utility. On the other hand, the top-down approaches refer to cutting down bulk sizes into nano architectures via grinding, milling or homogenization by applying high pressure. But this top-down practices face certain disadvantages due to involvement of higher energy consumption, use of expensive equipment and a high risk of contamination.[139-140] The preparation of the different types of organic nanoparticles depends evidently on the methods selected for their synthesis. Various methods of organic nanoparticles development include self-assembly, polymerization, macro-/micro-/mini emulsion, nanoprecipitation, reprecipitation, layer-by-layer (LbL) assembly, PRINT, electrospraying and microfluidics.[138, 141] Methods of preparation of ONPs, amphiphilicity of the building block, molecular weight of encapsulation matrices are some of the factors that determine the particle size.

Self-assembly method

Self-assembly, being the most practical approach for organic nanoparticle generation, deals with accumulating amphiphilic block copolymers, host-guest complexes or even small amphiphilic molecules. These comparatively weak interactions often bestow sensitivity towards external stimuli to the nanoparticles, widening their utility in temperature-responsive or pH sensitive systems. These assemblies may be based on co-ordination, thin film hydration or templates.[138]

Amphiphilic polymers have a tendency to assemble into nano structures in aqueous media.[84] When a mixture of amphiphilic polymer and organic emitter is dissolved in a "good" solvent and a surplus quantity of a "poor" solvent is rapidly introduced to the solution, the hydrophobic segments get aggregated keeping organic emitters at the centre and the hydrophilic chains accumulate at outer surface rendering proper stability to the organic nanoparticle. Alternatively, conjugation of organic emitters with the hydrophobic side chains of polymers produces FONPs with organic emitters implanted in the self-assembled matrix (Figure 20).[141] Furthermore, addition of explicit targeting moieties performs versatile biological tasks.

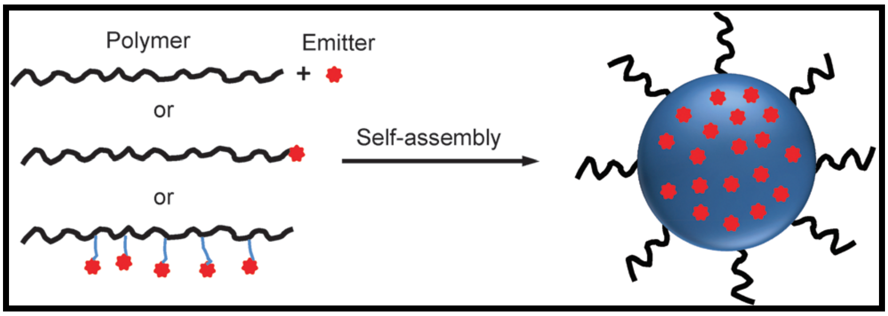

Figure 20. Schematic illustration of polymer-encapsulated organic nanoparticle preparation from self-assembly. (taken from reference 141)

Polymerization method

Monomers and organic emitters, dissolved in organic solvent are mixed with an emulsifier in aqueous solution and homogeneously dispersed droplets are produced via ultra-sonification.[84] The polymerization is initialized by addition of initiators into the emulsion that harvests organic nanoparticles (Figure 21).[141] Further solvent evaporation leads to the well-dispersed polymeric nanoparticles.

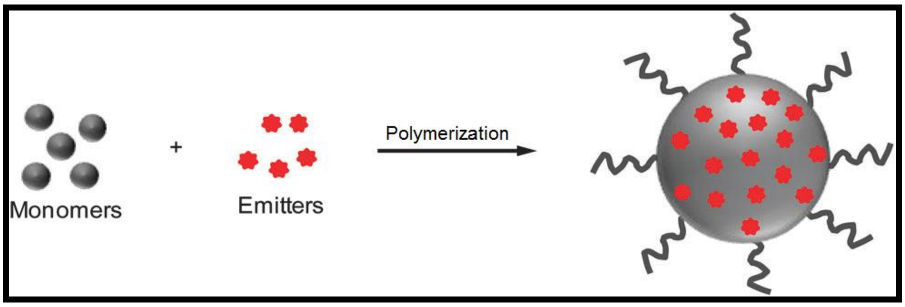

Figure 21. Schematic illustration of polymer-encapsulated organic nanoparticle preparation from *in situ* polymerization. (taken from reference 141)

Emulsion method

Emulsification is a convenient way to generate ONPs without the requirement of expensive equipment. In a distinctive emulsion process, the organic solvent (e.g., dichloromethane) used is immiscible with water. Emitters are dissolved in the organic solvent and emulsifiers remain in aqueous phase. All of them are put together and undergone ultra-sonification or vigorous stirring. Emulsions are normally categorized into three classes based on the sizes of the particles they generate: macroemulsion, miniemulsion and microemulsion. Although, macroemulsion produces ONPs with size larger than 1 μm, mini and microemulsion generates nanoparticles of dimension <500 nm.[141] Stable suspension of polymer encapsulated nanoparticles in water is attained after organic solvent evaporation (Figure 22).[141]

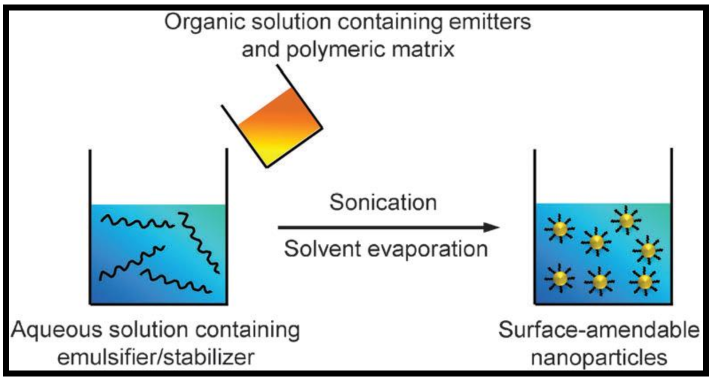

Figure 22. Schematic illustration of the preparation of polymer encapsulated organic nanoparticles from emulsion. (taken from reference 141)

Nanoprecipitation method

The principal difference between nanoprecipitation and emulsion is that in nanoprecipitation, the organic solvent here is miscible with water and no emulsifier is present in water.[141] In an archetypal nanoprecipitation process, the solution of emitters, the encapsulation matrix in an organic solvent (e.g., THF) and excess water are quickly mixed under ultra-sonification which eventually leads to sudden drop in solvent hydrophobicity and that results in aggregation of emitters into nanoparticles. (Figure 23).[141]

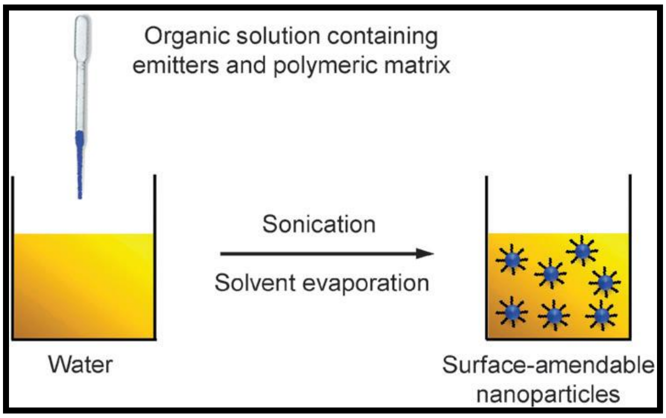

Figure 23. Schematic illustration of the preparation of polymer encapsulated organic nanoparticles from nanoprecipitation. (taken from reference 141)

Reprecipitation method

In a standard reprecipitation method (Figure 24), a target compound (final concentration range: mM) is first dissolved in an organic medium (e.g., THF, DMF, DMSO, acetone, alcohol etc.).[142-143] A few microliters of the diluted solution is inserted rapidly into poor solvent (commonly water) with continuous stirring at a constant temperature.[142] π-conjugated organic nanocrystals is obtained after reprecipitating the target compound in a poor solvent.

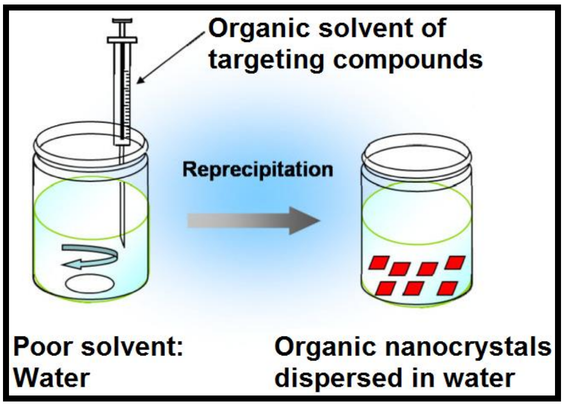

Figure 24. Schematic illustration of the preparation of organic nanoparticles from reprecipitation. (taken from reference 143)

Layer-by-Layer (LbL) assembly

Preparation of multifunctional nanoparticles has been made convenient by LbL assembly (Figure 25) method where nanoparticle cores are coated with polymers, biomolecules and surfactants by means of electrostatic forces, hydrogen bonding, biological recognition and host-guest interaction incorporating different functionalities in each layer making them well-suited for task-specific applications in biomedicine.[138]

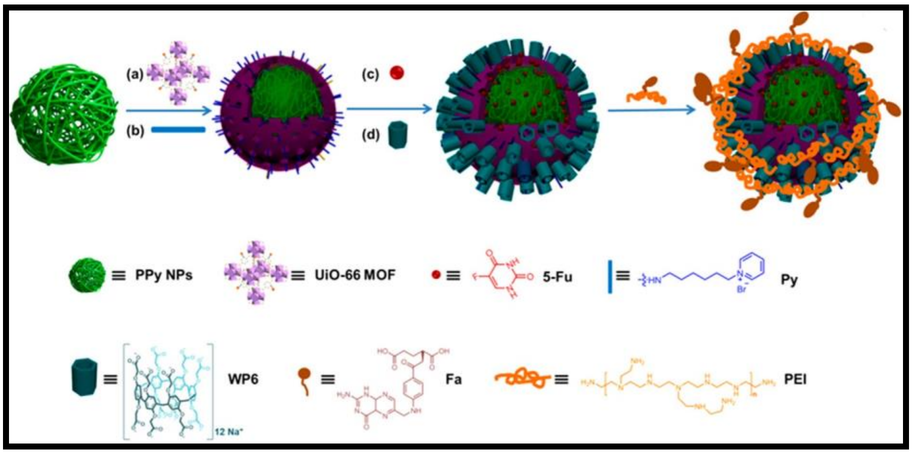

Figure 25. Schematic illustration of the preparation of organic nanoparticles from layer by layer assembly. (taken from reference 138)

Particle replication in nonwetting templates (PRINT)

One of the most efficient ways to fabricate nanoparticles (sizes staring from 20 nm) by "top-down" approach is particle replication in nonwetting templates (PRINT) technology (Figure 26), anticipated by DeSimone's group.[138, 144] Precise control over morphology, dimension and composition can be accomplished with the help of perfluoropolyether (PFPE)-based elastomer.

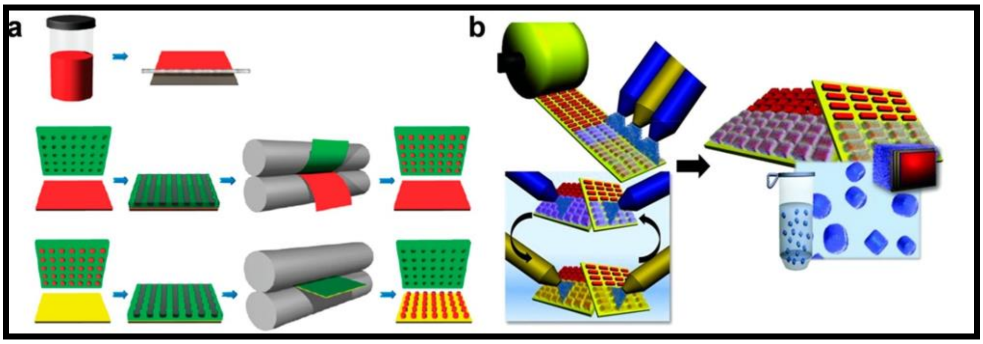

Figure 26. Schematic illustration of (a) the preparation of organic nanoparticles from PRINT method and (b) The spray-LbL on PRINT nanoparticles. (taken from reference 138)

Electrospraying

Electrospraying (Figure 27) is a handy, single-step process for the construction of organic nanoparticles of comparatively smaller size where the material is released from a syringe under high voltage in the very form of ONPs. Electrospray might be categorized as single needle, coaxial, multiaxial and multiplexed.[138] Generally, organic nanoparticles fabricated this way, are excellent delivery vehicles with their precise geometry, efficient loading percentages and outstanding reproducibility.

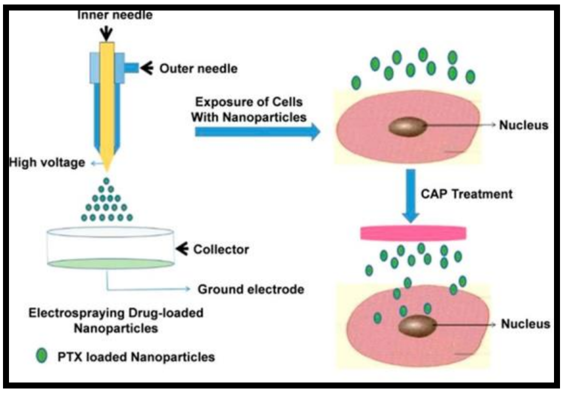

Figure 27. Schematic illustration of the preparation of organic nanoparticles from electrospraying method. (taken from reference 138)

Microfluidics

Microfluidic technology (Figure 28) deals with several picolitre to microlitres of fluids carefully handled in microchannels (10-100 μM), where the flow is majorly regulated by the viscous forces Nowadays, microfluidic devices are constructed with paper, glass, silicon, polydimethylsiloxane (PDMS) etc.[138] Microfluidic systems can be classified into single phase and multiphase (liquid-liquid and liquid-gas systems) and integrated microfluidic systems.[138]

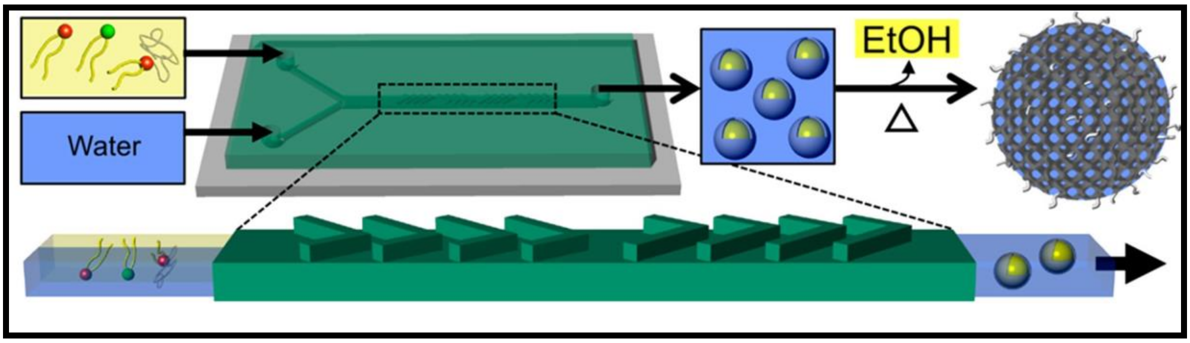

Figure 28. Schematic illustration of the preparation of organic nanoparticles from microfluidic method. (taken from reference 138)

APPLICATIONS OF ORGANIC NANOPARTICLES IN CELL BIOLOGY

Self-assembled nanoparticles as a biosensing platform

Organic nanoparticles derived from small molecules have tremendous application in sensing biomolecules or biohazardous agents. FONP-based probes are more advantageous over conventional fluorophores owing to their flexibility in structure, ease of synthesis, decent water solubility, cytocompatibility and high photostability.[139] Moreover, due to aggregation-induced emission, concentration quenching can be avoided as well as they don't require organic solvent (like traditional fluorophores) to exhibit their sensing properties. At large, most of the organic dyes with low concentration, after entering into the cellular insides, gets photobleached. Additionally, the intracellular dyes often diffuse back to the extracellular media due to the concentration gradient during the cell division. Consequently, the emission of the stained cells becomes significantly reduced as well as background becomes emissive and random staining takes place in a cell co-culture system. Therefore, fluorescent organic nanoparticles (FONPs) are intensively being used in recent years especially in biological labelling and long-term in situ in vivo monitoring of tumor growth (Figure 29).[140, 141]

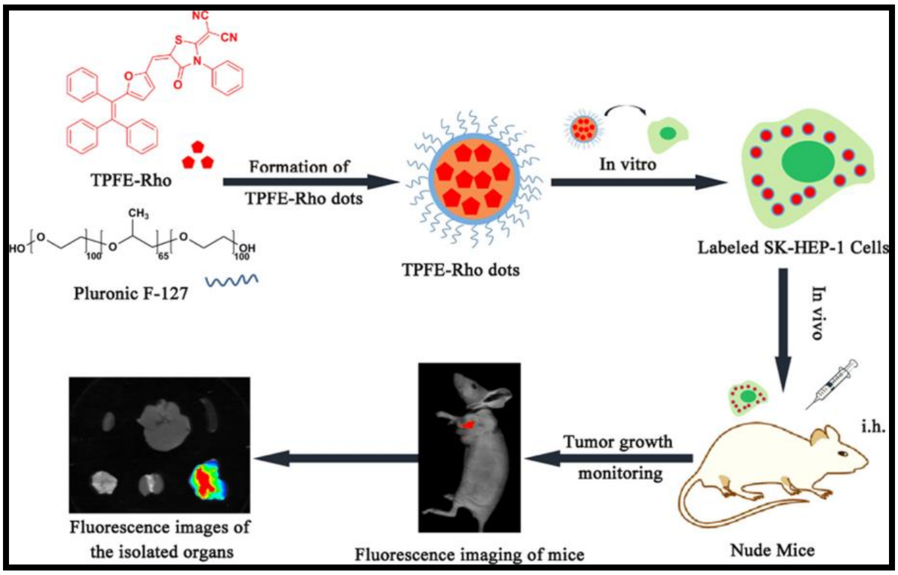

Figure 29. Schematic illustration of organic nanoparticles for non-invasive long-term monitoring of tumor growth. (taken from reference 141)

Delivery vehicle

Design and development of revolutionary drug-delivery systems that not only improves the bioavailability and efficiency of a particular drug, but also reduces toxicity associated with it, is in high demand.[142,143] Target specific delivery with negligeable side effects, sustained release of the drug as well as resistance towards degradation are some of the aspects scientists are trying to achieve. Furthermore, the DDSs have to show longer circulation times and increased permeability.[142] In this regard, organic nanoparticles are one of the most suitable choices for delivery of therapeutic payloads inside mammalian cells mainly due to their stability, low cytotoxicity and obviously their unique optical properties that enables them to be used as detectors for real time-monitoring of drug release (Figure 30).[144]

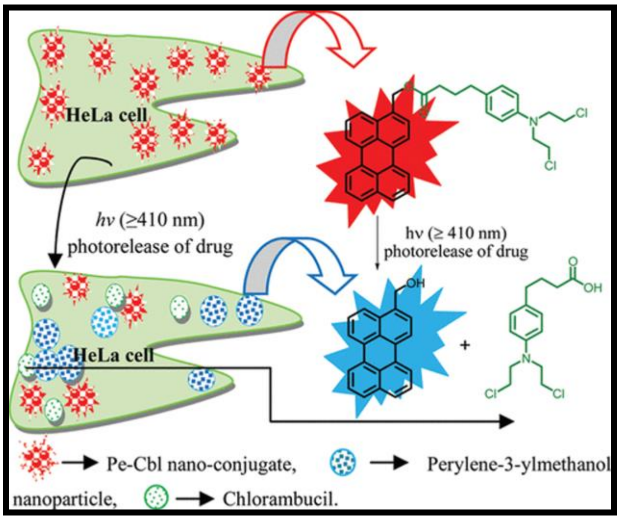

Figure 30. Schematic representation of photoinduced in vitro anticancer drug release. (taken from reference 144)

To this end, the present thesis delineates the development of stimuli responsive supramolecular self-aggregates with potential in task-specific applications highlighting generation of self-assembled vesicles for triggered drug release as well as designing fluorescent soft-materials for detection of analytes in biological systems.

PRESENT THESIS

Stimuli responsive disintegration of self-assembled vesicles derived from cholesterol-based hydrazone tethered amphiphiles…

Self-organization of small amphiphilic molecules, an excellent bottom-up technique for development of soft nanomaterials, give rise to diverse morphology by means of several non-covalent interactions. Due to reversibility of these structures, it is convenient to achieve a control over the association/dissociation of molecular tectons by external or internal triggers. There are several drug releasing sites in human body, that are acidic in nature like tumors, inflammatory tissues, and phagolysosomes of antigen presenting cells. In those cases, pH responsive drug release can be attained by developing self-assembled delivery vehicle that gets disintegrated in acidic medium. On the other hand, “hydrazone” is an easy to fabricate functionality that gets cleaved in acidic environment. Therefore, generation of self-assembled systems incorporating hydrazone bond may lead to acid sensitive destruction of self-assembly towards noteworthy importance in task specific applications.

To this end, in Chapter 1 of the present thesis, we synthesized cholesterol-based pH-responsive hydrazone-appended amphiphiles (**CBH-1-3**) varying the carbonyl moieties (that generated the "hydrazone" bond) from aldehyde (benzaldehyde (**CBH-1**), *p*-dimethylaminobenzaldehyde (**CBH-2**)) to ketone (benzophenone (**CBH-3**)) (Figure 31). Among them, **CBH-1** and **CBH-2** formed vesicular self-aggregates via *H*-type aggregation in 1:3 v/v, DMSO-water with diameter of ~50-120 nm and ~150-250 nm for **CBH-1** and **CBH-2** respectively. Furthermore, the formation of bilayer vesicles through highly ordered lamellar like structure was verified by low angle X-ray diffraction (XRD) patterns. These vesicles got disassembled at acidic pH (pH < 5.0) in contrast to showing stability in neutral environment. Cleavage of the hydrazone bond in acidic environment, that lead to destruction of self-assembly, was investigated by UV-visible, FTIR and mass spectrometric studies. In the transmission electron microscopic (TEM) images of the acid treated vesicles, absence of spherical structures established its disintegration. In addition, drug loading inside the vesicles and its pH-sensitive release from the **CBH-1** vesicles were confirmed using doxorubicin.

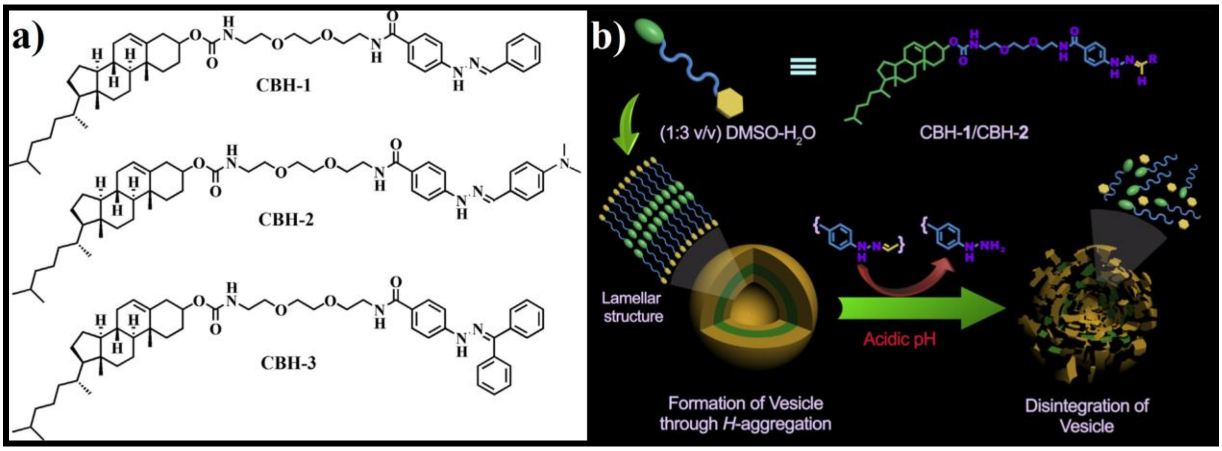

Figure 31. (a) Chemical structures of **CBH-1-3**. (B) Schematic presentation of formation of self-assembly by hydrazone-tailored amphiphiles through *H*-type of aggregation and pH-responsive disintegration of self-assemblies.

Naphthalimide-based azo-functionalized supramolecular vesicle as hypoxia-responsive drug delivery vehicle…

Supramolecular vesicles, with their interior aqueous core and hydrophobic outer part, are capable of encapsulating multiple hydrophobic and hydrophilic cargos efficiently. Introduction of stimuli responsive junctions within vesicles helps in developing spatiotemporal control in biomedicine by reducing random drug biodistribution. Among all the other triggers, hypoxia-responsive drug delivery vehicle generation is gaining importance day by day in tumour specific research especially at earlier stages of cancer because hypoxia acts as a marker for cancer cells by regulating tumour progression by controlling growth-factor signalling, cell proliferation and tissue invasion. As well, passage of an anticancer drug to hypoxic regions becomes difficult for solid tumours due to their distance from blood vessels. In this context, azoreductase enzyme, which is biomarker for hypoxic microenvironment, may be utilized in reductive cleavage of azo bond (–N=N–) incorporated within the delivery vehicle, leading towards hypoxia-responsive drug release

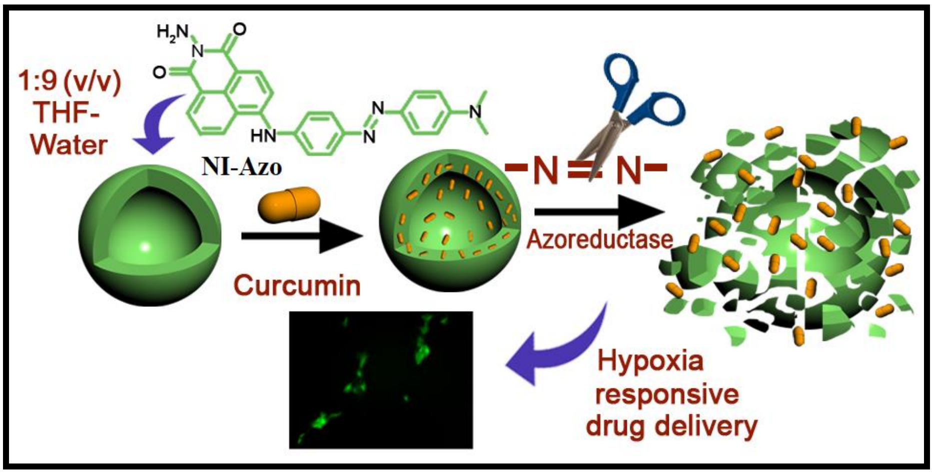

Figure 32. Schematic representation of hypoxia responsive curcumin release from **NI-Azo** vesicles.

To this end, in Chapter 2 of the present thesis, self-aggregated vesicle in 1:9 (v/v), tetrahydrofuran (THF)-water from naphthalimide-based azo moiety containing amphiphile (**NI-Azo**) through *H*-type of aggregation having diameter of 200-250 nm was developed (Figure 32). Azo (–N=N–) bond is subject to be reduced in the presence of the azoreductase enzyme, which is overexpressed in the hypoxic microenvironment. The optical density of this characteristic azo (–N=N–) moiety of **NI-Azo** vesicles at 458 nm got weakened in the presence of both extracellular and intracellular bacterial azoreductase extracted from Escherichia coli bacteria as well as sodium dithionite (chemical mimic of azoreductase). This signifies that azoreductase/sodium dithionite induces azo bond cleavage in **NI-Azo**, tha was verified from MALDI-TOF spectrometric data of the corresponding cleaved primary amine products. Anticancer drug curcumin was encapsulated within **NI-Azo** vesicles and that killed cancerous B16F10 cells in $CoCl_2$-induced hypoxic environment because of the azoreductase-sensitive drug release through the early apoptotic pathway, where the cell killing was 2.15-fold higher than that of the normoxic condition and 2.4-fold higher compared to that of native curcumin in the hypoxic environment. Also, cancer cell killing efficacy of curcumin-loaded **NI-Azo** vesicles was 4.5- and 1.9-fold higher than that of NIH3T3 cells (non-cancerous) in normoxic and hypoxic microenvironments, respectively.

Naphthalimide based fluorescent organic nanoparticles in selective detection of Fe^{3+} and its application as a diagnostic probe for Fe^{2+}/Fe^{3+} transition…

Fluorescent probes are advantageous over other alternative sensors in terms of selectivity, sensitivity and rapid detection. Moreover, the emergence of the revolutionary concept of aggregation-induced emission (AIE) has eliminated all the shortcomings of conventional fluorophores due to the highly emissive nature of the AIE-gens in aqueous medium. Again, fluorescent organic nanoparticles (FONPs) with the AIE properties are self-aggregated structures derived from p-conjugated oligomers or chromophores having flexible functionality that can be modified according to requirement, that makes them excellent choice for metal sensing. Fe^{3+} is biologically crucial metal ion, that is very much relevant in development of oxidative stress as reactive oxygen species (ROS) is generated due to interaction of Fe^{2+} with hydrogen peroxide in Fenton reactions. Therefore, detection of different redox state of Fe and monitoring the transition of is Fe^{2+} to Fe^{3+} is beneficial. In this aspect, development of easy to fabricate, cyto-compatible FONPs that sense Fe^{3+} and acts as a diagnostic probe for redox transition of iron inside living cell is an interesting research topic.

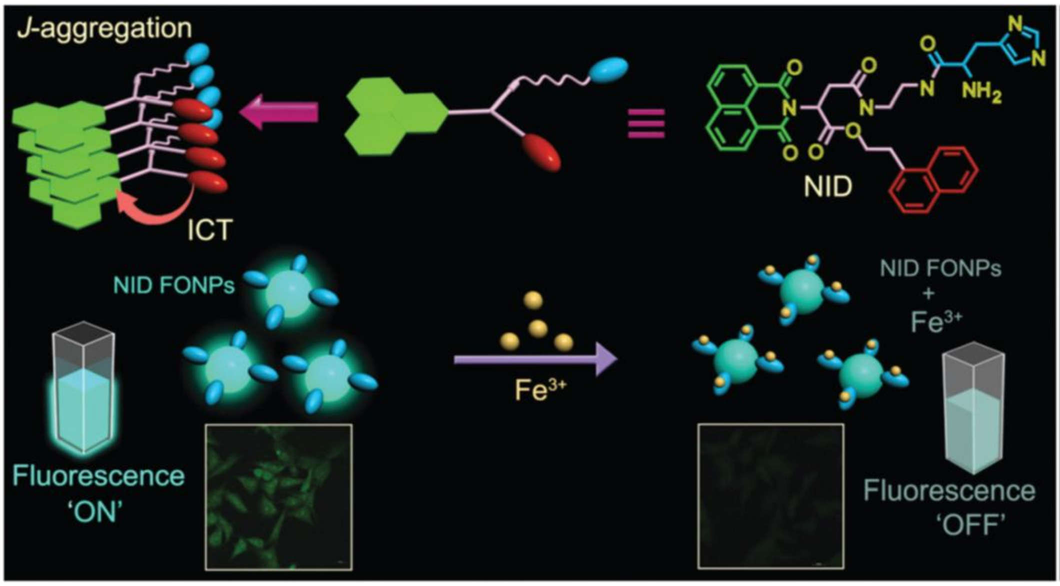

Figure 33. Schematic presentation of **NID** based fluorescent organic nanoparticles in the selective sensing of Fe^{3+} and as a diagnostic probe for Fe^{2+}/Fe^{3+} transition. ICT: intramolecular charge transfer.

To this end, in Chapter 3 of the present thesis, FONPs were developed from the naphthalimide based histidine appended amphiphile, **NID** in 99 vol% water in DMSO through *J*-type aggregation (Figure 33). Aggregation-induced emission (AIE) was observed with excimer formation at 470 nm having bluish green emission. These FONPs were employed in selective sensing of Fe^{3+} and bioimaging of Fe^{3+} inside cells due to their emissive properties and low toxicity. Fluorescence intensity of the FONPs got significantly reduced with addition of Fe^{3+} due to the formation of a 1 : 1 stoichiometric complex with the histidine part of **NID**. The limit of detection (LOD) of this turn-off sensor was calculated to be 12.5±1.2 μM having high selectivity over other metal ions. In view of the variable oxidative stress within different cells, **NID** FONPs were utilized for sensing Fe^{2+} to Fe^{3+} redox state transition selectively in cancer cells (B16F10) compared to non-cancerous cells (NIH3T3). Co-culture experiment and flow cytometry further confirmed selective sensing of cancer cells. Hence, **NID** FONPs can be a selective diagnostic tool for cancerous cells on account of their higher H_2O_2 amount.

Naphthalenediimide based various amino acids appended organic nanoparticles with tuneable aggregation-induced emission (AIE)…

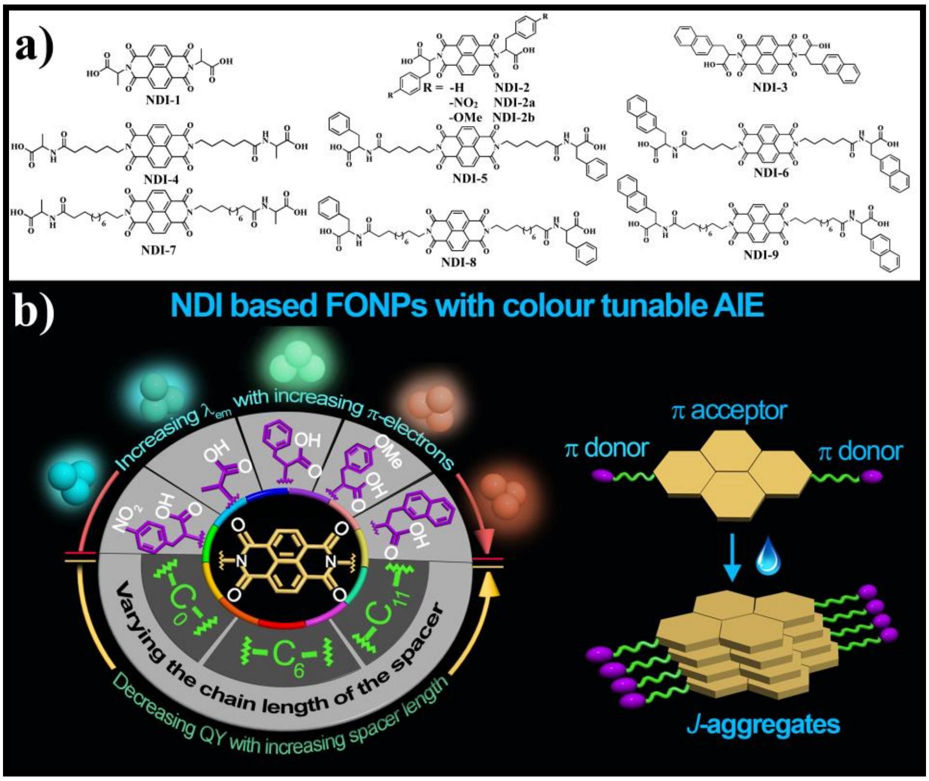

Figure 34. (a) Chemical structures of **NDI-1-9**, **2a** and **2b**. (B) Schematic representation of various amino acid containing NDI based FONPs with tuneable emission.

Fluorescent organic nanoparticles (FONPs) act as a bridge between supramolecular self-assemblies and emissive nanoparticles. FONPs, built on π-conjugated oligomers, have rich emissive properties along with photostability and excellent cytocompatibility that makes them appropriate choice for sensing and imaging applications. Moreover, due to AIE, they are immune towards concentration quenching. On the other hand, peptide-based amphiphiles get self-assembled into diverse aggregates like vesicle, hydrogel, nanoribbons, nanotube, fiber etc., simplifying and repurposing biomimetic structures utilizing molecular scaffold of naturally available amino acids. A control over the emission maxima of the FONP can be achieved by regulating the π-conjugated donor and accepter residues and amino acids with varying π-electron density can serve as excellent donor parts towards electron accepting naphthalenediimide core.

To this end, in Chapter 4 of the present thesis, we developed naphthalenediiimide (NDI) based amphiphiles (**NDI-1-9**) with varying amino acid substitution from L-alanine to L-phenyl alanine to 3-(2-naphthyl)-L-alanine with or without alkyl spacer (C-6, C-11) (Figure 34). Construction of self-aggregated organic nanoparticles of ~50 nm occurred 50 vol% water or methyl cyclohexane (MCH) onwards in DMSO/DMF or $CHCl_3$ via *J*-aggregation. **NDI-1-3** (amino acids are directly connected to the NDI) amphiphiles self-assembled into FONPs (MCH in $CHCl_3$) and displayed aggregation-induced emission (AIE) through excimer formation at 484 nm to 495 nm, and 590. Red shift was observed with increasing π-electrons donor side from **NDI-1** to **NDI-3**. FONPs of 6-amino caproic acid spacer containing NDI derivatives (**NDI-5** and **NDI-6**) showed AIE at 505 nm and 545 nm (water in DMF/DMSO) and 11-amino undecanoic acid containing analogues (**NDI-8** and **NDI-9**) showed AIE at 480 nm and 585 nm in $CHCl_3$-MCH and DMF/DMSO-water. The multi colour emission from blue-green to yellow-orange with enhancement of π-electron cloud in the side chain of NDI derivatives was detected probably due to the facilitated electron transfer at a lower energy to the electron deficient NDI core that caused red shifted emission maxima. This was again clarified by controlling the availability of π-electrons of phenyl ring of **NDI-2** by including electron withdrawing -NO_2 and donating -OMe groups at the molecular structure (**NDI-2a** and **NDI-2b)** that exhibited blue shifted (475 nm) and red shifted (570 nm) emission maxima compared to **NDI-2** (495 nm). Nevertheless, increased alkyl spacer length between side chain substitution and NDI core produced relatively lower quantum yield apparently due to the impeded electron transfer.

References

[1] Google image, https://www. boredpanda.com/

[2] L. Hu, Q. Zhang, X. Lic, M. J. Serpe, *Mater. Horiz.* **2019**, *6*, 1774.

[3] Google image, https://www.sciencephoto.com/

[4] Google image, https://garden.lovetoknow.com/

[5] Google image, https://www.britannica.com/

[6] Google image, https://www.organicauthority.com/

[7] Google image, https://edition.cnn.com/

[8] Google image, https://www.pexels.com/

[9] K. L. Wolf, H. Frahm, H. Harms, *Z. Phys. Chem. Abt. B* **1937**, *36*, 237.

[10] J. M. Lehn, *Science* **1993**, 260, 1762.

[11] F. M. Menger, *Langmuir* **2011**, *27*, 5176.

[12] S. Sarkar, P. Choudhury, S. Dinda, P. K. Das, *Langmuir* **2018**, *36*, 10449.

[13] C. Jiménez-Jiménez, M. Manzano, M. Vallet-Regí, *Biology* **2020**, *9*, 406.

[14] Google image, https://www.stock.adobe.com/

[15] R. Zana, J. Lang, K. L. Mittal, E. J. Fendler, *Solution Behavior of Surfactants (Vol. 2)*, Plenum, New York, **1984**.

[16] J. N. Israelachvili, D. J. Mitchell, B. W Ninham, *J. Chem. Soc., Faraday trans. II* **1976**, 72, 1525.

[17] J. H. van Esch, *Nature* **2010,** *466*, 193.

[18] M. J. Rosen, J. T. Kunjappu, *Surfactants and Interfacial Phenomenon (4th edition)*, John Wiley and Sons, Hoboken, New Jersey, **2012**.

[19] A. Blanazs, S. P. Armes, A. J. Ryan, *Macromol. Rapid Commun.* **2009**, *30*, 267.

[20] D. Lombardo, M. A. Kiselev, S. Magazù, P. Calandra, *Advances in Condensed Matter Physics Volume* **2015**, Article ID 151683

[21] J. H. Fuhrhop, T. Wang, *Chem. Rev.* **2004**, 104, 2901.

[22] W. C. Griffin, *J. Soc. Cosmet. Chem.* **1949**, 1, 311.

[23] W. C. Griffin, *J. Soc. Cosmet. Chem.* **1954**, 5, 249.

[24] Google image, https://www.wikiwand.com/

[25] Google image, https://www.water.Isbu.ac.uk/

[26] Google image, https://www.socratic.org/

[27] Google image, https://www.chemlibertexts.org/

[28] P. Choudhury, S. Dinda, P. K. Das, *Soft Matter* **2020**, *16*, 27.

[29] C. A. Angell, P. H. Poole, J. Shao, *Il Nuovo Cimento D* **1994**, *16*, 993.

[30] S. Magazu, F. Migliardo, A. Benedetto, *J. Phys. Chem. B* **2011**, 115, 7736.

[31] S. Clarke, *J. Chem. Educ.* **1981***, 58,* A246.

[32] J. L. Finney, *"The structural basis of the hydrophobic interaction," in Hydration Processes in Biology*, ed., M. C. Bellissent-Funel, IOS Press, **1999**, 115-124.

[33] R. Lipowsky, E. Sackmann, *Handbook of Biological Physics, 1st Edition*, Elsevier Science Publisher BV, **1995**.

[34] D. D. Lasic, *"Applications of liposomes,"* in *Handbook of Biological Physics*, ed., R. Lipowsky, E. Sackmann, Elsevier, The Netherlands, **1995**.

[35] B. Y. Wang, H. Xu, X. Zhang, *Adv. Mater.* **2009**, 21, 2849.

[36] M. Marguet, C. Bonduelle, S. Lecommandoux, *Chem. Soc. Rev.* **2013**, 42, 512.

[37] K. Werengowska-Cie'cwierz, M. Wisniewski, A. P. Terzyk, S. Furmaniak, *Adv. Cond. Matter Phys.* **2015**, Article ID 198175.

[38] A. V. Dubtsov, S. V. Pasechnik, D. V. Shmeliova, S. Kralj, R. Repnik, *Adv. Cond. Matter Phys.* **2015**, Article ID 803480.

[39] J. M. Lehn, *Chem. Soc. Rev.* **2007**, *36*, 151.

[40] F. Grieser, C. Drummond, *J. Phys. Chem.* **1988**, *92*, 5580.

[41] E. Gazit, *Chem. Soc. Rev.* **2007**, *36*, 1263.

[42] N. Kol, L. Adler-Abramovich, D. Barlam, R. Z. Shneck, E. Gazit, I. Rousso, *Nano Lett.* **2005**, *5*, 1343.

[43] A. Dominguez, A. Fernanadez, N. Gonzalez, E. Iglesius, L. Montenegro, *J. Chem. Educ.* **1997**, *74*, 1227.

[44] D. J. Macquarrie, *Topics in Catalysis*. **2009**, *52*, 1640.

[45] Google image, https://www.sciencephoto.com/

[46] B. K. Paul, S. P. Moulik, *J. Disper. Sci. Technol.* **1997**, *18*, 301.

[47] H. F. Eicke, P. Kvita, *Reverse Micelles*, ed., P. L. Luisi, B. E. Straub, Plenum Press, New York, **1984**.

[48] A. M. Klibanov, *Nature* **1995**, *374*, 596.

[49] P. Terech, R. G. Weiss, *Chem. Rev.* **1997**, *97*, 3133.

[50] K. Y. Lee, D. J. Mooney, *Chem. Rev.* **2001**, *101*, 1869.

[51] V. Jayawarna, M. Ali, T. A. Jowitt, A. F. Miller, A. Saiani, J. E. Gough, R. V. Ulijn, *Adv. Mater.* **2006**, *18*, 611.

[52] A. Barnard, P. Posocco, S. Pricl, M. Calderon, R. Haag, M. E. Hwang, V. W. T. Shum, D. W. Pack, D. K. Smith, *J. Am. Chem. Soc.* **2011**, *133*, 20288.

[53] N. Bruns, J. C. Tiller, *Nano Lett.* **2005**, *5*, 45.

[54] S. S. Babu, S. Prasanthkumar, A. Ajayaghosh, *Angew. Chem. Int. Ed.* **2012**, *51*, 1766.

[55] H. K. Yang, H. Zhao, P. R. Yang, C. H. Huang, *Colloids Surf. A* **2017**, *535*, 242.

[56] N. M. Sangeetha, U. Maitra, *Chem. Soc. Rev.* **2005**, *34,* 821.

[57] L. A. Estroff, A. D. Hamilton, *Chem. Rev.* **2004**, *104,* 1201.

[58] S. Banerje, R. K. Das, U. Maitra, *J. Mater. Chem.* **2009**, *19*, 6649.

[59] K. J. C. van Bommel, A. Friggeri, S. Shinkai, *Angew. Chem. Int. Ed.* **2003**, *42*, 980.

[60] D. Ma, K. Tu, L. M. Zhang, *Biomacromolecules* **2010**, *11*, 2204.

[61] D. Kalafatovic, M. Nobis, N. Javid, P. W. J. M. Frederix, K. I. Anderson, B. R. Saunders,

R. V. Ulijn, *Biomater. Sci.* **2015**, *3*, 246.

[62] P. K. Vemula, G. John, *Chem. Commun.* **2006**, 2218.

[63] S. Bhattacharjee, S. K. Samanta, P. Moitra, K. Pramoda, R. Kumar, S. Bhattacharya, C. N. R. Rao, *Chem. Eur. J.* **2015**, *21*, 5467.

[64] F. S. Schoonbeek, J. H. van Esch, R. Hulst, R. M. Kellogg, B. L. Feringa, *Chem. Eur. J.* **2000**, *6*, 2633.

[65] P. Moitra, K. Kumar, P. Kondaiah, S. Bhattacharya, *Angew. Chem. Int. Ed.* **2014**, *53*, 1113.

[66] P. Rajamalli, E. Prasad, *Langmuir* **2013**, *29*, 1609.

[67] L. Chen, S. Revel, K. Morris, L. C. Serpell, D. J. Adams, *Langmuir* **2010**, *26*, 13466.

[68] M. Suzuki, M. Yumoto, H. Shirai, K. Hanabusa, *Chem. Eur. J.* **2008**, *14*, 2133.

[69] H. Fenniri, P. Mathivanan, K. L. Vidale, D. M. Sherman, K. Hallenga, K. V. Wood, J. G. Stowell, *J. Am. Chem. Soc.* **2001**, *123*, 3854.

[70] J. F. Miravet, B. Escuder, *Chem. Commun.* **2005**, 5796.

[71] N. Yan, Z. Xu, K. K. Diehn, S. R. Raghavan, Y. Fang, R. G. Weiss, *Langmuir* **2013**, 29, 793.

[72] Y. Imura, K. Matsue, H. Sugimoto, R. Ito, T. Kondo, T. Kawai, *Chem. Lett.* **2009**, *38*, 778.

[73] K. Liu, N. Yan, J. Peng, J. Liu, Q. Zhang, Y. Fang, *J. Colloid Interface Sci.* **2008**, *327*, 233.

[74] https://pixels.com/featured/drug-delivery-liposome-alfred-pasieka.html

[75] A. D. Bangham, R. W. Horne, *J. Mol. Biol.* **1964**, *8*, 660.

[76] O. Savsunenko, H. Matondo, S. F. Messant, E. Perez, A. F. Popov, I. Rico-Lattes, A. Lattes, Y. Karpichev, *Langmuir* **2013**, *29*, 3207.

[77] R. Ghosh, J. Dey, *Langmuir* **2014**, *30*, 13516.

[78] C. G. Palivan, R. Goers, A. Najer, X. Zhang, A. Cara, W. Meier, *Chem. Soc. Rev.* **2016**, *45*, 377.

[79] S. Shaha, V. Dhawan, R. Holma, M. S. Nagarsenker, Y. Perrie, *Adv. Drug Delivery Rev.* **2020**, *154*, 102.

[80] S. Dinda, M. Ghosh, P. K. Das, *Langmuir* **2016**, *32*, 6701.

[81] Google image, https://www.google.com

[82] V. Shanmugam, S. Selvakumar, C. S. Yeh, *Chem Soc Rev.* **2014**, *43*, 6254.

[83] S. R. Sirsi, M. A. Borden, *Adv Drug Deliv Rev.* **2014**, *72*, 3.

[84] N. Lee, D. Yoo, D. Ling, M. H. Cho, T. Hyeon, J. Cheon, *Chem Rev.* **2015**, *115*, 10637.

[85] C, Loebel, C. B. Rodell, M. H. Chen, J. A. Burdick, *Nat Protoc.* **2017**, *12*, 1521.

[86] J. Liu, Y. Huang, A. Kumar, A. Tan, S. Jin, A. Mozhi, X. J. Liang, *Biotechnol Adv.* **2014**, *32*, 693.

[87] G. U. Dachs, G. J. Dougherty, I. J. Stratford, D. J. Chaplin, *Oncol Res.* **1997**, *9*, 313.

[88] M. Huo, J. Yuan, L. Tao, Y. Wei, *Polym. Chem.* **2014**, *5*, 1519.

[89] Q. Hu, P. S. Katti, Z. Gu, *Nanoscale* **2014**, *6*, 12273.

[90] L. Klouda, *Eur. J. Pharm. Biopharm.* **2015**, *97*, 338.

[91] B. A. Badeau, C. A. De Forest, *Annu. Rev. Biomed. Eng.* **2019**, *21*, 241.

[92] A.M. Vargason, A. C. Anselmo, S. Mitragotri, *Nat. Biomed. Eng.* **2021**, *5*, 951.

[93] *Controlled Drug Delivery: Fundamentals and Applications*, J. R. Robinson, V. H. Lee, ed., Dekker, **1987**.

[94] D. E. Owens III, N. A. Peppas, *Int. J. Pharm.* **2006**, *307*, 93.

[95] G. Tiwari, R. Tiwari, B. Sriwastawa, L. Bhati, S. Pandey, P. Pandey, S. K. Bannerjee, *Int. J. Pharm. Investig.* **2012**, *2*, 2.

[96] N. Kamaly, B. Yameen, J. Wu, O. C. Farokhzad, *Chem. Rev.* **2016**, *116*, 2602.

[97] S. P. Schwendeman, R. B. Shah, B. A. Bailey, A. S. Schwendeman, *J. Control. Release* **2014**, *190*, 240.

[98] S. Awwad, U. Angkawinitwong, *Pharmaceutics* **2018**, *10*, 83.

[99] D. Liu, F. Yang, F. Xiong, N. Gu, *Theranostics* **2016**, *6,* 1306.

[100] M. B. Subudhi, A. Jain, A. Jain, P. Hurkat, S. Shilpi, A. Gulbake, S. K. Jain, *Materials* **2015**, *8*, 832.

[101] E. S. Lee, K. T. Oh, D. Kim, Y. S. Youn, Y. H. Bae, *J. Control. Release* **2007**, *123*, 19.

[102] R. Cheng, F. Feng, F. Meng, C. Deng, J. Feijen, Z. Zhong, *J. Control. Release* **2011**, 152, 2.

[103] R. D. L. Rica, D. Aili, M. M. Stevens, *Adv. Drug Deliv. Rev.* **2012**, *64*, 967.

[104] Y. Zhao, X. Fan, D. Liu, Z. Wang, *Int. J. Pharm* **2011**, *409*, 229.

[105] VP. Torchilin, *Nat. Rev. Drug Discov.* **2014**, *13*, 813.

[106] S. Mura, J. Nicolas, P. Couvreur, *Nat. Mater.* **2013**, *12*, 991.

[107] G. Gregoriadis, B. Ryman, *Biochem. J.* **1971**, *124*, 58P.

[108] A. Akbarzadeh, R. Rezaei-Sadabady, S. Davaran, S. W. Joo, N. Zarghami, Y. Hanifehpour, M. Samiei, M. Kouhi, K. N. Koshki, *Nanoscale Res. Lett.* **2013**, *8*, 102.

[109] Y. C. Barenholz, *J. Control. Release* **2012**, *160*, 117.

[110] Google image, https://www.empr.com/drug/doxil/

[111] Google image, https://www.fiercepharma.com/

[112] J. Huwyler, D. Wu, W. M. Pardridge, *Proc. Natl. Acad. Sci.* **1996**, *93*, 14164.

[113] R. K. Chowdhary, I. Shariff, D. Dolphin, *J. Pharm. Pharm. Sci.* **2003**, *6*, 13.

[114] E. M. Bolotin, R. Cohen, L. K. Bar, N. Emanuel, S. Ninio, Y. Barenholz, D. D. Lasic, *J. Liposome Res.* **1994**, *4*, 455.

[115] P. R. Cullis, M. J. Hope, M. B. Bally, T. D. Madden, L. D. Mayer, D. B. Fenske, *Biochim. Biophys. Acta* **1997**, *1331*, 187.

[116] D. A. LaVan, T. McGuire, R. Langer, *Nature Biotechnol.* **2003**, *21*, 1184.

[117] X. Guo, F. C. J. Szoka, *Acc. Chem. Res.* **2003**, *36*, 335.

[118] K. J. Chen, E. Y. Chaung, S. P. Wey, K. J. Lin, F. Cheng, C. C. Lin, H. L. Liu, H. W. Tseng, C. P. Liu, M. C. Wei, C. M. Liu, H. W. Sung, *ACS Nano.* **2014**, *8*, 5105.

[119] K. Kono, T. Ozawa, T. Yoshida, *Biomaterials* **2010**, *31*, 7096.

[120] P. Pradhan, J. Giri, F. Rieken, C. Koch, O. Mykhaylyk, M. Döblinger, R. Banerjee, D. Bahadur, C. Plank, *J. Control. Release*. **2010**, *142*, 108.

[121] M. T. Peracchia, *Colloidal drug delivery systems*, J. Kreuter, ed., Marcel Dekker, New York, 1994, J. Control. Release **1995**, *35*, 181.

[122] P. Couvreur, *Crit. Rev. Ther. Drug. Carr. Syst.* **1988**, *5*, 1.

[123] F. Leblond, S. C. Davis, P. A. Valdes, B. W. Poque, *J. Photochem. Photobiol. B* **2010**, *98*, 77.

[124] V. R. Kondepati, H. M. Heise, J. Backhaus, *J. Anal. Bioanal. Chem.* **2008**, *390*, 125.

[125] M. F. Kircher, S. S. Gambhir, J. Grimm, *Nat. Rev. Clin. Oncol.* **2011**, *8*, 677.

[126] J. Allouche, *Synthesis of Organic and Bioorganic Nanoparticles: An Overview of the Preparation Methods*, Springer, London, 2013.

[127] D. A. Richards, A. Maruani, V. Chudasama, *Chem. Sci.* **2017**, *8*, 63.

[128] J. Mei, N. L. C. Leung, R. T. K. Kwok, J. W. Y. Lam, B. Z. Tang, *Chem. Rev.* 2015, 115, 11718.

[129] S. W. Thomas, G. D. Joly, T. M. Swager, *Chem. Rev.* **2007**, *107*, 1339.

[130] F. J. M. Hoeben, P. Jonkheijm, E. W. Meijer, A. P. H. J. Schenning, *Chem. Rev.* **2005**, *105*, 1491.

[131] F. Hide, M. A. D. Garcia, B. J. Schwartz, A. J. Heeger, *Acc. Chem. Res.* **1997**, *30*, 430.

[132] J. Mei, Y. Hong, J. W. Y. Lama, A. Quin, Y. Tang, B. Z. Tang, *Adv. Mater.* **2014**, 26, 5429.

[133] J. B. Birks, *Photophysics of Aromatic Molecules*, Wiley, London, **1970**.

[134] Y. Hong, J. W. Y. Lama, B. Z. Tang, *Chem. Soc. Rev.* **2011**, *40*, 5361.

[135] J. Luo, Z. Xie, J. W. Y. Lam, L. Cheng, H. Chen, C. Qiu, H. S. Kwok, X. Zhan, Y. Liu, D. Zhu, B. Z. Tang, *Chem. Commun.* **2001**, 1740.

[136] M. Kumar, S. J. George, *Nanoscale* **2011**, *3*, 2130.

[137] M. A. Kobaisi, S. V. Bhosale, K. Latham, A. M. Raynor, S. V. Bhosale, *Chem. Rev.* **2016**, *116*, 11685.

[138] F. Fang, M. Li, J. Zhang, C. S. Lee, *ACS Mater. Lett.* **2020**, *2*, 531.

[139] M. Ahmed, M. Faisal, A. Ihsan, M. M. Naseer, *Analyst* **2019**, *144*, 2480.

[140] F. Hua, B Liu, *Org. Biomol. Chem.* **2016**, *14*, 9931.

[141] Q. Xia, Z. Chen, Z. Yu, L. Wang, J. Qu, R. Liu, *ACS Appl. Mater. Interfaces* **2018**, *10*, 17081.

[142] P. Verderio, P. Bonetti, M. Colombo, L. Pandolfi, D. Prosperi, *Biomacromolecules* **2013**, *14*, 672.

[143] S. Mitragotri, P. Stayton, *MRS Bull.* **2014**, *39*, 219.

[144] A. Jana, K. Sanjana, P. Devi, T. K. Maiti, N. D. P. Singh, *J. Am. Chem. Soc.* **2012**, *134*, 7656.

* * *

Chapter 1

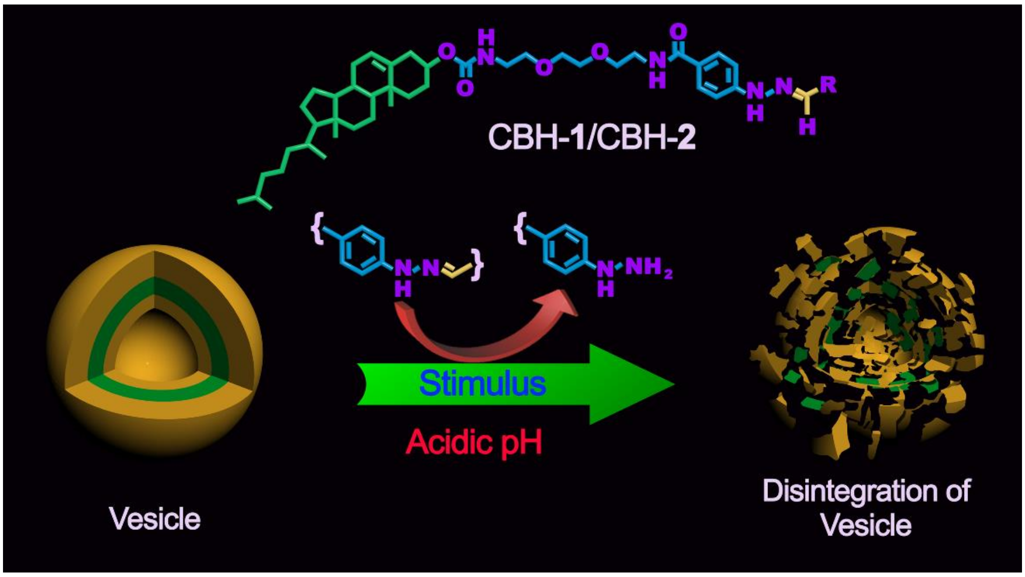

Stimuli responsive disintegration of self-assembled vesicles derived from cholesterol-based hydrazone tethered amphiphiles

1.1. INTRODUCTION

Supramolecular self-assembly is a basic phenomenon at the molecular level that results in the fabrication of different aggregated structures through bottom-up strategy.[1] Self-organization of amphiphiles lead to the development of diverse manifestations like micelles, vesicles, low-molecular-weight gels and other higher order aggregates so forth in which molecules remain at highly ordered form via different non-covalent interactions.[2-11] These self-aggregated architectures can be disintegrated or their assembled forms can be altered by applying external triggers.[12-18] Development of functional soft materials, that are sensitive to external stimuli such as light, heat, pH and enzyme have gained notable attention in drug release, disease diagnosis, tissue engineering and other fields.[15,19-26] Hamachi *et al.* developed *N*-acetylgalactosamine functionalized supramolecular hydrogel that undergoes pH-triggered shrinkage or swelling. Additionally, this can be further facilitated upon mixing with equimolar amount of amphiphilic carboxylic acids having C-6 chain length.[27] In another work, Ulijn and co-workers reported an enzyme responsive chemically cross-linked hydrogel that underwent swelling being treated with a target protease.[28] Hence, the suitable inclusion of stimuli responsive component in the molecular backbone can play a crucial role for macroscopic transformation of the self-aggregates when triggered with exogenous agents.

Molecules comprising carbon-nitrogen double bonds are ubiquitous in both chemical and biological domain.[29] The hydrazone functional group is prevalent in total synthesis, medicinal chemistry to supramolecular chemistry.[29-31] The effortless synthetic path and substantial stability have widened the utility of this hydrazone moiety in various applications including metal and covalent organic frameworks, dynamic combinatorial chemistry, dye and hole-transporting materials and others.[29,32-38] Stability at neutral pH is the most elegant feature of the hydrazone covalent bond, whereas it gets broken rapidly in acidic environment.[32,39] Alongside, there are many drug releasing sites in human body, that are acidic in nature like inflammatory cells, phagolysosomes of antigen presenting cells and also tumor cells.[40] In those requirements, it will be desirable to develop self-assembled structures that gets disintegrated at acidic pH leading towards selective drug release.[22,41] To this end, design and development of pH-responsive self-assemblies are finding striking importance in task specific applications.[41-43] Therefore, one can envisage incorporation of hydrazone motif into the amphiphilic scaffold to generate pH-sensitive self-assembled structures.

Herein, the present work describes synthesis and development of cholesterol-based hydrazone appended low molecular mass amphiphiles (**CBH-1-3**, Figure 1). The cholesteryl unit in the amphiphilic architecture was chosen because of its natural propensity to facilitate self-organization through hydrophobic interactions in aqueous milieu. The hydrazone residue was tuned by changing the carbonyl residues from aldehyde (benzaldehyde (**CBH-1**), *p*-dimethylaminobenzaldehyde (**CBH-2**)) to ketone (benzophenone (**CBH-3**)). Amphiphiles **CBH-1** and **CBH-2** formed vesicular self-aggregates through *H*-aggregation in 1:3 v/v, DMSO-water. Proper selection of the carbonyl moiety in the formation of hydrazone bond could be a principal factor to maintain the hydrophilic-lipophilic balance (HLB) in self-organization. Different microscopic and spectroscopic investigations were carried out for physicochemical characterizations of these vesicles. The degradation of the vesicular self-aggregates on account of the cleavage of hydrazone bond under acidic environment was inspected by UV-visible, FTIR and mass spectrometric study. Anticancer drug, doxorubicin was used for dye encapsulation and its pH-responsive release from the vesicles (prepared using **CBH-1**). The present study showed formation of self-assembled vesicles by hydrazone-tethered amphiphiles and pH-sensitive cleavage of hydrazone bond that resulted in the release of the entrapped drug molecules through destruction of the vesicular self-assembly.

1.2. RESULTS AND DISCUSSION

1.2.1. Hydrazone-tailored amphiphiles and their self-assemblies

With the motivation to develop stimuli-responsive small amphiphilic molecules, we have synthesized cholesterol-based hydrazone-tethered amphiphiles (**CBH-1-3**, Figure 1). Cholesterol moiety was chosen as one of the most ubiquitous natural components having known influence in self-assembling process. 4-Hydrazinobenzoic acid residue was included as the stimuli-responsive moiety within the amphiphile's structures. These two residues were linked through a hydrophilic spacer, 2,2′-(ethylenedioxy)bis(ethylamine) (Figure 1 and Scheme 1). Along with cholesterol and hydrazone motifs, this linker may also influence the amphiphile's hydrophilic-lipophilic-balance (HLB), which plays a crucial role in the development of well-defined self-aggregates. We have modified the hydrazone moiety by varying the carbonyl residue from aldehyde (benzaldehyde, *p*-dimethylaminobenzaldehyde) to ketone (benzophenone) (**CBH-1-3**). All these synthesized amphiphiles were characterized by ^{1}H-NMR and MALDI-TOF mass spectrometry.

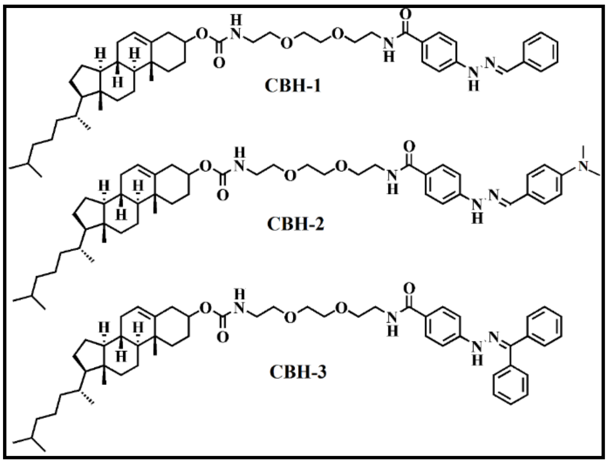

Figure 1. Chemical structures of hydrazone-tailored amphiphiles **CBH-1-3**.

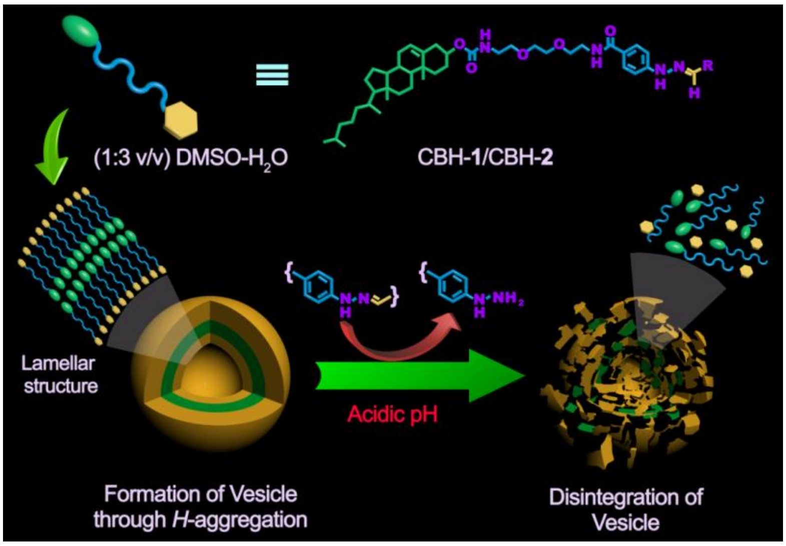

Scheme 1. Schematic presentation of formation of self-assembly by hydrazone-tailored amphiphiles through *H*-type of aggregation and pH-responsive disintegration of self-assemblies.

The solubility, stability and self-assembling behaviour of the hydrazone-tailored compounds (**CBH-1-3**) were investigated in dimethyl sulfoxide (DMSO) and DMSO-water binary solvent mixture. All three molecules were soluble in DMSO. With increase in water content in DMSO solution, transparent solutions gradually transformed to translucent solutions for **CBH-1** and **CBH-2**. Stable translucent solution formation took place in 1:3 v/v, DMSO-water mixture for **CBH-1** at 1.0 mg mL^{-1} and at 0.5 mg mL^{-1} for **CBH-2**. Visual appearance of stable translucent solution indicates the formation of vesicular self-assembly for **CBH-1** and **CBH-2** in 1:3 v/v, DMSO-water binary solvent system. Zeta (ζ) potential is used to determine the stability of a colloidal suspension. A high ζ potential value indicates better stability of the colloids due to repulsion between the surface charges on components present in the solution. The ζ potential of the self-aggregates of **CBH-1** and **CBH-2** in 1:3 v/v, DMSO-water solvent systems was found to be 14.2 and 17.9 mV, respectively. Such high ζ potential values indicate the considerable stability of the vesicular aggregates of **CBH-1** and **CBH-2** in the said binary solvent mixture. The presence of DMSO with its distinct electronic structure in the binary solvent system (1:3 v/v, DMSO-water) may also has a contribution in the measured zeta potential value of the self-aggregates.[44] In case of **CBH-2**, the solution lost its stability followed by precipitation upon aging (24-72 h) while the translucent solution was stable at least for one month in case of **CBH-1**. In contrast, **CBH-3** (0.5 mg mL^{-1}) showed very poor stability with immediate precipitation upon addition of water in its DMSO solution. **CBH-3** might have lost the critical HLB required for self-aggregation presumably due to the presence of an extra phenyl ring in the carbonyl residue (benzophenone) in comparison to other two hydrazone derivatives. Consequently, we investigated the self-aggregation behaviour of **CBH-1** and **CBH-2** in DMSO-water (1:3 v/v).

1.2.2. Microscopic investigations and DLS study of the self-assembly

The change in physical appearance upon addition of water to the DMSO solution of the amphiphiles (**CBH-1**, **CBH-2**) intrigued us to investigate the morphologies of the self-assemblies. In this context, we have taken TEM images of the translucent solution of **CBH-1** in 1:3 v/v, DMSO-water. Negatively stained TEM image of **CBH-1** (0.5 mg mL^{-1}) showed the formation of spherical shaped aggregates (vesicles) having diameter in the range of 40-80 nm (Figure 2a). The formation of vesicular self-assembly of **CBH-1** (0.5 mg mL^{-1}) was also confirmed by FESEM and AFM investigations. Spherical aggregates were observed in FESEM image having diameter of 60-100 nm (Figure 2b). The AFM image also supported the average size of the **CBH-1** vesicles in the range of ~100 nm (Figure 2c). Vesicle formation was further investigated from the fluorescence microscopic image of calcein, entrapped (fluorescent probe) within the self-assembly of **CBH-1**. The green emitting spheres substantiated the development of the vesicular aggregates by **CBH-1** in 1:3 v/v, DMSO-water binary mixture (Figure 2d). According to the DLS experiment, the hydrodynamic diameter of **CBH-1** vesicles in 1:3 v/v, DMSO-water was found to be in the range of 50-120 nm having average diameter of 80 nm (Figure 3). The observed size of the vesicles was found to be more or less in the same range irrespective of the spectroscopic or microscopic experiments. Similarly, both TEM and AFM images of **CBH-2** (0.5 mg mL^{-1}) in 1:3 v/v, DMSO-water binary mixture confirmed the formation of vesicles in 1:3 v/v, DMSO-water having diameter in the range of 150-250 nm (Figure 4). Moreover, the hydrodynamic diameter of the vesicles formed by **CBH-2** determined by DLS study (Figure 4) was found to be in the same range as observed in the microscopic investigations.

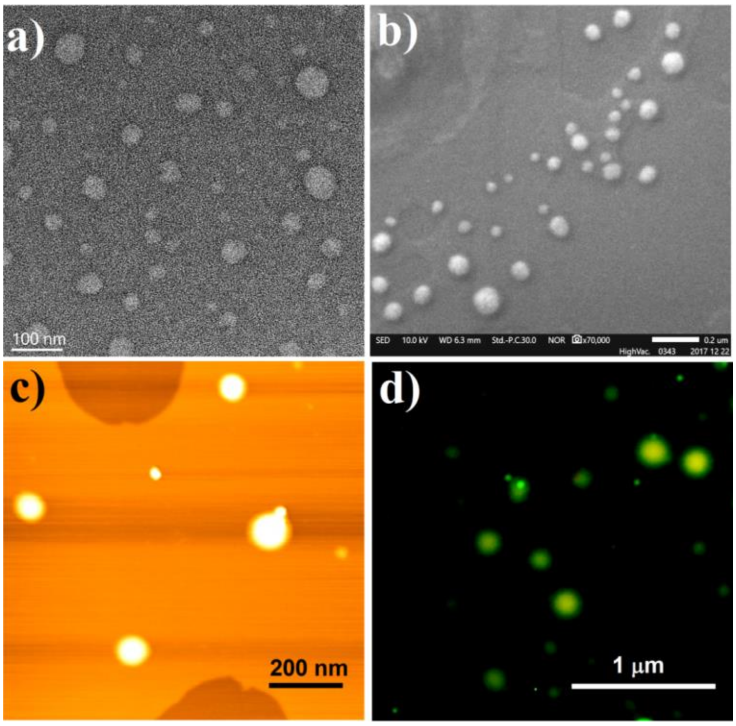

Figure 2. (a) Negatively stained TEM image, (b) FESEM image, (c) AFM image of **CBH-1** vesicles in 1:3 v/v, DMSO-water. (d) Fluorescence microscopic image (λ_{ex} = 450 nm) of encapsulated calcein within **CBH-1** vesicles prepared in 1:3 v/v, DMSO-water.

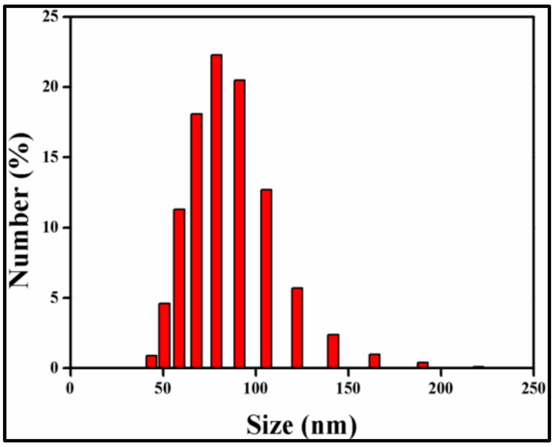

Figure 3. Size distribution profile of **CBH-1** vesicles by DLS in 1:3 v/v, DMSO-water solvent mixture ([**CBH-1**] = 0.5 mg mL^{-1}).

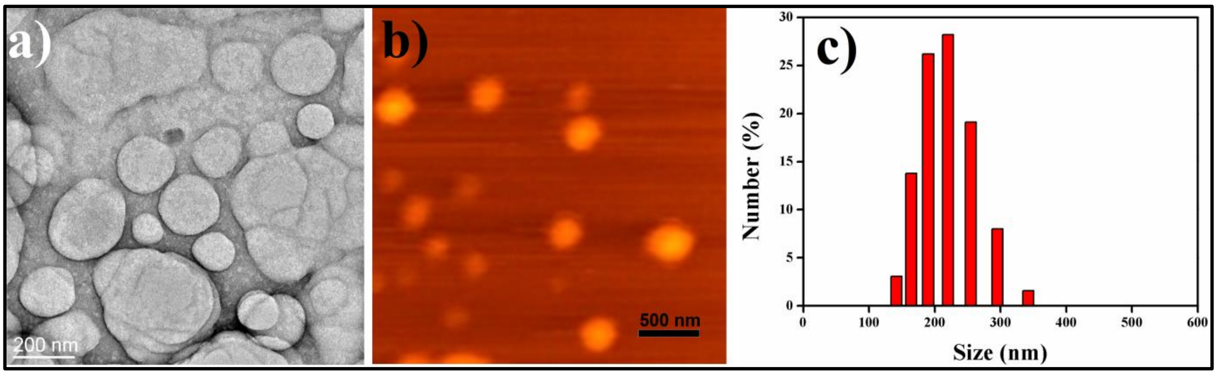

Figure 4. (a) Negatively stained TEM image, (b) AFM image, (c) size distribution profile of **CBH-2** vesicles by DLS in 1:3 v/v, DMSO-water solvent mixture ([**CBH-2**] = 0.5 mg mL^{-1}).

1.2.3. Spectroscopic studies of CBH-1 and CBH-2 vesicles

1.2.3.1. Steady-state fluorescence anisotropy

Steady state fluorescence anisotropy is generally used to investigate the microenvironment of an aggregated structure. Fluorescent probe, 1,6-diphenyl-1,3,5-hexatriene (DPH) is commonly used to determine the fluorescence anisotropy (r) for different self-aggregated structures. Herein, the r-value of DPH was measured for **CBH-1** self-aggregates in different compositions of DMSO-water mixtures (Table 1). With increase in the concentration of **CBH-1** from 0.25 to 1.0 mg mL^{-1}, the r value increased from 0.09 to 0.13, 0.10 to 0.16 and 0.16 to 0.21 in 2:1 v/v, 1:1 v/v and 1:3 v/v, DMSO-water mixtures, respectively. In case of **CBH-2**, the r-value improved from 0.16 to 0.26 in 1:3 v/v, DMSO-water upon changing the concentration from 0.25 to 0.50 mg mL^{-1}. DPH is a well-known membrane fluidity probe, which is susceptible to locate itself in the hydrophobic domain of the vesicle because of its rigid, rod-like structure. The enhancement in anisotropy value is observed possibly due to the higher restriction in the movement of DPH in the hydrophobic region of self-assemblies as well as because of the large sized aggregates. In general, DPH always exhibits greater fluorescence anisotropy in vesicles compared to that of micellar aggregates. Here also, the r-values of DPH in **CBH-1** and **CBH-2** self-assemblies are markedly higher (Table 1) compared to that of micellar aggregates of sodium dodecyl sulfate (r = 0.054).[8] This observation indicates the formation of vesicular aggregates by **CBH-1** and **CBH-2**. Moreover, an increasing trend in r-value from 0.13 to 0.21 (Table 1) was also noted upon gradual increment in water content within DMSO solution (from 2:1 v/v to 1:3 v/v) of **CBH-1** (1.0 mg mL^{-1}). Higher water percentage might have facilitated the formation of more stable vesicles by **CBH-1**.

Table 1. Steady-state fluorescence anisotropy (*r*) of DPH with varying concentrations of **CBH-1** in different ratios of DMSO-water solvent mixture.

Concentration (mg mL^{-1})	*r*-value (**CBH-1**)		
	2:1 v/v, DMSO-water	1:1 v/v, DMSO-water	1:3 v/v, DMSO-water
0.25	0.09	0.10	0.16
0.50	0.11	0.11	0.17
1.00	0.13	0.16	0.21

1.2.3.2. UV-visible study and aggregation pattern

The self-aggregation pattern of **CBH-1** and **CBH-2** that led to the formation of vesicles was investigated through a solvent dependent UV-vis spectroscopy. In UV-vis spectra, both the hydrazone derivatives, **CBH-1** (0.1 mg mL^{-1}) and **CBH-2** (0.1 mg mL^{-1}) showed the characteristic absorption maxima (λ_{max}) at 360 nm and 378 nm, respectively in pure DMSO i.e., in molecularly dissolved non-aggregated state (Figure 5a,b). With gradual increase in the water content to the DMSO solution, the λ_{max} showed hypsochromic shift with respect to the non-self-assembled state (in DMSO). At the highest water content (1:3 v/v, DMSO-water), the absorption maxima of **CBH-1** and **CBH-2** blue shifted to 355 nm and 372 nm, respectively (Figure 5a,b). As reported earlier, blue-shifted absorption maxima delineate the formation of self-assembly through parallel plane-to-plane stacking (sandwich-type array), which is referred as *H*-type aggregation.[8] Thus, the observed blue-shifted absorption maxima with increase in the water content within DMSO solution designates the possible *H*-type aggregation pattern for the self-assemblies of both **CBH-1** and **CBH-2** (Scheme 1).

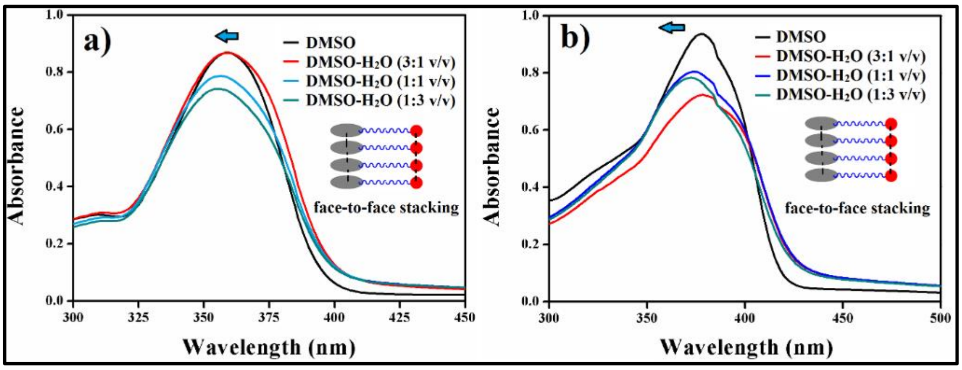

Figure 5. UV-visible spectra of (a) **CBH-1** and (b) **CBH-2** in different ratios of DMSO-water binary solvent mixture.

1.2.4. XRD study

The aggregation pattern of both the vesicles was further investigated by XRD studies. **CBH-1** showed sharp reflection at $2\theta = 2.04°$ (d = 43.4 Å) along with two additional less intense peaks at $2\theta = 3.65°$ (d = 24.2 Å) and $2\theta = 5.27°$ (d = 16.7 Å) in 1:3 v/v, DMSO-water (Figure 6a). Similarly, in the self-assembled state, **CBH-2** showed a sharp XRD peak at $2\theta = 2.02°$ (d = 43.7 Å) with two other peaks at $2\theta = 3.54°$ (d = 24.4 Å) and $2\theta = 5.22°$ (d = 16.9 Å) (Figure 6b). These characteristic diffraction patterns confirmed that the bilayer vesicular aggregates were formed through highly ordered lamellar like stacking (Scheme 1).[45,46]

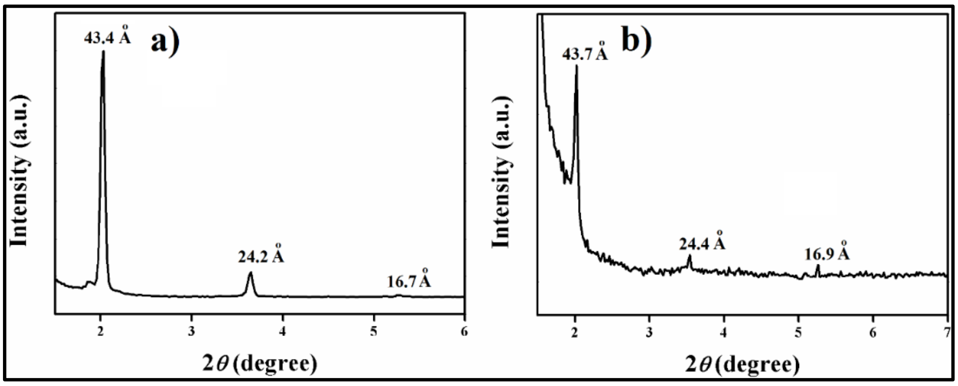

Figure 6. Small angle XRD pattern of (a) **CBH-1** and (b) **CBH-2** in 1:3 v/v, DMSO-water.

1.2.5. Participation of intermolecular non-covalent interactions in self-assembly

Participation of various non-covalent forces such as intermolecular hydrogen-bonding (*H*-bonding), hydrophobic interactions, π–π stacking during self-aggregation were investigated by FTIR and solvent dependent ^1H-NMR spectroscopy. The FTIR spectrum of **CBH-1** in CHCl3 (non-aggregated state) showed transmittance peaks at ν =3313, 1639 and 1535 cm^{-1} (Figure 7a) due to $\nu_{\text{N-H}}$ (amide A), $\nu_{\text{C=O}}$ (amide I, stretching) and $\delta_{\text{N-H}}$ (amide II, bending). These peaks got shifted to $\nu_{\text{N-H}}$ (amide A) = 3293-3511 cm^{-1} (broad band), $\nu_{\text{C=O}}$ (amide I, stretching) = 1604 cm^{-1} and $\delta_{\text{N-H}}$ (amide II, bending) = 1552 cm^{-1} in 1:3 v/v, DMSO-d$_6$-D$_2$O solvent mixture (Figure 7a). Analogous results were observed in case of **CBH-2**, where the transmittance peaks $\nu_{\text{N-H}}$ (amide A) = 3310 cm^{-1}, $\nu_{\text{C=O}}$ (amide I, stretching) = 1639 cm^{-1} and $\delta_{\text{N-H}}$ (amide II, bending) = 1521 cm^{-1} shifted to $\nu_{\text{N-H}}$ (amide A) = 3299-3505 cm^{-1}, $\nu_{\text{C=O}}$ (amide I, stretching) = 1620 cm^{-1} and $\delta_{\text{N-H}}$ (amide II, bending) = 1567 cm^{-1}, respectively (Figure 7b). These shifts in stretching and bending frequencies in DMSO-d$_6$-D$_2$O solvent mixture indicates the involvement of intermolecular hydrogen bonding between the carbonyl (C=O) and amide

N-H (i.e., C=O----H-N) in the process of self-assembly induced vesicle formation by **CBH-1** and **CBH-2**.

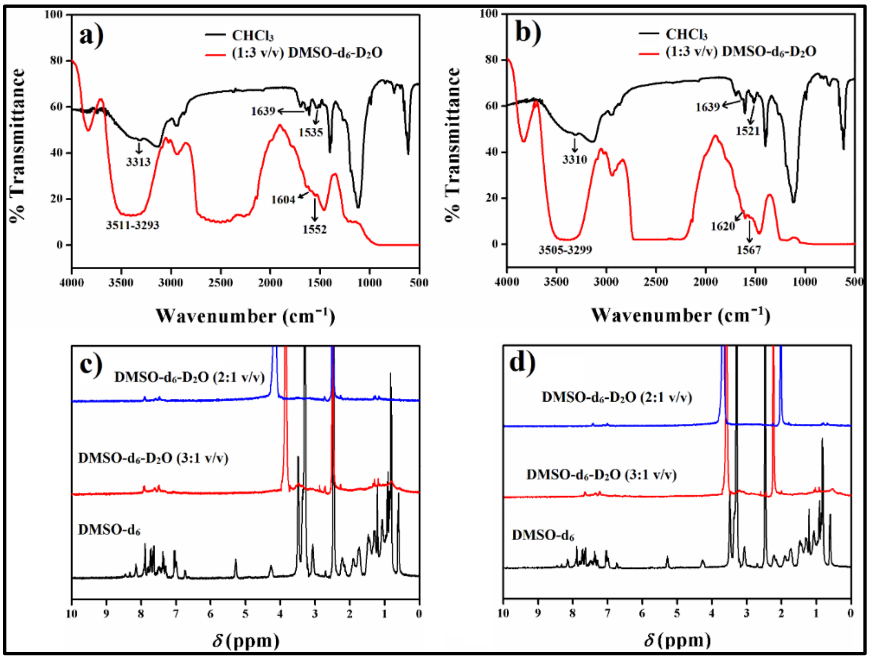

Figure 7. FTIR spectra of (a) **CBH-1** and (b) **CBH-2** in chloroform (non-self-aggregated state) and 1:3 v/v, DMSO-d_6-D_2O (self-aggregated state). Solvent dependent ^{1}H-NMR spectra of (c) **CBH-1** and (d) **CBH-2**.

Next, we carried out the solvent dependent ^{1}H-NMR of **CBH-1** and **CBH-2** by varying the D_2O content in DMSO-d_6 solution. In DMSO-d_6, cholesteryl and ethylenoxy protons of both **CBH-1** and **CBH-2** showed characteristic NMR signals at $\delta = 0.56$-3.54 ppm while the aromatic protons appeared at $\delta = 6.70$-8.39 ppm (Figure 7c,d). With the gradual increment in D_2O content (up to 2:1 v/v DMSO-d_6-D_2O), these characteristics NMR signals of both amphiphiles got notably suppressed. Such change in the nature of the NMR peaks with increased D_2O content took place possibly due to the participation of hydrophobic interactions between the steroidal moieties and aromatic rings (phenyl ring), which facilitates faster relaxation due to slower tumbling. In addition to this, the suppression of the aromatic protons also took place possibly due to π-π stacking (between the phenyl rings) during the formation of larger aggregates by cholesteryl based hydrazone-tethered amphiphiles (Figure 7c,d). Further increase in the D_2O amount did not show any notable change in the NMR peaks pattern. The above mentioned microscopic and spectroscopic experiments delineate the participation of several non-covalent interactions in the formation of self-assembled vesicles by **CBH-1** and **CBH-2**.

1.2.6. pH-responsive cleavage of hydrazone bond: dissipation of self-assembly

To investigate the stimuli-responsive dissipation of self-assembly, we examined the stability of these hydrazone-tailored self-assembled vesicles in varying pH (acidic, neutral and basic). Initially, we monitored the change in UV-vis spectra of both **CBH-1** and **CBH-2** at 0.1 mg mL^{-1} in 1:3 v/v, DMSO-water with varying pH. As mentioned in the preceding section, **CBH-1** (0.1 mg mL^{-1}) showed blue shifted absorption maxima (λ_{max}) at 355 nm in the self-assembled state (1:3 v/v, DMSO-water) (Figure 5a). At pH 7.0 and above, no significant changes in the spectral pattern or the λ_{max} was observed (Figure 9a,b). Next, the UV-vis spectra were recorded in acidic pH upon incubation with HCl of varying concentrations (0.025-0.25 M). The λ_{max} of the self-assembled solution of **CBH-1** in 1:3 v/v, DMSO-water was immediately red shifted to 361 nm in presence of 0.025 M HCl (Figure 8a). This λ_{max} gradually red shifted to 371 nm with the enhancement in HCl concentration up to 0.25 M (Figure 8a). Analogous result was found in case of **CBH-2** (0.1 mg mL^{-1}) where the λ_{max} at 370 nm (in self-aggregated state) exhibited bathochromic shift to 378 nm in presence of 0.15 M HCl (Figure 8b).

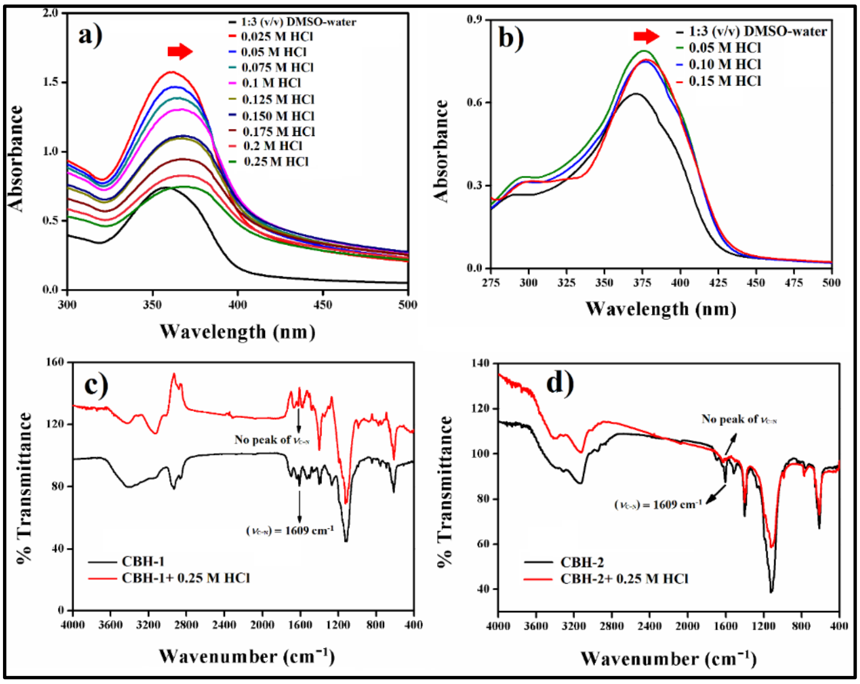

Figure 8. UV-visible spectra of (a) **CBH-1** and (b) **CBH-2** in 1:3 v/v, DMSO-water incubated with different concentration of HCl. FTIR spectra of (c) **CBH-1** and (b) **CBH-2** treated with and without 0.25 M HCl.

This pH-responsive changes in the UV-vis spectra of both **CBH-1** and **CBH-2** in 1:3 v/v DMSO-water were also monitored in the pH range of 2.0-5.0 using phosphate-HCl buffer

(20 mM) (Figure 9c,d). Similar red shift in the absorption maxima was observed in case of both amphiphiles (Figure 9c,d). These observations in UV-vis study evidently indicate that the self-assembled structure (vesicles) might have been disintegrated in the acidic environment possibly due to pH-responsive cleavage of hydrazone bond. Dissipation of self-assembled structures upon treating the vesicles of **CBH-1** and **CBH-2** (1:3 v/v, DMSO-water) with 0.25 M HCl was examined by taking the TEM images of the respective systems (Figure 10a,b). Absence of any spherical aggregates further confirmed the disintegration of vesicles due to the cleavage of the hydrazone linkage in acidic medium.

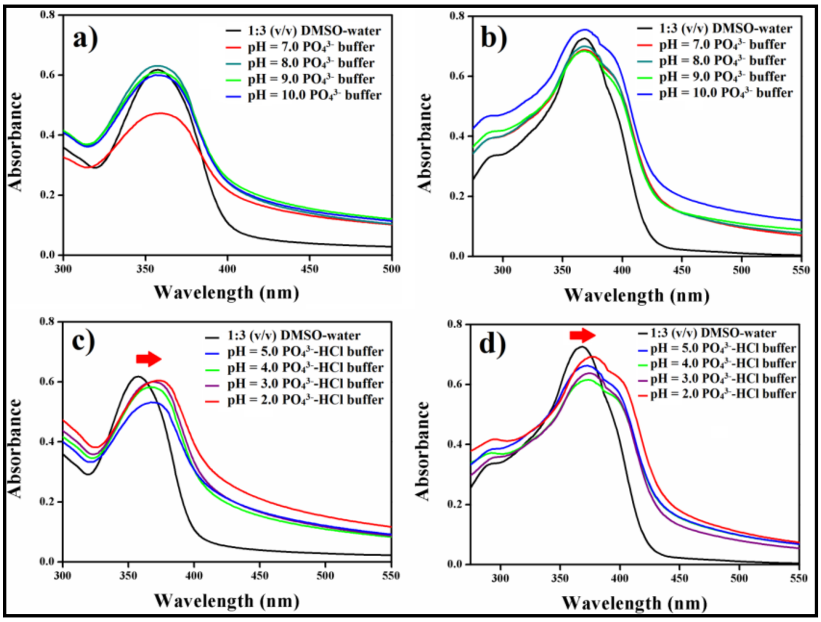

Figure 9. pH dependent UV-visible spectra of (a, c) **CBH-1** ([**CBH-1**] = 0.1 mg mL^{-1}) and (b, d) **CBH-2** ([**CBH-2**] = 0.1 mg mL^{-1}) in phosphate buffer (pH = 7.0-10.0) and phosphate-HCl buffer (pH = 2.0-5.0).

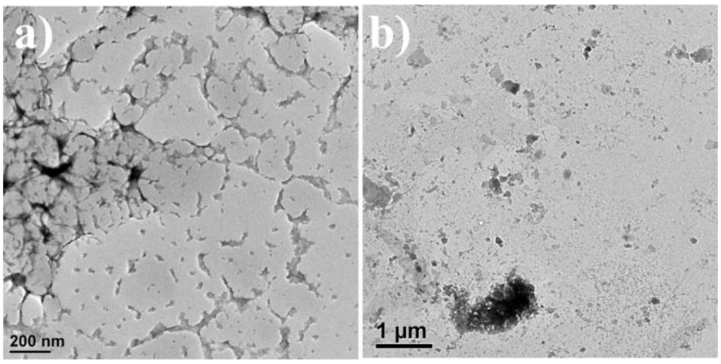

Figure 10. TEM images of destructed self-assemblies of (a) **CBH-1** and (b) **CBH-2** in 1:3 v/v, DMSO-water upon treating with 0.25 M HCl.

The dissipation of self-assembly owing to the breaking of hydrazone bond in acidic environment was characterized by mass and FTIR spectroscopy. The formation of the hydrazine and respective aldehyde upon cleavage of the hydrazone bond of **CBH-1** and **CBH-2** in presence of protic acid was monitored by MALDI-TOF mass spectrometry. The hydrazone bond is stable at neutral pH or above but rapidly gets destroyed in acidic environment as shown in Scheme 2. The observed mass of both the hydrazone derivatives **CBH-1** and **CBH-2** was found to be 805.837 ([M+Na]+) and 848.967 ([M+Na]+), respectively (Figure 11a, 12a). The vesicular solution of the amphiphiles (**CBH-1** and **CBH-2**) in 1:3 v/v, DMSO-water was treated with 0.25 M HCl for 6 h. The resulting mixture was lyophilized and the obtained residue was used for mass spectrometry. The hydrazone bond is known to get cleaved into two major fragments: hydrazine residue and carbonyl residue (Scheme 2). In both cases, the mass spectra of the self-aggregated amphiphiles (**CBH-1** and **CBH-2**) after treating with HCl showed the presence of common fragment i.e, hydrazine residue at 717.856 ([M1+Na]+) and 718.818 ([M1+H+Na]+) for **CBH-1** and **CBH-2**, respectively (Figure 11b, 12b). In addition, molecular ion peaks of the carbonyl residues were also observed at 106.088 (M^{2+}) and 149.178 (M^{2+}) for both **CBH-1** and **CBH-2**, respectively (Figure 11c, 12b). This observation clearly depicts that the degradation of the hydrazone residue in acidic environment leads to the disintegration of the vesicles.

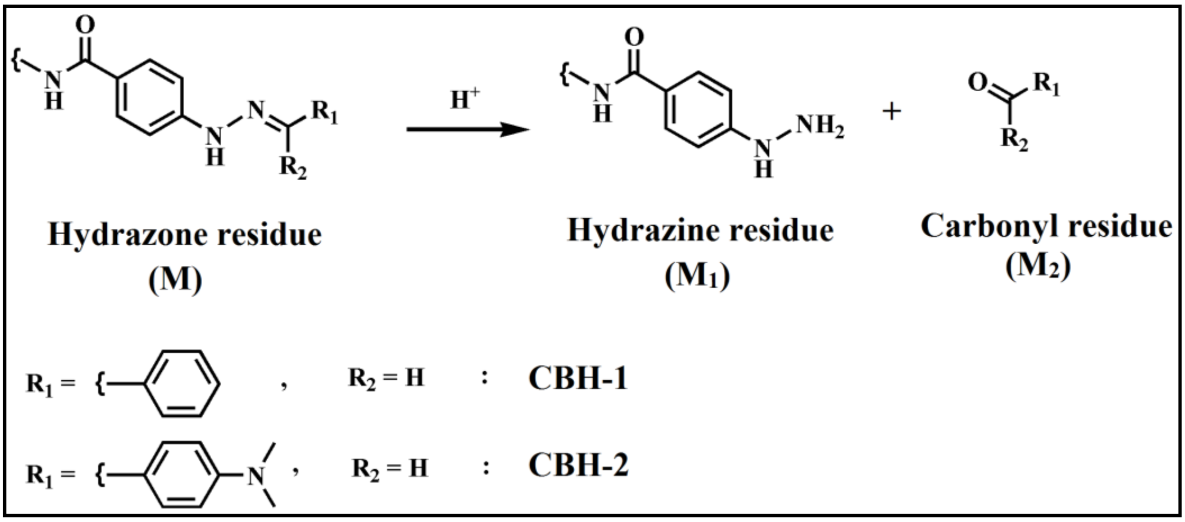

Scheme 2. Schematic presentation of chemical transformation of hydrazone derivative in acidic environment.

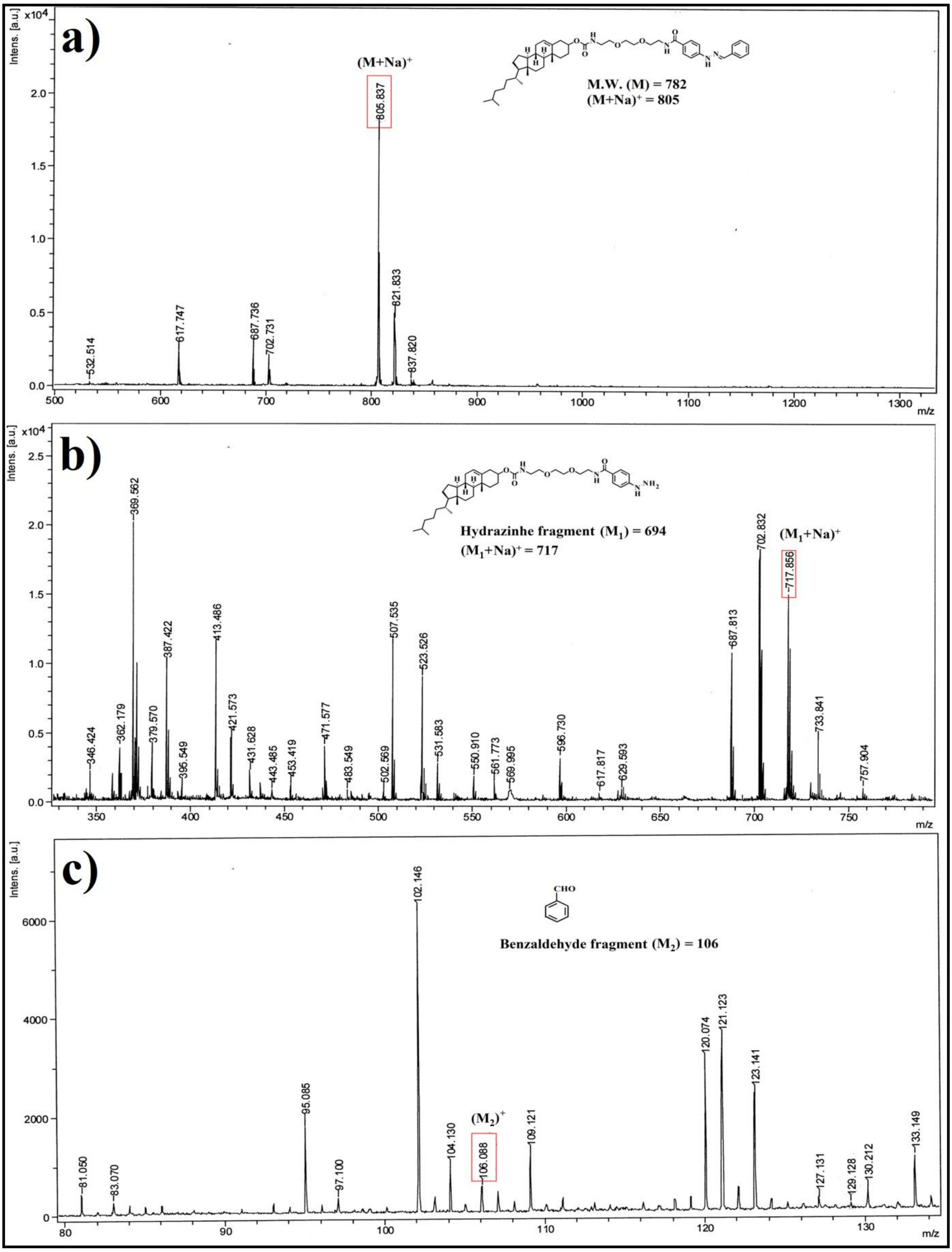

Figure 11. MALDI-TOF mass spectra of (a) **CBH-1** (without treatment of HCl), (b) and (c) fragmentation of **CBH-1** upon treating with 0.25 M HCl.

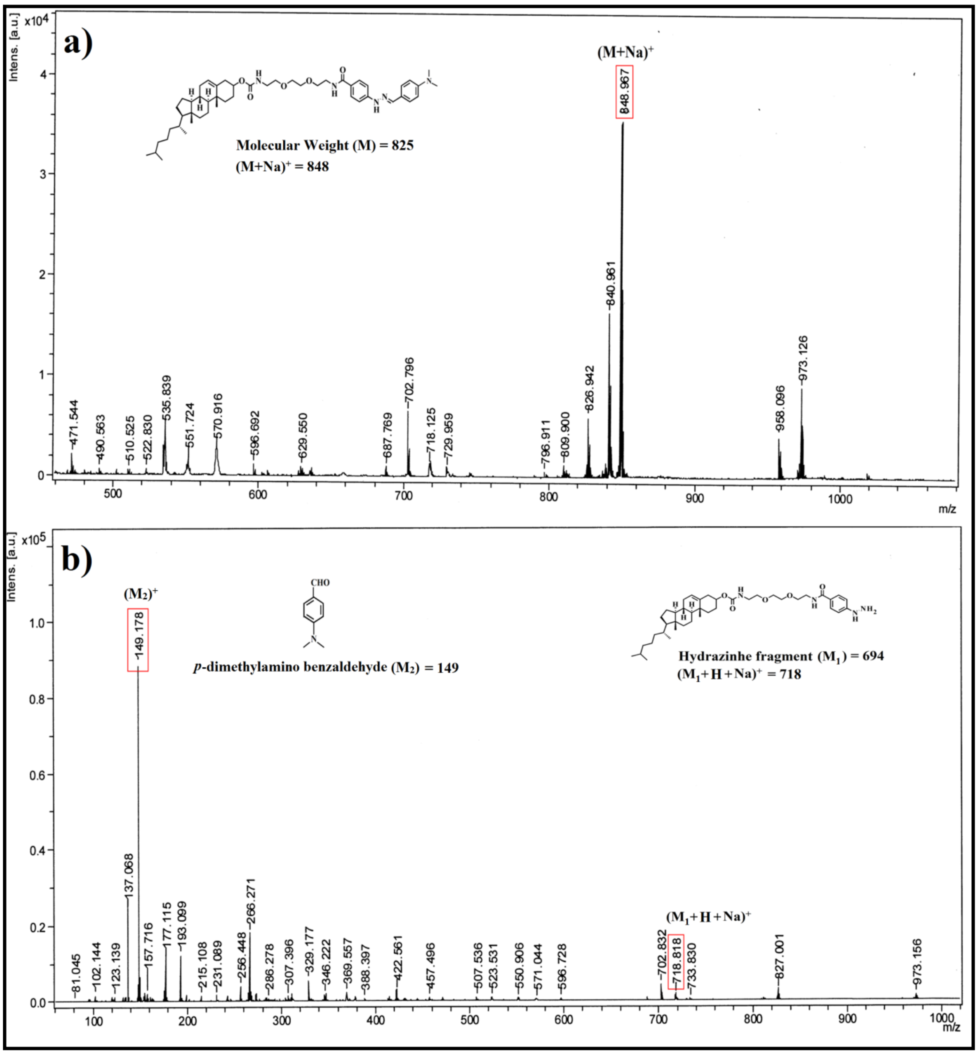

Figure 12. MALDI-TOF mass spectra of (a) **CBH-2** (without treatment of HCl), (b) fragmentation of **CBH-2** upon treating with 0.25 M HCl.

We have also investigated the FTIR spectra of both amphiphiles (**CBH-1** and **CBH-2**) in presence and absence of HCl for further confirmation of hydrazone bond cleavage. In FTIR spectra the stretching frequency of C=N appeared at $\nu_{C=N}$ (stretching) = 1609 cm^{-1} in case of native **CBH-1** and **CBH-2** (Figure 8c,d).[47] This characteristic peak in FTIR disappeared upon treatment with HCl, which is in concurrence to the above-mentioned mass spectroscopic data indicating the disintegration of hydrazone bond in acidic pH (Figure 8c,d). Herein, we observed the stimuli-responsive dissipation of vesicular self-assemblies formed by the cholesterol-based hydrazone-tailored amphiphiles (**CBH-1** and **CBH-2**) due to dissociation of the hydrazone bond in acidic environment.

1.2.7. Doxorubicin loading and release studies

After successful formation and stimuli-responsive degradation of CBH vesicles, anticancer drug (doxorubicin) encapsulation as well as its pH-induced release study was carried out using **CBH-1** vesicle. **CBH-1** vesicle was chosen for drug encapsulation and release study considering its prolong stability. The detail procedure of drug entrapment is described in the experimental section where doxorubicin was encapsulated within the **CBH-1** vesicles prepared in 1:3 v/v, DMSO-water. Drug encapsulated vesicles were separated from free doxorubicin by size exclusion chromatography using sephadex G-50. Entrapment of doxorubicin within the **CBH-1** vesicle was confirmed from the fluorescence microscopic image exhibiting the characteristic red emission (Figure 13a). The drug loading efficiency of **CBH-1** vesicles was found to be 57% (calculated after treating the doxorubicin entrapped vesicle with 0.25 M HCl and followed by comparing the absorbance of liberated doxorubicin with the standard calibration curve).[8] The release of encapsulated drug from the synthesized **CBH-1** vesicles was also confirmed by recording the fluorescence spectra of the drug molecule. The emission intensity of entrapped doxorubicin within **CBH-1** vesicles was found to be notably decreased in comparison to the emission intensity of free doxorubicin having the same concentration (Figure 13b). Interestingly, the emission intensity of doxorubicin regained upon addition of 0.25 M HCl within the drug entrapped **CBH-1** vesicles. The regained emission intensity is comparable to that of the free doxorubicin. This observation supports the release of encapsulated doxorubicin from vesicles to the bulk solvent through the cleavage of hydrazone bond in the presence of 0.25 M HCl that plays the key role in rupturing the vesicular aggregates.

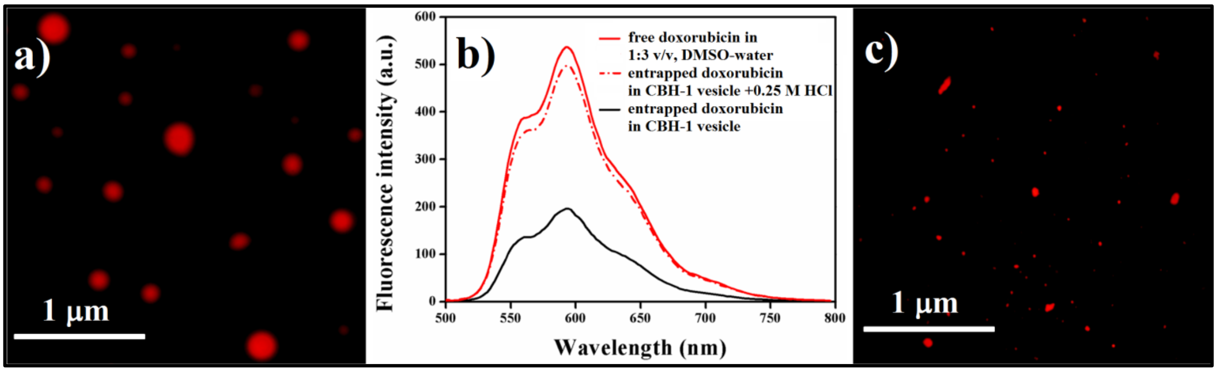

Figure 13. (a) Fluorescence microscopic image (λ_{ex} = 490 nm) of doxorubicin encapsulated **CBH-1** vesicles, (b) emission spectra of doxorubicin entrapped within **CBH-1** vesicles, after treating with 0.25 M HCl and free doxorubicin, (c) fluorescence microscopic image of released doxorubicin after treating with 0.25 M HCl.

The disintegration of vesicles was also confirmed from the fluorescence microscopic images that showed discrete presence of red emitting doxorubicin without the presence of any spherical structure (Figure 13c). Moreover, we have also studied the doxorubicin release from **CBH-1** vesicles in phosphate buffer saline (PBS) at different pH values (pH = 5.5-8.0), which are more similar to physiological conditions (Figure 14). This pH responsive release of doxorubicin was analyzed by fluorescence study. The emission intensity of entrapped doxorubicin within **CBH-1** vesicles at pH = 7.0-8.0 was found to be similar in comparison to the doxorubicin loaded vesicles in 1:3 (v/v) DMSO-water solvent mixture having same concentration (Figure 14). At pH = 6.5, an enhancement in the fluorescence intensity of doxorubicin loaded CBH-**1** vesicle was noted. On further lowering of pH to 6.0 and 5.5, the emission intensity steadily increased and became almost comparable to that of free doxorubicin (Figure 14). This observation further delineates that below pH= 6.5 the cargo loaded vesicles get ruptured possibly due cleavage of hydrazone bond which has led to the release of loaded doxorubicin.

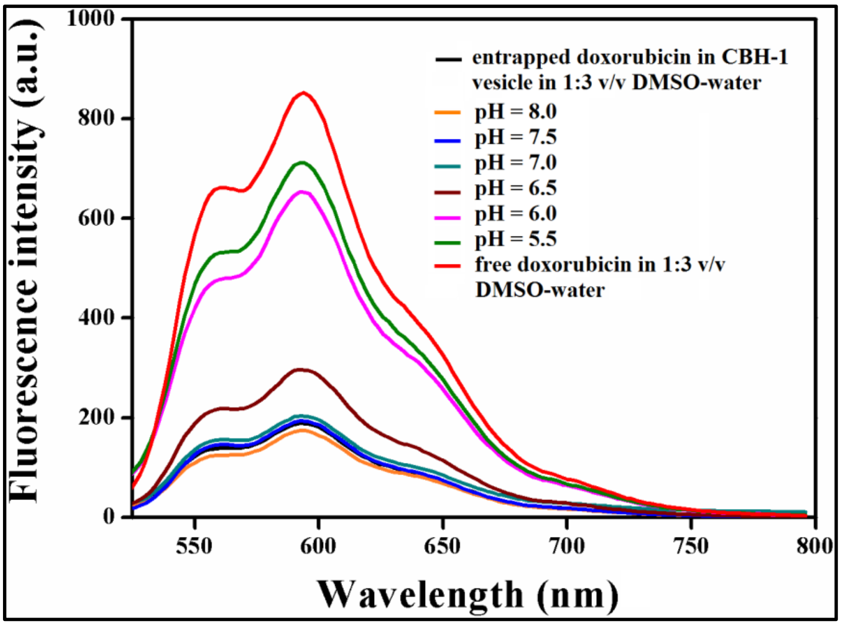

Figure 14. pH dependent doxorubicin release from doxorubicin loaded **CBH-1** vesicles in phosphate buffer saline (PBS) solution (pH = 5.5-8.0).

1.3. CONCLUSION

On the basis of previously reported pH-responsive drug release systems derived from different zwitterionic copolymers, dendrimers, this work demonstrated development of cholesterol based pH-responsive hydrazone-tethered small amphiphiles (**CBH-1-3**) by variation of the carbonyl unit in the hydrazone residue.[48,49] Among these amphiphiles, **CBH-1** and **CBH-2** formed self-aggregated vesicular structure in 1:3 v/v, DMSO-water via *H*-aggregation. Formation of bilayer vesicles by these amphiphiles took place possibly through highly ordered lamellar structure. These vesicles are stable at neutral pH and above but got disintegrated in acidic pH due to the cleavage of hydrazone bond. The disruption in the self-assembly in presence of acidic medium was monitored by different spectroscopic and microscopic techniques. The vesicle prepared from **CBH-1** was utilized for drug entrapment and its pH-induced release in acidic medium using doxorubicin as drug. Hence, these stimuli-responsive hydrazone appended small amphiphiles will have the potentials to be exploited in task specific applications. This finding also triggered our interest to design more hydrophilic segment containing stimuli-responsive amphiphiles, which will have the potential to form vesicular aggregates in pure water and hence exploit their potentials in diverse biological applications.

1.4. EXPERIMENTAL SECTION

1.4.1. Materials and methods

Silica gel of 60-120 mesh and 100-200 mesh, benzophenone, *N*-hydroxysuccinimide (NHS), *N*,*N*-dicyclohexylcarbodiimide (DCC), solvents and all other reagents were purchased from SRL, India. Milli-Q water was used throughout the study. Thin layer chromatography (TLC) was performed on Merck precoated silica gel 60-F_{254} plates. Cholesteryl chloroformate, 4-hydrazinobenzoic acid, 2,2′-(ethylenedioxy)bis(ethylamine), sephadex-G50, calcein, all deuterated solvents for NMR and FTIR were procured from Sigma-Aldrich. Doxorubicin was extracted from doxorubicin hydrochloride. Benzaldehyde was purchased from Avra Chemicals, India. *p*-Dimethylaminobenzaldehyde was procured from Loba Chemie, India. Virtis 4KBTXL-75 freeze drier was used for lyophilization. ^{1}H-NMR spectra were recorded in AVANCE 500 MHz (Bruker) and 300 MHz (Bruker) spectrometer. Mass spectrometric data were acquired through the electron spray ionization (ESI) technique on Q-tof-micro quadrupole mass spectrometer (Micromass). MALDI-TOF spectra were obtained on Bruker Ultaflex MALDI-TOF with 2,5-dihydroxy benzoic acid (DHB) as matrix.

1.4.2. Synthesis of hydrazone-tailored amphiphiles (CBH-1-3)

Synthetic procedure for the hydrazone-tailored amphiphiles (**CBH-1-3**) is briefly shown in **Scheme 3**.

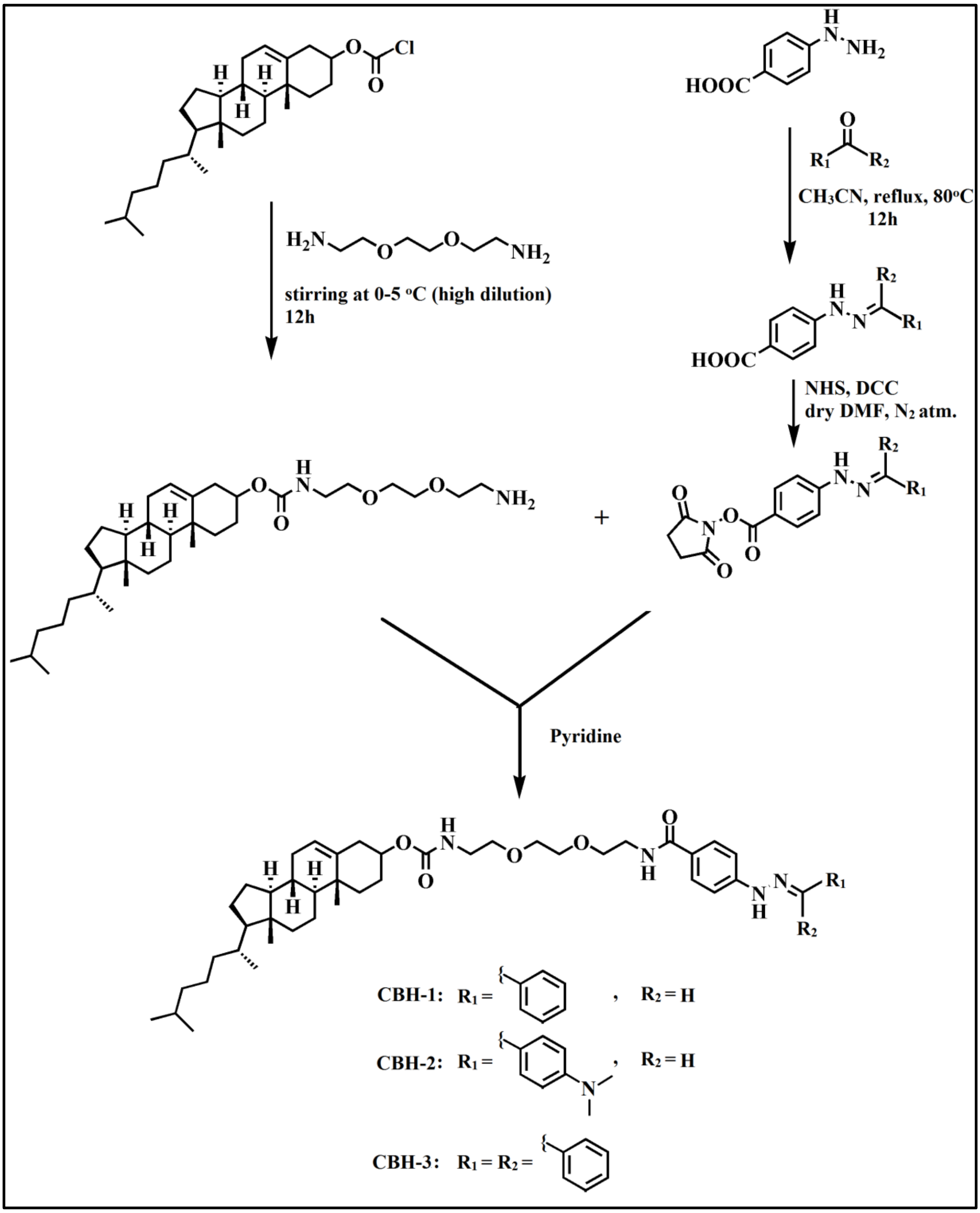

Scheme 3. Synthetic scheme for hydrazone-tailored amphiphiles **CBH-1-3.**

In case of **CBH-1**, mixture of 4-hydrazinobenzoicacid (1.32 mmol) and benzaldehyde (1.32 mmol) was refluxed at 80 °C in acetonitrile for 12 h. The reaction mixture was cooled to room temperature and evaporated to dryness to obtain yellowish orange mass.[50] The hydrazone protected benzoic acid was purified by 100-200 mesh column chromatography using methanol (3 %)/chloroform as the eluent. On the other hand, mono-cholesteryl protected 2,2′-(ethylenedioxy)bis(ethylamine) was prepared by adding drop wise cholesteryl chloroformate (11.2 mmol taken in dichloromethane (DCM)) from the dropping funnel to 2,2′-(ethylenedioxy)bis(ethylamine) (16.8 mmol) taken in a round bottom flask in excess DCM. This reaction was carried out at 0-5 °C in ice cold condition. The DCM mixture was then washed with Na_2CO_3 solution and the organic part was extracted in DCM. The product was purified through 60-120 mesh column chromatography using methanol (5 %)/chloroform as the eluent. The NHS linked hydrazone was prepared by using hydrazone of 4-hydrazinobenzoic acid (0.25 mmol), DCC (0.30 mmol), and NHS (0.28 mmol) in dry *N*, *N*-dimethylformamide (DMF) and stirred for 12 h under N_2 atmosphere. To this solution, mono-cholesteryl protected 2, 2′-(ethylenedioxy)bis(ethylamine) (0.25 mmol) and dry pyridine were added. The solution was stirred for 12 h and then DMF was distilled out under vacuum. The residue mixture was then purified through column chromatography by using 100-200 mesh silica gel and methanol (3 %)/chloroform as the eluent to obtain pure **CBH-1**. Similar synthetic protocol was followed to synthesize **CBH-2** and **CBH-3** using *p*-dimethylaminobenzaldehyde and benzophenone as carbonyl residue, respectively. All the synthesized compounds were characterized by ^{1}H-NMR, HR-MS and MALDI-TOF mass spectrometry.

1.4.3. Preparation of vesicles

CBH-1 and **CBH-2** were found to be insoluble in pure water. Hence, these two compounds (1.0 mg of **CBH-1** and 0.5 mg of **CBH-2**) were initially dissolved in DMSO to obtain a clear homogeneous solution. To this DMSO solution, Milli-Q water was added to maintain a volume ratio of 1:3 v/v, DMSO-water (1 mL) that produced a translucent vesicular solution of both **CBH-1** and **CBH-2**. In case of **CBH-3**, addition of water in its DMSO solution resulted in the immediate precipitation of the compound.

1.4.4. Transmission electron microscopy (TEM) study

Transmission electron microscopic investigation was carried out using 4 mL of both **CBH-1** and **CBH-2** (0.5 mg mL^{-1}) solution taken in 1:3 v/v, DMSO-water which was deposited on a 300-mesh carbon coated copper grid and dried. With freshly prepared uranyl acetate solution (1 mL, 1% w/v) the copper grid was negatively stained and the excess solution was immediately blotted with a filter paper. The sample was dried for 4 h in vacuum before taking the image. The TEM images were studied in JEOL JEM 2010 microscope.

1.4.5. Field-emission scanning electron microscopy (FESEM)

For performing FESEM study, 5 µL of **CBH-1** (0.5 mg mL^{-1}) solution in 1:3 v/v, DMSO-water was placed on a piece of cover slip and dried overnight. Then, it was kept for few hours under vacuum before imaging. FESEM images were obtained on a JSM-IT300HR microscope.

1.4.6. Atomic force microscopy (AFM) study

To capture AFM images, 5 mL solution of both **CBH-1** (0.5 mg mL^{-1}) and **CBH-2** (0.5 mg mL^{-1}) were taken in 1:3 v/v, DMSO-water and deposited separately on freshly cleaved (1 cm x 1 cm) mica followed by overnight drying before obtaining the images. The AFM images were taken on a Veeco, model AP0100 instrument in non-contact mode.

1.4.7. Fluorescence microscopy study

Fluorescence microscopic investigation was carried out by mixing **CBH-1** (5.0 mg) with 20 µL of calcein (2 mM) solution in water, and making up the volume to 1 mL maintaining 1:3 v/v, DMSO-water. The final concentrations of **CBH-1** and calcein were 5.0 mg mL^{-1} and 40 µM, respectively. The solution was kept overnight under stirring condition. The resulting solution was then loaded into a sephadex G-50 column (15 cm height and 1.2 cm diameter) pre-equilibrated with 1:3 v/v, DMSO-water and eluted with the same solvent mixture. Vesicular solutions were eluted just after the void volume. The eluent was collected in 1 mL fractions. The absorbance for all fractions was measured at 490 nm that confirmed the presence of calcein in each fraction containing vesicles. Finally, the filtration was carried out until the complete removal of un-entrapped calcein. Calcein entrapped vesicles were separated from the free calcein by the gel filtration technique. Next, 10 mL solution of calcein entrapped **CBH-1** in 1:3 v/v, DMSO-water solvent mixture was placed on a glass slide, dried and examined under fluorescence microscope (Olympus BX-61) at 40× magnification.

1.4.8. Dynamic light scattering (DLS) and zeta (ζ) potential measurements

Mean hydrodynamic diameter of the self-aggregates of both **CBH-1** (0.5 mg mL^{-1}) and **CBH-2** (0.5 mg mL^{-1}) in 1:3 v/v, DMSO-water mixture was determined by DLS using a fixed-angle apparatus (Zen 3690 Zetasizer Nano ZS instrument (Malvern Instrument Ltd.)). The scattering intensity was measured at an angle of 175°. The same instrument was also used to measure the zeta (ζ) potential measurements of **CBH-1** and **CBH-2** taken in 1:3 v/v, DMSO-water having 0.5 mg mL^{-1} of each amphiphile. An average of three successive measurements was noted for each sample.

1.4.9. Fluorescence anisotropy

Fluorescence spectra were recorded using the hydrophobic fluorescent probe 1,6-diphenyl-1,3,5-hexatriene (DPH) in a Varian Cary Eclipse fluorescence spectrophotometer. The steady-state anisotropy (*r*) of DPH was measured in individual solution of **CBH-1** in different solvent compositions i.e. (1:3 v/v), (1:1 v/v), (2:1 v/v) DMSO-water and solution of **CBH-2** in 1:3 v/v, DMSO-water binary mixture. A stock solution of DPH (0.2 mM) was prepared in tetrahydrofuran (THF), and in each investigating solution (1 mL) the final concentration of DPH was maintained at 1 μM. The DPH included **CBH-1** and **CBH-2** solutions were excited at 370 nm. The emission intensity was measured at 450 nm using an emission cutoff filter at 430 nm to avoid any scattering due to turbidity of the solution. The excitation and emission slit widths were kept at 5 nm. The fluorescence anisotropy (*r*) was calculated by the instrument software using following equation

$$r = (I_{VV} - GI_{VH}) / (I_{VV} + 2GI_{VH}) \qquad (1)$$

where I_{VV} and I_{VH} are the intensities of the emission spectra obtained with vertical and horizontal polarization (for vertically polarized light), respectively, and $G = I_{HV} / I_{HH}$ is the instrumental correction factor, where I_{HV} and I_{HH} are the emission intensities obtained with vertical and horizontal polarization (for horizontally polarized light), respectively. The fluorescence measurements were performed at least five times for each sample at 25 °C.

1.4.10. UV-visible study

To understand the self-aggregation mechanism of the synthesized amphiphiles, UV-vis spectra were recorded on a Perkin Elmer Lambda 25 spectrophotometer. We have taken the UV-visible spectra of both **CBH-1** (0.1 mg mL^{-1}) and **CBH-2** (0.1 mg mL^{-1}) in different solvent mixture of DMSO-water with varying ratio of DMSO and water (3:1 v/v, 1:1 v/v, 1:3 v/v DMSO-water binary mixtures). We also monitored pH-responsive change in UV-vis spectra of self-assembly of both **CBH-1** and **CBH-2** in 1:3 v/v, DMSO-water treated with HCl having different concentrations and also at different pH (pH =2.0-5.0 using phosphate-HCl buffer (20 mM) and pH = 7.0 and above up to 10.0 using phosphate buffer, 20 mM).

1.4.11. FTIR study

FTIR measurements were performed at the non-self-assembled state in $CHCl_3$ and in the self-aggregated state in 1:3 v/v, DMSO-d_6-D_2O for both **CBH-1** and **CBH-2** at room temperature. All the experiments were performed using 1 mm CaF_2 cell (in $CHCl_3$ solution and (1:3 v/v, DMSO-d_6-D_2O) in a Perkin Elmer Spectrum 100 FTIR spectrometer. To monitor the cleavage of hydrazone bond in acidic medium, both the vesicular solutions of **CBH-1**(1.0 mg mL^{-1}) and **CBH-2** (0.5 mg mL^{-1}) prepared in 1:3 v/v, DMSO-water was treated with 0.25 M HCl for 6 h. The resulting reaction mixture was lyophilized and FTIR study was carried out for the residual masses using KBr pellets.

1.4.12. Solvent dependent ^{1}H-NMR study

Solvent dependent ^1H-NMR spectra of **CBH-1** and **CBH-2** were recorded on an Avance 300 MHz (Brucker) spectrometer at a concentration of 1.0 mg mL^{-1} in DMSO-d_6 and in 3:1 v/v, 2:1 v/v DMSO-d_6-D_2O.

1.4.13. X-ray diffraction (XRD) study

50 mL solution of each **CBH-1** (1.0 mg mL^{-1}) and **CBH-2** (0.5 mg mL^{-1}) taken in 1:3 v/v, DMSO-water solvent mixture was placed separately on glass slide. This drop cast solutions was air-dried to obtain a thin film. The XRD study of the dried films was carried out in a Bruker D8 Advance diffractometer, and the source used was CuK_α radiation (λ = 0.15406 nm) with a voltage of 50 kV and current of 30 mA.

1.4.14. MALDI-TOF mass spectrometry study

pH-responsive cleavage of hydrazone residue to the corresponding fragments (hydrazine and carbonyl residue) was investigated using MALDI-TOF mass spectrometry. Both the vesicular solutions of **CBH-1**(1.0 mg mL^{-1}) and **CBH-2** (0.5 mg mL^{-1}) prepared in 1:3 v/v, DMSO-water were treated with 0.25 M HCl for 6 h. The resulting reaction mixture was lyophilized to obtain the solid mass. The residual mass was further dissolved in methanol and the mass spectrometric study was performed in Bruker Ultraflex MALDI-TOF.

1.4.15. Doxorubicin loading and release

We have chosen the anti-cancer drug doxorubicin to check the loading capacity of **CBH-1** vesicles prepared in 1:3 v/v, DMSO-water. Initially, **CBH-1** (5.0 mg) and doxorubicin (2.0 mg) were taken in a glass vial and 1:3 v/v, DMSO-water (500 μL) was added to it. The mixture was kept overnight under stirring condition. This resulting solution was then loaded into a sephadex G-50 column (15 cm height and 1.2 cm diameter) pre-equilibrated with 1:3 v/v, DMSO-water. Elution was carried out with the same solvent mixture. Right after the void volume drug loaded vesicular solutions were eluted. The eluent was collected in 1 mL fractions. Presence of doxorubicin was confirmed by measuring the absorbance for all the vesicular fractions at 490 nm. The filtration was continued until the complete removal of un-entrapped doxorubicin from the sephadex column. Vesicle containing eluent was collected until no detectable absorbance of doxorubicin was obtained. Finally, 0.25 M HCl was used to rupture the vesicles and the percentage of drug loading was estimated (~57%) following the standard protocol using a standard calibration curve.[8] Drug release studies were performed by recording the fluorescence spectra before and after the addition of 0.25 M HCl. Moreover, pH responsive doxorubicin release from the CBH-1 vesicles in phosphate buffer saline (PBS) at different pH (pH = 5.5, 6.0, 6.5, 7.0, 7.5, 8.0) was also monitored by fluorescence spectroscopy. Drug loaded **CBH-1** vesicular solution was also investigated before and after the treatment of 0.25 M HCl under a fluorescence microscope (Olympus BX-61) at 40 × magnification.

1.5. CHARACTERIZATION DATA

1.5.1. Characterization of CBH-1

^{1}H-NMR (500 MHz, $CDCl_3$, 25 °C, TMS): δ/ppm 8.22 (s, 1H, -N=C$\underline{H}$-C_6H_5), 7.61-7.79 (m, 2H, *o*-protons of 4-hydrazinobenzoic acid residue), 7.28-7.45 (m, 5H, -$C_6\underline{H}_5$), 7.09-7.15 (m, 2H, *m*-protons of 4-hydrazinobenzoic acid residue), 5.29-5.41 (m, 1H, vinylic proton of cholesteryl group), 4.39-4.48 (m, 1H, C$\underline{H}$-O-(CO) of cholesteryl proton), 4.29-4.31 (m, 1H, -N$\underline{H}$-N=C-), 3.36-3.68 (m, 12H, oxyethelene proton) 2.24-2.32 and 1.9-1.98 (m, 4H, allylic cholesteryl protons), 0.63-1.82 (m, 39H, cholesteryl protons). ESI-MS: *m*/*z*: 805.535 $[M+Na]^+$ (calculated); found: 805.731 $[M+Na]^+$, MALDI-TOF MS: *m*/*z*: found: 805.837 $[M+Na]^+$.

1.5.2. Characterization of CBH-2

^{1}H-NMR (500 MHz, $CDCl_3$, 25 °C, TMS):δ/ppm 8.00 (s, 1H, -N=C$\underline{H}$-C_6H_5), 7.64-7.74 (m, 2H, *o*-protons of 4-hydrazinobenzoic acid residue), 7.45-7.46 (m, 2H, *o*-protons of *p*-dimethylaminobenzaldehyde residue), 7.10-7.11 (m, 2H, *m*-protons of 4-hydrazinobenzoic acid residue), 6.68-6.71 (m, 2H, *m*-protons of *p*-dimethylaminobenzaldehyde residue), 5.15-5.32 (m, 1H, vinylic proton of cholesteryl group), 5.09-5.11 (m, 1H, -N$\underline{H}$-N=C-), 4.46 (m, 1H, C$\underline{H}$-O-(CO) of cholesteryl protons), 3.01-3.66 (m, 12H, oxyethelene proton), 2.87 and 2.94 (s, 6H, N-$(C\underline{H}_3)_2$), 2.23-2.3 and 1.9-1.98 (m, 4H, allylic cholesteryl protons), 0.63-1.81 (m, 39H, cholesteryl protons). ESI-MS: *m/z*: 848.577 $[M+Na]^+$ (calculated); found: 848.288 $[M+Na]^+$, MALDI-TOF MS: *m/z*: found: 848.967 $[M+Na]^+$.

1.5.3. Characterization of CBH-3

^{1}H-NMR (300 MHz, DMSO-d_6, 25 °C, TMS): δ/ppm 7.81-7.98 (m, 4H, *o*-protons of benzophenone residue), 7.58-7.59 (m, 2H, *o*-protons of 4-hydrazinobenzoic acid residue), 7.46-7.50 (m, 6H, *m*-protons and *p*-protons of benzophenone residue), 7.09-7.11 (m, 1H, -N$\underline{H}$-N=C-), 6.63-6.71 (m, 2H, *m*-protons of 4-hydrazinobenzoic acid residue), 5.21-5.31 (m, 1H, vinylic proton of cholesteryl group), 4.15-4.26 (m, 1H, C$\underline{H}$-O-(CO) of cholesteryl proton), 2.98-3.59 (m, 12H, oxyethelene proton), 1.90-1.97 and 2.05-2.07 (m, 4H, allylic cholesteryl protons), 0.61-1.62 (m, 39H, cholesteryl protons). MALDI-TOF MS: *m/z*: 860.189 $[M+H]^+$ (calculated); found: 860.017 $[M+H]^+$.

1.6. REFERENCES

[1] J. M. Lehn, *Angew. Chem. Int. Ed.* **2013**, *52*, 2836.

[2] P. Walde, A. Goto, P. A. Monnard, M. Wessicken, P. L. Luisi, *J. Am. Chem. Soc.* **1994**, *116*, 7541.

[3] P. Walde, K. Cosentino, H. Engel, P. Stano, *ChemBioChem.* **2010**, *11*, 848.

[4] S. Liu, Y. I. González, E. W. Kaler, *Langmuir* **2003**, *19*, 10732.

[5] H. T. Jung, B. Coldren, J. A. Zasadzinski, D. J. Iampietro, E. W. Kaler, *Proc. Natl. Acad. Sci. U. S. A.* **2001**, *98*, 1353.

[6] F. Cuomo, A. Ceglie, M. Piludu, M. G. Miguel, B. Lindman, F. Lopez, *Langmuir* **2014**, *30*, 7993.

[7] F. E. Antunes, E. F. Marques, R. Gomes, K. Thuresson, B. Lindman, M. G. Miguel, *Langmuir* **2004**, *20*, 4647.

[8] S. Dinda, M. Ghosh, P. K. Das, *Langmuir* **2016**, *32*, 6701.

[9] J. H. Mondal, T. Ghosh, S. Ahmed, D. Das, *Langmuir* **2014**, *30*, 11528.

[10] B. O. Okesola, D. K. Smith, *Chem. Soc. Rev.* **2016**, *45*, 4226.

[11] L. A. Estroff, A. D. Hamilton, *Chem. Rev.* **2004**, *104*, 1201.

[12] K. J. C. van Bommel, C. van der Pol, I. Muizebelt, A. Friggeri, A. Heeres, A. Meetsma, B. L. Feringa, J. van Esch, *Angew. Chem. Int. Ed.* **2004**, *43*, 1663.

[13] M. D. S. Maset, V. J. Nebot, J. F. Miravet, B. Escuder, *Chem. Soc. Rev.* **2013**, *42*, 7086.

[14] J. H. Mondal, S. Ahmed, T. Ghosh, D. Das, *Soft Matter* **2015**, *11*, 4912.

[15] M. Wiemann, R. Niebuhr, A. Juan, E. Cavatorta, B. J. Ravoo, P. Jonkheijm, *Chem. Eur. J.* **2018**, *24*, 813.

[16] M. N. Chaur, D. Collado, J. M. Lehn, *Chem. Eur. J.* **2011**, *17*, 248.

[17] D. Mandal, S. Dinda, P. Choudhury, P. K. Das, *Langmuir* **2016**, *32*, 9780.

[18] D. Mandal, P. Choudhury, D. Sarkar, P. K. Das, *Chem. Commun.* **2017**, *53*, 7844.

[19] C. Maity, W. E. Hendriksen, J. E. van Esch, R. Eelkema, *Angew. Chem. Int. Ed.* **2015**, *54*, 998.

[20] D. J. Cornwell, O. J. Daubney, D. K. Smith, *J. Am. Chem. Soc.* **2015**, *137*, 15486.

[21] H. Cao, J. Jiang, X. Zhu, P. Duan, M. Liu, *Soft Matter* **2011**, *7*, 4654.

[22] D. Schmaljohann, *Adv. Drug Deliv. Rev.* **2006**, *58*, 1655.

[23] M. Zelzer, S. J. Todd, A. R. Hirst, T. O. McDonald, R. V. Ulijn, *Biomater. Sci.* **2013**, *1*, 11.

[24] Y. Qiu, K. Park , *Adv. Drug Deliv. Rev.* **2001**, *53*, 321.

[25] C. H. Alarcön, S. Pennadam, S. Alexander, *Chem. Soc. Rev.* **2005**, *34*, 276.

[26] P. Xing, Y. Wang, M. Yang, Y. Zhang, B. Wang, A. Hao, *ACS Appl. Mater. Interfaces* **2016**, *8*, 17676.

[27] S. L. Zhou, S. Matsumoto, H. D. Tian, H. Yamane, A. Ojida, S. Kiyonaka, I. Hamachi, *Chem. Eur. J.* **2005**, *11*, 1130.

[28] P. D. Thornton, R. J. Mart, R. V. Ulijn, *Adv. Mater.* **2007**, *19*, 1252.

[29] X. Su, I. Aprahamian, *Chem. Soc. Rev.* **2014**, *43*, 1963.

[30] S. Kobayashi, Y. Mori, J. S. Fossey, M. M. Salter, *Chem. Rev.* **2011**, *111*, 2626.

[31] P. Vicini, M. Incerti, P. L. Colla, R. Loddo, *Eur. J. Med. Chem.* **2009**, *44*, 1801.

[32] J. Kalia, R. T. Raines, *Angew. Chem.* **2008**, *120*, 7633.

[33] F. J. U. Romo, C. J. Doonan, H. Furukawa, K. Oisaki, O. M. Yaghi, *J. Am. Chem. Soc.* **2011**, *133*, 11478.

[34] X. P. Zhou, Y. Wu, D. Li, *J. Am. Chem. Soc.* **2013**, *135*, 16062.

[35] Y. Jin, C. Yu, R. J. Denman, W. Zhang, *Chem. Soc. Rev.* **2013**, *42*, 6634.

[36] R. Raue, A. Brack, K. H. Lange, *Angew. Chem. Int. Ed. Engl.* **1991**, *30*, 1643.

[37] R. Lygaitis, V. Getautis, J. V. Grazulevicius, *Chem. Soc. Rev.* **2008**, *37*, 770.

[38] S. Follonier, C. Bosshard, U. Meier, G. Knöpfle, C. Serbutoviez, F. Pan, P. Günter, *J. Opt. Soc. Am. B* **1997**, *14*, 593.

[39] R. J. Johnson, J. Stieglitz, *J. Am. Chem. Soc.* **1934**, *56*, 1904.

[40] A. S. Trevani, G. Andonegui, M. Giordano, D. H. López, R. Gamberale, F. Minucci, J. R. Geffner, *J. Immunol.* **1999**, *162*, 4849.

[41] A. Shome, S. Debnath, P. K. Das, *Langmuir* **2008,** *24,* 4280.

[42] J. R. guez-Hernández, S. Lecommandoux, *J. Am. Chem. Soc.* **2005**, *127*, 2026.

[43] Y. Zimenkov, S. N. Dublin, R. Ni, R. S. Tu, V. Breedveld, R. P. Apkarian, V. P. Conticello, *J. Am. Chem. Soc.* **2006**, *128*, 6770.

[44] M. E. Labib, R. Williams, *J. Colloid Interface Sci.* **1984**, *97*, 356.

[45] C. J. Su, S. S. Wu, U. S. Jeng, M. T. Lee, A. C. Su, K. F. Liao, W. Y. Lin, Y. S. Huang, C. Y. Chen, *Biochim. Biophys. Acta* **2013**, *1828*, 528.

[46] M. R. Molla, S. Ghosh, *Chem. Eur. J.* **2012**, *18*, 1290.

[47] H. H. Monfareda, O. Pouralimardana, C. Janiak, *Z. Naturforsch* **2007**, *62b*, 717.

[48] Y. Chen, H. Han, H. Tong, T. Chen, H. Wang, J. Ji, Q. Jin, *ACS Appl. Mater. Interfaces* **2016**, *8*, 21185.

[49] Y. Chang, X. Meng, Y. Zhao, K. Li, B. Zhao, M. Zhu, Y. Li, X. Chen, J. Wang, *J. Colloid Interface Sci.* **2011**, *363*, 403.

[50] F. F. Tian, F. L. Jiang, X. L. Han, C. Xiang, Y. S. Ge, J. H. Li, Y. Zhang, R. Li, X. L. Ding, Y. Liu, *J. Phys. Chem. B* **2010**, *114*, 14842.

* * *

Chapter 2

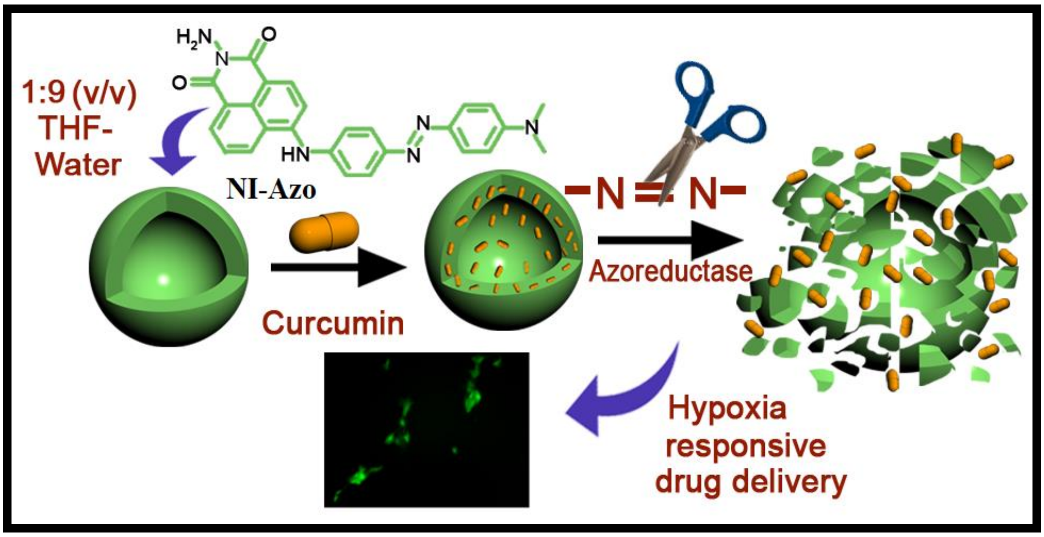

Naphthalimide-based azo-functionalized supramolecular vesicle as hypoxia-responsive drug delivery vehicle

2.1. INTRODUCTION

Supramolecular self-assembly, a ubiquitous natural phenomenon, has been revealing its enormous involvements across the scientific disciplines.[1-2] The autonomous organization of small amphiphiles by various simple interactions (hydrophobic, van der Waals, π-stacking, H-bonding, ionic, co-ordination) leads to the formation of diverse ordered manifestations of self-assembly (micelles, reverse micelles, vesicles, supramolecular gels and higher order self-aggregates) predominantly at nanoscale.[3-10] Vesicles, the spherical shaped self-assembled structures, with its interior aqueous core and hydrophobic surroundings, are capable of encapsulating a large number of hydrophobic and hydrophilic cargos.[11-12] Improved spatiotemporal control of therapeutics can be achieved through the development of self-assembled structures-based drug delivery vehicles that potentially can reduce random drug biodistribution. By tuning the functionalities of building blocks, vesicles can be judicially triggered by several endogenous environmental conditions (pH, redox, temperature, hypoxia, enzymes) or exogenous stimuli (ultrasound, light, mechanical force, magnetic field).[13-17] For example, Holme *et al.* reported the elevated shear stress induced release of drug from lenticular-shaped vesicles of 1,3-diaminophospholipid.[18] Kim *et al.* developed electrically switchable vesicles that reversibly break into smaller micelles under oxidative voltage.[19] Similarly, pH-responsive release of anti-cancer drug doxorubicin in acidic medium was reported from a hydrazone-based vesicle and a nitric oxide responsive supramolecular vesicle connected by tyrosol linkage was reported to released drug by cleavage of benzyl bond.[20,21]

In the context of tumor specific delivery, hypoxia responsive drug delivery systems (DDS) are finding notable significance in particular at early stage of cancer.[22-26] Hypoxia is defined as decreased oxygen tension or insufficient oxygen delivery to organs, tissues or cells due to reduced supply or augmented consumption of oxygen. Hypoxia inducible factor alpha (HIF-1α) is known to get stabilized in hypoxic microenvironment and regulates the function of various genes.[27,28] Apart from its characteristic impact in cardiopathy, ischemia and vascular diseases, hypoxia is also responsible for tumor progression by controlling several pathways including growth-factor signaling, cell proliferation, tissue invasion, and metastasis.[27-32] Hypoxic cells are less susceptible to conventional anti-proliferating drugs, radiation therapy.[30] Also, transportation of anticancer drug to hypoxic regions becomes challenging for solid tumors due to their distance from blood vessels. Hypoxia driven drug resistance can be generated due to upregulation of several genes (e.g. P-glycoprotein).[33] To overcome this issue, hypoxia-sensitive prodrug, HIF-1α targeting treatment has emerged along with development of hypoxia-responsive carrier for tumor specific delivery.[22-26,34,35] To this end, azoreductase (biomarker for hypoxic microenvironment) may be used in reduction and/or cleaving of azo bond (-N=N-) for hypoxia-responsive release of drug from DDS.[23,36-39] However, in contrast to the different stimuli responsive tumor targeting approaches, hypoxia responsive nanocarriers including supramolecular vesicles are rarely explored.

Herein, we report the development of hypoxia responsive azo (-N=N-) containing naphthalimide amphiphile (**NI-Azo**) that formed vesicles of ~250 nm in 1:9 (v/v) tetrahydrofuran (THF)-water through *H*-aggregation. The supramolecular vesicle formation was characterized by both spectroscopic and microscopic techniques. Cleavage of azo (-N=N) bond was demonstrated by treating **NI-Azo** vesicles with azoreductase extracted from *E. coli* bacteria and sodium dithionite ($Na_2S_2O_4$, a mimic of azoreductase), by UV-vis spectroscopy. $Na_2S_2O_4$ induced breaking of azo bond of **NI-Azo** was analyzed by functional group test and mass spectroscopy of the aromatic amine fragments. The anti-cancer drug, curcumin loaded **NI-Azo** vesicles successfully killed cancer cells (B16F10) in $CoCl_2$ induced hypoxic environment with 2.4-fold higher efficiency than that of native curcumin. Notably, cancer cell killing efficiency of curcumin loaded **NI-Azo** vesicles was 4.5-fold and 1.9-fold higher compared to that of NIH3T3 cells in normoxic and hypoxic environment, respectively.

2.2. RESULTS AND DISCUSSION

2.2.1. Molecular designing of NI-Azo

With the aim to develop a hypoxia responsive self-aggregating building block, naphthalimide appended azo (-N=N-) group containing amphiphilic molecule was synthesized (**NI-Azo**, Figure 1). The azo group was incorporated as the stimuli responsive motif due to its intrinsic tendency to get reduced in hypoxic environment by azoreductase.[23,36-39] Naphthalimide core was chosen so that it can facilitate the self-aggregation of the amphiphilic molecule through π-π interactions between the hydrophobic aromatic rings.[41] Synthesized **NI-Azo** was characterized by ^{1}H-NMR and MALDI-TOF spectra.

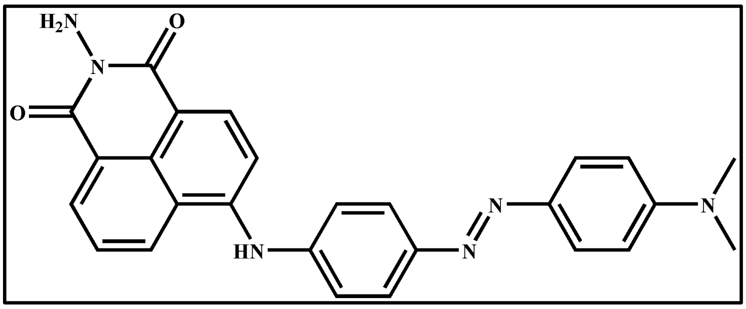

Figure 1. Structure of **NI-Azo** molecule.

2.2.2. Investigation of microscopic structure and size distribution of the self-assembly of NI-Azo

The solubility and the self-assembling behavior of the **NI-Azo** was investigated in tetrahydrofuran (THF) and THF-water binary solvent system. NI-Azo was completely soluble in THF and the transparent THF solution of **NI-Azo** turned translucent with gradual addition of water indicating the possible self-assembly by **NI-Azo**. Stable translucent solution formation of **NI-Azo** took place at 1:9 (v/v) of THF-water composition (Figure 2a). Similarly, **NI-Azo** was found to be soluble in dimethyl sulfoxide (DMSO) and this transparent solution slowly turned to translucent with the increase in water content up to 75 vol% (Figure 2b). Translucent solution of **NI-Azo** in 1:3 (v/v), DMSO-water indicated the formation of self-assembled structures. However, further increase in water concentration led to the destabilization of the aggregated solution leading to the precipitation of amphiphilic compound. Considering the potential biomedicinal applications of **NI-Azo** self-assemblies, most of the studies were carried out using the self-aggregates formed at higher water content (90 vol%) in 1:9 (v/v), THF-water.

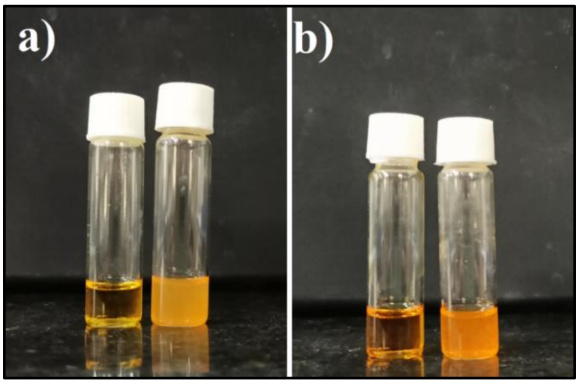

Figure 2. (a) Photographs of vials containing **NI-Azo** (0.25 mg/mL) in THF (left vial) and 1:9 (v/v), THF-water (right vial). (b) Photographs of vials containing **NI-Azo** (0.25 mg/mL) in DMSO (left vial) and in 1:3 (v/v), DMSO-water.

Critical aggregation concentration (CAC) of **NI-Azo** was measured by plotting the ratio of I_{383} and I_{372} (I_3/I_1) (discussed in experimental section) against the logarithm of the concentration (mg/mL) of all the samples containing **NI-Azo** vesicle solutions in 1:9 v/v, THF-water of by varying concentration from 0.5 μg/mL to 7.5 μg/mL and 1 μM pyrene as the polarity probe. Initially, the ratio of I_{383} and I_{372} (I_3/I_1) increased slowly with increasing concentration of **NI-Azo** vesicles and then it showed a sudden jump. CAC was calculated from the interception point of two straight lines in the plot and was found to be 4.15 μg/mL (9.21 μM) (Figure 3a,b). CAC was 4.03 μg/mL (8.94 μM) and 4.29 μg/mL (9.51 μM) at pH = 4.0 and 9.0 (Figure 3c,d,e,f).

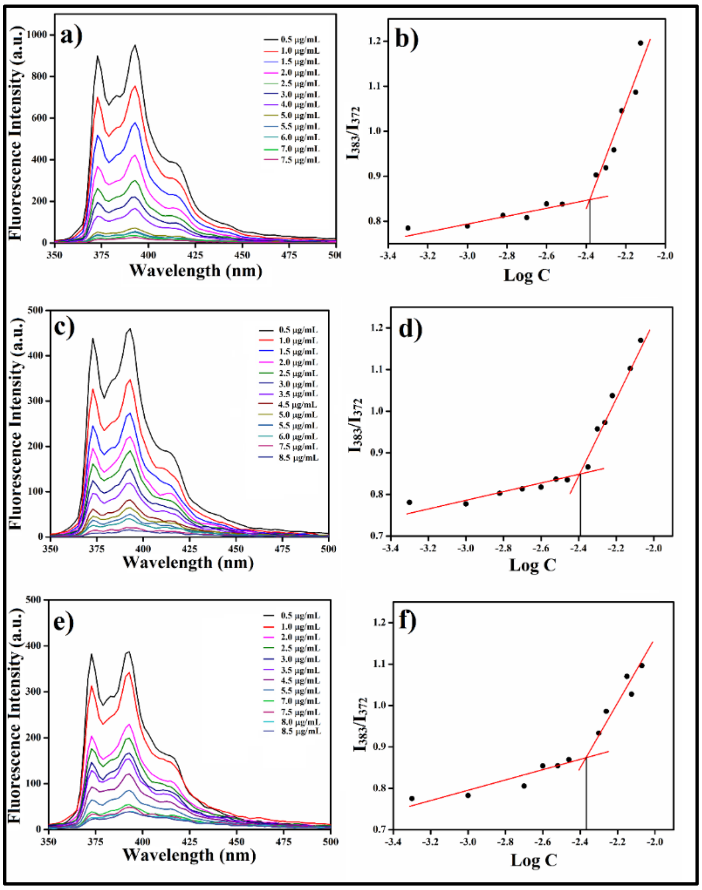

Figure 3. Fluorescence intensity of pyrene (1 μM) in varying **NI-Azo** concentration in (a) experimental solution (Milli-Q water), (c) pH = 4.0, (e) pH = 9.0. CAC calculation at (b) experimental solution (Milli-Q water), (d) pH = 4.0, (f) pH = 9.0.

The morphology of the self-assembled structures formed by **NI-Azo** was examined by different microscopic techniques. TEM image of **NI-Azo** (25 μM, f_w = 90 vol% in THF) confirmed the formation of vesicular self-assembly having a diameter of 200-250 nm (Figure 4a). Corresponding FESEM image also showed supramolecular spherical aggregates with dimension of ~250 nm (Figure 4b). Likewise, spherical morphology having diameter of 200-250 nm was found in the respective AFM image of **NI-Azo** (25 μM, f_w = 90 vol% in THF) (Figure 4c). Large population of spherical objects with dimension of 200-250 nm were observed in cryo-TEM images of **NI-Azo** (25 μM, f_w = 90 vol% in THF), which are in concurrence with the other microscopic investigations (Figure 4d).

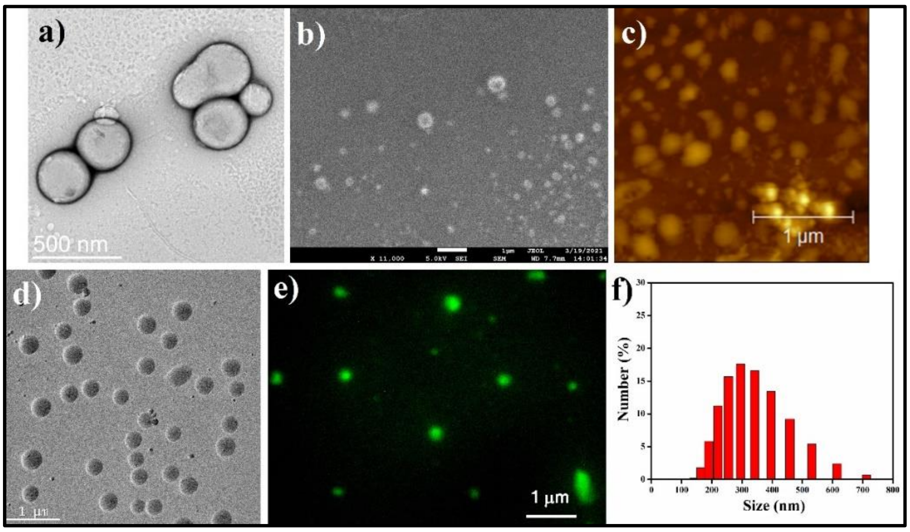

Figure 4. (a) Negatively stained TEM image, (b) FESEM image, (c) AFM image, (d) cryo-TEM image, (e) fluorescence microscopic image, (f) size distribution DLS plot of **NI-Azo** in (1:9, v/v) THF-water binary solvent mixture ([**NI-Azo**] = 25 µM)

Supramolecular vesicle formation was further substantiated by fluorescent microscopic studies. Calcein (fluorophore) was encapsulated within the self-assembly of **NI-Azo** in 1:9 (v/v), THF-water (details are given in the experimental section). Green emitting spherical moieties were observed under the microscope that corroborates the formation of the vesicles (Figure 4e). Moreover, in accordance to the number averaged size distribution by DLS experiment, mean hydrodynamic diameter (D_h) of **NI-Azo** (25 µM, f_w = 90 vol% in THF) was in the range of 200-400 nm with an average diameter of ~300 nm (Figure 4f). Corresponding correlogram of the DLS was provided in Figure 5. All the observed data obtained by different methods are mostly in concurrence with respect to the size and morphology of the self-aggregated vesicles.

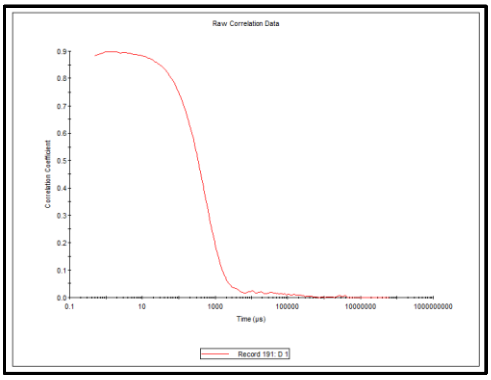

Figure 5. Correlogram of the DLS of **NI-Azo** in (1:9, v/v) THF-water binary solvent mixture ([**NI-Azo**] = 25 µM)

2.2.3. Spectroscopic investigation for self-aggregation of NI-Azo

After ensuring the formation of vesicular aggregates by **NI-Azo**, nature of self-aggregation in THF-water binary solvent was investigated by different spectroscopic technique. Solvent dependent UV-vis spectroscopic studies revealed the aggregation pattern of self-assembly formed by **NI-Azo** amphiphile. The THF solution of **NI-Azo** (15 μM) showed sharp absorbance at 400-490 nm with maxima (λ_{max}) at 429 nm and a shoulder peak at 469 nm corresponding to n-π^* transition in azobenzene moiety and a characteristic UV band in the range 360-380 nm having a peak at 373 nm, which may be ascribed to the π–π^* transition of naphthalimide chromophore (Figure 6a).[42-44] The absorbance intensity got decreased and the peaks got broadened with increasing water content in THF from 3:1 (v/v) to 1:9 (v/v) of THF-water. The absorbance maxima got blue shifted with gradual addition of water from 429 to 419 nm in 1:3 (v/v), THF-water. Finally, an extensively broad with much lower absorbance intensity peak was observed at 413 nm in 1:9 (v/v), THF-water with a blue shift of 16 nm (Figure 6a). The hypsochromic shift was also observed for the peak at 469 nm, which got blue shifted to 458 nm in 1:9 (v/v), THF-water (Figure 6a). Such hypsochromic shift with increasing water content denoted the possible *H*-aggregation through face-to-face stacking of π moieties during the self-assembly of **NI-Azo**. We also carried out pH dependent UV-vis spectroscopic investigation of **NI-Azo** (15 μM) in 1:9 (v/v), THF-water binary solvent system with varying pH of the aqueous domain from 4.0 to 9.0 using phosphate buffer (10 mM) (Figure 7). In all the cases, the spectra resembled each other and showed absorbance maxima at 458-459 nm which was in concurrence to the preceding solvent dependent UV-vis studies that indicated the self-assembly (Figure 6).

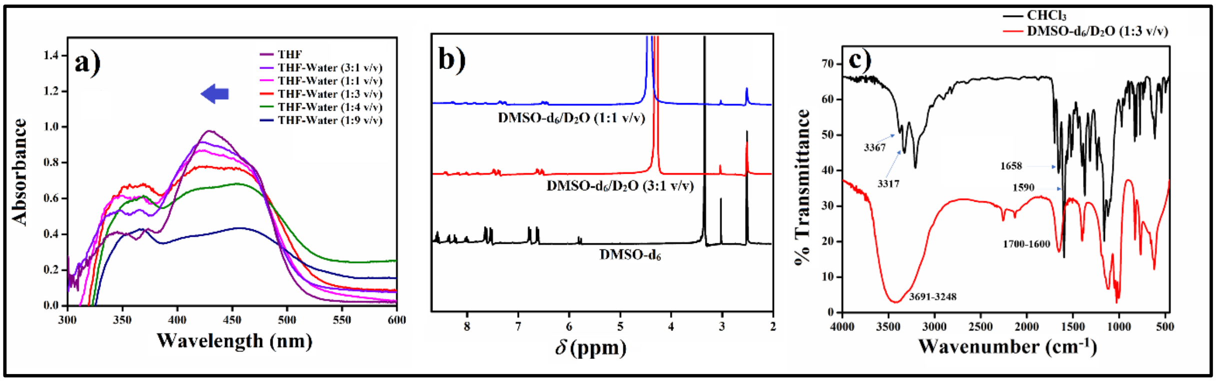

Figure 6. (a) UV-visible spectra of **NI-Azo** (10 μM) in varying THF-water solvent mixtures, (b) solvent dependent ^{1}H-NMR spectra of **NI-Azo** (1 mM), (c) solvent dependent FTIR spectra of **NI-Azo**.

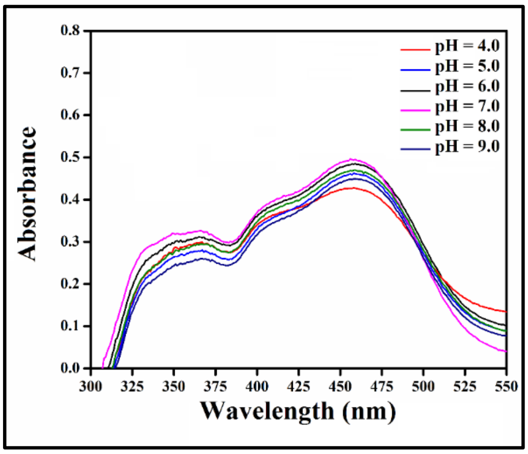

Figure 7. UV-vis spectra of **NI-Azo** (15 μM) in 1:9 (v/v), THF-water solvent system varying the pH of the aqueous domain using phosphate buffer (10 mM).

CAC was calculated to be 4.15 μg/mL (9.21 μM), 4.03 μg/mL (8.94 μM) and 4.29 μg/mL (9.51 μM) in the experimental solution and at pH = 4.0 and pH = 9.0, respectively (Figure 3b,c,d.e). Similar CAC values indicated that change in pH has little effect on self-assembly. Also, considering the physiological pH value around 7.4, it is required to develop a delivery vehicle that is stable in this pH range. The pH of the vesicular solution was found to be 7.5. Also, the zeta potential of **NI-Azo** (25 μM) in 1:9 (v/v), THF-water was found to be 1.55 mV, which is generally considered to be in the range of neutral charge. Similarly, the DMSO solution of **NI-Azo** (10 μM) showed sharp absorbance with maxima (λ_{max}) at 467 nm and a shoulder peak at 430 nm (Figure 8). Here too, the absorbance intensity got decreased with increase in water concentration. With gradual enhancement in water content, the λ_{max} got blue shifted by 7 nm from 467 nm to 460 nm at 1:3 v/v, DMSO-water (Figure 8). This hypsochromic shift with increasing water content further confirmed the participation of predominant *H*-type self-aggregation of **NI-Azo** through face-to-face π stacking.

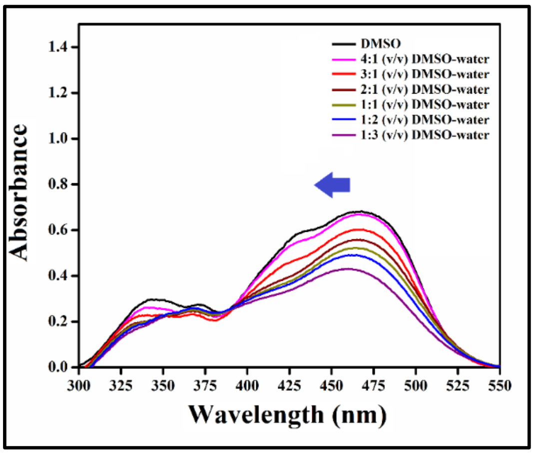

Figure 8. UV-visible spectra of **NI-Azo** (10 μM) in varying DMSO-water solvent mixtures.

We further investigated the participation of different non-covalent interactions during self-assembly of **NI-Azo** by solvent-dependent ^{1}H-NMR and FTIR spectral studies (Figure 6b,c). In case of ^{1}H-NMR, the aromatic proton peaks of **NI-Azo** in DMSO-d_6 (molecular state) was observed in the region δ= 7.49-7.56, 7.97-8.05, 8.33-8.39, 8.53-8.63 ppm (for aromatic core of naphthalimide) and δ= 6.58-6.64, 6.74-6.82, 7.61-7.68, 8.20-8.26 ppm (for benzene rings) (Figure 6b). Upon gradual increase in the D_2O content from 0% to 50%, the aromatic protons peaks got broadened and upfield shifted to δ= 7.23-7.28, 7.58-7.67, 8.00-8.06, 8.23-8.33, ppm and δ = 6.4-6.46, 6.48-6.57, 7.31-7.38, 7.83-7.89 ppm for naphthalimide core and benzene rings, respectively (Figure 6b). Thus, the increment in the D_2O content enabled the π–π stacking between the aromatic core as well as with the benzene rings of the amphiphile demonstrating the self-assembly of **NI-Azo**. Also, in the solvent dependent ^{1}H NMR spectra, methyl groups of the molecule showed peaks at δ= 2.9 ppm for all three solvent compositions (Figure 6b). No shift in methyl group protons with variation in the polarity solvent systems further confirmed that the shift in aromatic region was primarily due to the self-aggregation of **NI-Azo** and not due to polarity change of solvent compositions.

The FTIR spectrum of **NI-Azo** in $CHCl_3$ (molecular state) showed transmittance peaks at $\nu_{N\text{-}H}$ = 3367, 3317 cm^{-1}, $\nu_{C=O}$ = 1658 and $\delta_{N\text{-}H}$ = 1590 cm^{-1} (Figure 6c). The respective peaks got shifted to 3248-3691 cm^{-1} (broad band), 1600-1700 cm^{-1} (broad band) upon increasing the D_2O content in 1:3 (v/v), DMSO-d_6-D_2O solvent mixture (Figure 6c). These shifts in stretching and bending frequencies with introduction of D_2O validated the participation of intermolecular hydrogen bonding between the amine (N-H) and carbonyl (C=O) (i.e., N-H----O=C) during the self-assembly of **NI-Azo** amphiphile that led to the development of self-aggregated supramolecular vesicle.

The X-ray diffraction (XRD) spectrum of **NI-Azo** (25 μM) in self-assembled state 1:9 (v/v), THF-water binary solvent system showed the peak at $2\theta \sim 23.14°$ (Figure 9), that represents distinct and compact π-π stacking interaction between the aromatic rings of amphiphiles.[8] This interaction eventually led to the formation of vesicular aggregates. This obtained data is in concurrence with solvent dependent UV-vis and ^{1}H NMR studies.

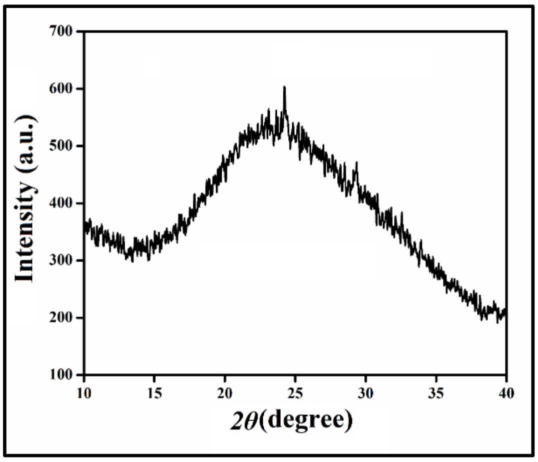

Figure 9. XRD plot of **NI-Azo** (25 μM) in 1:9 (v/v), THF-water solvent.

2.2.4. Hypoxia-responsive cleavage of azo bond (-N=N-): obliteration of self-aggregates

Azo moiety is known to get reduced by consecutive reactions and eventually cleaved to amine derivatives in presence of azoreductase enzyme.[23,36-39] Azoreductase is known to be highly expressed in hypoxic environment.[45,46] Based on this, several hypoxia responsive sensing and imaging probes have emerged and drug delivery vehicles as well as bio-reductive pro-drugs have been developed.[24,25,36,45-47] Herein, we aim to explore the hypoxia-responsive nature of **NI-Azo** vesicles owing to the presence of azo bond (-N=N-) in its molecular backbone and subsequently in selective killing of cancer cells by the uploaded drug within the vesicles. *Escherichia coli* (*E. coli*) is a predominant anaerobic bacterium with established azoreductase activities.[48] To investigate the responsiveness of -N=N- bond of **NI-Azo** amphiphile, we performed UV-vis spectroscopic study of **NI-Azo** vesicles (10 μM) in 1:9 (v/v), THF-water upon treating with extracellular and intracellular azoreductase extracted from *E. coli* bacteria (details is given in the experimental section). **NI-Azo** (10 μM) vesicles in 1:9

(v/v), THF-water showed characteristic absorbance maxima at 458 nm for azo moiety (Figure 6a, 10a). The absorbance intensity of this characteristic azo (-N=N-) peak at 458 nm got significantly decreased in presence of both extracellular and intracellular bacterial azoreductase. This plummeted absorbance intensity delineates the possible cleavage of the azo bond (Figure 10a).

To mimic the function of azoreductase enzyme in vitro, sodium dithionite ($Na_2S_2O_4$) was employed as an alternative reductant for azo group in **NI-Azo**.[49,50] UV-vis spectra of **NI-Azo** (10 μM) vesicles in 1:9 (v/v), THF-water were recorded upon gradual addition of $Na_2S_2O_4$ with varying the concentration from 0 to 1.0 mM. Here too the intensity of the characteristic absorbance peak of azo moiety at 458 nm was found to be steadily decreased with increasing $Na_2S_2O_4$ concentration for **NI-Azo** (10 μM) vesicles in 1:9 (v/v), THF-water (Figure 10b). Notably, the absorbance intensity of the peaks at 350-370 nm steadily increased with increasing $Na_2S_2O_4$ concentration. At 1 mM concentration of $Na_2S_2O_4$, the typical peak of azo at 458 nm was insignificant indicating almost complete cleavage of the azo bond (-N=N-) in reducing environment by $Na_2S_2O_4$ (Figure 10b).

Disintegration of **NI-Azo** vesicles was further confirmed by the cleavage of azo bond (-N=N-) analyzed by mass spectrometry. Treatment with $Na_2S_2O_4$ leads to the reduction of **NI-Azo** through cleavage of azo bond and by yielding of two different aniline derivative (aromatic amine) fragments from azo benzene compound. In case of **NI-Azo** amphiphile, these fragments are **A** and **B** having molar mass of 318.33 (M_1) and 136.19 (M_2), respectively (Figure 10c). $Na_2S_2O_4$ treated **NI-Azo** reaction mixture (details is given in experimental section) was freeze dried and followed by MALDI-TOF spectra were taken to analyze the fragments. As to our expectation, mass peaks were observed at 318.746 and 137.273 corresponding to ($[M_1]^+$) and ($[M_2 + H]^+$), respectively delineating the cleavage of the azo bond (-N=N-) of **NI-Azo**.

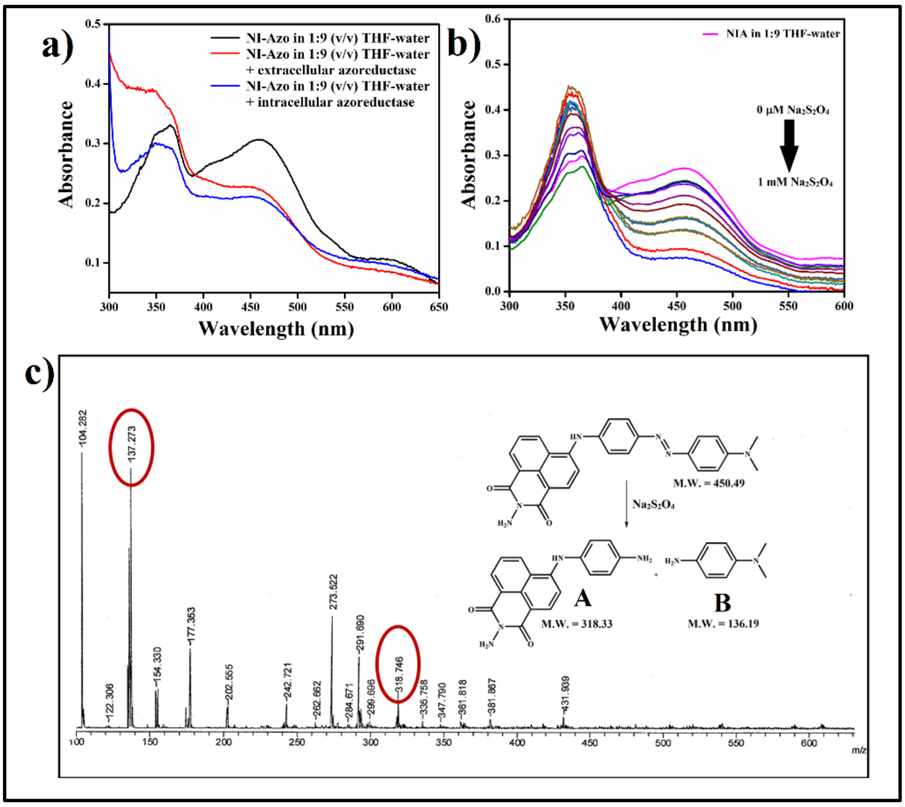

Figure 10. UV-visible spectra of **NI-Azo** (10 μM) in 1:9 (v/v) THF-water solvent mixtures in absence and presence of (a) extracellular and intracellular azoreductase, (b) varying concentration of $Na_2S_2O_4$. (c) MALDI-TOF spectra of fragments after azo bond (-N=N-) bond cleavage of **NI-Azo** by $Na_2S_2O_4$.

This cleavage of -N=N- could led to disintegration of self-assembly. In this regard, the photographs of **NI-Azo** (0.25 mg/mL) vesicles in 1:9 (v/v), THF-water inside a glass vial were captured in absence and presence of $Na_2S_2O_4$ (100 mM). Notably, the vesicular solution completely lost its translucency and it got transformed to a transparent solution along with slight change in colour (Figure 11a). This macroscopic observation affirmed the possible disintegration of the self-aggregated supramolecular vesicles from by **NI-Azo**. Next, the functional group of the produced primary aromatic amine (two aniline derivatives were formed after azo bond breakage, Figure 10c) was analyzed by azo dye test. 100 μL of $Na_2S_2O_4$ stock solution (1 M) was added to the vesicular solution of **NI-Azo** (1.0 mg/mL) in 1:9 v/v, THF-water and it was stirred for 8 h keeping the 100 mM final concentration of $Na_2S_2O_4$. Solid mass obtained upon lyophilization was dissolved in dilute HCl and taken in a test tube. Aqueous solution of $NaNO_2$ and alkaline (NaOH) solution of *β*-naphthol were taken separate test tubes. All the solutions in test tubes were cooled in ice bath for 10 min. Initially cold solution of lyophilized mass (aniline derivates) was mixed with aqueous $NaNO_2$ solution. Subsequently, alkaline (NaOH) solution of *β*-naphthol was added in that mixed solution. Orange precipitation was observed due to azo dye formation (Figure 11b) that further confirmed the formation of aromatic primary amines due to the cleavage of azo bond (-N=N-) in **NI-Azo** (Figure 11c).

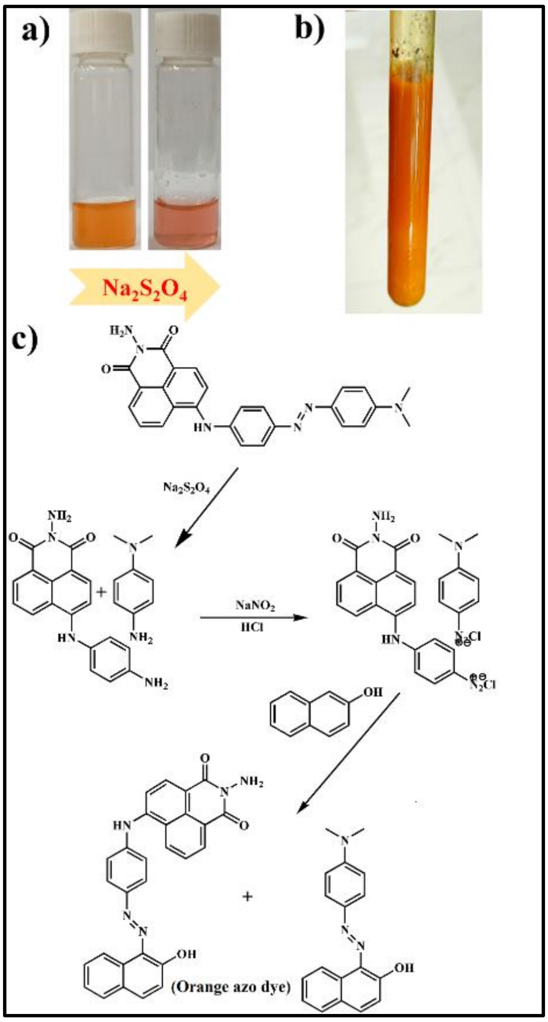

Figure 11. (a) Photographs of vials containing **NI-Azo** (0.25mg/mL) vesicles formed in 1:9 (v/v), THF-water in absence and presence of $Na_2S_2O_4$ (100 μM). (b) Azo-dye test for aromatic primary amine. (c) Synthetic scheme of azo dye test.

Cleavage of the azo bond would obviously lead to the disintegration of the supramolecular vesicular structure. To confirm further, TEM image of $Na_2S_2O_4$ (1 mM) treated **NI-Azo** vesicles (25 μM) in 1:9 (v/v), THF-water was captured (Figure 12).

Absence of any spherical aggregates denoted the disassembly of the supramolecular vesicle in reducing environment created by $Na_2S_2O_4$ through the cleavage of the azo bond. As mentioned earlier, $Na_2S_2O_4$ imitate the function of azoreductase enzyme which gets upregulated in hypoxic condition. So, supramolecular vesicles formed by **NI-Azo** would also exhibit hypoxia-responsive disintegration.

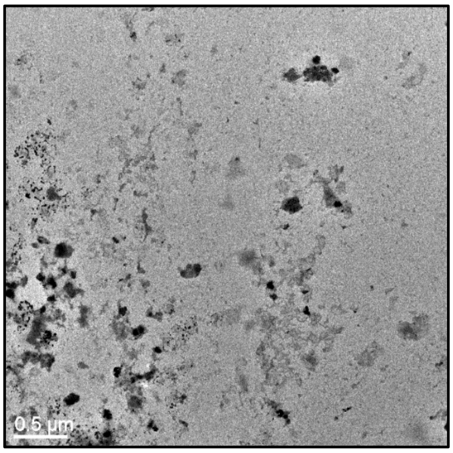

Figure 12. Negatively stained TEM image of **NI-Azo** in (1:9, v/v) THF-water binary solvent mixture ([**NI-Azo**] = 25 µM) treated with 1.0 mM $Na_2S_2O_4$.

2.2.5. Curcumin loading and release studies

After ensuring successful formation and hypoxia-responsive disintegration of **NI-Azo** vesicles, we aim to entrap anticancer drug curcumin inside the supramolecular vesicles and subsequently hypoxia-induced release of the drug. The anticancer activity of curcumin is limited primarily owing to its poor water solubility, low cellular uptake, less bio availability and chemical instability. Thus, curcumin loading within a stimuli-responsive nanocarrier would be obviously a better alternative with the expectation of higher therapeutic efficacy. The detailed process of curcumin loading and separation from free drug using sephadex G-50 column (size exclusion chromatography) was discussed in the experimental section. Successful encapsulation of curcumin in **NI-Azo** vesicle was monitored by UV-vis, fluorescence spectroscopy and also by fluorescence microscopy. In accordance to the UV-vis spectra, native curcumin had an absorbance maximum at 420 nm while curcumin encapsulated **NI-Azo** vesicles showed absorbance maxima at 445 nm with reduced absorbance intensity (Figure 13). Similarly, a significant decrease in the emission intensity of curcumin was noted upon loading in **NI-Azo** vesicle in comparison to its native fluorescence (Figure 13b). Moreover, bright green (characteristic emission of curcumin) spherical shaped objects of the drug loaded **NI-Azo** vesicles under fluorescence microscope validated the entrapment of curcumin with in **NI-Azo** vesicle (Figure 13c,d). The drug loading efficiency of **NI-Azo** vesicles was found to be 49% (calculated after rupturing the curcumin loaded vesicle with $Na_2S_2O_4$ treatment and subsequently comparing the absorbance intensity of the released curcumin with native curcumin from the standard calibration curve). The release of encapsulated curcumin from **NI-Azo** vesicles was also investigated by UV-vis and fluorescence spectroscopy. Treatment of **NI-Azo** vesicles with $Na_2S_2O_4$ led to the shifting of absorbance maxima of curcumin from 445 nm to 426 nm (corresponding to free curcumin) with enhanced optical density compared to that of curcumin encapsulated **NI-Azo** vesicles (Figure 13a). These findings suggest that the release of curcumin in presence of $Na_2S_2O_4$ in drug loaded **NI-Azo** vesicles imitating the azoreductase enzyme activity. Similarly, the emission intensity of released curcumin was found to be recovered after treating the drug entrapped **NI-Azo** vesicles with 1 mM $Na_2S_2O_4$ (Figure 13b). The regained emission of released curcumin was almost comparable to that of the free curcumin. Therefore, it is evident that curcumin loaded **NI-Azo** vesicles got disintegrated in presence of 1 mM $Na_2S_2O_4$ (mimicking azoreductase activity) due to cleavage of azo (-N=N-) bond resulting in the release of entrapped curcumin.

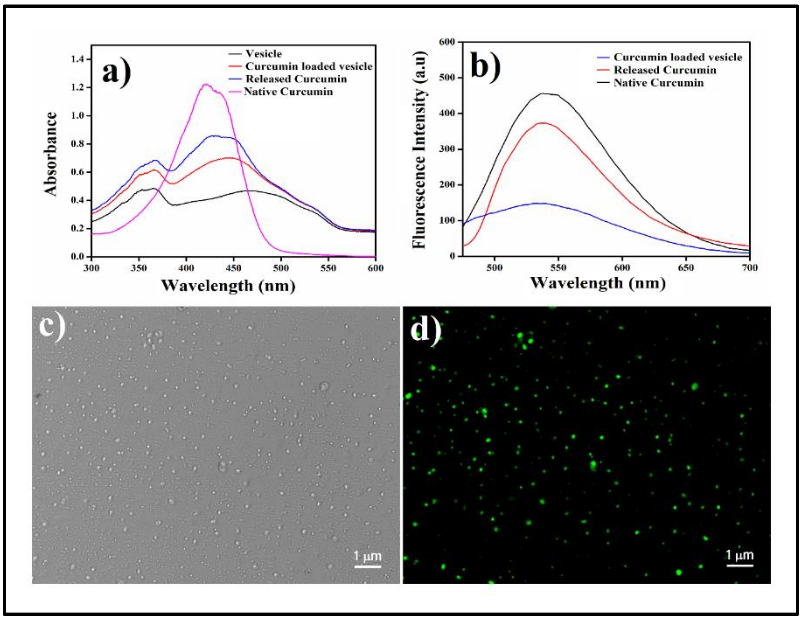

Figure 13. (a) Absorbance spectra of **NI-Azo** vesicles, free curcumin, curcumin entrapped within **NI-Azo** vesicles and after treating with 1 M $Na_2S_2O_4$, (b) emission spectra of curcumin entrapped within **NI-Azo** vesicles, after treating with 1 M $Na_2S_2O_4$ and free curcumin. (c) bright field and (d) fluorescence microscopic image (λ_{ex} = 420 nm) of curcumin encapsulated **NI-Azo** vesicles.

Corresponding fluorescence microscopic image of $Na_2S_2O_4$ treated curcumin loaded **NI-Azo** vesicles also confirmed the disassembly of supramolecular vesicles through irregular shaped discrete presence of green emitting curcumin instead of green sphere-shaped structures (Figure 14).

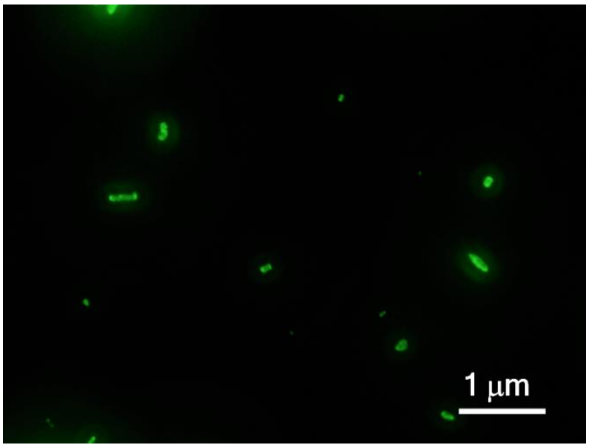

Figure 14. Fluorescence microscopic image (λ_{ex} = 420 nm) of curcumin encapsulated **NI-Azo** vesicles treated with 1 mM $Na_2S_2O_4$.

Extinction coefficient of curcumin in vesicles is somewhat lesser than the extinction coefficient of curcumin in other organic solvents like THF. The molar extinction coefficient of Curcumin is calculated to be 60098 $mol^{-1}dm^3cm^{-1}$ using equation A = €cl where "c" denotes the concentration in mol/dm^3 and "l" represents the path length in cm (Figure 13a). Here, "c" is 7.5 mg/mL and "l" is 1 cm. According to the spectra of released curcumin, the concentration of curcumin is estimated to be 4.96 μg/mL (using the standard calibration curve of curcumin). It implies that the curcumin concentration loaded inside the vesicle is also 4.96 μg/mL. Therefore, from the absorbance value of loaded curcumin, the molar extinction coefficient of loaded curcumin is calculated to be 51,492 $mol^{-1}dm^3cm^{-1}$.

2.2.6. Cytocompatibility of NI-Azo vesicles

Before exploring the **NI-Azo** vesicles in hypoxia-responsive drug delivery, it is crucial to determine its cytocompatibility against mammalian cells. The cytocompatibility of **NI-Azo** vesicles (10-50 μg/mL) in 1:9 (v/v), THF-water was tested by MTT assay in non-cancerous (NIH3T3) and cancerous (B16F10) cells. For NIH3T3, ~85-95% and for B16F10 ~86-94% cells were found to be alive after 24 h incubation with **NI-Azo** vesicles (Figure 15). Hence, these **NI-Azo** vesicles were sufficiently biocompatible and appropriate to be used as a cargo transporter inside mammalian cells.

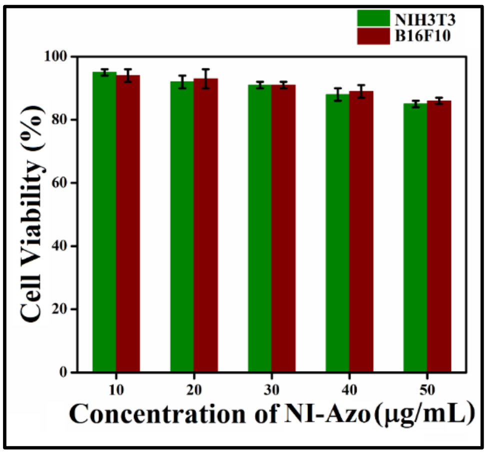

Figure 15. MTT-based % cell viability of NIH3T3 (non-cancer cells) and B16F10 (cancer cells) in presence of varying concentration of **NI-Azo** vesicles formed in 1:9 (v/v), THF-water over the incubation period of 24 h. Percent errors are within ± 5% in triplicate experiments.

2.2.7. Bioimaging

To use **NI-Azo** vesicles as a cellular transporter, it is essential to ensure successful drug internalization as well as releasing of drug through the disintegration of the delivery vehicle. **NI-Azo** vesicles get disassembled through the cleavage of azo bond in presence of azoreductase enzyme which is overly expressed in hypoxic environment. In this regard, we made attempt to induce hypoxia within cancer cells by introducing cobalt chloride $CoCl_2$.[51,52] Hypoxia is generally induced by decreasing atmospheric oxygen concentrations or by utilization of mimetic chemical agents such as cobalt chloride ($CoCl_2$) and desferrioxamine (DFO). Chemical agents are more useful in experimental environments as they maintain steady oxygen tension and artificially induce hypoxia through blocking the degradation of HIF-1α. Cobalt chloride has been reported to occupy the Fe^{2+} binding site and block the degradation of HIF-1α.[52] It is demonstrated that the effects of hypoxia-mimetic agents are comparable to those resulting from reduced atmospheric oxygen levels. Herein, we used $CoCl_2$ as hypoxia imitating agent. Cancerous (B16F10) cells were incubated (6 h) with curcumin loaded **NI-Azo** vesicles (50 μM) under $CoCl_2$ (200 μM) induced hypoxic condition. Bright green fluorescence of curcumin inside the cancer cells validated its internalization as well release from the **NI-Azo** vesicles possibly through disintegration of vesicle (Figure 16a,b). The corresponding flow cytometry data showed significant mean fluorescence intensity (9172) that substantiated the internalization curcumin loaded **NI-Azo** vesicles and its release inside the cancer cells (Figure 16c). In contrast, under normoxic condition (in absence of $CoCl_2$) keeping all other experimental conditions identical, comparatively less intensified green emitting B16F10 cells were observed having distinctly lower mean fluorescence intensity (4732) in flow cytometry (Figure 17). Under normoxic condition, **NI-Azo** vesicles could not get disrupted adequately possibly due to downregulated azoreductase in comparison to that in hypoxic condition. Hence, less amount of curcumin got released from the supramolecular **NI-Azo** vesicle inside the mammalian cells.

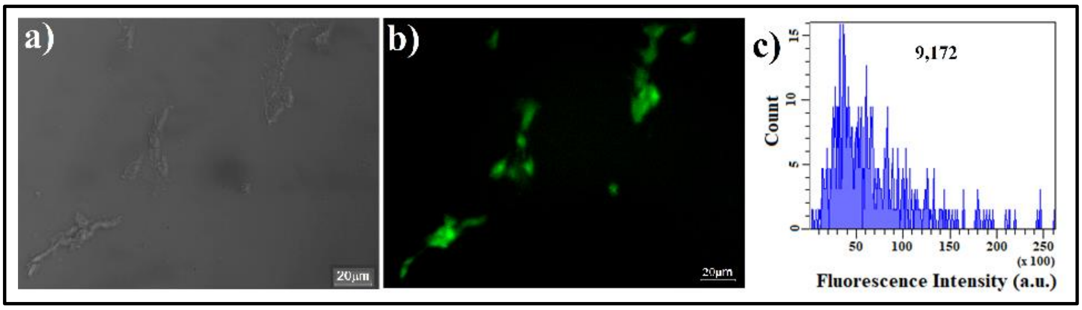

Figure 16. (a) Bright-field, (b) fluorescence microscopic image and (c) corresponding flow cytometric plots of hypoxic B16F10 cells incubated with curcumin within **NI-Azo** vesicles for 6 h in $CoCl_2$ (200 µM) induced hypoxic condition. The mean fluorescence value is given in the inset.

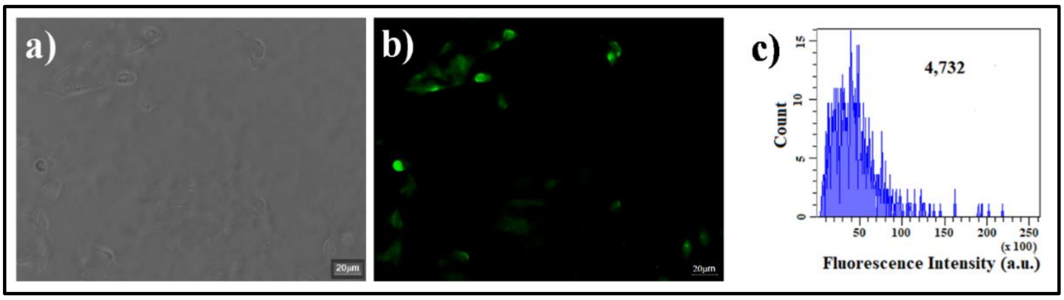

Figure 17. (a) Bright-field, (b) fluorescence microscopic image and (c) corresponding flow cytometric plots of B16F10 cells incubated with loaded curcumin for 6 hours in normoxic condition (without $CoCl_2$). The mean fluorescence value is given in the insets.

Similar fluorescence microscopic images were captured for B16F10 cells under both hypoxic (in presence of $CoCl_2$) and normoxic (in absence of $CoCl_2$) conditions using only native curcumin (in absence of **NI-Azo** vesicles) (Figure 18a-b,d-e). Here too poorly intense green emitting cells were observed with a low mean fluorescence intensity of 3133 (hypoxic) and 3431 (normoxic) possibly due to less internalization of free curcumin (Figure 18c,f). Hence, under hypoxic condition, **NI-Azo** vesicles could selectively improve the concentration of the anticancer drug curcumin inside cancer cells, which may have influence on its therapeutic efficiency.

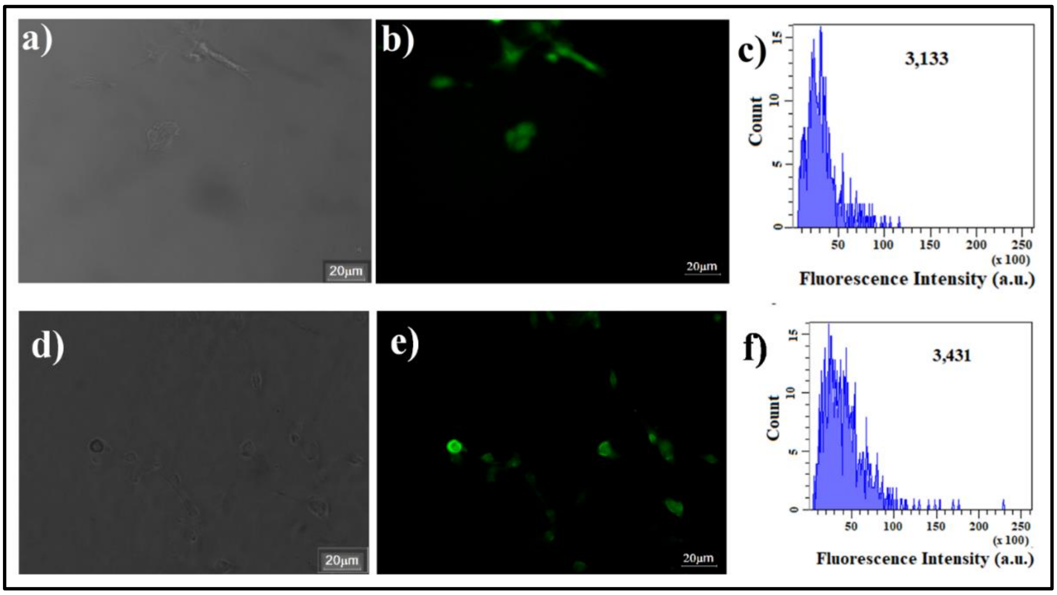

Figure 18. (a) Bright-field, (b) fluorescence microscopic image and (c) corresponding flow cytometric plots of B16F10 cells incubated with native curcumin for 6 h in $CoCl_2$ (200 μM) induced hypoxic condition. The mean fluorescence values are given in the insets. (d) Bright-field, (e) fluorescence microscopic image and (f) corresponding flow cytometric plots of B16F10 cells incubated with native curcumin for 6 h in normoxic condition (without $CoCl_2$). The mean fluorescence values are given in the insets.

2.2.8. Killing ability of curcumin loaded NI-Azo vesicles via hypoxia-responsive drug release

Next, we investigated the mammalian cell killing ability by **NI-Azo** vesicle loaded curcumin under hypoxic environment. To this end, the % killing of B16F10 (cancer) and NIH3T3 (non-cancer) cells by native curcumin and **NI-Azo** vesicles loaded curcumin (**NI-Azo-cur**) was tested by MTT assay under both hypoxic and normoxic conditions (Figure 19a,b). B16F10 and NIH3T3 cells were incubated with $CoCl_2$ (200 μM) for 24 h to induce hypoxia. Subsequently, the cells were treated with native curcumin and loaded curcumin (**NI-Azo-cur**) for 24 h with varying concentrations of curcumin (10-50 μg/mL). For B16F10 cells, 11 ± 2 to 34 ± 3 % cells and 15 ± 1 to 40 ± 2 % cells were killed by native curcumin (10-50 μg/mL) and loaded curcumin ([curcumin] = 10-50 μg/mL, [**NI-Azo** vesicle] = 10 to 50 μg/mL), respectively in normoxic condition (without inducing hypoxia) (Figure 19a). Interestingly, in hypoxic condition, % killing of B16F10 cells by **NI-Azo-cur** was found to be 18 ± 3 to 86 ± 1 which was ~2.15-fold higher (at 50 μg/mL of curcumin) than normoxic condition (Figure 19b). This was primarily due to the stimuli (hypoxia) responsive release of curcumin from the internalized **NI-Azo-**

cur through azoreductase induced disintegration of vesicular aggregates. Native curcumin (10-50 μg/mL) killed 11 ± 2 to 36 ± 2 % cancer cells in hypoxic environment which was comparable with that of normoxic condition. Expectedly, hypoxia had no influence on the free curcumin in absence of supramolecular vesicle (Figure 19b). So, in hypoxic environment, curcumin loaded within **NI-Azo** vesicles exhibited ~2.4-fold higher killing efficiency of cancer cells than that of native curcumin at experimental highest concentration (50 μg/mL).

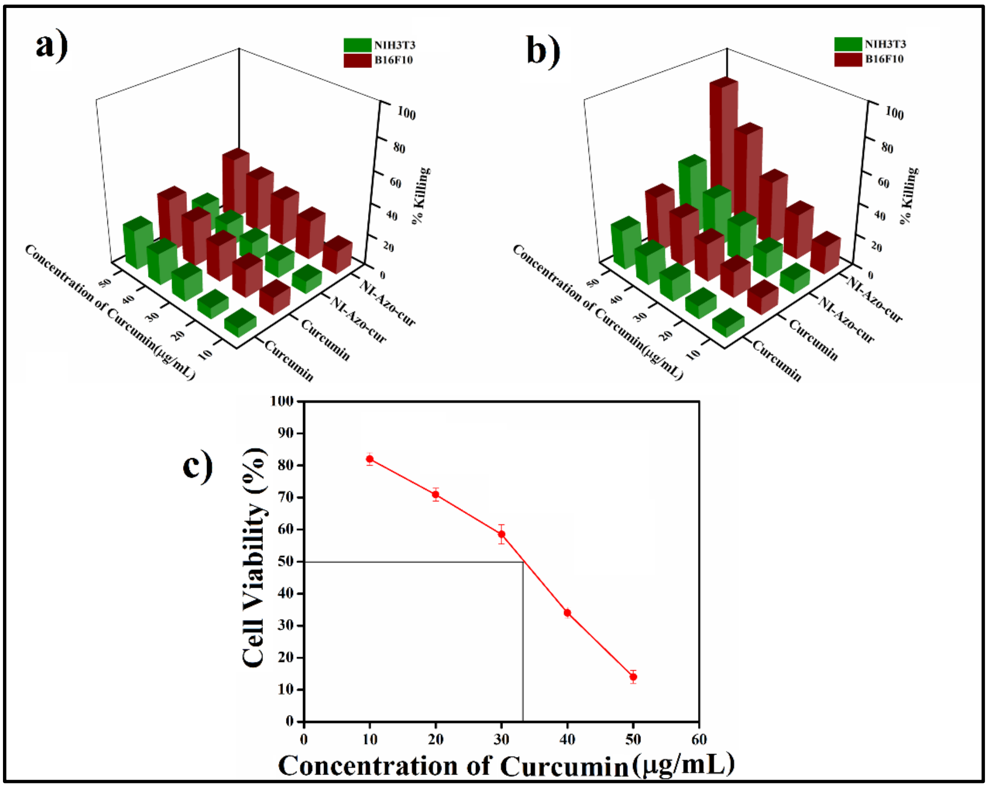

Figure 19. % Killing of cells determined by MTT assay. NIH3T3 and B16F10 cells incubated with varying concentrations of curcumin (10-50 μg/mL) and **NDI-Azo-cur** ([curcumin] = 10-50 μg/mL) (a) normoxic condition (in absence of $CoCl_2$), (b) with $CoCl_2$ induced hypoxia. (c) IC_{50} determination of **NDI-Azo-cur** ([curcumin] = 10-50 μg/mL) after 24 h incubation of B16F10 cells in $CoCl_2$ (200 μM) induced hypoxic environment. The standard deviation and experimental errors were in the range of ~1-3 %, respectively, in triplicate experiments.

In case of non-cancerous NIH3T3 cells, 9 ± 3 to 45 ± 2 % cells got killed upon incubation with loaded (10-50 μg/mL) curcumin (**NI-Azo-cur**) in hypoxic microenvironment, which was 8 ± 3 to 19 ± 2 % in normoxic environment. As expected, native curcumin showed similar killing efficiency 6 ± 2 to 25 ± 2 % against NIH3T3 cells under both normoxic and hypoxic conditions (Figure 19a,b). Thus, the % killing of B16F10 cells by curcumin loaded **NI-Azo** vesicles (**NI-Azo-cur**, [curcumin] = 50 μg/mL) was ~4.5-fold and

~1.9-fold higher compared to % killing of NIH3T3 cells in normoxic and hypoxic environment, respectively. Therefore, it is evident that curcumin delivery by **NI-Azo** vesicles leads to selective killing of hypoxic cancer cells due to stimuli responsive drug release through azoreductase induced disruption of nanocarrier.

The half-inhibitory concentration (IC_{50}) was found to be 33 μg/mL for **NI-Azo-cur** in case of hypoxic B16F10 cells (Figure 19c). Under the given experimental concentration range of curcumin (10-50 μg/mL), IC_{50} value could not be determined for **NI-Azo-cur** in hypoxic NIH3T3 as well as for native curcumin in hypoxic and normoxic conditions for both the cancer and non-cancer cell lines. Similarly, we could not measure IC_{50} value for **NI-Azo-cur** in normoxic condition for both cell lines under mentioned experimental conditions. Hence, it further confirms that curcumin loaded **NI-Azo** vesicles have higher therapeutic efficacy in killing cancer cells selectively under hypoxic microenvironment.

We also checked the cytotoxicity of the organic solvent, THF that were used in cell culture experiments. We used 0.164% THF in MTT assay experiments and 0.244% THF in bioimaging and flow cytometry experiments. THF having percentages 0%, 0.164% and 0.244% were incubated in NIH3T3 and B16F10 incubated in separate 96 well plates for 24 h. In both the cases we observed ~ 95% cells were alive (Figure 20).

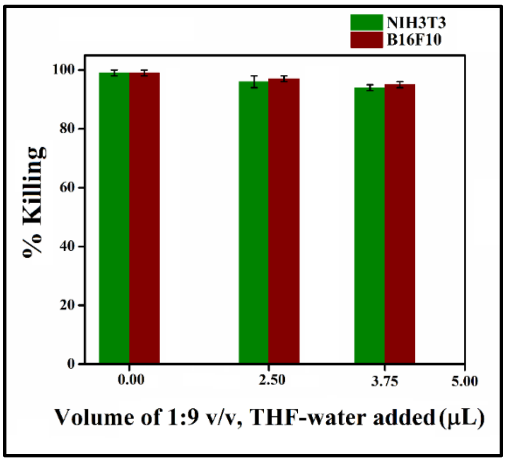

Figure 20. MTT-based % cell viability of NIH3T3 (non-cancer cells) and B16F10 (cancer cells) in presence of varying amount of 1:9 (v/v), THF-water added to 150 μL cell culture media.

Furthermore, we tested the stability of the **NI-Azo** vesicles upon dilution in the cell culture medium. Here, 2.5 μL of curcumin (50 μg/mL) loaded within **NI-Azo** vesicles (**NI-Azo-Cur**) (9:1 water:THF) were incubated in 150 μL PBS (0.164% THF) for 24 h. Bright green (characteristic emission of curcumin) spherical shaped objects of the drug loaded **NI-Azo** vesicles were observed under fluorescence microscope (Figure 21) which confirmed the stability of vesicle in 0.164% THF used in cell culture experiments.

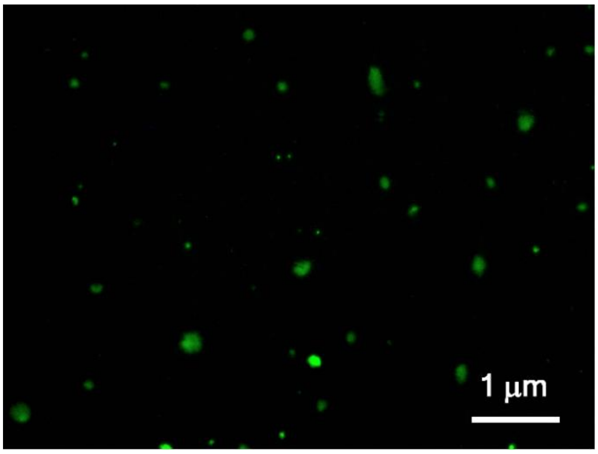

Figure 21. Fluorescence microscopic image of 2.5 μL of curcumin (50 μg/mL) loaded **NI-Azo** vesicles (**NI-Azo-Cur**) (9:1, v/v water:THF) diluted in 150 μL PBS.

2.2.9. Cell apoptosis

The cell killing pathway of B16F10 cells by free and loaded curcumin (within **NI-Azo** vesicles) was analyzed by an Annexin V-FITC/PI-based flow cytometric assay (Figure 22a-e). There are four distinct quadrants in the scatter plot of Annexin V-FITC and PI (Propidium Iodide): Q1 (Annexin V-FITC -ve, PI +ve), Q2 (both Annexin V-FITC and PI +ve), Q3 (both Annexin V-FITC and PI -ve), and Q4 (Annexin V-FITC +ve, PI -ve) that represent the population of necrotic cells, late apoptotic cells, viable cells and early apoptotic cells, respectively. B16F10 cells were treated with 200 μM $CoCl_2$ for 24h to make them hypoxic in nature. B16F10 cells in hypoxic and normoxic environment were separately incubated with 50 μg/mL of free curcumin and loaded curcumin (**NI-Azo-cur**) for 6 h. The cells were then detached and incubated with the AnnexinV-FITC/PI apoptotic kit and subjected to flow cytometry investigation. For untreated cells, all the population was naturally present in Q3 proving them to be unaltered and viable (Figure 22a). In normoxic situation, B16F10 cells treated with free curcumin and loaded curcumin as well as in hypoxic condition treated with free curcumin displayed a significant population at Q3, some at Q4, and a few distributed between Q1 and Q2 (Figure 22b-d) indicating an early apoptotic killing of cancer cells although most cells were viable. Notably, in hypoxic microenvironment, B16F10 cells treated with loaded curcumin (**NI-Azo-cur**) showed maximum population at Q4 and some at Q2 and Q3. This observation clearly demonstrates that cancer cell killing took place primarily through early apoptosis and a minor amount by late apoptosis. Based on all the preceding findings, it can be concluded that curcumin loaded **NI-Azo** vesicles (**NI-Azo-cur**) killed B16F10 cells selectively in hypoxic condition via early and late apoptotic pathway.

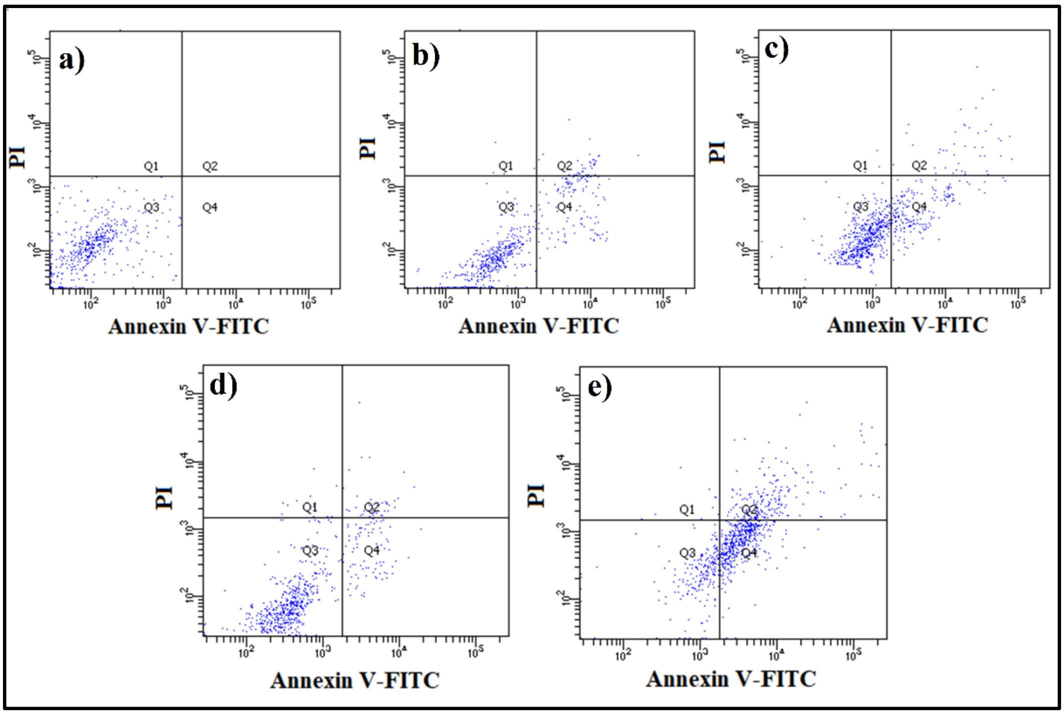

Figure 22. Flow cytometric analysis of apoptosis in (a) untreated B16F10 cells; B16F10 cells incubated with (b) free curcumin (50 μg/mL) in normoxic environment, (c) loaded curcumin (50 μg/mL) in **NI-Azo** vesicles in normoxic environment, (d) free curcumin (50 μg/mL) in $CoCl_2$ (200 μM) induced hypoxic environment, (e) loaded curcumin (50 μg/mL) in **NI-Azo** vesicles in $CoCl_2$ (200 μM) induced hypoxic environment.

2.3. CONCLUSION

In this work, naphthalimide based azo moiety containing amphiphile **NI-Azo** was synthesized that formed self-assembled vesicles in 1:9 (v/v), THF-water with azo moiety acting as the stimuli responsive junction. The self-assembly of **NI-Azo** took place through *H*-type of aggregation generating vesicles with a dimension of 200-250 nm. These vesicles got ruptured through the reduction of azo bond in presence of azoreductase enzyme (overexpressed in hypoxic microenvironment) and its mimic sodium dithionite. Formation of aniline (aromatic amine) derivatives through the cleavage of azo bond by azoreductase and sodium dithionite was confirmed by UV spectroscopic study of **NI-Azo** vesicles and MALDI-TOF spectrometric study of fragments obtained after sodium dithionite treatment. The anti-cancer drug, curcumin was entrapped inside **NI-Azo** vesicles and drug internalization was demonstrated by bioimaging and flow cytometry. Curcumin loaded **NI-Azo** vesicles killed B16F10 cells (cancer cells) through early apoptotic pathway in $CoCl_2$ (200 μM) induced hypoxic environment owing to stimuli responsive drug release, with 2.4-fold higher efficiency than that of native curcumin. Evidently, the cancer cell killing efficiency of curcumin loaded **NI-Azo** vesicles was 4.5-fold and 1.9-fold higher compared to that of NIH3T3 cells in normoxic and hypoxic environment, respectively. Harnessing the properties of extremely complicated tumor microenvironment in theranostic strategies, hypoxia responsive nanocarriers may manifest the idea of emerging pathway in cancer therapy.

2.4. EXPERIMENTAL SECTION

2.4.1. Materials and methods

4-Bromo-1,8-naphthalene anhydride was purchased from TCI Chemicals, India. N, N-Dimethyl-4,4'-azodianiline, thiazolyl blue tetrazolium bromide (MTT), Annexin V-FITC, PI dye and $CDCl_3$, DMSO-d_6, D_2O were bought from Sigma-Aldrich. Hydrazine hydrate, sodium dithionite ($Na_2S_2O_4$), cobalt chloride ($CoCl_2$), sodium sulfate (Na_2SO_4), silica gel (mesh size: 100-200), methoxy ethanol and all organic solvents were bought from SRL, India. Dulbecco's modified Eagle's media (DMEM), fetal bovine serum (FBS) and trypsin were procured from Thermo Fisher scientific, India. Milli-Q water was used for all the experimentations. NIH3T3, and B16F10 cells were procured from NCCS, Pune, India. ^{1}H-NMR and MALDI-TOF spectra were recorded in AVANCE (Bruker) and Ultraflex MALDI-TOF (Bruker) spectrometer, respectively.

2.4.2. Synthesis of NI-Azo

1,8-naphthalimide based azo bond containing amphiphile was synthesized following the pathway as depicted in Scheme 1. At first, 4-bromo-1,8-naphthalene anhydride (1 equiv) and hydrazine hydrate (1 equiv) were refluxed (80 °C) in dry EtOH for 4 h under inert atmosphere. After cooling to room temperature, the precipitate was filtered and washed with ethanol and dried under vacuum at 60 °C overnight to afford light yellow solid (yield = 81%). This yellow intermediate product (1 equiv) and *N*,*N*-dimethyl-4,4'-azodianiline (1.5 equiv) were dissolved in methoxy ethanol and heated at 120 °C for 4 h under reflux condition. The reaction mixture was cooled to room temperature and poured into 50 mL ice cold distilled water. The mixture was filtered and the filtrate was vacuum evaporated to get an orange solid. This solid was purified in 100-200 mesh silica gel chromatography using 2% methanol in chloroform (v/v) as eluent to obtain the **NI-Azo** (yield = 78%) (Scheme 1). **NI-Azo** and intermediate were characterized by ^{1}H NMR and mass spectroscopy.

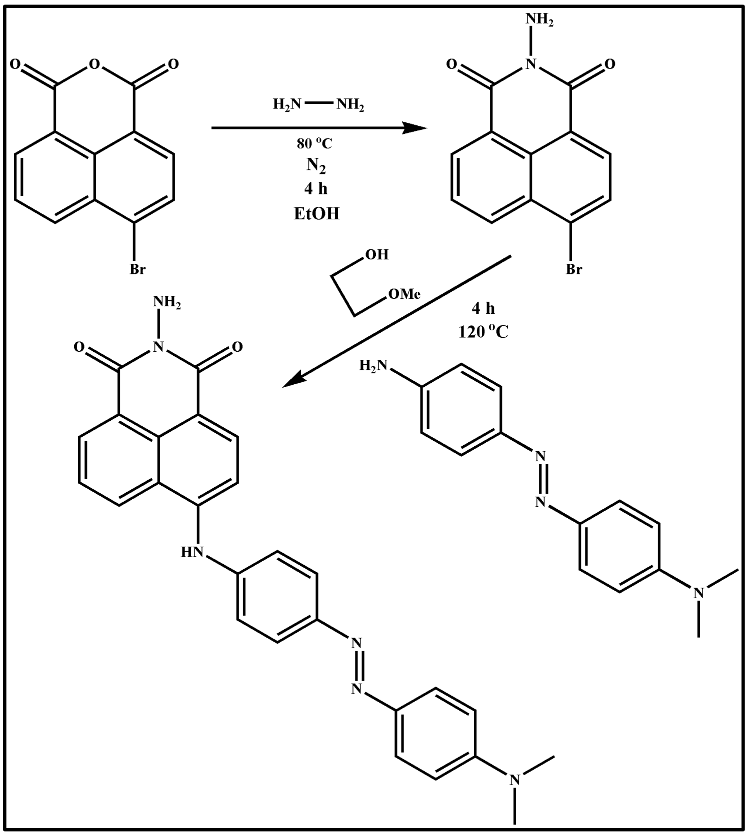

Scheme 1. Synthetic scheme of **NI-Azo**.

2.4.3. Determination of critical aggregation concentration (CAC)

The critical aggregation concentration (CAC) for **NI-Azo** was determined through fluorescence spectroscopy by employing pyrene as the polarity probe. Pyrene is used to investigate the polarity changes in the microenvironment (micelle or vesicle) from polarity changes in the macroenvironment (bulk solvent). The ratio of the emission peaks at $\lambda_{em} = 372$ nm for the 0-0 band (I_1) and at λ_{em} = 383 nm corresponding to the third principal vibronic band (I_3) in water, is sensitive to polarity of the medium. A series of **NI-Azo** vesicle sample solutions in 1:9 v/v, THF-water was prepared by varying the concentration from 0.5 μg/mL to 7.5 μg/mL. A 1.0 mM stock solution of pyrene was prepared in THF. 1 μL of this, was added to each vesicular solution so that the final concentration of pyrene in each sample was 1 μM. Emission intensity was measured by exciting those solutions at $\lambda_{ex} = 317$ nm. The ratio of I_{383} and I_{372} (I_3/I_1) was plotted against the logarithm of the concentration (mg/mL). CAC was also measured in the similar way at pH = 4.0 and pH = 9.0 by varying **NI-Azo** concentration (0.5 to 8.5 μg/mL).

2.4.4. Preparation of vesicular solution

NI-Azo was completely soluble in tetrahydrofuran (THF) and insoluble in water. Therefore, it was first dissolved in THF and then Milli-Q water was gradually added into it, which gradually turned the clear solution to a translucent one indicating the self-aggregation at 1:9 (v/v) THF-water. A stock solution (10 mM) was prepared by dissolving the estimated amount of **NI-Azo** in THF. Varying concentrations of **NI-Azo** solution for different spectroscopic and microscopic investigations were prepared by adding the desired aliquot of the stock solution into 90 vol% water in THF. Similarly, **NI-Azo** was also dissolved in dimethyl sulfoxide (DMSO), which turned to a translucent solution after addition of water up to 75 vol%. It indicates the formation of self-assembly at 1:3 (v/v), DMSO-water. Increase in the water percentage above 75 vol% resulted in precipitation of **NI-Azo**.

2.4.5. Transmission electron microscopy (TEM)

4 μL solution of 25 μM **NI-Azo** in 90 vol% water in THF was deposited on a carbon covered Cu (copper) grid (300 mesh). The sample was desiccated for 4 h, followed by stained with uranyl acetate solution (1 μL (1% w/v)) and again dried. After keeping the sample under vacuum for 4 h, TEM images were recorded in JEOL JEM 2010 microscope.

2.4.6. Field-emission scanning electron microscopy (FESEM)

6 μL solution of 25 μM **NI-Azo** in 90 vol% water in THF was drop cast on coverslips and kept in vacuum for few hours. Then, the FESEM images were taken in JEOL-6700F microscope.

2.4.7. Atomic force microscopy (AFM) study

5 μL **NI-Azo** solution (25 μM) in 90 vol% water in THF was drop cast on glass slide and dried for overnight and AFM images were acquired from Asylum Research MFP-3D AFM.

2.4.8. Cryogenic transmission electron microscopy (Cryo-TEM)

4 μL solution of 25 μM **NI-Azo** in 90 vol% water in THF was deposited on a carbon covered Cu (copper) grid (300 mesh) followed by immediate vitrification of the grids by placing it inside the GATAN CP3 cryo-plunger. After that, TEM images were recorded by placing the vitrified Cu grids under JEOL JEM-2100 PLUS microscope.

2.4.9. Dynamic light scattering (DLS) study and zeta (ζ) potential measurement

Mean hydrodynamic diameter (D_h) of **NI-Azo** (25 µM) in 1:9 (v/v) THF-water was determined in Zen 3690 Zetasizer (Malvern Instrument Ltd.). The angle at which scattering intensity was measured was 175° and data were evaluated by a Cumulant Fit in Malvern Zetasizer software. The zeta (ζ) potential measurements were performed with solution of **NI-Azo** (25 µM) in 1:9 (v/v) THF-water at room temperature. An average of three successive measurements was noted for the sample.

2.4.10. Fluorescence microscopy

NI-Azo (2 mg) and 20 µL of calcein solution (2 mM) in Milli-Q water were mixed maintaining 1:9 (v/v), THF-water with final concentration of **NI-Azo** and calcein being 2.0 mg/mL and 40 µM, respectively. The solution was stirred overnight and then it was loaded into a G-50 sephadex column (height: 15 cm and diameter: 1.2 cm). The column was pre-equilibrated and eluted with 90 vol% water in THF. The eluent was collected in fractions having 1 mL volume each time. Absorbance of all fractions was measured at 490 nm that ensured the existence of calcein in each fraction inside vesicles. This gel filtration was continued until complete separation of entrapped calcein from the free calcein. Next, 10 µL solution of calcein entrapped **NI-Azo** in THF-water (f_w = 90 vol%) was drop cast on glass slides and air-dried before imaging in IX83 inverted microscope at 40x magnification.

To investigate stability of vesicles upon dilution in the cell culture medium, we used 2.5 µL of curcumin (50 µg/mL) loaded within **NI-Azo** vesicles (**NI-Azo-Cur**) (9:1, v/v water:THF) in 150 µL PBS (phosphate saline buffer solution, pH = 7.4) i.e., 0.164% THF in a 24 well plate and incubated for 24 h. Next, 10 µL solution of curcumin entrapped **NI-Azo** was drop casted on glass slides and air-dried before imaging in IX83 inverted microscope at 40x magnification.

2.4.11. UV-visible study

Self-aggregation pattern of **NI-Azo** was analyzed by recording solvent dependent UV-vis spectra on Perkin Elmer Lambda 25 spectrophotometer. UV-visible spectra of **NI-Azo** (15 µM, 1 mL) in THF-water solvent mixtures was observed by increasing the water content from non-self-assembly (monomeric state at THF) towards self-assembled states that are 3:1, 1:1, 1:3, 1:4 and 1:9 (v/v), THF-water. We carried out pH dependent UV-vis spectroscopic investigation of **NI-Azo** (15 µM) in 1:9 (v/v), THF-water binary solvent system varying the pH of the aqueous domain from 4.0 to 9.0 using phosphate buffer (10 µM). Also, UV-visible spectra of

NI-Azo (10 μM, 1 mL) in DMSO-water solvent mixtures was observed by gradually increasing the water content from non-self-assembly (monomeric state at DMSO) towards self-assembled states 1:3 (v/v), DMSO-water. The stimuli-responsive reduction of the azo bond was monitored by taking UV-vis spectra of **NI-Azo** (10 μM, 1 mL) in 1:9 (v/v) THF-water in absence and presence of azoreductase enzyme and $Na_2S_2O_4$ (chemical mimic of azoreductase).

2.4.12. Solvent-dependent ^{1}H-NMR study

^{1}H-NMR spectra of **NI-Azo** (1 mM) in DMSO-d6, 3:1 (v/v) DMSO-d6-D2O and 1:1 (v/v) DMSO-d6-D2O were recorded on Avance 300 MHz spectrometer (Bruker).

2.4.13. Solvent-dependent FTIR study

FTIR spectra of **NI-Azo** were taken in the non-self-aggregated ($CHCl_3$) and in the self-aggregated state (1:3 (v/v), DMSO-d_6-D_2O) in a Perkin Elmer Spectrum 100 FTIR spectrometer using 1 mm CaF_2 cell.

2.4.14. X-ray diffraction

X-ray diffraction (XRD) spectrum of a dried film of **NI-Azo** vesicular solution was obtained on a Bruker D8 Advance diffractometer with Cu Kα radiation source (α = 0.15406 nm), 40 kV voltage and 30 mA current. 25 μM **NI-Azo** vesicular solution formed in 1:9 (v/v), THF-water was placed over a glass slide and dried to form a thin film. The sample was scanned in the angle range of 10-40°.

2.4.15. MALDI-TOF mass spectrometry

Stimuli-responsive cleavage of azo residue in presence of $Na_2S_2O_4$ was investigated using MALDI-TOF mass spectrometry. 100 μL of $Na_2S_2O_4$ stock solution (2 M) was added to the vesicular solution of **NI-Azo** (0.5 mg/mL) in 1:9 (v/v) THF-water and was stirred for 8 h keeping the final concentration of $Na_2S_2O_4$ to be 200 mM. Solid mass was obtained by lyophilizing the reaction mixture and it was dissolved in methanol for executing the mass spectrometric study in Bruker Ultraflex MALDI-TOF.

2.4.16. Microorganisms and culture conditions

Gram negative bacteria *Escherichia coli* was utilized for azoreductase extraction to perform hypoxia responsive cleavage of azo bond and subsequently disintegration of supramolecular vesicles. Luria Broth (LB) agar (1.0 g tryptone, 0.5 g yeast extract, 1 g NaCl, and 3.5 g agar in 100 mL of sterile Milli-Q water) was used as a solid medium for bacterial growth. Bacterial strains were procured from Institute of Microbial Technology, Chandigarh, India. After opening the freeze-dried ampules of bacterial strain, a loopful of culture was spread on the solid LB agar media and incubated for 24 h at 37 °C. The cells were collected in 0.9 weight % saline water and diluted. All the required dilutions were made in autoclaved sterile milli-Q water. Cells were centrifuged at 6000 g for 10 min at 4 °C and the supernatant was collected to obtain extracellular azoreductase enzyme. Cell pellets were washed twice with lysozyme (final concentration:1 mg/mL). The bacterial cells were then disrupted by sonication using sonicator probe for 2 × 10 seconds pulses for 5 min interval at 60 Hz. at 4 ± 0.2 °C. It was further centrifuged at 15,000 g for 15 min at 4 °C to remove cellular debris and unruptured cells and the supernatant was collected to get the intracellular azoreductase enzyme.[40]

2.4.17. Curcumin loading and release

We checked the loading capacity of **NI-Azo** vesicles formed in 1:9 (v/v), THF-water using curcumin as the anti-cancer drug. **NI-Azo** and curcumin were mixed in 1:9 v/v, THF-water with final concentration of **NI-Azo** and curcumin both being 1.0 mg/mL. The solution was stirred overnight and then it was loaded into a G-50 sephadex column (height: 15 cm and diameter: 1.2 cm). The column was pre-equilibrated and eluted with 90 vol% water in THF. The eluent was collected in fractions having 1 mL volume each time. We measured the absorbance of all fractions at 426 nm that ensured the existence of curcumin in each fraction inside vesicles. Gel filtration was continued until complete separation of entrapped curcumin from the free curcumin which was determined by no detectable absorbance of curcumin in the collected fraction. Finally, introduction of $Na_2S_2O_4$ disrupted the vesicles through cleavage of azo bond and the drug loading percentage was estimated (~49%) following the typical procedure using a standard calibration curve. We studied the drug release by taking absorbance and fluorescence spectra (by Varian Cary Eclipse luminescence spectrometer) before and after treatment with 1 mM $Na_2S_2O_4$ to curcumin encapsulated vesicles and comparing them with the calibrated plot of native curcumin. Fluorescence microscopic images were also captured before and after treatment of **NI-Azo** vesicles with 1 mM $Na_2S_2O_4$ under a IX83 inverted microscope at 10x and 40x magnification respectively.

2.4.18. Cell culture

Cancer cells B16F10 and non-cancer cells NIH3T3 were cultured in DMEM media with FBS (10%), streptomycin and penicillin keeping in 5% CO_2 incubator at 37 °C. These were used for checking cytocompatibility, bioimaging and performing flow cytometry experiments.

2.4.19. MTT assay

Cytocompatibility of **NI-Azo** vesicles in THF-water (f_w = 90 vol%) was investigated by MTT assay. Live cells excrete mitochondrial dehydrogenase that reduces soluble tetrazolium to insoluble formazan, which is further dissolved in DMSO and estimated spectrophotometrically in this assay. The number of alive cells can be determined from the generation of formazan. Lower absorbance represents killing of the cells. Cells were cultured in a 96-well plate (number of cells per well: 2×10^4) for 24 h in 150 µL culture media. 2.5 µL of **NI-Azo** vesicles (f_w = 90 vol% in THF) with 10-50 µg/mL concentration, were incubated with both the cells for 24 h. 10 µL of MTT stock solution (5 mg/mL) taken in PBS was added followed by further incubation of 4h. The precipitated formazan was dissolved in DMSO and absorbance was recorded in Bio Tek1 Elisa Reader at 570 nm. The number of viable cells was calculated as % viability by the given equation:

$$\%\text{viability}=(A_{570}\,(\text{treated cells}) - \text{background})/(A_{570}\,(\text{untreated cells}) - \text{background}) \times 100 \quad (1)$$

Similarly, the % killing of the above-mentioned cancer cell B16F10 and non-cancer cell NIH3T3 by 2.5 µL of free curcumin (10-50 µg/mL) and 2.5 µL of curcumin (10-50 µg/mL) loaded within **NI-Azo** vesicles (**NI-Azo-Cur**) under normoxic (5% CO_2 incubator at 37 °C) and hypoxic (200 µM $CoCl_2$ induced hypoxia) environment was investigated by the mentioned MTT assay and calculated using the equation 1.

Cytocompatibility was further tested in presence of THF having percentages 0%, 0.164% and 0.244% i.e., 0 µL, 2.5 µL, 3.75 µL of 1:9 (v/v), where THF-water was added in 150 µL cell culture media, respectively and incubated for 24h in presence of cancer cell B16F10 and non-cancer cell NIH3T3. The result was investigated by above mentioned procedure and calculated using the equation no 1.

2.4.20. Flow cytometry

Cultured B16F10 cells were incubated 10 µL of curcumin (50 µg/mL) and 10 µL of curcumin loaded **NI-Azo** ([curcumin] = 50 µg/mL) for 6 h in 400 µL culture media. Next, we washed the cells with DMEM media and PBS buffer for removal of the excess compounds from cellular medium. Trypsin was added to detach the cells from culture flask and centrifugation for 5min. After centrifugation, we took the precipitated cells suspended in PBS (500 µL) and performed the flow cytometry experiment. BD FACS Aria™ III flow cytometer was employed to inspect the fluorescence intensity within the cells at emission wavelength using a 510 ± 40 nm bandpass filter upon excitation at 405 nm.

To determine the pathway of cellular death, free curcumin, loaded curcumin within **NI-Azo** vesicles were incubated with B16F10 cells for 12 h under similar experimental condition as mentioned above. After centrifugation, pellets were suspended in of 1x binding buffer (500 µL) consisting propidium iodide (PI, 1.0 µg) and Annexin V-FITC (0.25 µg). After incubation for 15 min in the dark at room temperature, the cells were analyzed using a BD FACS Aria III flow cytometer using excitation wavelength 488 nm, and the emission wavelength was recorded at a 533 ± 30 (FL-1) bandpass filter for Annexin V-FITC and 585 ± 40 nm (FL-2) bandpass filter for PI.

2.5. CHARACTERIZATION DATA

2.5.1. Characterisation of NI-Azo

^{1}H-NMR (400 MHz, $CDCl_3$, 25 °C): δ/ppm: 8.69-8.72 (d, 2H, aromatic proton attached to C5 and C7 of napthalimide core), 8.61-8.63 (d, 1H, aromatic proton attached to C2 of napthalimide core), 8.45-8.47 (d, 2H, aromatic proton present in azodianiline residue meta to -NH), 8.07-8.09 (d, 2H, aromatic proton meta to $-N(CH_3)_2$), 7.86-7.90 (m, 1H, aromatic proton attached to C6 of napthalimide core, 7.77-7.79 (m, 1H, aromatic proton attached to C3 of napthalimide core), 7.17-7.22 (d, 2H, aromatic proton present in azodianiline residue ortho to -NH), 6.73-6.75 (d, 2H, aromatic proton ortho to $-N(CH_3)_2$), 3.12-3.14 (m, 6H, $N(C\underline{H}_3)_2$) MALDI-TOF: m/z: 473.48 $[M+Na]^+$(calculated); 473.955 (found) and 489.59 $[M+K]^+$ (calculated); 489.986 (found). The elemental analysis data is found to be C 68.66 % , H 4.72 %, N 18.88 % as compared to the theoretical value of C 69.32 % , H 4.92 %, N 18.66 %

2.5.2. Characterisation of intermediate

^{1}H-NMR (400 MHz, $CDCl_3$, 25 °C): δ/ppm: 8.68-8.78 (d, 1H, aromatic proton attached to C5 of napthalimide core), 8.60-8.62 (d, 1H, aromatic proton attached to C7 of napthalimide core), 8.44-8.46 (d, 1H, aromatic proton attached to C2 of napthalimide core), 8.06-8.08 (d, 1H, aromatic proton attached to C3 of napthalimide core), 7.85-7.89 (m, 1H, aromatic proton attached to C6 of napthalimide core), MALDI-TOF: m/z: 291.1 $[M]^+$(calculated); 291.425 (found) and 314.1 $[M+Na]^+$ (calculated); 314.451 (found).

2.6. SPECTRA

2.6.1. ^{1}H-NMR spectra

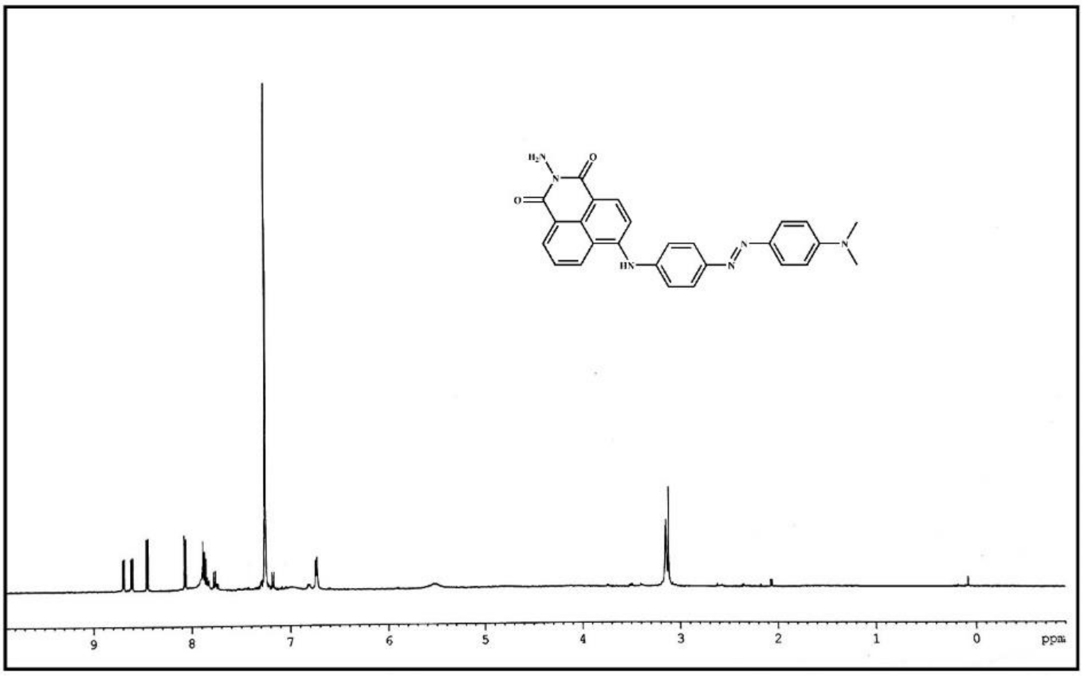

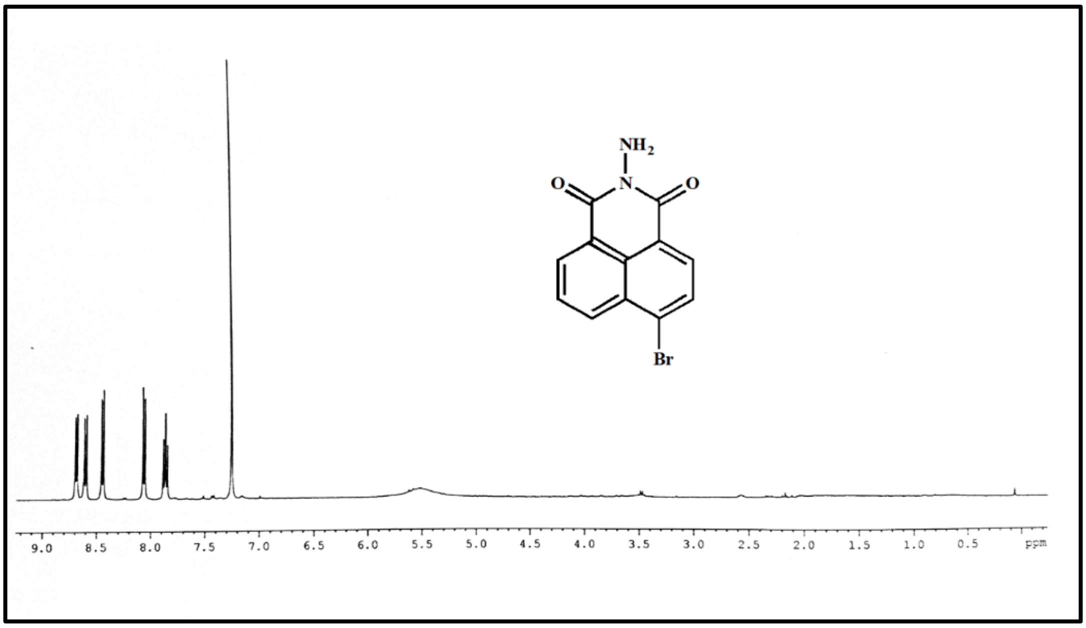

2.6.2. Mass spectra

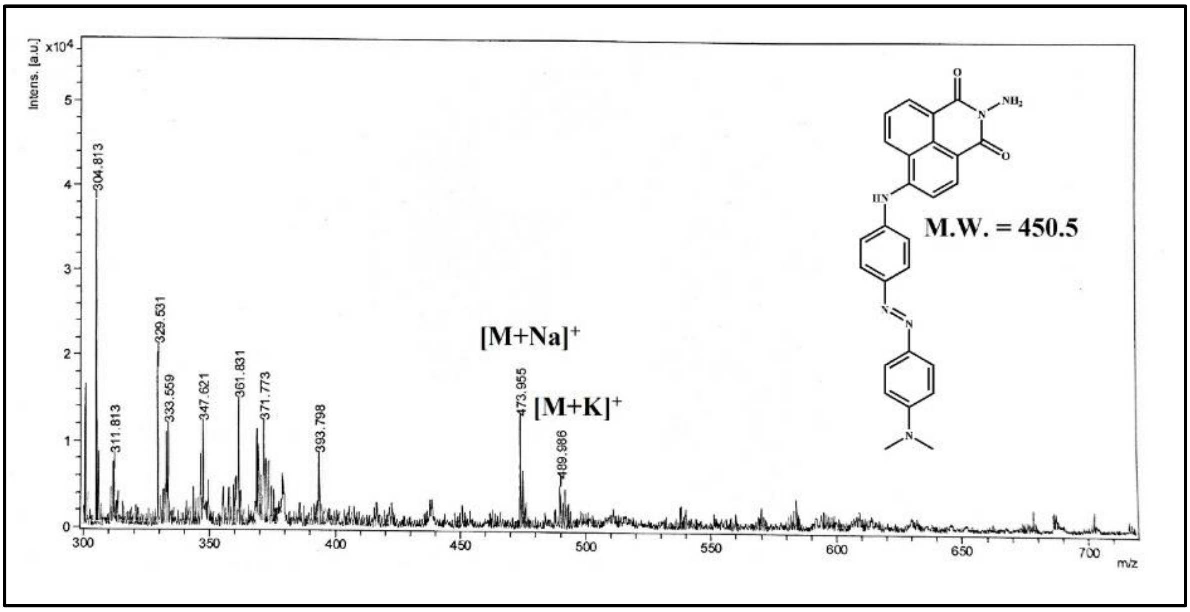

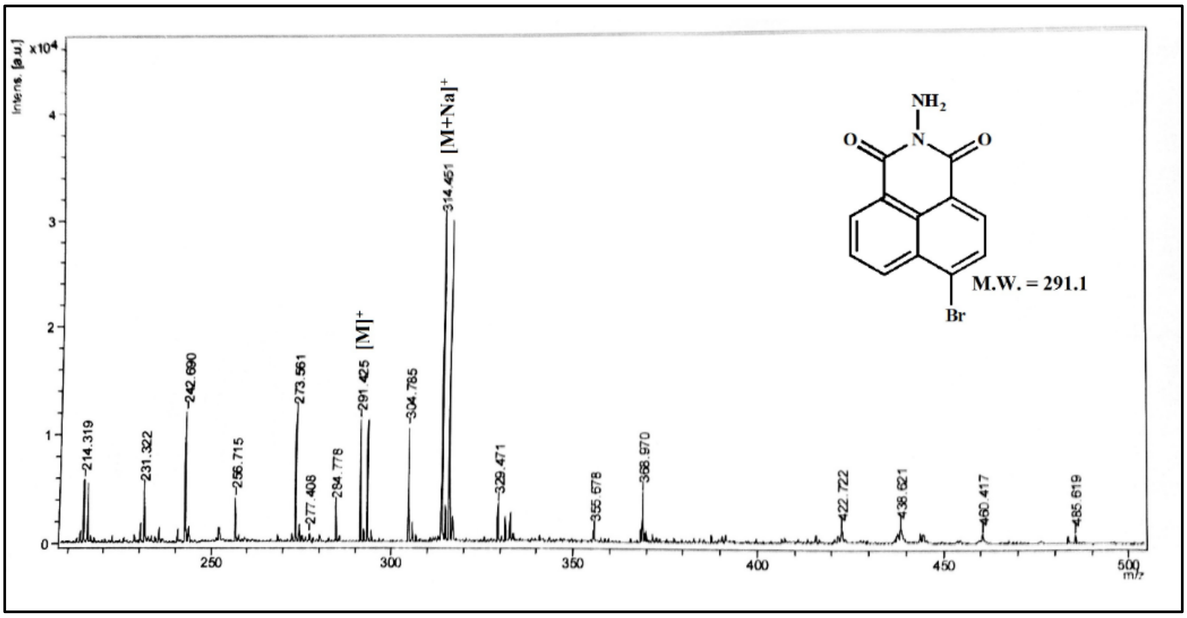

2.7. REFERENCES

[1] J. M. Lehn, *Angew. Chem. Int. Ed.* **1990**, *29*, 1304.

[2] G. M. Whitesides, J. P. Mathias, C. T. Seto, *Science* **1991**, *254*, 1312.

[3] P. Walde, A. Goto, P. A. Monnard, M. Wessicken, P. L. Luisi, *J. Am. Chem. Soc.* **1994**, *116*, 7541.

[4] J. H. Mondal, T. Ghosh, S. Ahmed, D. Das, *Langmuir* **2014**, *30*, 11528.

[5] F. Razaei, Y. Yamani, M. A. Moradi, *J. Chromatogr. A* **2014**, *1327*, 155.

[6] B. O. Okesola, D. K. Smith, *Chem. Soc. Rev.* **2016**, *45*, 4226.

[7] H. T. Jung, B. Coldren, J. A. Zasadzinski, D. J. Iampietro, E. W. Kaler, *Proc. Natl. Acad. Sci.* **2001**, *4*, 1353.

[8] S. Dinda, M. Ghosh, P. K. Das, *Langmuir* **2016**, *32*, 6701.

[9] K. J. C. Van Bomel, C. Van der Pol, I. Muizebet, A. Friggeri, A. Heeres, A. Meetsma, B. L. Feringa, J. Van Esch, *Angew. Chem. Int. Ed.* **2004**, *43*, 1663.

[10] M. D. Segarra-Maset, V. J. Nebot, J. F. Miravet, B. Escuder, *Chem. Soc. Rev.* **2013**, *42*, 7086.

[11] J. H. Mondal, S. Ahmed, T. Ghosh, D. Das, *Soft Matter* **2015**, *11*, 4912.

[12] R. Ghosh, J. Dey, *Langmuir* **2014**, *30*, 13516.

[13] U. Kauscher, M. N. Holme, M. Bjornmalm, M. M. Stevens, *Adv. Drug Deliv. Rev.* **2019**, *138*, 259.

[14] F. Meng, Z. Zhong, J. Feijen, *Biomacromolecules* **2009**, *10*, 197.

[15] A. B. Cook, P. Decuzzi, *ACS Nano* **2021**, *15*, 2068.

[16] O. Onaca, R. Enea, D. W. Hughes, W. Meier, *Macromol. Biosci.* **2009**, *9*, 129.

[17] M. H. Li, P. Keller, *Soft Matter* **2009**, *5*, 927.

[18] M. N. Holme, I. A. Fedotenko, D. Abegg, J. Althaus, L. Babel, F. Favarger, R. Reiter, R. Tanasescu, P. L. Zaffalon, A. Ziegler, B. Muller, T. Saxer, T. Zumbueh, *Nat. Nanotechnol.* **2012**, *7*, 536.

[19] M. S. Kim, D. W. Lee, K. Park, S. J. Park, E. J. Choi, Park, E. S.; Kim, H. R. *Colloids Surf. B* **2014**, *116*, 17.

[20] D. Sarkar, P. Choudhury, P. K. Das, *J. Colloid Interface Sci.* **2018**, *530*, 67.

[21] Z. H. Li, Z. L. Tan, A. X. Ding, B. Gong, Z. L. Lu, L. He, *Chem. Commun.* **2017**, *53*, 3535.

[22] X. Zheng, X. Wang, H. Mao, W. Wu, B. Liu, X. Jiang, *Nat. Commun.* **2015**, *6*, 5834.

[23] T. Thambi, J. H. Park, D. S. Lee, *Chem. Commun.* **2016**, *52*, 8492.

[24] W. Wang, L. Lin, X. Ma, B. Wang, L. Sanrong, X. Yan, S. Li, H. Tian, X. Yu, *ACS Appl. Mater. Interfaces* **2018**, *10*, 19398.

[25] M. I. Confeld, B. Mamnoon, L. Feng, H. Jensen-Smith, P. Ray, J. Froberg, J. Kim, M. A. Hollingsworth, M. Quadir, Y. Choi, S. Mallik, *Mol. Pharmaceutics* **2020**, *17*, 2849.

[26] P. Zhang, H. Yang, W. Shen, W. Liu, L. Chen, C. Xiao, *ACS Biomater. Sci. Eng.* **2020**, *6*, 2167.

[27] S. Kizaka-Kondoh, S. Tanaka, H. Harada, M. Hiraoka, *Adv. Drug Deliv. Rev.* **2009**, *61*, 623.

[28] J. A. Bertout, S. A. Patel, M. C. Simon, *Nat. Rev. Cancer* **2008**, *8*, 967.

[29] W. R. Wilson, M. P. Hay, *Nat. Rev. Cancer* **2011**, *11*, 393.

[30] J. M. Brown, W. R. Wilson, *Nat. Rev. Cancer* **2004**, *4*, 437.

[31] A. L. Harris, *Nat. Rev. Cancer* **2002**, *2*, 38.

[32] M. Takasawa, R. R. Moustafa, J. C. Baron, *Stroke* **2008**, *39*, 1629.

[33] R. Callaghan, S. Potter, *J. Clin. Pharmacol.* **2008**, *48*, 365.

[34] Q. Wang, L. Tian, J. Xu, B. Xia, J. Li, F. Lu, X. Lu, W. Wang, W. Huang, Q. Fan, *Chem. Commun.* **2018**, *54*, 10328.

[35] G. L. Semenza, *Nat. Rev* **2003**, *3*, 726.

[36] C. Huang, J. Zheng, D. Ma, N. Liu, C. Zhu, J. Li, R. Yang, *J. Mater. Chem. B* **2018**, *6*, 6424.

[37] J. Rao, A. Khan, *J. Am. Chem. Soc.* **2013**, *135*, 14056.

[38] S. H. Medina, M. V. Chevliakov, G. Tiruchinapally, Y. Y. Durmaz, S. P. Kuruvilla, M. E. H. ElSayed, *Biomaterials* **2013**, *34*, 4655.

[39] W. Piao, S. Tsuda, Y. Tanaka, S. Maeda, F. Liu, S. Takahashi, Y. Kushida, T. Komatsu, T. Ueno, T. Terai, T. Nakazawa, M. Uchiyama, K. Morokuma, T. Nagano, K. Hanaoka, *Angew. Chem. Int. Ed.* **2013**, *52*, 13028.

[40] S. A. Zahran, M. A. Tammam, A. M. Hashem, R. K. Aziz, A. E. Ali, *Sci. rep*. **2019**, 9:5508.

[41] X. Cao, L. Meng, Z. Li, Y. Mao, H. Lan, L. Chen, Y. Fan, T. Yi, *Langmuir* **2014**, *30*, 11753.

[42] N. J. Dunn, W. H. Humphries, A. R. Offenbacher, T. L. King, J. A. Gray, *J. Phys. Chem. A* **2009,** *113,* 13144.

[43] A. Ayadi, D. G. Branzea, M. A. Benmensour, A. Boucekkine, N. Zouari, A. El-Ghayoury, *Tetrahedron* **2015**, *71*, 7911.

[44] D. Jacquemin, E. A. Perpète, G. Scalmani, I. Ciofini, C. Peltier, C. Adamo, *Chem. Phys.* **2010**, *372*, 61.

[45] C. Zhu, Z. Zou, C. Huang, J. Zheng, N. Liu, J. Li, R. Yang, *Chem. Commun.* **2019**, *55*, 3235.

[46] C. Huang, W. Tan, J. Zheng, C. Zhu, J. Huo, R. Yang, *ACS Appl. Mater. Interfaces* **2019**, *11*, 25740.

[47] Zhou, Y.; Maiti, M.; Sharma, A.; Won, M.; Yu, L.; Miao, L. X.; Shin, J.; Podder, A.; Bobba, K. N.; Han, J.; Bhuniya, S.; Kim, J. S. Azo-based small molecular hypoxia responsive theranostic for tumor-specific imaging and therapy. *J. Control. Release* **2018**, *288*, 14.

[48] J. Feng, T. M. Heinze, H. Xu, C. E. Cerniglia, H. Chen, *Protein Pept Lett.* **2010**, *17*, 578.

[49] A. Chevalier, C. Mercier, L. Saurel, S. Orenga, P. Y. Renard, A. Romieu, *Chem. Commun.* **2013**, *49*, 8815.

[50] P. Verwilst, J. Han, J. Lee, S. Mun, H. G. Kang, J. S. Kim, *Biomaterials* **2017**, *115*, 104.

[51] N. K. Rana, P. Singh, B. Koch, *Biol. Res.* **2019**, 52:12

[52] G. Teti, S. Focaroli, V. Salvatore, E. Mazzotti, L. Ingra', A. Mazzotti, M. Falconi, *Stem Cells Int.* **2018**, *2018*, 3237253.

* * *

Chapter 3

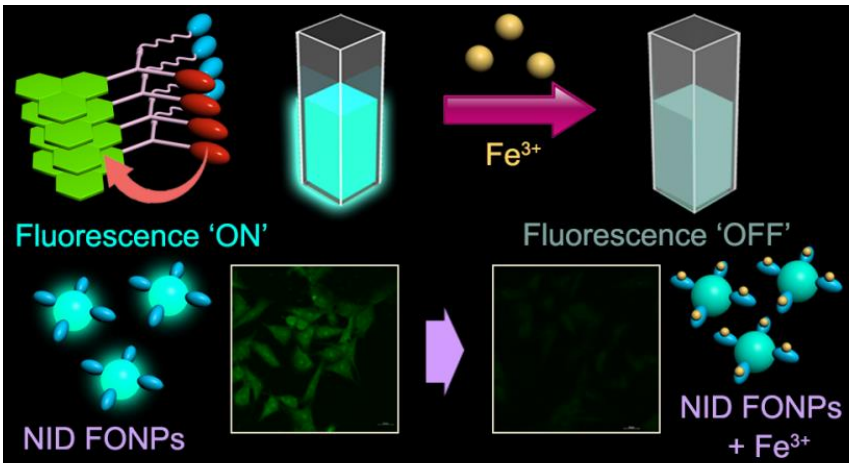

Naphthalimide based fluorescent organic nanoparticles in selective detection of Fe^{3+} and its application as a diagnostic probe for Fe^{2+}/Fe^{3+} transition

3.1. INTRODUCTION

Fluorescence sensing has been an expansive research arena in many fields like chemistry, biotechnology, clinical biology, environmental science and many more.[1-3] Fluorescence based probes have momentous advantages over other class of sensors for the detection of biologically and environmentally pertinent metal ions as it provides convenient, fast and sensitive detection of target analyte with high selectivity.[4-7] As a whole, fluorophores have a demerit of concentration-quenching owing to the aggregation caused quenching (ACQ), small Stokes' shift and poor photostability.[8] In contrast to that, Tang *et al.* devised the concept of aggregation-induced emission (AIE) through the discovery of a unique luminophore that showed remarkably enhanced emission in the aggregated state in 2001.[9] Restricted intramolecular rotation of the constituent amphiphile, that facilitates the conversion of the consumed excitation energy from non-radiative relaxation to radiative decay, is one of the most prominent reason of AIE.[10-12] At large, these luminogens are weakly/non emissive in solution phase. AIE unlocks new possibilities in sensing with advantages of precision, low limit of detection, excellent selectivity and photostability etc.[13-15] Fluorescent Organic nanoparticles (FONPs) having AIE property are fascinating manifestation of self-aggregates derived from π-conjugated oligomers, polymers, or chromophores having flexible functionalisation.[16-19]

The AIE active FONPs have been receiving a lot of attention as a result of their ease of fabrication, synthetic variety, water solubility and bio-compatibility.[16,20-22] In view of its high signal-to-noise ratio, FONPs are getting distinguished in selective sensing of different analytes including metal ions.[21] Numerous transition metal ions have wide range of biological and environmental significance. Among all the transition metals, iron (Fe) is physiologically most abundant as well as vital in biological systems. Oxygen uptake, electron transfer, enzyme catalysis, cellular metabolism, transcriptional regulation and several other processes in living systems are being regulated by iron.[23-25] However, both its deficit and excess can cause a various diseases in the human body.[26-28] It is present in multiple oxidation states like Fe^{2+} or Fe^{3+} (or transient higher oxidative states) and its reactivity uniquely depends on the redox state. Therefore, for better understanding of its physiological and pathological roles of iron, it is required to able to detect and differentiate iron at its different redox states. Transition from Fe^{2+} to Fe^{3+} occurs in living system during generation of reactive oxygen species (ROS) upon interaction of Fe^{2+} with hydrogen peroxide in Fenton reactions.[29-31] Uncontrolled ROS production causes oxidative damage of cellular components leading towards a condition known as oxidative stress.[32-33] To diagnose such situation, development of selective fluorescent sensors for Fe^{3+} and monitoring of Fe^{2+}/Fe^{3+} transition in cellular system is indispensable. Even though detection of Fe^{3+} ion has drawn notable attention,[34-37] reports on FONPs based Fe^{3+} sensing with high sensitivity and selectivity as well as monitoring of Fe^{2+} to Fe^{3+} transition inside living cells are indeed scarce.

Herein, we synthesized naphthalimide based amphiphilic molecule (**NID**, Figure 1) having histidine substitution at the side chain as Fe^{3+} recognition unit. **NID** self-assembled to form spherical aggregated FONPs in 99 vol% water in DMSO and exhibited AIE at 470 nm (bluish green emission) through excimer formation together with intramolecular charge transfer. Among the various metal ions, luminescence of **NID** FONPs selectively got quenched by Fe^{3+} with a detection limit of 12.5 ± 1.2 μM. Notably, the complex formation of Fe^{3+} with **NID** led to the transformation of morphology of the FONPs from spherical to spindle. Fe^{3+} ion sensing by **NID** FONPs was also investigated inside mammalian cells through bioimaging. **NID** FONPs can detect Fe^{2+} to Fe^{3+} transition selectively inside the cancer cells (B16F10) in comparison to non-cancerous cell (NIH3T3) by exploiting higher content of H_2O_2 in cancer cells.

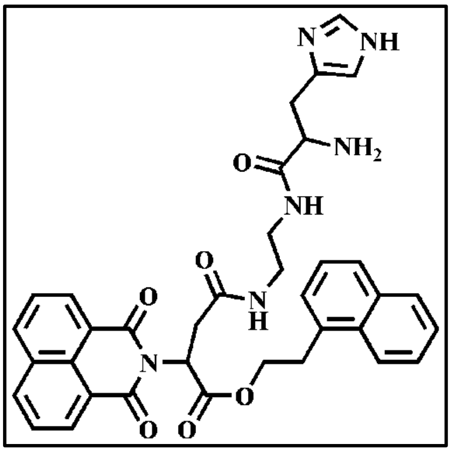

Figure 1. Structure of **NID** molecule.

3.2. RESULTS AND DISCUSSION

3.2.1. Molecular designing of NID

Aggregation-induced emission (AIE) is a direct result of restricted intramolecular rotation of luminogens as clusters/aggregates. Naphthalimide core is a widely known fluorophore unit considering its unique photophysical properties and high condensed-state emission behavior that is being explored extensively in various applications.[38] To date, naphthalimide derivatives have been reported with high quantum yields in solid or aggregated state in a large number contrary to aggregation caused quenching (ACQ).[39] *N*-functionalization of naphthalimide or inclusion of different organic moieties at fourth position of NI core is reported to influence AIE owing to the restricted intramolecular rotation (RIR) and loss in the planarity of molecule.[40-43] As the naphthalimide core is electron acceptor in nature, it can be functionalized with π-conjugated electron-donating units to have intramolecular charge transfer from donor ligands to electron deficient molecular scaffold, which may have a significant contribution towards achieving AIE property.[40] Considering these parameters, we have designed naphthalimide-based amino acid-linked amphiphilic molecule (**NID**, Figure 1) where the hydrophobic aromatic ring of the naphthalimide core may assist during self-aggregation. Chirality of the L-aspartic acid and histidine is expected to induce RIR in the self-aggregated state owing to their twisted nature in the molecular backbone.[15,19] Consequently, the molecule will be highly emissive as it is expected to relax through radiative pathways in the condensed state. To explore the AIE property of the luminogen in selective metal sensing, histidine was incorporated in the **NID** structure via amide linkage having imidazole 'N' and amino 'N' free to serve as a metal chelating moiety. Its co-ordination with a metal ion could cause an enhancement of the fluorescence emission, called chelation enhanced fluorescence effect (CHEF) or a quenching of the fluorescence, called chelation enhancement quenching effect (CHEQ).[44]

3.2.2. Microscopic investigations and DLS study of the self-assemblies of NID

The synthesized **NID** was soluble in DMSO. The transparent solution turned to translucent in presence of 60% and above water content (Figure 2). The formation of translucent solution presumably indicates the initiation of self-assembly by **NID** amphiphiles. With increase in the water proportion up to 99%, translucency of the **NID** solution got significantly enhanced probably owing to the development of self-aggregates. Several microscopic techniques were employed to examine the structures of the possible self-assembled units formed by **NID** derivative. TEM images of **NID** (10 μM, f_w = 99 vol%) showed spherical aggregates with diameter of 70-100 nm (Figure 3a). The formation of organic nanoparticles by **NID** (10 μM, f_w = 99 vol%) with spherical morphology having dimension of 90-120 nm was also confirmed from FESEM images (Figure 3b). The observed diameter of the spherical aggregates in the corresponding AFM image was also in a range of 70-120 nm (Figure 3c). Fluorescent microscopic images exhibited green emitting spherical nanoparticles (Figure 3d). Additionally, mean hydrodynamic diameter (D_h) of **NID** organic nanoparticles was found to be in the range of 50-250 nm with an average diameter of ~100 nm in dynamic light-scattering

(DLS) experiment for both number averaged and intensity averaged distribution (Figure 3e, Figure 4a). The correlogram with good Cumulant Fit for **NID** is provided in Figure 4b. All the microscopic evidences and the DLS data were mostly in concurrence with each other.

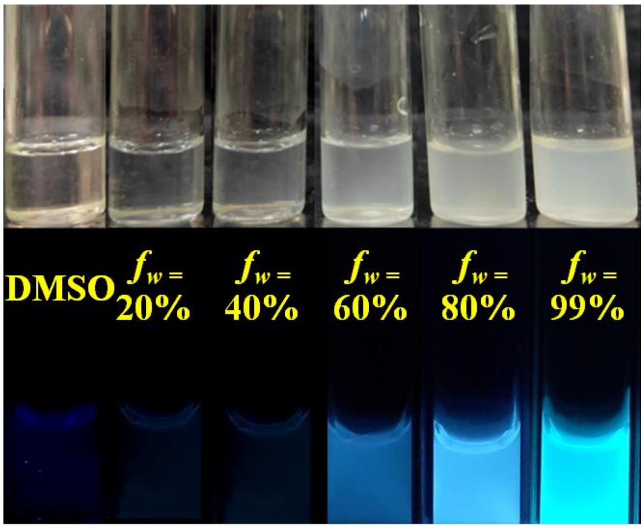

Figure 2. Photograph of formation of translucent solutions with increasing water content in DMSO for **NID** (50 μM) and corresponding change in emission colour of **NID** (50 μM) upon UV-light irradiation (λ_{ex} = 365 nm).

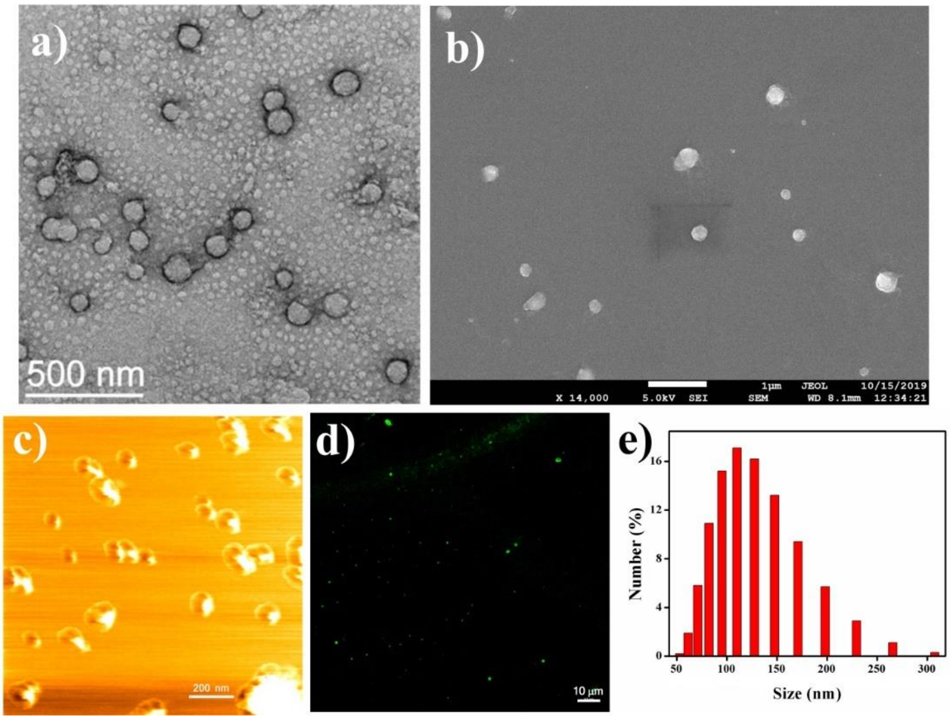

Figure 3. (a) Negatively stained TEM image, (b) FESEM image, (c) AFM image, (d) fluorescence microscopic image (e) DLS plot of particles size distribution of **NID** in (1:99, v/v) DMSO-water binary solvent mixture ([**NID**] = 10 μM).

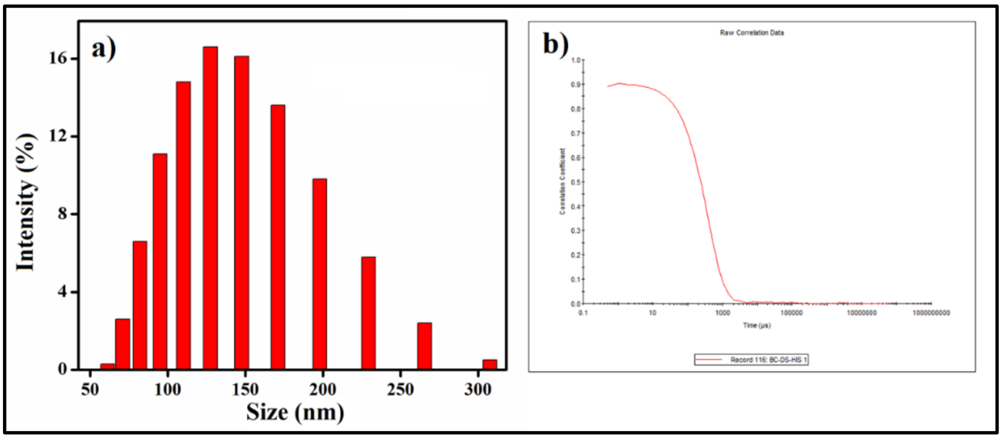

Figure 4. (a) DLS plot of particles size distribution (intensity averaged), (b) correlogram obtained by DLS of **NID** in (1:99, v/v) DMSO-water binary solvent mixture ([**NID**] = 10 µM).

3.2.3. Spectroscopic study for self-assembly of NID amphiphile

Self-aggregation of **NID** towards the formation of organic nanoparticles was initially examined by UV-visible spectroscopy in varying compositions of DMSO-water. In pure DMSO (molecularly dissolved state), **NID** (50 µM) showed a characteristic UV band in the range 330-360 nm having λ_{max} at 343 nm, which may be ascribed to the π-π^* transition of **NID** chromophore (Figure 5a).[45] With gradual increase in the water amount within DMSO, the absorption maxima slightly but steadily got red-shifted. At f_w = 99 vol%, the λ_{max} was observed at 347 nm (Figure 5a). This red shift of λ_{max} implied the generation of self-aggregates possibly via *J*-aggregation (head-to-tail fashion arrangement). The extinction coefficients of **NID** in DMSO, 20 vol%, 40 vol%, 60 vol%, 80 vol%, 99 vol% water in DMSO were 0.009, 0.0096, 0.01, 0.0104, 0.0114, 0.0122 μM^{-1} cm^{-1}, respectively.

Involvement of different non-covalent interactions during self-assembly (e.g. hydrophobic interaction and π-π stacking) was investigated by solvent-dependent ^{1}H-NMR study (Figure 5b). The aromatic protons of **NID** exhibited sharp NMR signal in the region δ = 8.36-8.55 ppm (aromatic core of **NID**) and δ = 6.74-8.09 ppm (naphthyl ring) in DMSO-d_6, in its non-assembled state (Figure 5b). With increasing the D_2O content gradually from 0% to 30% and 50%, NMR signals of both the **NID** aromatic core and the naphthyl group got broadened and shifted to δ = 7.86-8.29 ppm and δ = 6.24-7.81 ppm, respectively (Figure 5b). The π-π stacking between the chromophore and the naphthyl moieties of the molecules is facilitated with the addition of D_2O that eventually results in the upfield shift in the ^{1}H-NMR signals indicating the formation of self-aggregated structures.

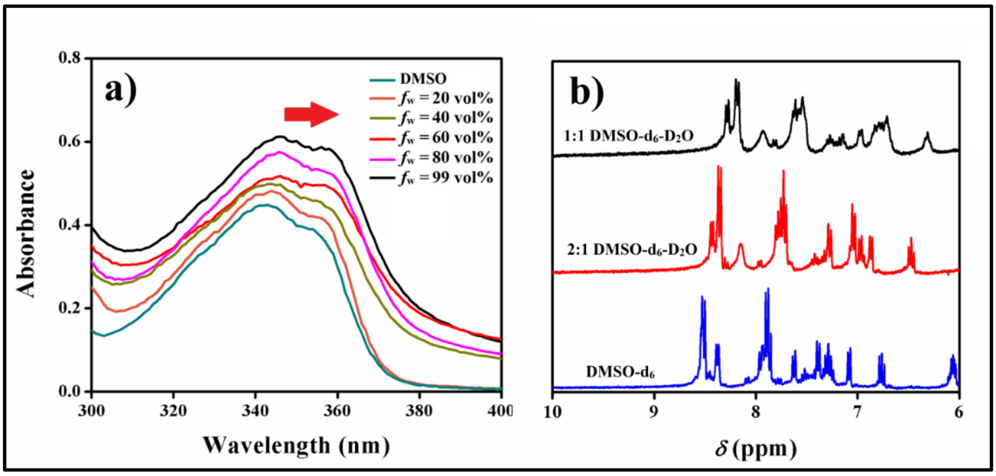

Figure 5. (a) UV-Visible spectra of **NID** (50 μM) in varying DMSO-water solvent mixtures; (b) solvent dependent ^{1}H-NMR spectra of **NID** (1 mM).

3.2.4. Investigation of the emissive nature of organic nanoparticles

Intrigued by the change in the UV-vis spectral nature of **NID** during self-aggregation, we investigated the emission behavior of **NID** in DMSO-water solvent mixtures. Emission spectrum of **NID** (10 μM) in DMSO showed almost negligible fluorescence intensity (Figure 6a). Moreover, no significant fluorescence intensity was observed with increasing water content upto 50% within the DMSO solution (f_w = 50 vol%). Interestingly, an excimer peak appeared having emission maxima at 470 nm at 60% water content (f_w = 60 vol%). Further addition of water resulted in stronger emission for self-aggregated **NID** having its highest intensity at f_w = 99 vol% (Figure 6a). This is in concurrence with the absorption spectroscopic behaviour of **NID** (Figure 5a). **NID** Amphiphiles started engaging in self-assembly apparently through the stacking of the chromophoric units with increase in water content. It resulted in excimer peak formation at 470 nm owing to AIE. The emission intensity of **NID** was many-fold higher at f_w= 99 vol%, than at pure DMSO (Figure 6a,b). Relative fluorescence quantum yield of **NID** at f_w= 99 vol% is calculated to be 8% (with respect to quinine sulfate hydrate). This AIE behavior was also examined by irradiating **NID** in different DMSO-water compositions (1 mL) under UV lamp having λ_{ex} = 365 nm (Figure 2,5b). DMSO solution of **NID** (50 mM) showed no significant fluorescence and from 60% water content a bluish green emission was witnessed, which became maximum at f_w= 99 vol%, due to AIE via the excimer formation (470 nm). Subsequently, concentration-dependent fluorescence spectra of **NID** at f_w= 99 vol% were recorded within a concentration range of 10-90 μM (Figure 6c). With increase in **NID** concentration, the luminescence intensity of the characteristic excimer band

(λ_{em} at 470 nm) consistently enhanced and became saturated at and above 70 µM (Figure 6c). This observation delineates that with increase in the concentration of **NID**, enhancement in the AIE was noted possibly due to the self-aggregation of a greater number of amphiphilic molecules which became saturated beyond a specific concentration.

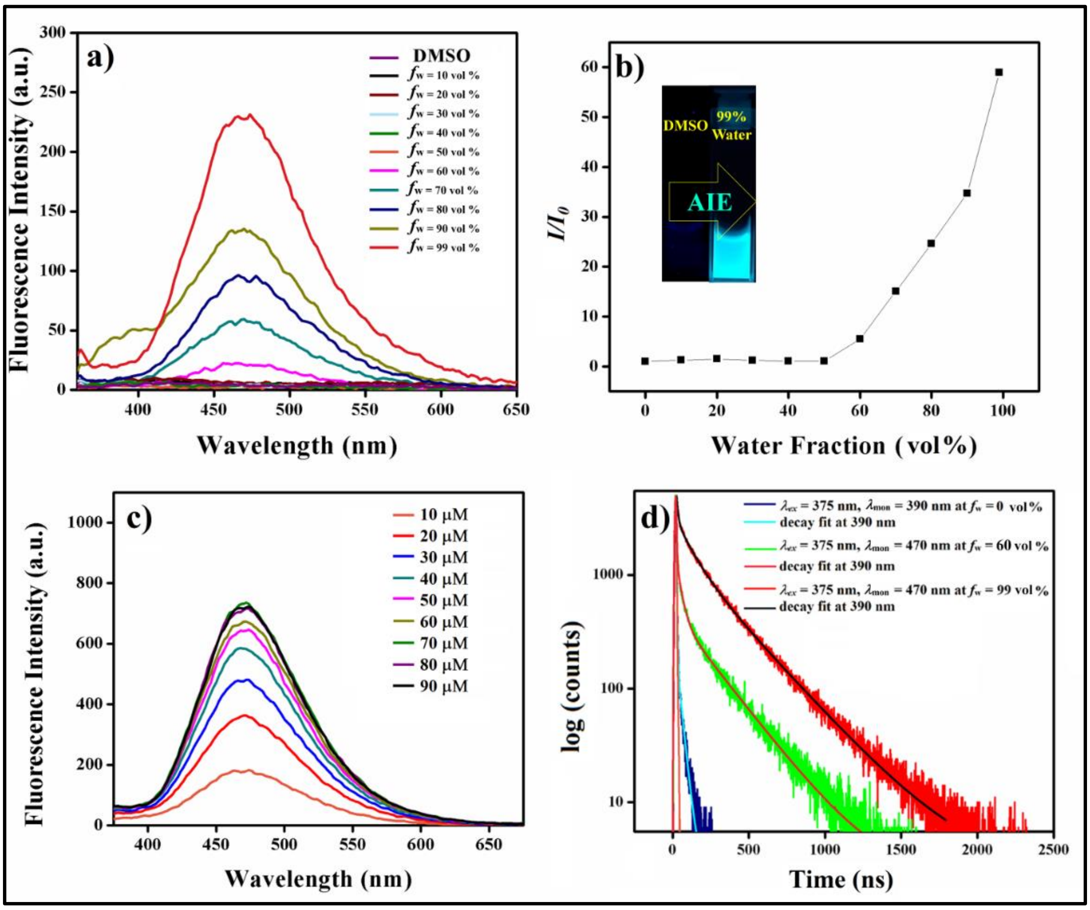

Figure 6. (a) Fluorescence spectra (λ_{ex} = 350nm) of **NID** (10 µM) in DMSO-water solvent mixture. (b) Plot of relative emission intensity (I/I_o) vs the fraction of water in DMSO of **NID** where, I_o = Emission intensity in pure DMSO solution, (c) concentration dependent emission spectra of **NID** at 99% water content in DMSO, (d) TCSPC decay profiles of **NID** (20 µM) monitored at 390 nm (pure DMSO) and 470 nm in (2:3 v/v), (1:99, v/v) DMSO-water mixture upon excitation at 375 nm.

For better understanding of the AIE phenomenon in **NID**, TCSPC study was carried out with picosecond excitation at 375 nm for **NID** (20 µM) in pure DMSO, 60% and 99% water content in DMSO (Figure 6d). In all cases, triexponentially fitted decay curves were attained. For DMSO solution of **NID**, the emission was monitored at λ_{mon} = 390 nm and the average lifetime value ($\langle\tau\rangle$) was 0.0456 ns (Table 1). The $\langle\tau\rangle$ value monitored at λ_{mon} = 470 nm for f_w = 60 vol % and 99 vol% in DMSO, was found to be 4.04 ns and 6.87 ns, respectively (Table 1).

Pre-associated excimer in the AIE resulted in the long decay lifetime at higher percentage of water.

Table 1. Lifetime values of **NID** in presence of different fractions of water in DMSO (λ_{ex} = 375 nm)

[**NID**] (μM)	Fraction of water (f_w) (vol%)	λ_{mon}(nm)	τ_1 (ns) (a_1)	τ_2 (ns) (a_2)	τ_3 (ns) (a_3)	Average lifetime (τ) (ns)
20	0	390	0.04(1.000)	2.95(0.0003)	0.00(0.000)	0.0456
20	60	470	3.00(0.023)	22.60(0.008)	0.15(0.969)	4.04
20	99	470	9.25(0.178)	27.10(0.175)	0.77(0.648)	6.87

Furthermore, we also analyzed the influence of intramolecular charge transfer process (ICT) on the AIE phenomenon by checking the UV-vis and emission spectra of **NID** (50 μM) in varying organic solvents having distinct polarities (Figure 7a-c). Alteration in the solvent from non-polar xylene to polar diethyl ether did not show any considerable changes in the absorbance maxima (Table 2 and Figure 7a). The molar extinction coefficients of **NID** in diethyl ether, toluene, anisole, *m*-xylene and *o*-xylene were 0.0132, 0.013, 0.011, 0.0056, 0.0034 μM^{-1} cm^{-1}, respectively. Nevertheless, the λ_{em} significantly red-shifted with gradual enhancement in polarity of solvent (Table 2 and Figure 7b). The Stokes shift ($\Delta\nu$) of **NID** in different solvents was determined and the solvatochromic property was also quantitatively expressed by the Lippert-Mataga equation.[46-47]

$$\Delta\nu = \nu_a - \nu_e = \frac{2\Delta f}{hca^3}(\mu_E - \mu_G)^2 + constant \qquad (1)$$

where ν_a = maximum absorbance wavenumber, ν_e = maximum emission wavenumber, h = Planck's constant, c = speed of light, a = Onsager solvent cavity, μ_E = excited-state dipole moment and μ_G = ground-state dipole moment. The solvent polarity parameter (orientational polarizability) Δf, represented in eq, is the measure of solvent polarity.

$$\Delta f = \frac{\varepsilon-1}{2\varepsilon+1} - \frac{n^2-1}{2n^2+1} \qquad (2)$$

where ε = static dielectric constant and n = optical refractive index of the solvent. For **NID.** linearity between $\Delta\nu$ vs Δf with positive solvatochroism was observed, which represented ICT from the naphthyl unit (donor part) to the **NID** core (acceptor part) (Figure 7c, Scheme 1).

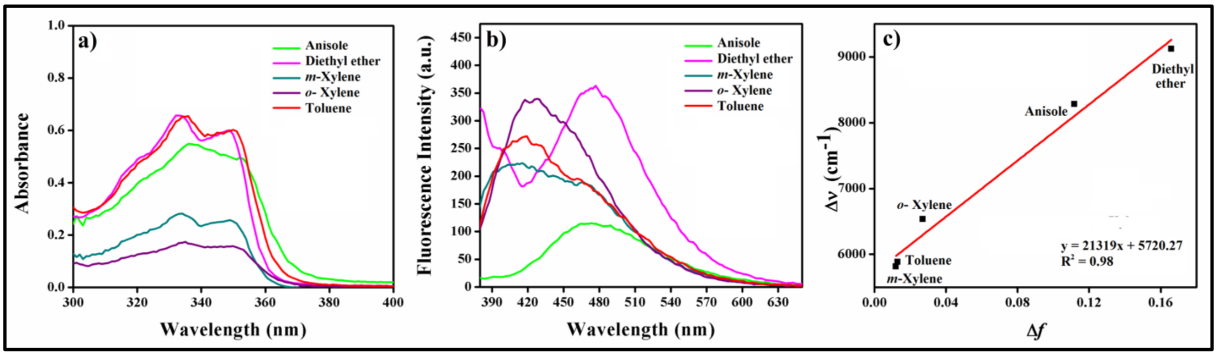

Figure 7. (a) Absorption and (b) emission spectra of **NID** (50 μM) in different solvents. (c) Plot of Stokes shift ($\Delta\nu$) of **NID** vs solvent polarity parameter (Δf).

Table 2. Photophysical property of **NID**[a]

Solvent	Δf	λ_{ab} (nm)	λ_{em} (nm)	$\Delta\nu$ (cm^{-1})
m-Xylene	0.012	333.24	413.30	5813
Toluene	0.013	335.28	417.65	5882
o-Xylene	0.027	334.48	428.03	6534
Anisole	0.1118	336.30	466.10	8281
Diethyl ether	0.166	332.45	477.16	9122

[a] Abbreviation: Δf = solvent polarity parameters, λ_{ab} = absorption maximum, λ_{em} = emission maximum, $\Delta\nu$ = Stokes shift. Excitation wavelength (λ_{ex} = 350 nm); [NID] = 50 μM

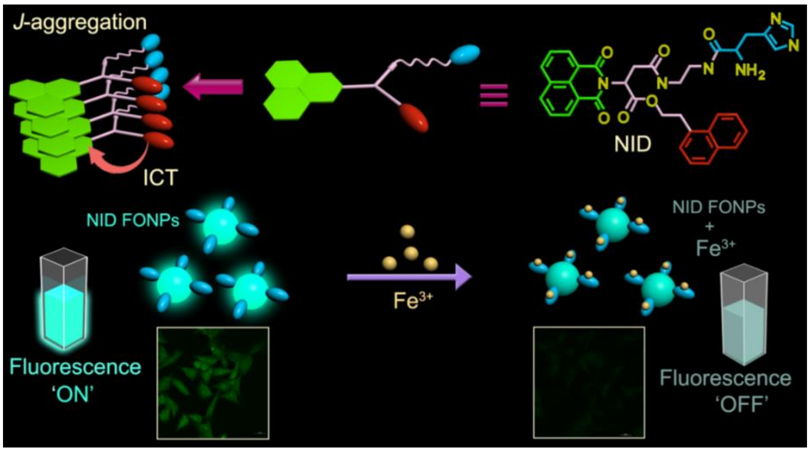

Scheme 1. Schematic representation of **NID** based fluorescent organic nanoparticle in selective sensing of Fe^{3+} and as diagnostic probe for Fe^{2+}/Fe^{3+} Transition. ICT: intramolecular charge transfer.

We also performed time dependent UV-vis spectroscopic study as well as photoluminescence study to know the stability of **NID** FONPs. The relative absorbance (A/A_0) and relative fluorescence intensity (I/I_0) of **NID** FONPs were recorded with time (Figure 8a,b). Here A_0 and A were original absorbance and absorbance on different days, respectively. Similarly, I_0 and I represent original fluorescence intensity and fluorescence intensity on different days. No significant change in the relative absorbance and fluorescence intensities was noted for 7 days. Also no precipitation was observed in the translucent **NID** solutions for 7 days (Figure 8c). Hence, these FONPs were stable for a considerable time period.

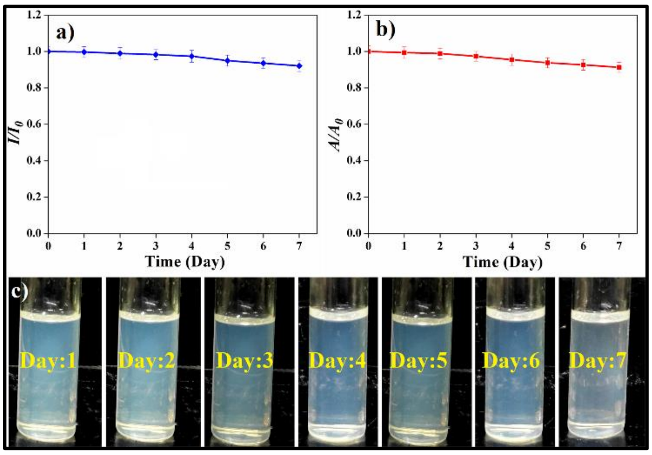

Figure 8. Ratio of (a) absorbance value, (b) fluorescence intensity over time for **NID** FONP at f_w = 99 vol% in DMSO. (c) photographs of **NID** FONP solution for 7 days.

3.2.5. Fluorimetric sensing of Fe^{3+}

After ensuring the formation of **NID** FONPs, we intended to explore the emissive behavior of the FONPs in Fe^{3+} sensing owing to the presence of histidine in the amphiphile backbone. Histidine is well known chelating agent for Fe^{3+}.[48] Among all the transition metals, iron plays vital roles in oxygen uptake, electron transfer, cellular metabolism, enzyme catalysis, and many other biochemical processes. Therefore, we aim to utilize **NID** FONPs towards selective detection of Fe^{3+}. Consequently, the fluorescence spectra of **NID** FONPs (50 μM) was recorded in DMSO-water, f_w= 99 vol% (1 mL) upon titration with Fe^{3+} (aqueous solution of $FeCl_3$) (Figure 9a). The emission intensity of **NID** FONPs at λ_{ex} = 470 nm was found to be decreased gradually along with the increase in concentration of Fe^{3+} from 10 μM onwards. The quenching effect by Fe^{3+} steadily increased up to 560 μM and thereafter no significant changes in quenching effect was noted (experimentally investigated up to 650 μM). This quenching by Fe^{3+} on the emission of **NID** FONPs was noted possibly due to the complex formation between Fe^{3+} and the histidine residue of the **NID** amphiphile (Scheme 1). In a wide variety of metal complexes, the formally forbidden intersystem crossing (ISC) becomes faster due to the presence of a paramagnetic metal ion in the proximity of the fluorophore. In the present study, the observed quenching of fluorescence by Fe^{3+} ions may be ascribed due to the cooperative influence of size compatibility as well as the paramagnetic nature of Fe^{3+} which result in chelation-enhanced quenching (CHEQ).[44] The coordination between Fe^{3+} and histidine took place among one of the N atoms from imidazole ring and another N atom from the free amine.[48] The quenching of **NID** FONPs by Fe^{3+} was analyzed quantitatively by using Stern-Volmer equation,

$$F/F_o = 1 + K_{SV}[Q] \qquad (3)$$

In this equation, F and F_o are the fluorescence intensities of **NID** FONP in the presence/absence of Fe^{3+} respectively; K_{SV} is the Stern-Volmer constant; and [Q] is quencher concentration. The change in F/F_o of **NID** FONP with Fe^{3+} up to 70 μM is observed and the Stern-Volmer plot showed linearity in fluorescence quenching of **NID** by Fe^{3+} with K_{SV} of 0.0035 μM^{-1} (Figure 9b).

As the **NID** FONP displayed a sensitive turn off response to Fe^{3+}, thereby we measured the detection limits of Fe^{3+}. The emission intensity of **NID** FONPs at 470 nm decreased in proportion to the concentration of Fe^{3+} ranging from 10 to 560 μM (Figure 9a). The sensitivity was measured based on the relationships between the ratio of fluorescence emission intensity at 470 nm in presence and absence of Fe^{3+}. A good linear behavior was obtained between (F_o

– F)/F_0 and Fe^{3+} in the lower concentration range (upto 70 μM) where F_0 and F were emission intensities of **NID** FONPs at 470 nm in the absence and presence of Fe^{3+}, respectively (Figure 9c). The linear regression equation was F_0 - F/F_0 = -8.78645 + 0.00351x concentration of Fe^{3+} (μM); correlation coefficient (R^2) of 0.99114. The limit of detection (LOD) of Fe^{3+} was found to be 12.5±1.2 μM as calculated based on 3σ/S where σ was the standard deviation and S was the slope of the calibration curve (experiment was repeated thrice).

To determine the binding ratio between luminescent **NID** and Fe^{3+}, the stoichiometric ratio of **NID** and Fe^{3+} was calculated through Job's plot (Figure 9d and Figure 10).[38] The stoichiometric ratio of **NID** and Fe^{3+} was established by plotting the mole fraction (x) of **NID** and the product of emission intensity change (F_0 - F, where F_0 and F were emission intensities of **NID** FONPs at 470 nm in the absence and presence of Fe^{3+}, respectively) and the mole fraction (x) of **NID.** Fluorescent intensities of 1 mL solutions of **NID** + Fe^{3+} in different ratios, each having total concentration of 80 μM were measured. The product of F_0 - F and mole fraction (x) of **NID** went through maxima at x = 0.501 as shown in Figure 9d, indicating the formation of 1:1 stoichiometric complexes between **NID** and Fe^{3+} that led to the quenching of the emission intensity of **NID** FONPs.

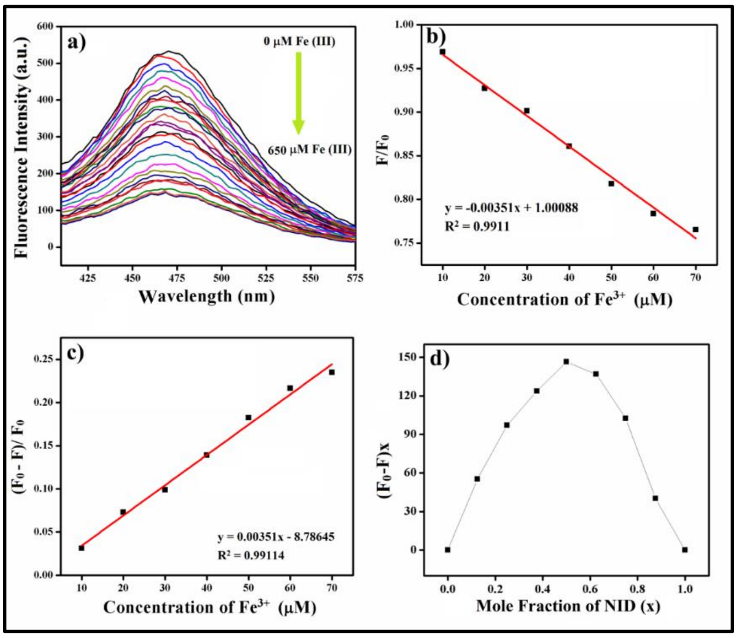

Figure 9. (a) Fluorescence spectra of **NID** FONPs (50 μM) in absence and presence of varying concentration of Fe^{3+} (excitation wavelength = 350 nm), (b) Stern-Volmer plot of Fe^{3+} doped in (1:99, v/v) DMSO-water solution of **NID** (50 μM), (c) Fluorescence response of **NID** FONPs towards Fe^{3+} sensing with varying concentration of Fe^{3+} in (1:99, v/v) DMSO-water ([**NID**] = 50 μM), (d) Job's plot for stoichiometry of metal complex.

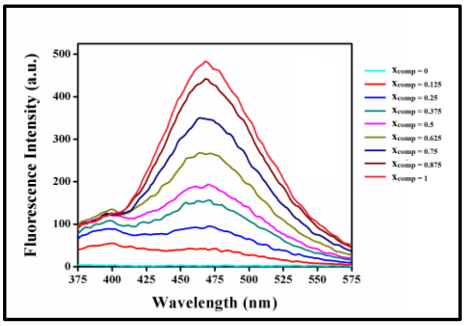

Figure 10. Emission spectra of different mole fraction of **NID** / Fe^{3+} in 1:99 (v/v) DMSO-water. X_{comp} = Mole fraction of **NID**.

After confirming the Fe^{3+} sensing by **NID** FONP, we were curious to investigate the selectivity of **NID** against the other metal ions. This is a very essential parameter to estimate the performance of a new fluorescence sensor. To this end, 1 mL of **NID** FONP solution (50 μM) was treated with different metal ions. Emission spectra of **NID** were recorded in the presence of different monovalent (Na^+, K^+), divalent (Co^{2+}, Zn^{2+}, Fe^{2+}, Pb^{2+}, Ni^{2+}, Mn^{2+}), trivalent (Cr^{3+}, V^{3+}) metal ions and Fe^{3+}, having concentration of 500 μM for each metal ions. Interestingly, none of these metal ions could quench the fluorescence of **NID** FONP significantly except Fe^{3+} (Figure 11). This experiment was repeated thrice and the error bar reflects the standard deviation. The effect of the different metal ions on the emission of the **NID** FONPs was also examined by irradiating the samples (**NID** + metal ion solution in 99% water in DMSO) under UV lamp (λ_{ex} = 365 nm) (Figure 12). The bluish green emission of **NID** FONPs remain unchanged for all the used metal ions except Fe^{3+} containing solution. In presence of Fe^{3+}, the emission intensity got drastically quenched indicating further the selective sensing of Fe^{3+} by **NID** FONPs.

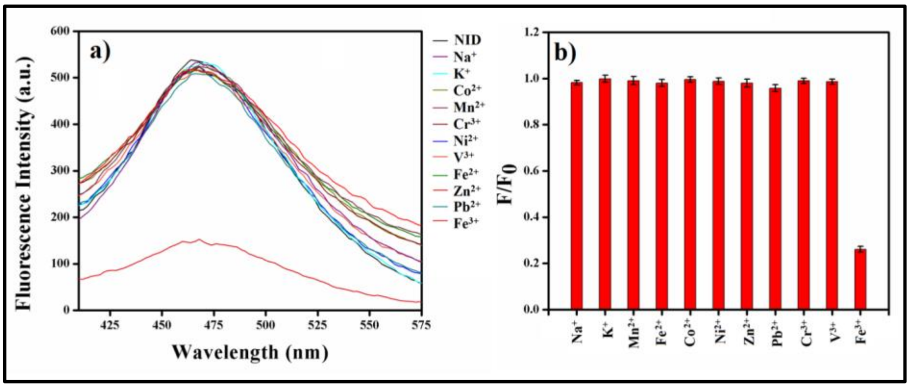

Figure 11. Selectivity of **NID** FONPs ([**NID**] = 50 μM) to Fe^{3+} over other metal ions [metal] = 500 μM in (1:99, v/v) DMSO-water solution. a) Fluorescence intensity plot b) relative

intensity of **NID** FONPs in presence of different metal ions. The error bars represent the standard deviations.

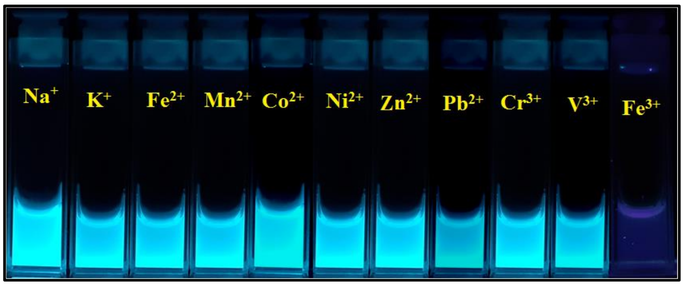

Figure 12. Photograph of selectivity of **NID** FONPs ([**NID**] = 50 μM) to Fe^{3+} over other metal ions (500 μM) in (1:99, v/v) DMSO-water solution upon UV-light irradiation (λ_{ex} = 365 nm).

All these preceding experiments were carried out using Milli-Q water. To investigate whether the complexation of Fe^{3+} with **NID** has any influence on the pH of the medium and subsequently the AIE properties of **NID** FONPs, we carried out Fe^{3+} detection in aqueous phosphate buffer solution (pH = 7.4, 10 mM). **NID** FONPs and Fe^{3+} stock solutions were prepared in phosphate buffer medium. With the gradual increase in Fe^{3+} concentration, the fluorescence intensity quenched gradually up to 560 μM in concurrence with the preceding observation (Figure 13a). No further quenching was observed up to 650 μM of Fe^{3+}. This quenching was similarly analyzed quantitatively by using the Stern-Volmer equation (7). The Stern-Volmer plot of change in F/F_0 of **NID** FONPs with Fe^{3+}, showed linearity in the fluorescence quenching of **NID** by Fe^{3+} up to 55 μM with K_{SV} of 0.0037 μM^{-1}, which was 0.0035 μM^{-1} in the case of Milli-Q water. We also carried out the selectivity experiments taking other monovalent, divalent, and trivalent metal ions in aqueous buffer medium (pH = 7.4, 10 mM). Here also, the **NID** FONPs showed similar selectivity towards Fe^{3+} (Figure 13c,d) against the other tested metal ions.

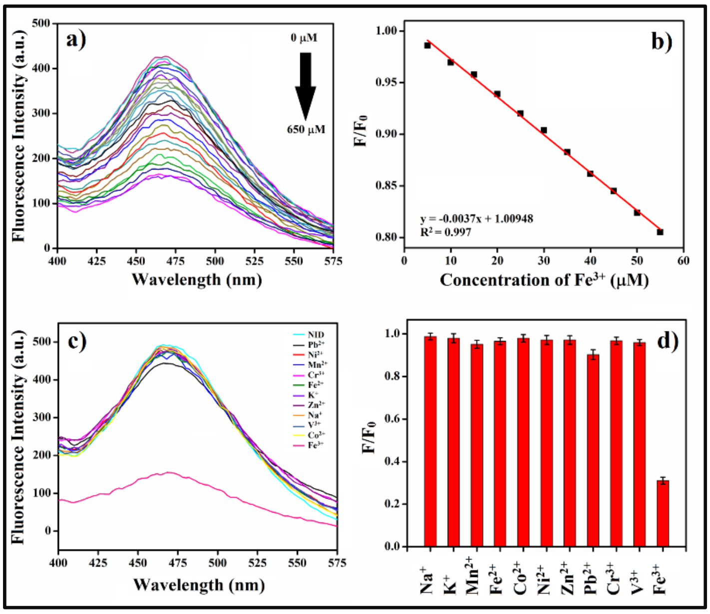

Figure 13. (a) Fluorescence spectra of **NID** FONPs (50 μM) in absence and presence of varying concentration of Fe^{3+} (excitation wavelength = 350 nm), (b) Stern-Volmer plot of Fe^{3+} doped in (1:99, v/v) DMSO-aqueous phosphate buffer (10 mM, pH = 7.4) solution of **NID** (50 μM), Selectivity of **NID** FONPs ([**NID**] = 50 μM) to Fe^{3+} over other metal ions [metal] = 500 μM in (1:99, v/v) DMSO-aqueous phosphate buffer (10 mM, pH = 7.4) solution. (c) Fluorescence intensity plot (d) relative intensity of **NID** FONPs in presence of different metal ions. The error bars represent the standard deviations.

Next, we wanted to investigate the chelation between **NID** FONPs and Fe^{3+} with respect to other Fe^{3+} binding agents. To this end, we recorded the photoluminescence spectra of Fe^{3+} (500 μM) containing solution of **NID** FONPs (50 μM) at f_w = 99 vol% water in DMSO treated with several Fe^{3+} chelating agents like 2-aminopyridine, citric acid, L-Dopa, EDTA, folic acid and glycine having concentrations of 500 μM and 1000 μM, respectively. As mentioned earlier, the fluorescence of **NID** FONPs (50 μM) is quenched in the presence of Fe^{3+} (500 μM) (Figure 9a). However, no significant increase or recovery in the fluorescence intensity took place in the presence of 2-aminopyridine, citric acid, L-Dopa, EDTA, folic acid and glycine (Figure 14). Hence, it may be inferred that the co-ordination between **NID** FONPs and Fe^{3+} is quite strong. We again carried out the experiment with the same concentration of **NID** FONPs (50 μM) and Fe^{3+} (50 μM) with twice the concentration of EDTA (100 μM) both in aqueous and phosphate buffer (pH = 7.4, 10 mM) media (Figure 15). The concentration was kept equivalent to eliminate the fluorescence suppressing phenomena. No regaining of fluorescence took place in the presence of EDTA to the **NID** FONP solution treated with Fe^{3+}. This further confirmed the strong binding nature of **NID** FONPs to Fe^{3+}.

As mentioned before, oxidative stress is an important parameter for a living cell. The oxidative stress can be varied owing to the uncontrolled production of ROS through Fe^{2+}/Fe^{3+} transition in presence of hydrogen peroxide.[32-33] In view of the unique reactivity of iron at different redox states, it would be highly important to detect Fe^{2+}/Fe^{3+} transition. Initially, we investigated this Fe^{2+}/Fe^{3+} transition in a cuvette using **NID** FONP in presence of H_2O_2 (as an oxidizing agent). In a cuvette containing 50 μM of **NID** FONP at f_w= 99 vol% (1 mL), requisite volume of Fe^{2+} ($FeCl_2$) solution was added so that resultant Fe^{2+} concentration became 500 μM. The **NID** FONP solution was irradiated under UV lamp at λ_{ex} = 365 nm before and after addition of Fe^{2+} and no change in the bluish green emission was noted (Figure 16). Interestingly, the addition of equivalent amount of H_2O_2 (500 μM) resulted in the complete quenching of the emission (Figure 16) possibly by Fe^{3+} that formed through oxidation of Fe^{2+} in presence of H_2O_2. Notably, addition of H_2O_2 (500 μM) to the only **NID** FONPs solution (in absence of Fe^{2+}) did not exhibit any marked change in its emission.

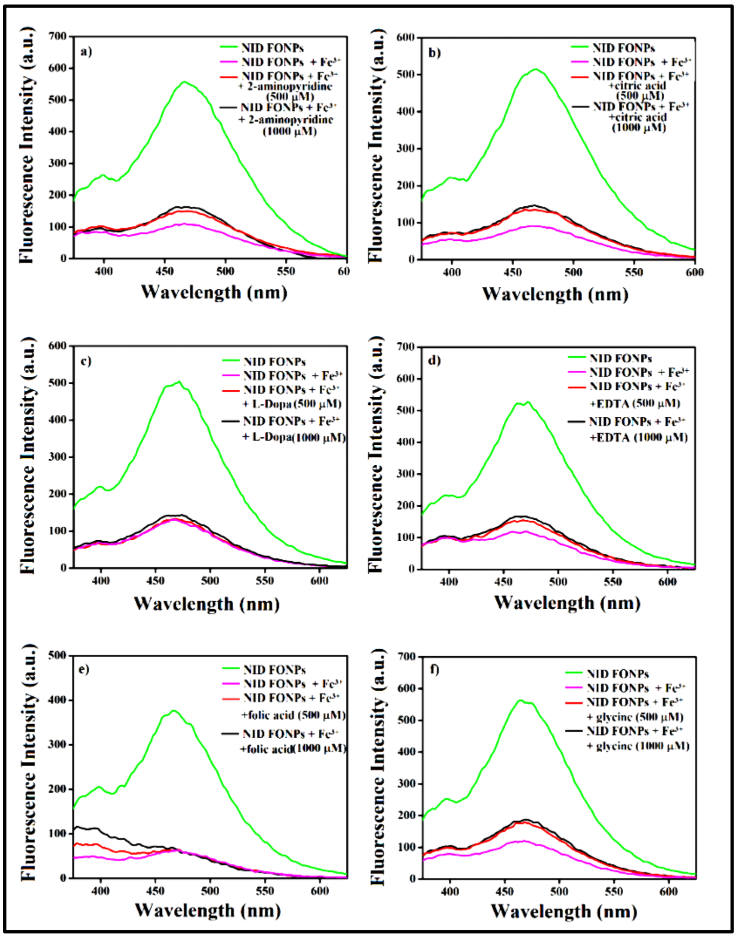

Figure 14. Emission spectra of of **NID** FONPs (50 μM) and mixture of **NID** FONPs (50 μM) + Fe^{3+} (500 μM) in absence and presence of 500 & 1000 μM of (a) 2-aminopyridine, (b) citric acid, (c) L-Dopa, (d) EDTA, (e) folic acid and (f) glycine.

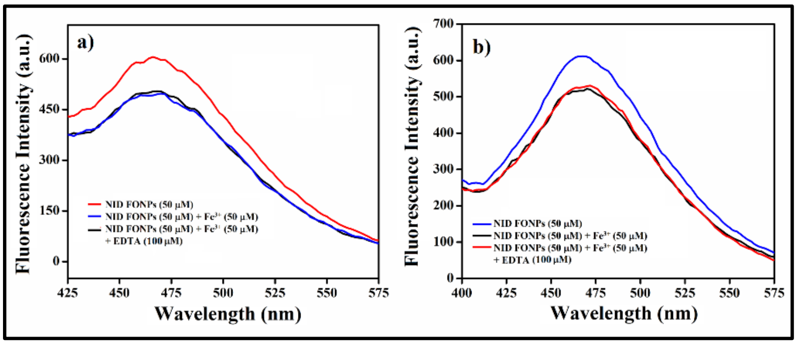

Figure 15. Emission spectra of **NID** FONPs (50 µM) and mixture of **NID** FONPs (50 µM) $+Fe^{3+}$ (50 µM) in absence and presence of 100 µM EDTA in (a) Milli-Q water and (b) aqueous phosphate buffer (pH = 7.4, 10 mM).

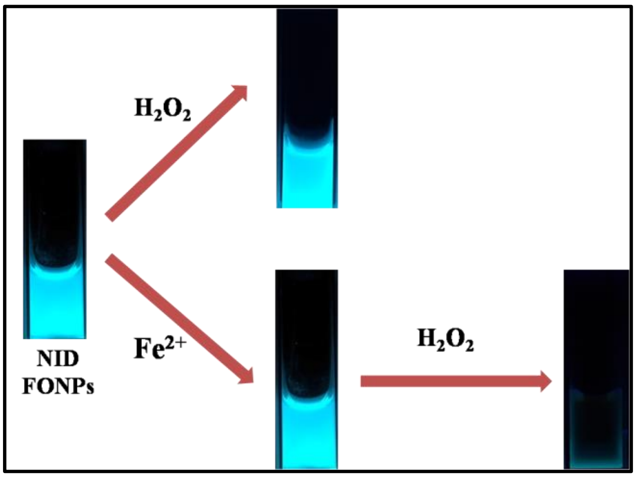

Figure 16. Photographs **NID** FONPs ([**NID**] = 50 µM), **NID** FONPs + Fe^{2+} ([**NID**] = 50 µM, [Fe^{2+}] = 500 µM), **NID** FONPs + H_2O_2 ([**NID**] = 50 µM and [H_2O_2]= 500 µM) and **NID** FONPs + Fe^{2+} + H_2O_2 ([**NID**] = 50 µM, [Fe^{2+}] = 500 µM and [H_2O_2] = 500 µM) in (1:99, v/v) DMSO-water solution upon UV-light irradiation (λ_{ex} = 365 nm).

3.2.6. Influence of Fe^{3+} on the morphology of self-aggregated NID FONPs

Selective and sensitive detection of Fe^{3+} by **NID** FONPs made us curious to investigate whether coordination of Fe^{3+} with histidine moiety of **NID** has any influence on the morphology of self-aggregates. FESEM images taken for 10 µM solution of **NID** $+Fe^{3+}$ (mixed in equimolar proportion) at f_w= 99 vol% showed spindle shaped morphologies having length of ~ 200 nm and width of 60-70 nm (Figure 17a). Similar morphologies were observed in the AFM images where the aggregates had length in the range of 200-250 nm and width of 60-80 nm (Figure

17b). It is evident that chelation of **NID** with Fe^{3+} led to the morphological transformation from spherical to spindle in the structure of self-aggregates.

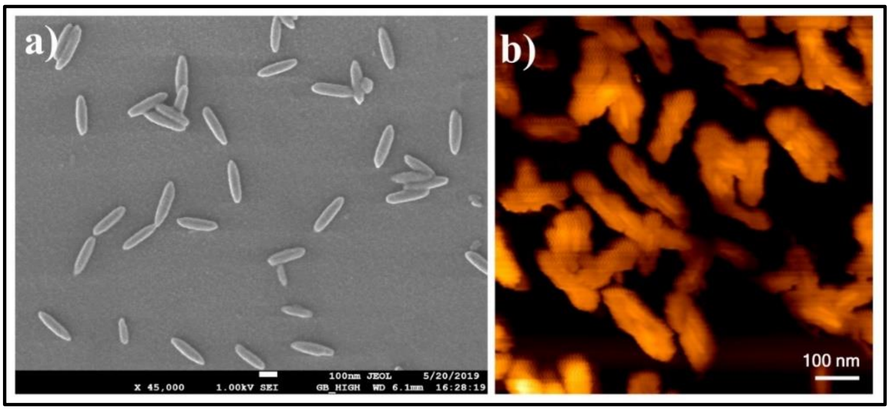

Figure 17. (a) FESEM image, (b) AFM image of **NID** (10 μM) + Fe^{3+} (10 μM) in (1:99, v/v) DMSO-water binary solvent mixture.

3.2.7. Circular dichroism (CD) study

The effect of chiral amino acid moieties in the self-assembly of **NID** was investigated by CD spectroscopy. In pure DMSO (molecularly dissolved state) **NID** showed chirality without any characteristic CD signal (Figure 18a). Upon gradual increase in the water content, a change in the CD spectral pattern with the possible emergence of chiral bias was noted. At the highest percentage of water (f_w = 99%) in DMSO, the CD spectra with a positive band at 240 nm and a negative band at 248 nm was observed (Figure 18a) which resembles the possible β-sheet type (not by the position of the peaks) arrangement of the self-aggregates. This manifestation of chiral bias possibly resulted from the supramolecular organization of the amino acid containing chiral building block, **NID**. The positive band observed in the CD could be attributed to the π–π* transition of the amide bond and negative band at longer wavelength to n-π* transition of the same. With introduction of Fe^{3+} (5 mM), this characteristic peak disappeared (Figure 18b) as a result of the alteration in the supramolecular arrangement of the self-aggregates that led to the change in morphology of the self-aggregates (Figure 17).

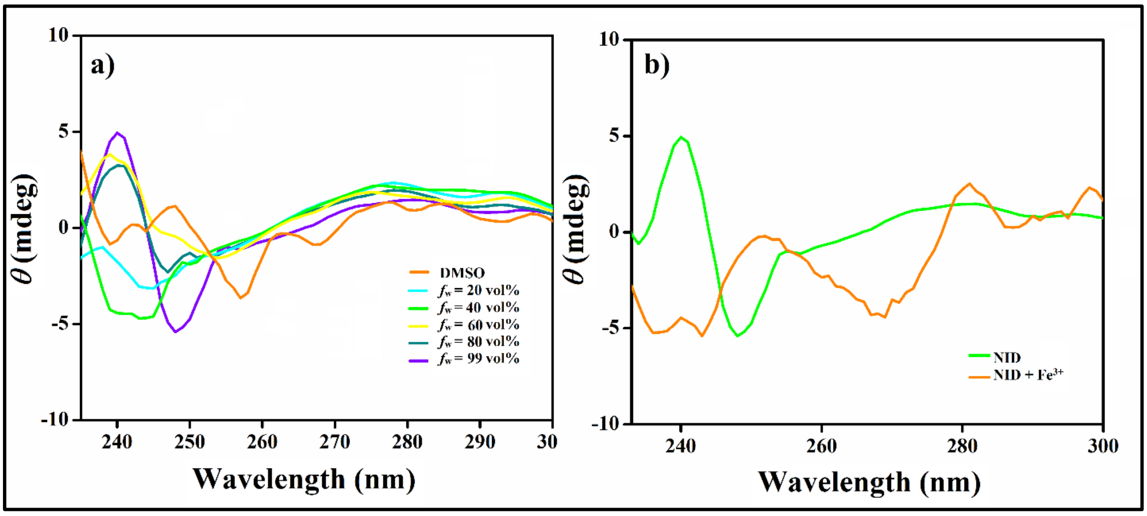

Figure 18. CD spectra of (a) **NID** (500 µM) in different ratios of DMSO-water, (b) **NID** (500 µM) at f_w = 99% in DMSO in presence of Fe^{3+} (5 mM).

3.2.8. Cytocompatibility of NID derivative-based FONPs

The cytocompatibility of **NID** FONPs against mammalian cells is crucial for exploring the AIE-gens in bioimaging and Fe^{3+} sensing within cellular environment. The cytocompatibility of **NID** FONPs (10-50µM) prepared at f_w = 99 vol% was examined by MTT assay in non-cancer (NIH3T3) and cancer (B16F10) cells. In each case, after 12 h and 24 h incubation ~85-90% and ~82-90% eukaryotic cells (normal and cancer cells) were found to be alive (Figure 19). Therefore, these **NID** FONPs were found to be adequately biocompatible and suitable for cellular imaging.

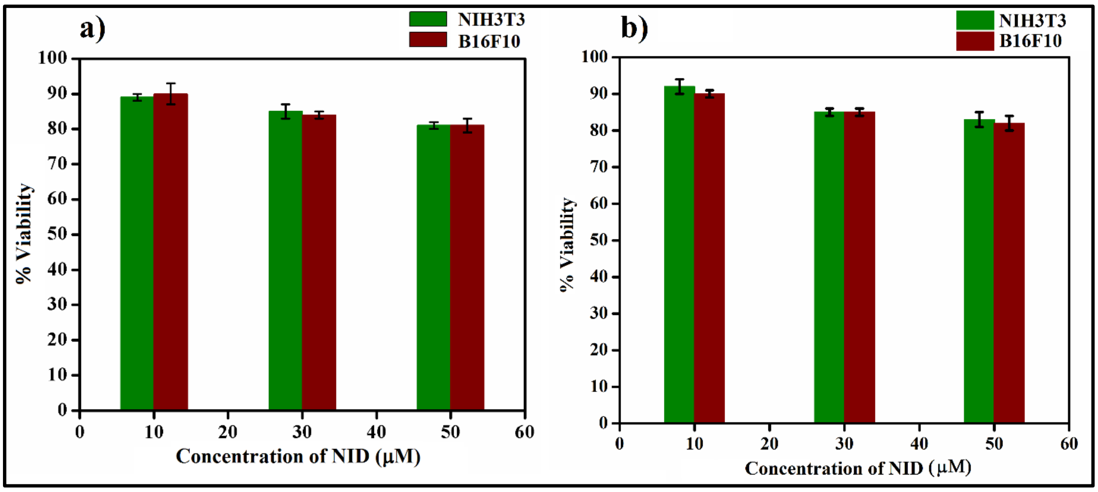

Figure 19. MTT-based % cell viability of NIH3T3 (non-cancer cells) and B16F10 (cancer cells) in presence of varying concentration of FONPs derived from **NID** in 1:99 v/v, DMSO-water over the incubation period of (a)12 h, (b) 24 h. Percent errors are within ± 5% in triplicate experiments.

3.2.9. Bioimaging

NID-derived biocompatible FONPs were utilized in bioimaging of the mammalian cells. Both non-cancerous (NIH3T3) and cancerous (B16F10) cells were incubated with 25 µM of **NID** FONPs (f_w= 99 vol%) for 6 h. Fluorescence microscopic images showed green fluorescence inside both the cells indicating significant internalization of the **NID** FONPs within the cells and mean fluorescence intensity was found to be 1067 for NIH3T3 and 1035 for B16F10 (Figure 20a-c, 21a-c). This cell-staining ability of the FONPs in the visible range has potential utility in diagnostics as bio-probes. Fluorescence microscopic images were further taken to investigate the ability of **NID** FONPs towards sensing Fe^{3+} as well as monitoring Fe^{2+}/Fe^{3+} transition inside cells. Incubation of exogenous Fe^{3+} (250 µM) along with **NID** FONP with NIH3T3 and B16F10 cells exhibited substantially quenched fluorescence inside both the cells having mean fluorescence intensity of 133 and of 204, respectively (Figure 20d-f, 21d-f, Scheme 1). Moreover, as discussed above, Fe^{2+} ions are highly relevant in case of oxidative stress where through Fenton reaction Fe^{2+} ion reacts with hydrogen peroxide to generate highly reactive oxygen species and got oxidized to Fe^{3+} state. In this context, cancer cells are known to possess more H_2O_2 compared to normal alive cells.[49-51] Considering this fact, we incubated the mentioned mammalian cells with Fe^{2+} (250 µM) and **NID** FONP for 6 h. In case of non-cancerous NIH3T3 cells, no significant quenching in the green emission of **NID** FONP was observed. The mean fluorescence intensity was found to be 1010 (Figure 20g-i), which is comparable to that of native **NID** FONPs. Notably, in B16F10 cancer cells, green fluorescence of **NID** FONP within the cells got significantly quenched with a low mean fluorescence intensity of 342. This was possibly due to the oxidation of included Fe^{2+} to Fe^{3+} by H_2O_2 inside cancer cells (Figure 21g-i), which could not take place in the non-cancerous one owing to the less H_2O_2 content.

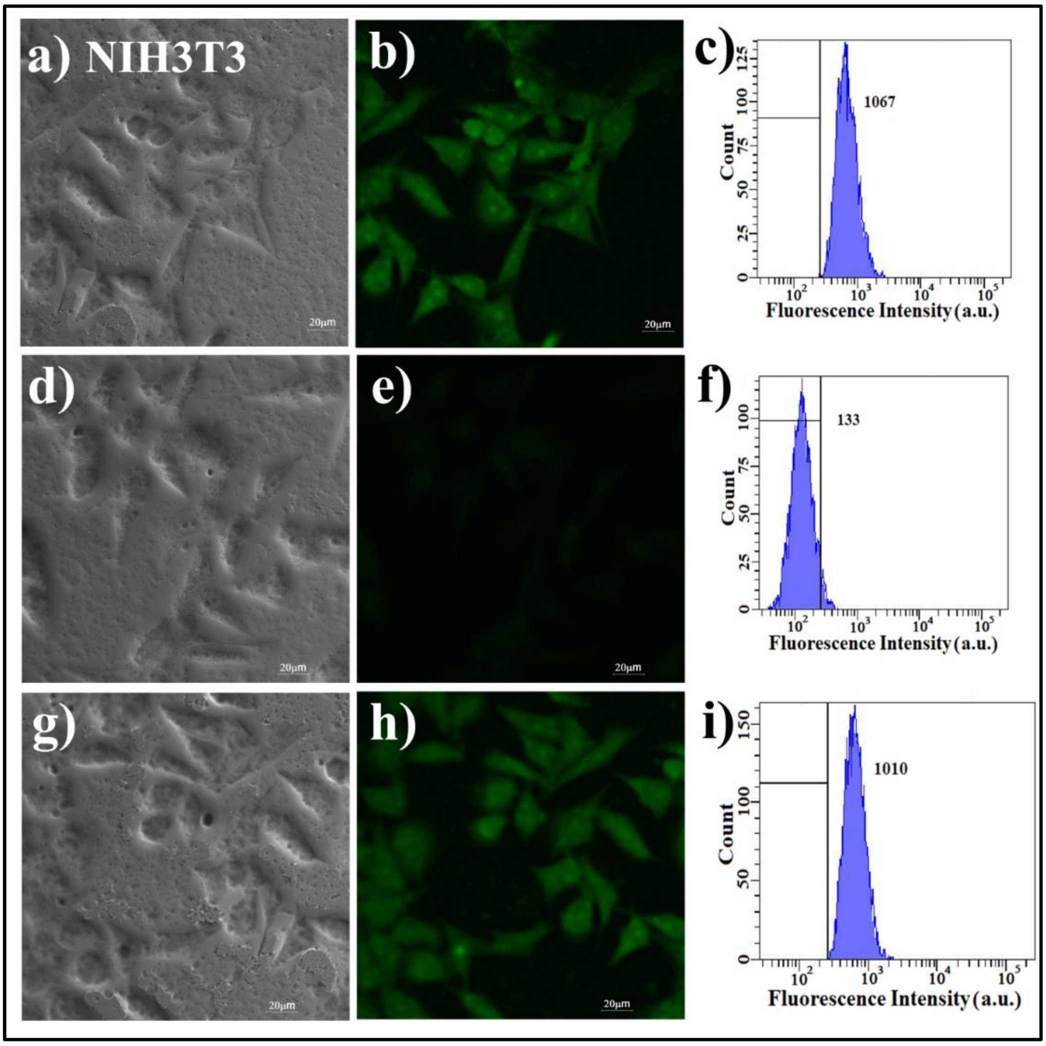

Figure 20. Bright-field, fluorescence microscopic images and corresponding flow cytometric plots of NIH3T3 cells after 6 h incubation with (a, b, c) **NID** FONPs (25 μM), (d, e, f) **NID** FONPs (25 μM) + Fe^{3+} (250 μM) and (g, h, i) **NID** FONPs (25 μM) + Fe^{2+} (250 μM). The mean fluorescence values are given in the insets.

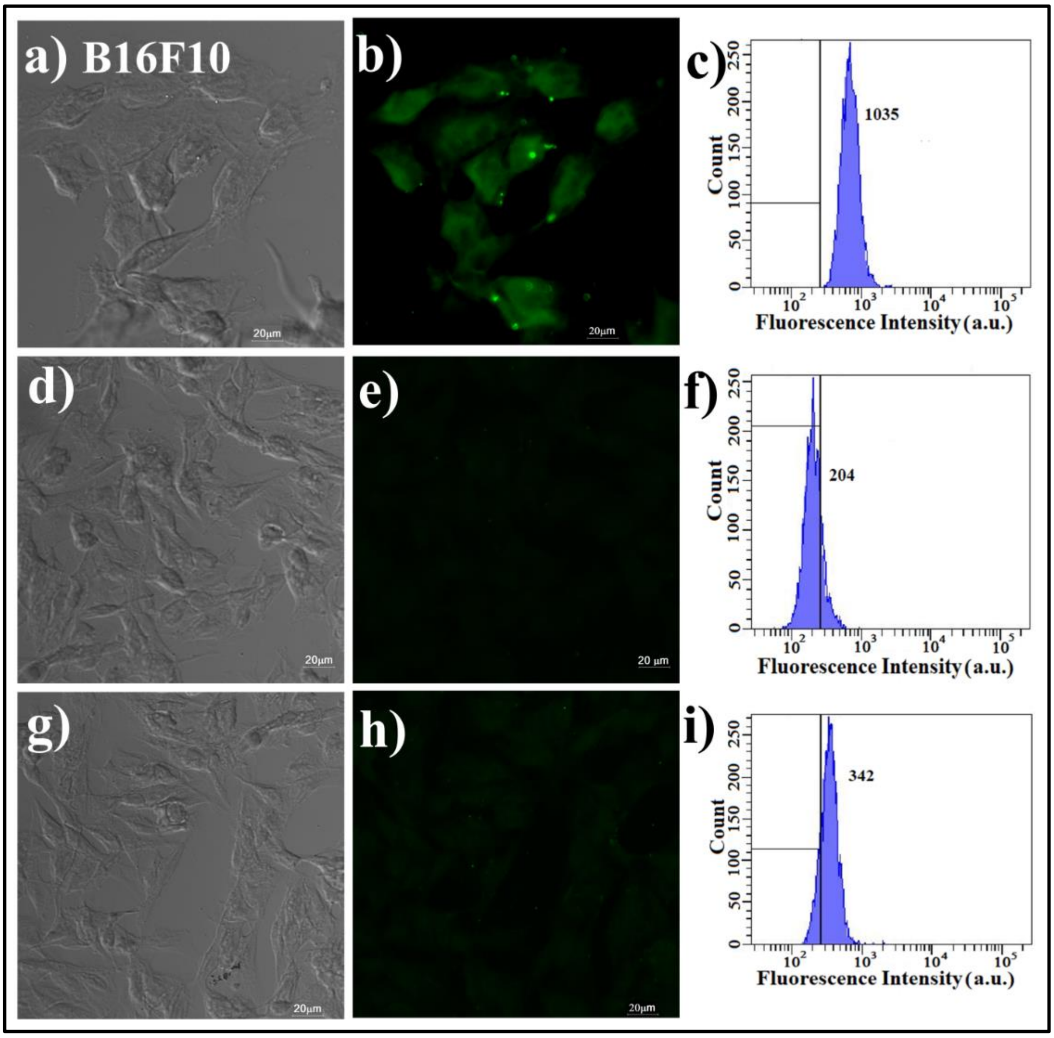

Figure 21. Bright-field, fluorescence microscopic images and corresponding flow cytometric plots of B16F10 cells after 6 h incubation with (a, b, c) **NID** FONPs (25 μM), (d, e, f) **NID** FONPs (25 μM) + Fe^{3+} (250 μM) and (g, h, i) **NID** FONPs (25 μM) + Fe^{2+} (250 μM). The mean fluorescence values are given in the insets.

We also carried out real time bioimaging of NIH3T3 and B16F10 cells taken in chamber slides by incubating **NID** FONPs (25 μM, f_w = 99 vol%) for 3 h and 6 h and again further in presence of Fe^{2+} (250 μM) and Fe^{3+} (250μM) for 6 h (Figure 21,22**)**. We observed similar type of results in concurrence to fixed cells as mentioned above. To demonstrate it further, we co-cultured both the normal cell (NIH3T3) and cancer (B16F10) cells together and incubated the cells with Fe^{2+} (250 μM) and **NID** FONP (25 μM) for 6 h. In contrast to the number of cells present in the bright field image, comparatively lower number of cells exhibited green luminescence under fluorescence microscopic image in the mixed population of both non-cancer (NIH3T3) and cancer (B16F10) cells (Figure 23). Fe^{2+} upon internalization within cancer cells easily got oxidized to Fe^{3+} state through Fenton reaction because of the high H_2O_2 content. Consequently, it quenched the fluorescence of included **NID** FONPs inside the cancer cells (B16F10). However, this same Fe^{2+}/Fe^{3+} transition and subsequently fluorescence quenching of **NID** FONPs did not take place in case of non-cancer cells (NIH3T3) owing to its lack of H_2O_2 content. This result corroborates with the fact that in cancer cells the fluorescence of **NID** FONPs quenched in presence of Fe^{3+}. Hence, this newly developed **NID** FONP can be successfully utilized in selective sensing Fe^{3+} inside and outside of cellular environment as well as for monitoring Fe^{2+}/Fe^{3+} transition selectively inside cancer cells as a marker of oxidative stress.

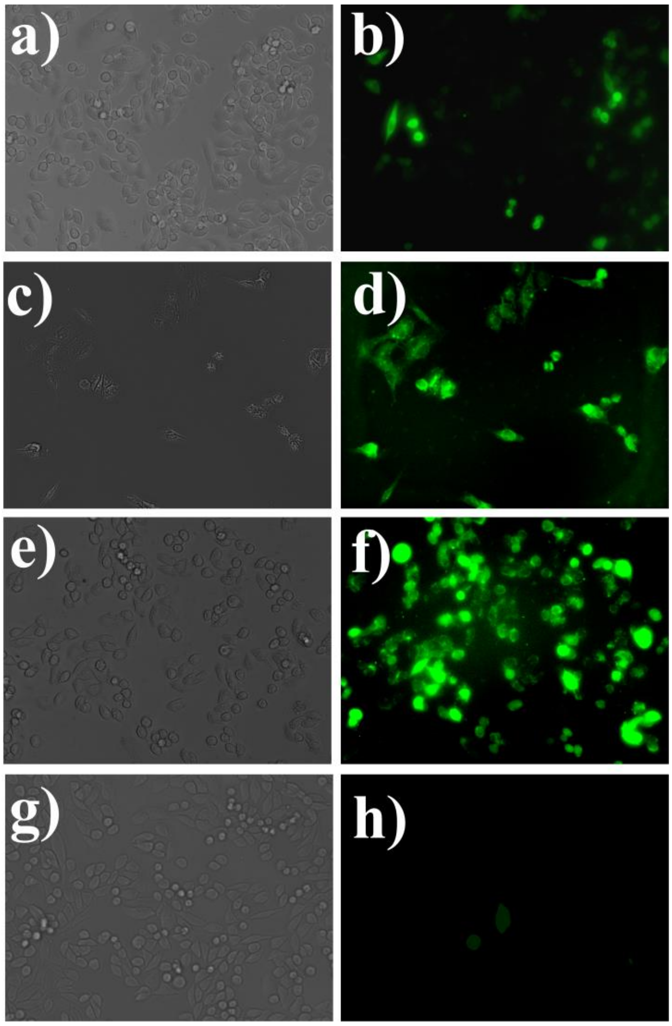

Figure 21. Bright-field, fluorescence microscopic images of NIH3T3 cells after incubation with **NID** FONPs (25 μM) for 3 h (a,b) and 6 h (c,d) incubation with **NID** FONPs (25 μM) + Fe^{2+} (250 μM), (e, f) **NID** FONPs (25 μM) + Fe^{3+} (250 μM) (g, h) for 6 h.

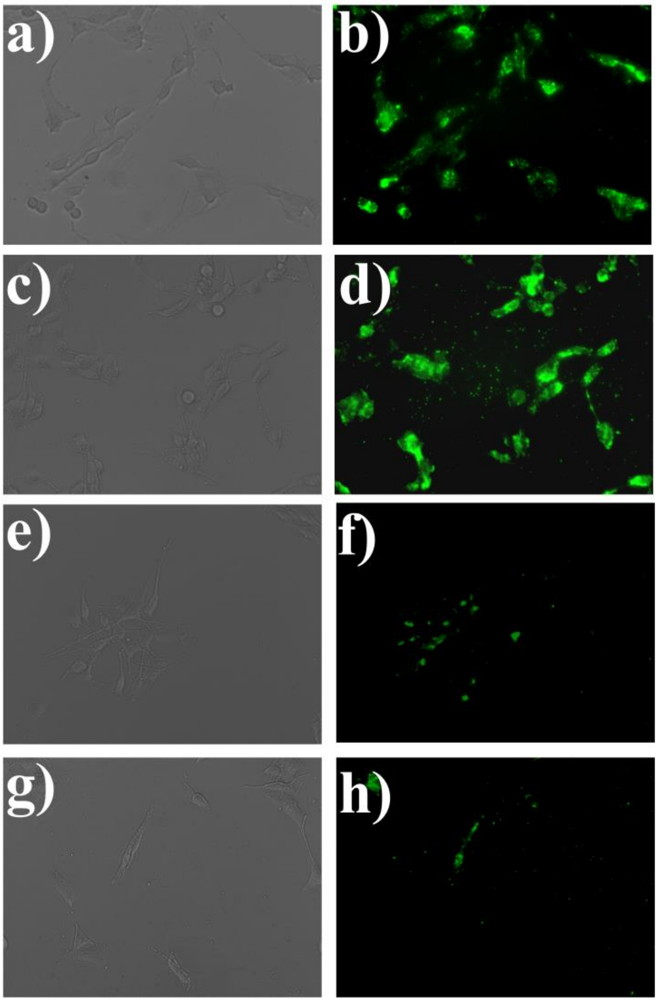

Figure 22. Bright-field, fluorescence microscopic images of B16F10 cells after incubation with **NID** FONPs (25 µM) for 3 h (a,b) and 6 h (c,d) incubation with **NID** FONPs (25 µM) + Fe^{2+} (250 µM), (e, f) **NID** FONPs (25 µM) + Fe^{3+} (250 µM) (g, h) for 6 h.

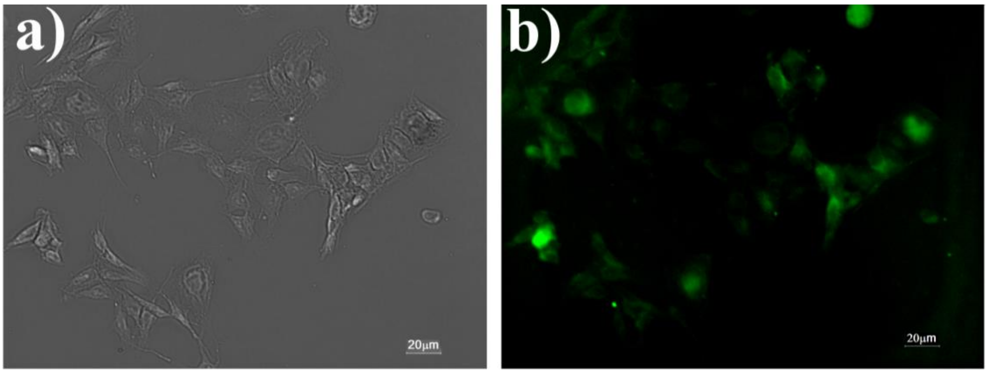

Figure 23. a) Bright-field, b) fluorescence microscopic image of co-cultured NIH3T3 and B16F10 cells after 6 h incubation with **NID** FONPs (25 µM) + Fe^{2+} (250 µM).

3.3. CONCLUSION

In this present work, we have synthesized naphthalimide based L-histidine appended amphiphile (**NID**) which formed bluish green emitting FONPs in 99% water-DMSO binary solvent system via *J*-type aggregation. The amphiphile showed negligible emission in DMSO (non-self-assembled state) but became highly emissive at 60% and above water content at the aggregated state. Aggregation-induced emission was observed through excimer formation, having the emission maximum at 470 nm upon excitation at 350 nm. Among the various tested metal ions, presence of Fe^{3+} led to the selective quenching of the emission intensity of **NID** FONPs due to 1:1 stoichiometric complex formation with the histidine residue. Consequently, the spherical morphology of the self-aggregated organic particle transformed to spindle shaped particles as confirmed by microscopic techniques. **NID** FONP was used as an efficient AIE based turn-off sensor for Fe^{3+} with a LOD of 12.5 ± 1.2 μM having high selectivity over other metal ions. Concurrently, **NID** FONP was successfully employed for bioimaging of Fe^{3+} ions via fluorescence quenching within living cells as well as detecting Fe^{2+}/Fe^{3+} transition selectively inside cancer cell due to its high H_2O_2 content. Hence, **NID** FONP can be a selective diagnostic probe for cancer cells.

3.4. EXPERIMENTAL SECTION

3.4.1. Materials and methods

N-(tert-butoxycarbonyl)-L-aspartic acid 4-benzyl ester, 1-naphthaleneethanol, 1,8-naphthalic anhydride, thiazolyl blue tetrazolium bromide (MTT) and solvents for NMR were procured from Sigma-Aldrich. *N*,*N*-(dimethylamino)pyridine (DMAP), *N*,*N*-dicyclohexylcarbodiimide (DCC), 4-*N*-hydroxybenzotriazole (HOBT), palladium 10% on activated charcoal, trifluoroacetic acid (TFA), L-histidine, di-tert-butyl dicarbonate, ethylene diamine, benzyl chloroformate, silica gel (100-200 mesh and 60-120 mesh), sodium sulfate (Na_2SO_4), 2-aminopyridine, citric acid, L-Dopa, EDTA, folic acid, glycine and all organic solvents, were bought from SRL, India. Dulbecco's modified Eagle's medium (DMEM), Fetal bovine serum (FBS) and trypsin were purchased from Thermo Fisher scientific, India. We used Milli-Q water for all the experiments. NMR spectra were recorded in AVANCE (Bruker) spectrometer. Electron spray ionization (ESI) technique was used to record high resolution mass spectra (HRMS) in a Q-TOF-micro quadruple mass spectrometer. The specific rotation of the synthesized compound was measured in Anton Paar (MCP-200) polarimeter.

3.4.2. Synthesis of NID

1,8-Naphthalimide based L-histidine functionalized amphiphile was synthesized by given pathway (Scheme 2). At first, coupling reaction between N-(tert-butoxycarbonyl)-L-aspartic acid 4-benzyl ester (1.2 equiv) and 1-naphthaleneethanol (1.0 equiv) was carried out using DCC (1.1 equiv), HOBT (1.1 equiv) DMAP (1.1 equiv), in dry methylene chloride (DCM). The reaction mixture was stirred for 12 h under nitrogen atmosphere. 1N HCl was used to wash the organic part and consequently it was dried over anhydrous Na_2SO_4. The residue obtained after evaporation was purified by column chromatography using 60-120 mesh silica gel as the stationary phase and the eluent was 1% methanol in chloroform (yield = 80%). The BOC group was deprotected in 5 h using TFA (1.5 equiv) in dry DCM. After solvent removal, the crude mass taken in ethyl acetate was twice washed with 10% aqueous Na_2CO_3 solution and water. Drying and evaporation of the solvent resulted in the formation of free amine (yield = 81%). 1,8-naphthalic anhydride (1.0 equiv) and the free amine (1.1 equiv) were refluxed (75 °C) in dry EtOH for 12 h. The residue obtained after removal of EtOH was taken in DCM and washed with water. Purification of the condensed product was carried out in 100-200 mesh silica gel using 3% MeOH/$CHCl_3$ as eluent (yield = 72%). Consequently, this product was dissolved in dry THF and hydrogenated using Pd on activated charcoal. The desired acid derivative was obtained after filtration and evaporation of the solvent, THF (yield = 85%). On the other hand, one end of ethylene diamine (1 equiv) was coupled with di-tert-butyl dicarbonate (1 equiv) by drop wise addition of di-tert-butyl dicarbonate in DCM at 0-5 °C for 5 h. The solution was stirred for 8 h and washed with water and brine. Mono-BOC protected ethylenediamine was purified in 100-200 mesh silica gel chromatography using methanol-chloroform (5% v/v) as the eluent (yield = 86%). The previously prepared acid was conjugated with this amine using DCC coupling method as mentioned above. The residue obtained after working up, drying and evaporation was purified in 60-120 mesh silica gel chromatography using 3% methanol in chloroform (v/v) as eluent (yield = 78%). The tert-butoxycarbonyl group was deprotected using TFA (1.5 equiv) in previously mentioned way and the free amine derivative was obtained (yield = 86%). On the other hand, N-carbobenzoxy-L-histidine was synthesized adding benzyl chloroformate (1 eqiv) dropwise to NaOH-dioxane solution of L-histidine (1 eqiv) and stirring the solution overnight. Afterwards, it was dried and acidified with 1 N HCl and extracted in DCM (yield = 76%). This was conjugated with the previously prepared amine derivative using DCC coupling method. The coupled product was purified in 60-120 mesh silica gel chromatography using 3% methanol in chloroform (v/v) as eluent (yield = 79%). Next, the benzyl group was deprotected through hydrogenation using Pd on activated charcoal in THF.

Finally, the end product **NID** (yield = 78%) was obtained by filtration and evaporation of the solvent, THF (Scheme 2).

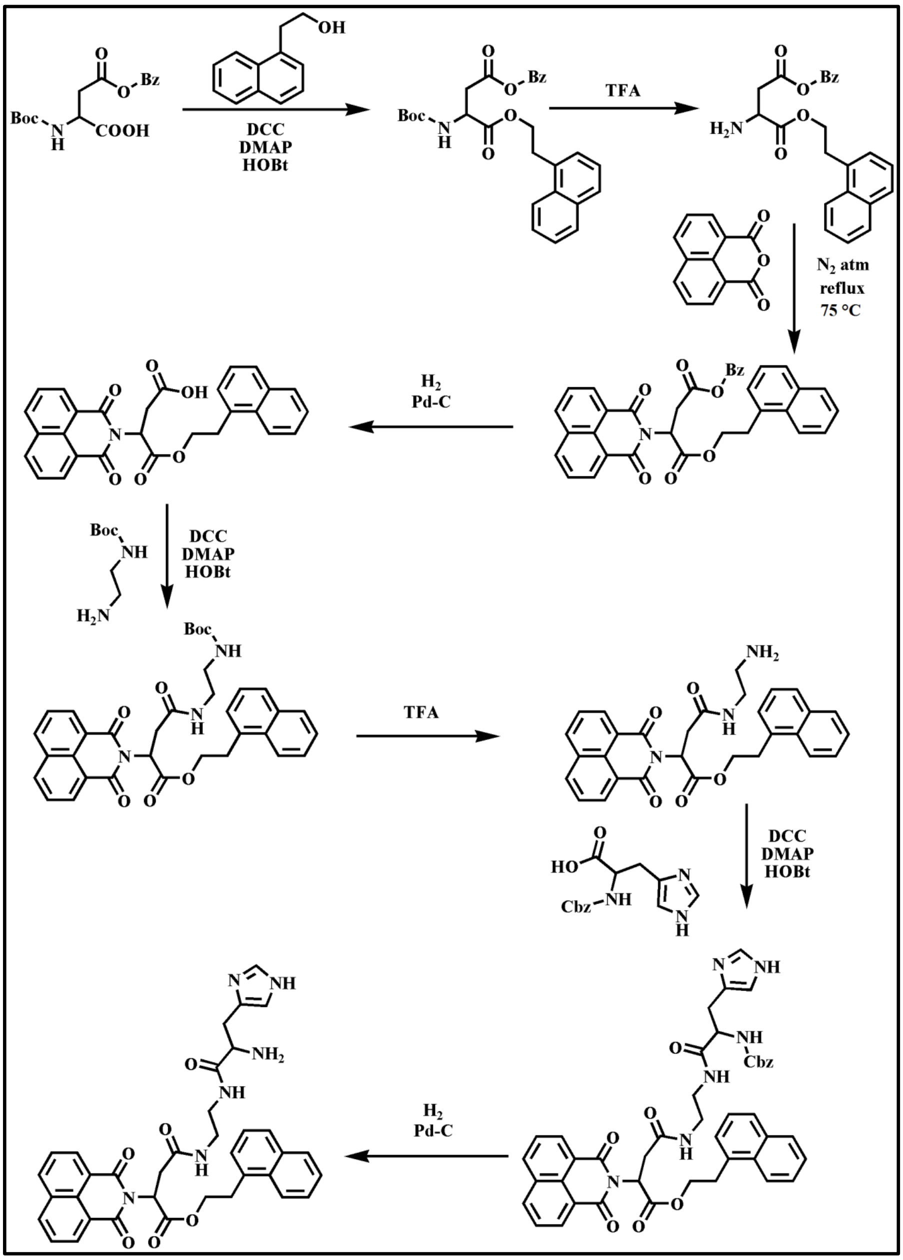

Scheme 2. Synthetic scheme of **NID**.

3.4.3. Preparation of organic nanoparticles

A stock solution (10 mM) of synthesized naphthalimide derivative was prepared by dissolving the calculated amount of **NID** in DMSO. The desired aliquot of this stock solution was added to the varying DMSO-water solvent systems (0-99% water content) to achieve 10-80 µM of **NID**, which was used for all experiments.

3.4.4. Transmission electron microscopy (TEM) study

TEM images were taken in JEOL JEM 2010 microscope. 4 μL solution of **NID** (10 μM) in 99% water in DMSO (f_w = 99 vol%) was drop cast on a carbon coated 300 mesh copper grid and dried. The negative staining of the copper grid was done with uranyl acetate solution (1 μL (1% w/v)). TEM images were obtained after keeping the samples under vacuum for 4 h.

3.4.5. Field-emission scanning electron microscopy (FESEM)

FESEM images were recorded in JEOL-6700F microscope. 6 μL solutions of **NID** (10 μM) and **NID** + Fe^{3+} (10 μM **NID**, 10 μM Fe^{3+}) taken in DMSO-water (f_w = 99 vol%) was deposited on glass coverslips. The FESEM images were captured after keeping the samples under vacuum for 3 h.

3.4.6. Atomic force microscopy (AFM) study

Veeco, AP0100 instrument in noncontact mode was utilized to obtain the AFM images. 10 mL of solution of **NID** (10 μM) and **NID** + Fe^{3+} (10 μM **NID**, 10 μM Fe^{3+}) taken in DMSO-water (f_w = 99 vol%) was deposited on mica (1 cm × 1 cm) and dried overnight.

3.4.7. Fluorescence microscopy Study

Fluorescence microscopic images were taken in a IX83 inverted microscope at 40x magnification. 10 μL solution of **NID** (20 μM) in DMSO-water (f_w = 99 vol%) was drop cast on glass slides. The solutions were air-dried before imaging.

3.4.8. Dynamic light scattering (DLS) study

Zen 3690 Zetasizer (Malvern Instrument Ltd.) was used for measurement of mean hydrodynamic diameter (D_h). The scattering intensity was at 175° angle and Malvern Zetasizer software was used for data analyzing to determine the D_h (for both number averaged and intensity averaged distribution) of **NID** (10 μM) in DMSO-water (f_w = 99 vol%) and also the correlogram.

3.4.9. UV-visible study

Solvent dependent UV-vis spectra were recorded on Perkin Elmer Lambda 25 spectrophotometer to understand self-aggregation of **NID**. UV-visible spectra of **NID** (50 μM) in DMSO-water solvent mixtures (1 mL) was observed by varying the content of DMSO from

100% to 1% in water. UV-vis spectra of **NID** (50 μM) were also taken in organic solvents (*m*-xylene, *o*-xylene, toluene, anisole, diethyl ether) with different polarities.

3.4.10. Solvent-dependent ^{1}H-NMR study

^{1}H-NMR spectra of **NID** (1 mM) in DMSO-d_6, 2:1 (v/v) DMSO-d_6-D_2O and 1:1 (v/v) DMSO-d_6-D_2O were recorded on Avance 300 MHz spectrometer (Bruker).

3.4.11. Photoluminescence study

Fluorescence spectra of **NID** solutions (excited at (λ_{ex}) = 350 nm) were recorded in Varian Cary Eclipse luminescence spectrometer. Emission spectra of **NID** (10 μM) were monitored in DMSO-water (1 mL) of variable compositions (f_w = 0-99 vol %). Concentration dependent emission spectra were taken in 99% water in DMSO with varying concentrations (10-90 μM) of **NID**. Emission spectra of **NID** (50 μM) were taken in several organic solvents (*m*-xylene, *o*-xylene, toluene, anisole, diethyl ether) of different polarities. Interaction of aggregated **NID** FONPs (50 μM) with Fe^{3+} ($FeCl_3$ solution) was recorded by luminescence study. Stern-Volmer constant (K_{SV}) of the kinetics of fluorescence quenching of **NID** FONPs with respect to Fe^{3+} concentration was found out using the equation: $F/F_o = 1 + K_{SV}[Q]$, where F and F_o are the fluorescence intensities of **NID** FONPs in presence/absence of Fe^{3+} and [Q] denotes concentration of quencher Fe^{3+} ion. Fe^{3+}detection limit was evaluated the from the linear curve obtained from $(F_o – F)/F_o$ vs the Fe^{3+} concentration and the selectivity of **NID** FONP (50 μM) against different metal ions having concentration of 500 μM was also studied. We also recorded the photoluminescence spectra of the solution of **NID** FONPs (50 μM) at f_w = 99 vol% water in DMSO and Fe^{3+} (500 μM) in presence of several Fe^{3+} chelating agents like 2-aminopyridine, citric acid, L-Dopa, EDTA, folic acid and glycine having concentration of 500 μM and 1000 μM. Photographs of cuvette containing **NID** solutions (1 mL) of different DMSO-water compositions, **NID** solutions in presence and absence of different metal ions in DMSO-water (f_w = 99 vol%) and with Fe^{2+} and H_2O_2 were taken upon irradiation under UV lamp (λ_{ex} = 365 nm).

3.4.12. Quantum yield (QY) measurement

The QY of the unknown fluorophore **NID** (ϕ_u) was measured in comparison to a common fluorophore having a known QY (ϕ_s) using the following equation

$$\emptyset_u = \left(\frac{A_s F_u n_u^2}{A_u F_s n_s^2}\right)\emptyset_s \qquad (4)$$

A_u and A_s are the absorbance of the unknown and reference sample at respective λex. Integrated emission intensities of unknown and known samples at same λex are F_u and F_s, respectively. Refractive indices of solvents are n_u and n_s in which unknown and known sample were dissolved. For the determination of the QY, solutions with similar absorbance (<0.01) were used. Quinine sulfate in sulfuric acid (0.1 M) was used as the reference having QY (ϕ_s) = 54.0%.

3.4.13. Time-resolved study

For the time-correlation single photon count (TCSPC) measurement, samples were excited in NANO-LED IBH-375 and Hamamatsu MCP photomultiplier was used to collect the fluorescence decays. To perform the experiment, 2 mL solutions of **NID** (20μM) were prepared in DMSO, DMSO-water (2:3 v/v, 1:99 v/v). All amphiphilic solutions were excited (λ_{ex}) at 375 nm and their emission (λ_{mon}) was monitored at 390 nm for only DMSO and at 470 nm for other two solvent mixtures. Time-resolved fluorescence decay *p(t)* was analyzed by following equation 5

$$p(t) = b + \sum_{i}^{n} \alpha_i \, e^{\left(\frac{-t}{\tau_i}\right)} \tag{5}$$

Here, n = number of discrete emissive species, b = baseline correction ("dc" offset), α_i = pre-exponential factors, and τ_i = excited state fluorescence lifetimes for the i-th component, respectively. For multiexponential decays, the average lifetime was calculated using equation 6

$$\langle \tau \rangle = \sum_{i=1}^{n} \alpha_i \tau_i \tag{6}$$

Here, $\alpha_i = \frac{\alpha_i}{\sum \alpha_i}$ depicts the contribution of a decay component.

3.4.14. Job's plot measurements

Two stock solutions of **NID** and Fe^{3+} were prepared each having 80 μM concentration. Varying volume (0, 125, 250, 375, 500, 625, 750, 875, 1000 μL) of **NID** solution was mixed with different volume (1000, 875, 750, 625, 500, 375, 250, 125, 0 μL) of Fe^{3+} solution, respectively having total volume of 1 mL in each vial. Following gentle agitation of the vials for few minutes, fluorescence spectra were recorded at room temperature.[38]

3.4.15. Circular dichroism (CD) study

CD spectra of **NID** (500 µM) in different ratios of DMSO-water mixtures in absence and presence of Fe^{3+} (5 mM) at f_w = 99% in DMSO and in different organic solvents like diethyl ether, toluene, anisole, *m*-xylene and *o*-xylene were recorded by using a quartz cuvette of 1 mm path length in a JASCO J-815 CD spectropolarimeter.

3.4.16. Cell culture

B16F10 (cancer cells) and NIH3T3 (non-cancer cells) were brought from NCCS, Pune. The cells were cultured in DMEM media with 10% FBS, streptomycin and penicillin and kept in incubator (5% CO_2) at 37 °C. Above mentioned cells were used to perform cytocompatibility and bioimaging experiments. All the cellular experiments were investigated using **NID** FONPs at f_w = 99 vol%, as they have maximum luminescence compared to other DMSO-water solution.

3.4.17. MTT assay

Cytotoxicity of **NID** FONPs in DMSO-water (f_w = 99 vol%) was investigated by MTT assay. In this assay, soluble tetrazolium gets reduced to insoluble formazan by mitochondrial dehydrogenase excreted from viable cells. Insoluble formazan was dissolved in DMSO and estimated spectrophotometrically. The formation of formazan is proportional to the number of alive cells. Lower the absorbance means the killing of cells. First, NIH3T3 and B16F10 cells were grown in a 96-well plate (2×10^4 cells per well) for 24 h. **NID** FONPs (f_w = 99 vol%) having concentration of 10-50 µM was incubated with both the cells for 12 h and 24 h. 10 µL of MTT stock solution (5 mg mL^{-1}) in phosphate buffered saline (PBS) was added and cells were incubated further for 4 h. The precipitated formazan was dissolved in DMSO and the absorbance was recorded using Bio Tek1 Elisa Reader at 570 nm. The number of alive cells was calculated as % viability by following the equation

% viability = (A_{570} (treated cells)-background)/(A_{570} (untreated cells)-background) × 100 (7)

3.4.18. Bioimaging

B16F10 and NIH3T3 cells grown in a chamber slide were treated with i) **NID** FONPs (25 µM, f_w = 99 vol%), ii) **NID** FONPs (25µM, f_w = 99 vol%) + Fe^{3+}(250µM), iii) **NID** FONPs (25 µM, f_w = 99 vol%) + Fe^{2+}(250 µM) for 6 h. Cells were consequently washed with PBS thrice, and thereafter fixed using paraformaldehyde (4%). The cells were mounted on a slide using Glycerol (50%), covered with a cover slip and kept for 24 h. Images were taken in a IX83 inverted microscope at 40x and 20x magnification. We carried out real time bioimaging experiment for normal cells (NIH3T3) and cancer cells (B16F10) in 4 well chamber slides. First, we incubated both type of cells separately in different chamber slides for 24 h (5% CO2) at 37 °C. Followed by we incubated **NID** FONPs in (25 µM, f_w = 99 vol%) in both type of cells for 3 h and carried out fluorescence imaging. We took the cells within chamber slides again in the CO2 incubator for another 3 h and carried out the same experiment till overall 6 h incubation of the FONPs. After that we incubated Fe^{2+} (250 µM) and Fe^{3+} (250 µM) separately in different wells of chamber slides where compound was already incubated. Subsequently, we carried out the imaging experiment for 6 h incubation of Fe^{2+} and Fe^{3+} included within both type of cells.

3.4.19. Co-culture experiment

Normal cells (NIH3T3) and cancer cells (B16F10) both were cultured separately in cell culture flask using DMEM media with 10% FBS, streptomycin and penicillin and kept in incubator (5% CO2) at 37 °C for 3 days. For co-culture experiment we trypsinized both type of cells and plated them in each well of 4 well chamber slide as a mixed population (NIH3T3:B16F10= 1:1) for 24 h in incubation. Then we loaded **NID** FONPs (25 µM, f_w = 99 vol%) + Fe^{2+} (250 µM) and incubated it for 6 h. After 6 h incubation cells were consequently washed with PBS thrice, and thereafter fixed using paraformaldehyde (4%). The cells were mounted on a slide using glycerol (50%), covered with a coverslip and kept for 24 h. Imaging was done in a IX83 inverted microscope at 20x magnification.

3.4.20. Flow cytometry

Both the normal cell (NIH3T3) and cancer cell (B16F10) were culturally grown for 24h. Then we incubated i) **NID** FONPs (25 µM, f_w = 99 vol%), ii) **NID** FONPs (25 µM, f_w = 99 vol%) + Fe^{3+} (250 µM), iii) **NID** FONPs (25 µM, f_w = 99 vol%) + Fe^{2+} (250 µM) with both type of cells for 6h. After 6h, we washed both the incubated cells with DMEM media and PBS buffer to remove the excess compounds from cell medium. We used trypsin to detached the cells from culture flask and centrifuge it for 5 min. After centrifugation we took the precipitated cells suspended in PBS (500 µL) and carried out the cytometric experiment. BD FACS Aria™ III flow cytometer was employed to inspect the cells at emission wavelength using a 510 ± 40 nm bandpass filter upon excitation at 405 nm.

3.5. CHARACTERISATION DATA

^{1}H-NMR (400 MHz, $CDCl_3$, 25 °C): δ/ppm: 8.500-8.539 (m, 3H, C-3, C-8 proton of naphthalimide, C-2 proton of imidazole), 8.365-8.389 (m, 2H, C-5, C-6 proton of naphthalimide), 7.853-7.964 (m, 4H, C-4, C-5, C-8 protons of naphthyl ring, C-5 proton of imidazole), 7.608-7.639 (m, 2H, C-4, C-7 protons of naphthalimide), 7.418-7.438 (d, 1H, C-7 proton of naphthyl ring), 7.336-7.372 (t, 1H, C-6 proton of naphthyl ring), 7.154-7.285 (m, 1H, C-3 proton of naphthyl ring), 6.967-7.005 (m, 1H, C-2 proton of naphthyl ring), 6.239-6.274 (m, 1H, chiral centre of L-aspartic acid residue), 5.071-5.091 (m, 2H, O-C$\underline{H}_2$-CH_2-$C_{10}H_7$), 4.453-4.497 (m, 1H, chiral centre of L-histidine residue), 3.489-3.569 (m, 6H, -N-C$\underline{H}_2$-C$\underline{H}_2$-N- and O-CH_2-C$\underline{H}_2$-$C_{10}H_7$), 3.274-3.366 (m, 2H, methylene protons of L-histidine residue), 2.969-3.029(m, 2H, methylene protons of L-asparticacid residue).^{13}C-NMR (400 MHz, CDCl3): 170.48, 168.95, 160.68, 135.43, 134.55, 134.15, 133.55, 132.24, 131.95, 131.79, 128.98, 127.61, 127.44, 127.25, 127.16, 127.12, 126.16, 125.77, 125.63, 123.78, 119.08, 63.19, 50.05, 49.38, 36.35, 29.65, 28.97. HRMS: m/z: 647.69 $[M+H]^+$(calculated); 647.5857 (found).$[\alpha]_D^{25}$= -13.78° (c = 0.58g/100mL) in $CHCl_3$).

3.6. SPECTRA

3.6.1. ^{1}H-NMR spectra

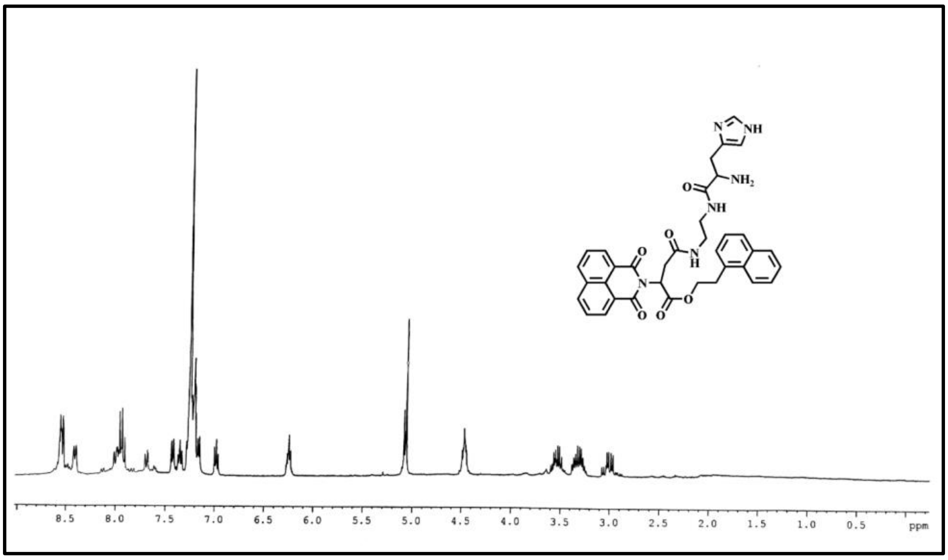

3.6.2. ^{13}C-NMR spectra

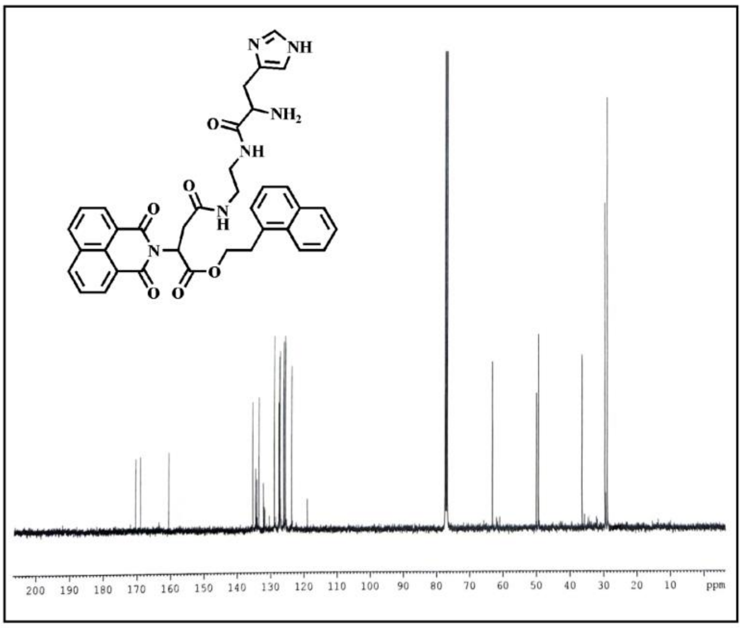

3.6.3. Mass spectra

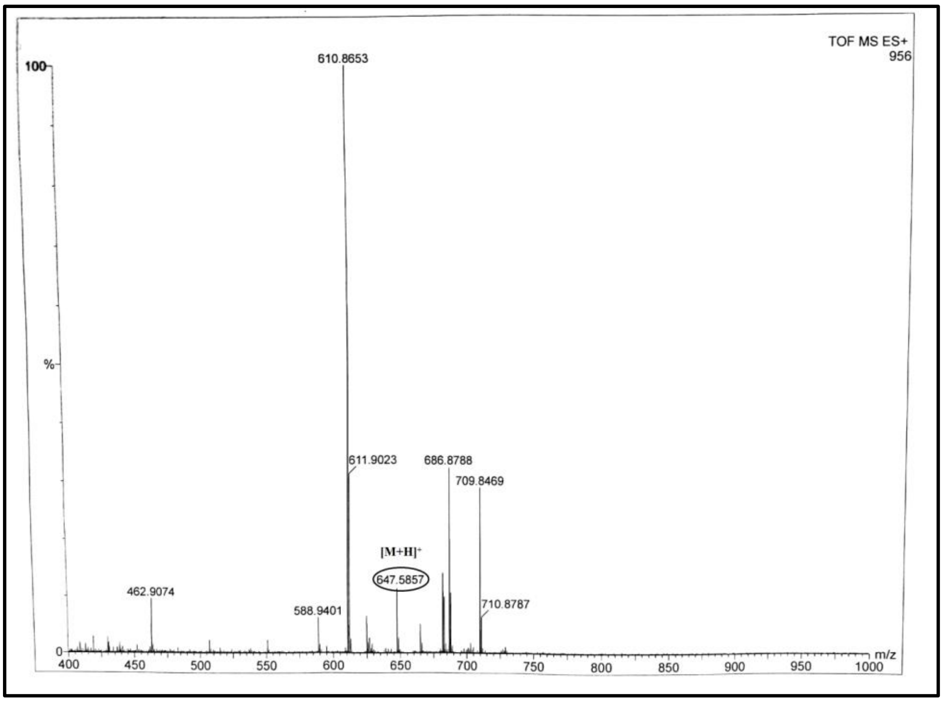

3.7. REFERENCES

[1] J. Wu, W. Liu, J. Ge, H. Zhang, P. Wang, *Chem. Soc. Rev.* **2011**, *40*, 3483.

[2] H. Kobayashi, M. Ogawa, R. Alford, P. L. Choyke, Y. Urano, *Chem. Rev.* **2010**, *110*, 2620.

[3] B. Kong, A. Zhu, C. Ding, X. Zhao, B. Li, Y. Tian, *Adv. Mater.* **2012**, *24*, 5844.

[4] X. Li, X. Gao, W. Shi, H. Ma, *Chem. Rev.* **2014**, *114*, 590.

[5] Z. Liu, W. He, Z. Guo, *Chem. Soc. Rev.* **2013**, *42*, 1568.

[6] J. S. Kim, D. T. Quang, *Chem. Rev.* **2007**, *107*, 3780.

[7] K. P. Carter, A. M. Young, A. E. Palmer, *Chem. Rev.*, **2014**, *114*, 4564.

[8] J. Malkin, CRC: Boca Raton FL, **1992**.

[9] J. Luo, Z. Xie, J. W. Y. Lam, L. Cheng, H. Chen, C. Qiu, H. S. Kwok, X. Zhan, Y. Liu, D. Zhu, B. Z. Tang, *Chem. Commun.* **2001**, 1740.

[10] Y. Hong, J. W. Y. Lam, B. Z. Tang, *Chem. Soc. Rev.* **2011**, *40*, 5361.

[11] J. Mei, N. L. C. Leung, R. T. K. Kwok, J. W. Y. Lam, B. Z. Tang, *Chem. Rev.* **2015**, *115*, 11718.

[12] J. Qian, B. Z. Tang, *Chem* **2017**, *3*, 56.

[13] M. Gao, B. Z. Tang, *ACS Sens.* **2017**, *2*, 1382.

[14] D. D. La, S. V. Bhosale, L. A. Jones, S. V. Bhosale, *ACS Appl. Mater. Interfaces* **2018**, *10*, 12189.

[15] A. K. Ghosh, P. Choudhury, P. K. Das, *Langmuir* **2019**, *35*, 15180.

[16] B. K. An, S. K. Kwon, S. D. Jung, S. Y. Park, *J. Am. Chem. Soc.* **2002**, *124*, 14410.

[17] M. Kumar, S. J. George, *Nanoscale* **2011**, *3*, 2130.

[18] A. Kaeser, I. Fischer, R. Abbel, P. Besenius, D. Dasgupta, M. A. J. Gillisen, G. Portale, A. L. Stevens, L. M. Herz, A. P. H. J. Schenning, *ACS Nano* **2013**, *7*, 408.

[19] P. Choudhury, S. Sarkar, P. K. Das, *Langmuir* **2018**, *34*, 14328.

[20] X. Zhang, S. Wang, L. Xu, L. Feng, Y. Ji, L. Tao, S. Li, Y. Wei, *Nanoscale* **2012**, *4*, 5581.

[21] M. Ahmed, M. Faisal, A. Ihsan, M. M. Naseer, *Analyst* **2019**, *144*, 2480.

[22] Z. Wang, T. Y. Yong, J. Wan, Z. H. Li, H. Zhao, Y. Zhao, L. Gan, X. L. Yang, H. B. Xu, C. Zhang, *ACS Appl. Mater. Interfaces* **2015**, *7*, 3420.

[23] S. Dai, C. Schwendtmayer, P. Schurmann, S. Ramaswamy, H. Eklund, *Science* **2000**, *287*, 655.

[24] A. Atkinson, D. R. Winge, *Chem. Rev.* **2009**, *109*, 4708.

[25] E. C. Theil, D. J. Goss, *Chem. Rev.* **2009**, *109,* 4568.

[26] D. A. Weinstein, C. N. Roy, M. D. Fleming, M. F. Loda, J. I. Wolfsdorf, N. C. Andrews, *Blood* **2002**, *100*, 3776.

[27] W. H. Hörl, *J. Am. Soc Nephrol.* **2007**, *18*, 382.

[28] S. Altamura, M. U. Muckenthaler, *J.Alzheimer's Dis.* **2009**, *16*, 879.

[29] S. M. H. Sadrzadeh, E. Graf, S. S. Panter, P. E. Hallaway, J. W. Eaton, *J. Biol. Chem.* **1984**, *259*, 14354.

[30] D. Chakraborty, S. Sarkar and P. K. Das, *ACS Sustainable Chem. Eng.* **2018**, *6*, 4661.

[31] S. Dinda, P. K. Das, *ACS Appl. Bio Mater.* **2019**, *2*, 3737.

[32] N. Bresgen, P. M. Eckl, *Biomolecules* **2015**, *5*, 808.

[33] S. Puntarulo, *Mol. Asp. Med.* **2005**, *26*, 299.

[34] M. H. Lee, T. V. Giap, S. H. Kim, Y. H. Lee, C. Kang, J. S. Kim, *Chem. Commun.* **2010**, *46*, 1407.

[35] X. Qu, Q. Liu, X. Ji, H. Chen, Z. Zhou, Z. Shen, *Chem. Commun.* **2012**, *48*, 4600.

[36] S. K. Sahoo, D. Sharma, R. K. Bera, G. Crisponi, J. F. Callan, *Chem. Soc. Rev.* **2012**, *41*, 7195.

[37] B. Sui, S. Tang, T. Liu, B. Kim, K. D. Belfield, *ACS Appl. Mater. Interfaces* **2014**, *6*, 18408.

[38] X. Yang, X. Chen, X. Lu, C. Yan, Y. Xu, X. Hang, J. Qu, R. Liu, *J. Mater. Chem. C* **2016**, *4*, 383.

[39] S. Banerjee, E. B. Veale, C. M. Phelan, S. A. Murphy, G. M. Tocci, L. J. Gillespie, D. O. Frimannsson, J. M. Kelly, T. Gunnlaugsson, *Chem. Soc. Rev.* **2013**, *42*, 1601.

[40] P. Gopikrishna, N. Meher, P. K. Iyer, *ACS Appl. Mater. Interfaces* **2018**, *10*, 12081.

[41] H. H. Lin, Y. C. Chan, J. W. Chen, C. C. Chang, *J. Mater. Chem.* **2011**, *21*, 3170.

[42] C. Han, T. Huang, Q. Liu, H. Xu, Y. Zhuang, J. Li, J. Hu, A. Wang, K. Xu, *J. Mater. Chem. C* **2014**, *2*, 9077.

[43] C. F. León, F. Galindo, J. F. Miravet, *Nanoscale* **2018**, *10*, 17060.

[44] M. Formica, V. Fusi, L. Giorgi, M. Micheloni, *Coord. Chem. Rev.* **2012**, *256*, 170.

[45] D. Jacquemin, E. A. Perpète, G. Scalmani, I. Ciofini, C. Peltier, C. Adamo, *Chem. Phys.* **2010**, *372*, 61.

[46] E. Lippert, *Z. Naturforsch., A: Astrophys. Phys. Phys. Chem.* **1955**, *10*, 541.

[47] N. Mataga, Y. Kaifu, M. Koizumi, *Bull. Chem. Soc. Jpn.* **1956**, *29*, 465.

[48] J. Guan, L. Jiang, J. Li, W. Yang, *J. Phys. Chem. C* **2008**, *112*, 3267.

[49] T. P. Szatrowski, C. F. Nathan, *Cancer Res.* **1991**, *51*, 794.

[50] R. H. Burdon, *Free Radical Biol. Med.* **1995**, *18*, 775.

[51] S. Toyokuni, K. Okamoto, J. Yodoi, H. Hiai, *FEBS Lett.* **1995**, *358*, 1.

* * *

Chapter 4

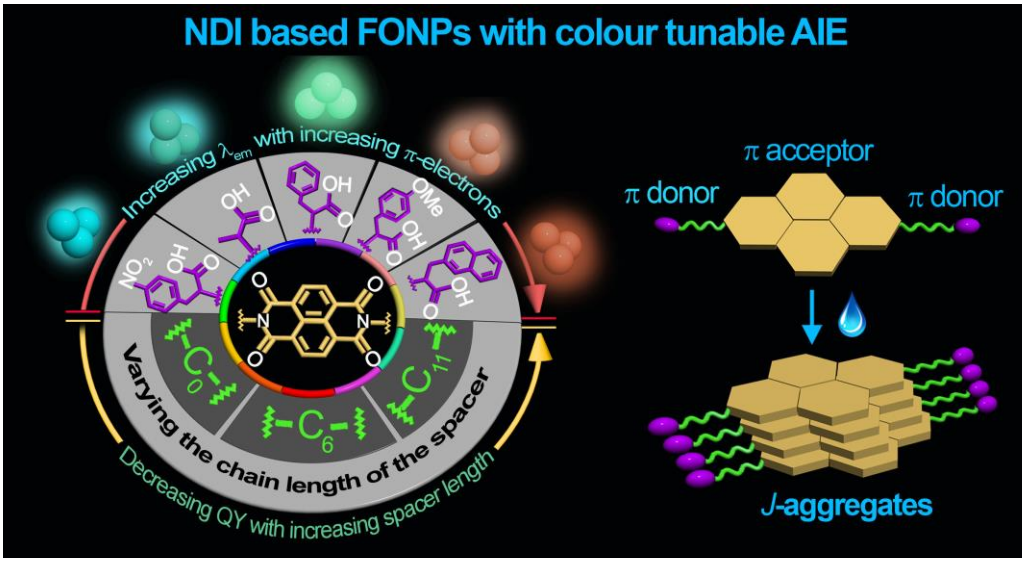

Naphthalenediimide based various amino acids appended organic nanoparticles with tuneable aggregation-induced emission (AIE)

4.1. INTRODUCTION

One of the most prominent examples of "Chemistry beyond molecule" is supramolecular self-assembly.[1,2] Supramolecular architectures are built on the spontaneous self-organization of surfactant molecules by means of hydrophobic, van der Waals, π-π stacking, H-bonding, electrostatic and other non-covalent interactions.[3-8] These non-covalent forces play the central role in developing self-aggregates with diverse morphology and varying dimensions. Peptide-based self-assemblies serve the goal of simplifying or repurposing biomimetic structures through the exploitation of molecular scaffold of naturally available amino acids.[9-15] Peptide-based amphiphiles get self-assembled into vesicle, hydrogel, nanotube, fibril and other aggregated structures with the prospective applications in cellular transportation, tissue engineering, regenerative medicines and others. [16-23] Even a single amino acid is quite capable of composing miscellaneous nanoscale structures that may be attributed to presence of specific non-covalent interactions. [16,24,25]

Fluorescent organic nanoparticles (FONPs) are a category of supramolecular self-aggregates, built on π-conjugated oligomers with rich emissive properties and photostability. [26-31] In case of FONPs, the limitations caused by aggregation caused quenching (ACQ) get eliminated by the emergence of aggregation-induced emission (AIE), the anomalous property first reported by Tang *et al.* [32] Those luminogens are non or weakly emissive in molecular state and shine brightly in aggregated form chiefly due to restricted intramolecular rotation (RIR) and loss of planarity. [33-35] Utility of FONPs is superior to their alternatives in numerous ways with regard to easy functionalization, low cytotoxicity for their application in sensing, imaging as well as in theranostic.

Tuning of the emission wavelength of fluorescent nanoparticle is a promising approach in the vast realm of materials and biomedical sciences. A control over the fluorescence maxima of the FONP can be achieved by modifying the π-conjugated donor and accepter residues. In this regard, naphthalenediimide (NDI), the smallest homologue of the rylene diimides has huge potentials in organic electronic and photovoltaic devices on account of its electron accepting nature.[36,37] Würthner and co-workers showed that core-substitution of NDI with heteroatom (N, O, or S) donors could generate multiple colours.[38] Lately, Choudhury *et. al.*, demonstrated aggregation-induced multicolour emission for NDI derivatives with substituted side chains.[39] Similarly, Tonga *et al.* demonstrated the influence of π-conjugation on AIE in α-cyanostilbene based polycyclic aromatic hydrocarbons.[40] Amino acids with varying π-electron density, linked to the NDI core at N-substituted position could also lead to tuneable emission of the FONPs. A systematic investigation on the structure-property correlation of such amphiphilic compounds possibly can define the role different molecular segments in modulating the emitting parameters of FONPs.

To this end, we have developed NDI based amino acid appended amphiphilic molecules (**NDI-1-9**, Figure 1) with or without alkyl spacer (C6 and C11) between the NDI core and amino acids. **NDI-1-9** self-assembled into organic nanoparticles (~50 nm) in different solvent systems of DMSO/DMF-water, $CHCl_3$-methyl cyclohexane (MCH) via *J*-aggregation. At 99 vol% MCH in $CHCl_3$, **NDI-1-3** (L-alanine, L-phenylalanine and 3-(2-naphthyl)-L-alanine are directly linked with NDI core) exhibited AIE having excimer peaks at 484 nm, 495 nm, and 590 nm, respectively. Upon inclusion of C-6 (6-amino caproic acid, **NDI-5** and **NDI-6**) and C-11 (11-amino undecanoic acid, **NDI-8** and **NDI-9**) spacer between NDI and aromatic amino acids, AIE of corresponding FONPs was observed at 505 nm, 545 nm, 480 nm and 585 nm, respectively in 99 vol% of water in DMF/DMSO and/or MCH in $CHCl_3$. Increase in alkyl spacer length was found to generate relatively lower quantum yield. Remarkably, enhancement of π-electron cloud in the side chain substitution of NDI in presence or absence of alkyl spacer led to red shifting in emission of FONPs from blue-green to yellow-orange array of colours. This was further corroborated by the *p*-substitution of $-NO_2$ (**NDI-2a**) and -OMe (**NDI-2b**) in the aromatic ring of L-phenylalanine that showed blue shifted (475 nm) and red shifted (570 nm) emission maxima with respect to **NDI-2** (495 nm).

4.2. RESULTS AND DISCUSSION

4.2.1. Molecular designing of naphthalenediimides based amphiphiles NDI-1-9

Naphthalenediimides are unique class of aromatic compounds with a capability of forming supramolecular self-organization owing to its robust planar geometry.[36,37] It's physical and electronic properties can be modulated by substitution at diimide position or directly at the core.[38,39,41,42] These substituted NDI derivatives generate diverse nanoarchitectures through self-aggregation with participation of H-bonding and π-π stacking. [43-45] Alongside in many instances, it exhibits aggregation induced emission (AIE) in contrast to aggregation caused quenching (ACQ) because of its restricted intramolecular rotation (RIR) and loss of planarity.[39,42] To understand the influence of varying substitutions in regulating the emission of the aggregated organic nanoparticles, this study aims to develop a structure-property correlation through the designing of amino acid substituted naphthalenediimide (NDI) based amphiphilic molecules. Variation in the π-electron density in the side chain substitution of amino acids may tune the emission maxima of the aggregated organic nanoparticles derived from NDI-based amphiphiles.

To this end, we have synthesized naphthalenediimide-based amino acid containing amphiphilic molecules **NDI-1-9** (Figure 1) by varying the side chain substitution from L-alanine to L-phenylalanine to 3-(2-naphthyl)-L-alanine. Alongside, we introduced different chain length alkyl spacer (C-6 and C-11) between the NDI core and amino acid. NDI core and other aromatic rings may lead to self-assembly of the amphiphiles through π-π stacking while amide bonds would facilitate the self-aggregation via intermolecular H-bonding. Chirality of the amino acids have potential to impart RIR in the aggregated form of those amphiphiles on account of their twisted nature. Therefore, these self-assembled structures might also be highly emissive in its aggregated state owing to AIE. Moreover, **NDI-2a** and **NDI-2b** (Figure 1) were synthesized by incorporating electron withdrawing group -NO_2 and electron donating group -OMe in the L-phenylalanine substituted amphiphile (**NDI-2**), respectively in an attempt to corroborate the effect of extended π electron clouds with manifested AIE.

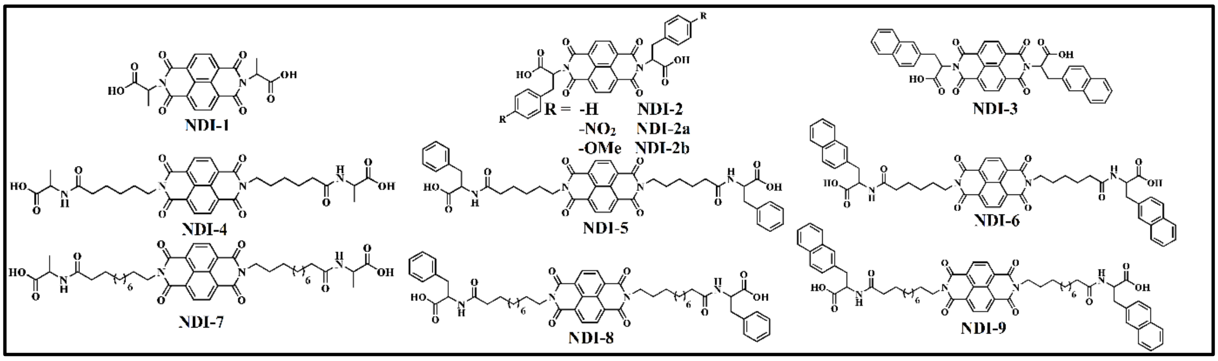

Figure 1. Structures of naphthalenediimide (NDI) derivatives, **NDI-1-9**, **NDI-2a** and **NDI-2b**.

4.2.2. Self-aggregation of amphiphiles

The synthesized NDI amphiphiles (**NDI-1-9**) were soluble in DMSO. Addition of water led to translucency of the medium indicating the possible self-assembly of amphiphiles. In all the cases, transparent solution in DMSO turned to translucent on gradual addition of water from f_w = 60-80 vol% (Figure 2). The self-assembled translucent solutions were stable up to 99 vol% water in DMSO and the translucency of the solutions was maximum at f_w = 99 vol%. In addition, we checked the solubility of synthesized NDI derivatives in DMF and $CHCl_3$ to investigate their prospect of self-assembly by introducing water and methyl cyclohexane (MCH), respectively. For **NDI-1**, **NDI-2**, **NDI-3** and **NDI-8** translucency distinctly appeared from 80 vol%, 80 vol%, 60 vol% and 99 vol% MCH in $CHCl_3$ (Figure 3a,b,e,f,). In case of other NDI derivatives, obtained translucent solutions were not stable for a longer period of time, in particular at higher MCH content. Furthermore, we tested the self-assembling ability L-phenylalanine substituted NDI-derivates with varying spacer length (**NDI-2**, **NDI-5** and

NDI-8) in DMF-water binary solvent systems. Here too the transparent DMF solutions of **NDI-2**, **NDI-5** and **NDI-8** transformed to translucent with gradual addition of water from f_w = 80 vol% and the translucency got increased to maximum at f_w = 99 vol% in DMF (Figure 3g-i).

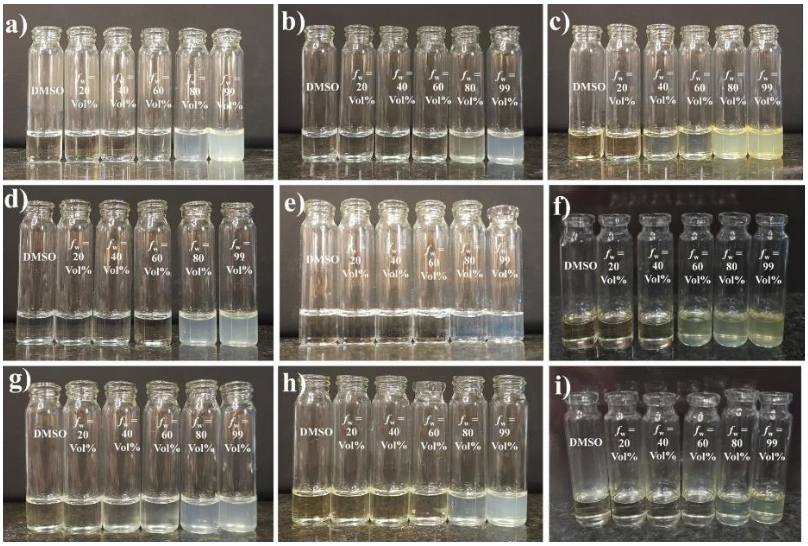

Figure 2. Photographs of formation of translucent solutions with increasing water content in DMSO for 250 μM of (a) **NDI-1**, (b) **NDI-2**, (c) **NDI-3**, (d) **NDI-4**, (e) **NDI-5**, (f) **NDI-6**, (g) **NDI-7**, (h) **NDI-8** and (i) **NDI-9**.

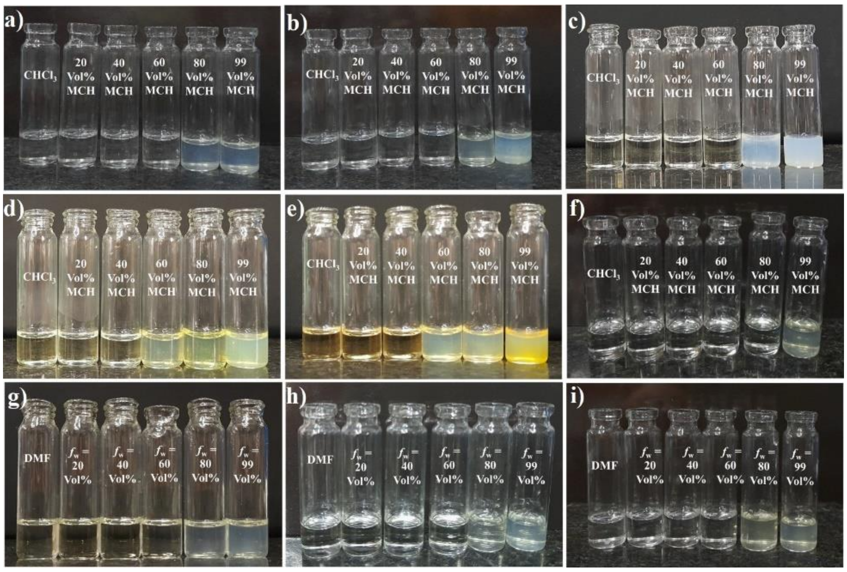

Figure 3. Photographs of formation of translucent solutions with increasing MCH content in $CHCl_3$ for 250 μM of (a) **NDI-1**, (b) **NDI-2**, (c) **NDI-2a**, (d) **NDI-2b**, (e) **NDI-3**, (f) **NDI-8** and water content in DMF for (g) **NDI-2**, (h) **NDI-5**, (i) **NDI-8**.

4.2.3. Microscopic study and DLS measurements

As translucency signifies possible self-aggregation, thus it was intriguing to confirm the formation of self-assembled structures by **NDI-1-9**. Consequently, all the translucent solutions formed by **NDI-1-9** in different binary solvent systems (99 vol% water in DMSO/DMF and MCH in $CHCl_3$ having maximum translucency) were investigated by microscopic techniques. TEM images of **NDI-1-9** (20 μM, f_w = 99 vol% in DMSO) exhibited almost spherical aggregates having dimension in the range of ~25-50 nm (Figure 4). Similarly, formation of organic nanoparticles of **NDI-1-9** (20 μM, f_w = 99 vol% in DMSO) having diameter of ~50 nm was observed in the respective FESEM images (Figure 5). Mean hydrodynamic diameters (D_h) of **NDI-1-9** (20 μM, f_w = 99 vol% in DMSO) organic nanoparticles measured by dynamic light-scattering (DLS) experiment, were found to be in the range of 40-175 nm with an average diameter of ~70, 60, 55, 45, 58, 60, 40, 38 and 60 nm, respectively (Figure 6). Corresponding correlogram data is provided in Figure 7.

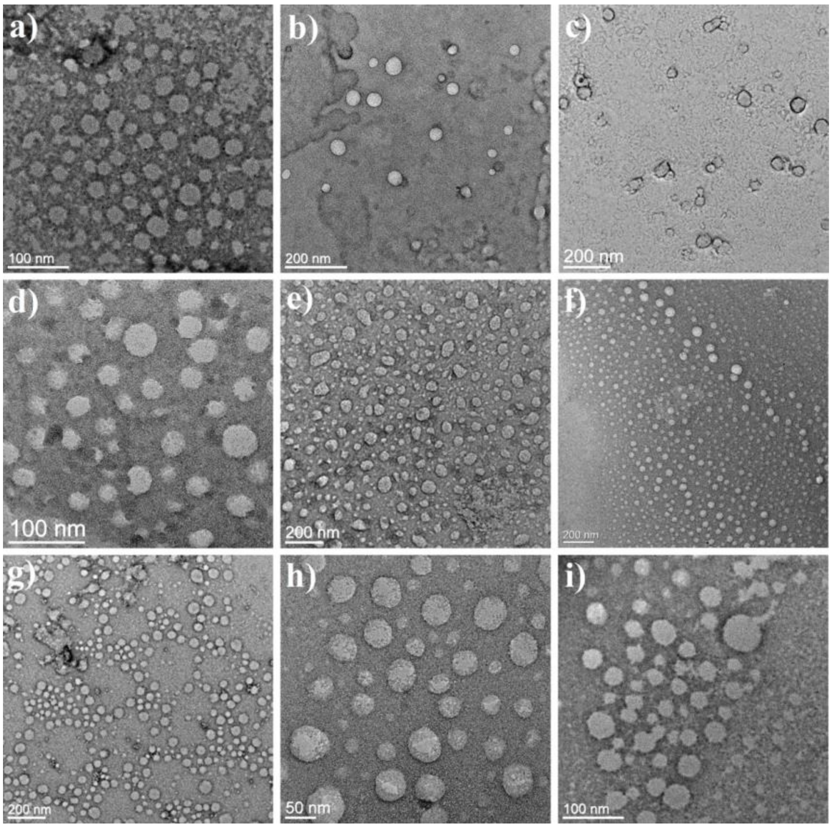

Figure 4. Negatively stained TEM images of 20 μM of (a) **NDI-1**, (b) **NDI-2**, (c) **NDI-3**, (d) **NDI-4**, (e) **NDI-5**, (f) **NDI-6**, (g) **NDI-7**, (h) **NDI-8** and (i) **NDI-9** in 1:99 (v/v) DMSO-water binary solvent mixture.

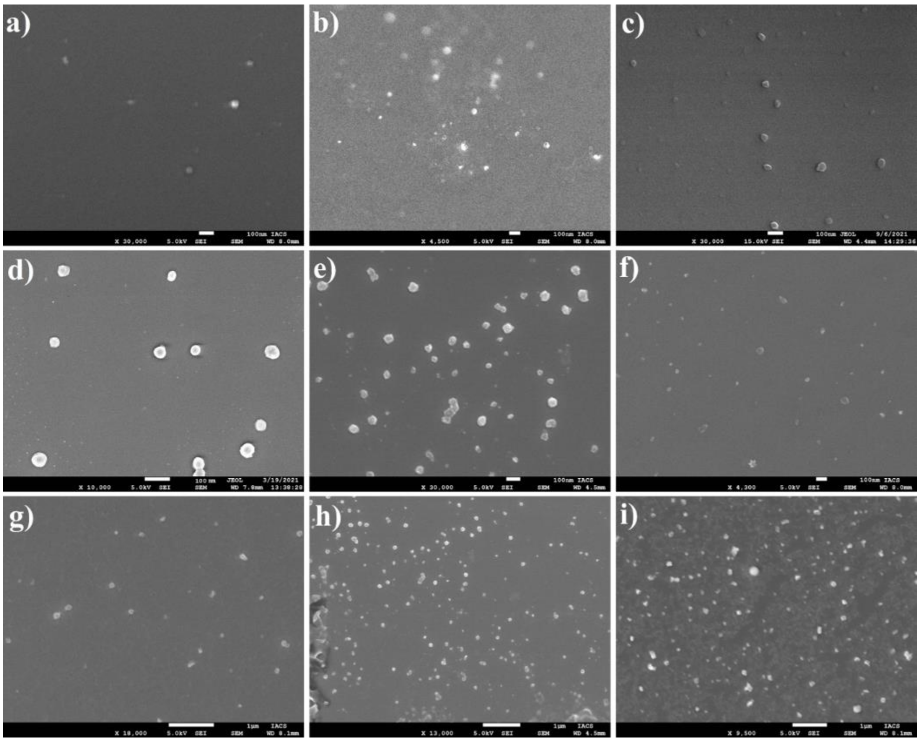

Figure 5. FESEM images of 20 μM of (a) **NDI-1**, (b) **NDI-2**, (c) **NDI-3**, (d) **NDI-4**, (e) **NDI-5**, (f) **NDI-6**, (g) **NDI-7**, (h) **NDI-8** and (i) **NDI-9** in 1:99 (v/v) DMSO-water binary solvent mixture.

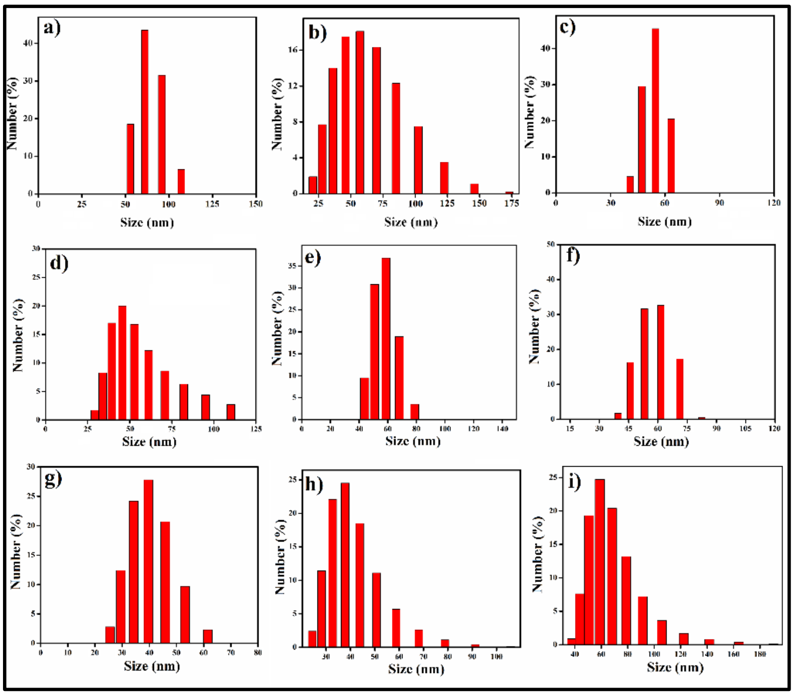

Figure 6. DLS plots of particles size distribution of 20 μM of (a) **NDI-1**, (b) **NDI-2**, (c) **NDI-3**, (d) **NDI-4**, (e) **NDI-5**, (f) **NDI-6**, (g) **NDI-7**, (h) **NDI-8** and (i) **NDI-9** in 1:99 (v/v) DMSO-water binary solvent mixture.

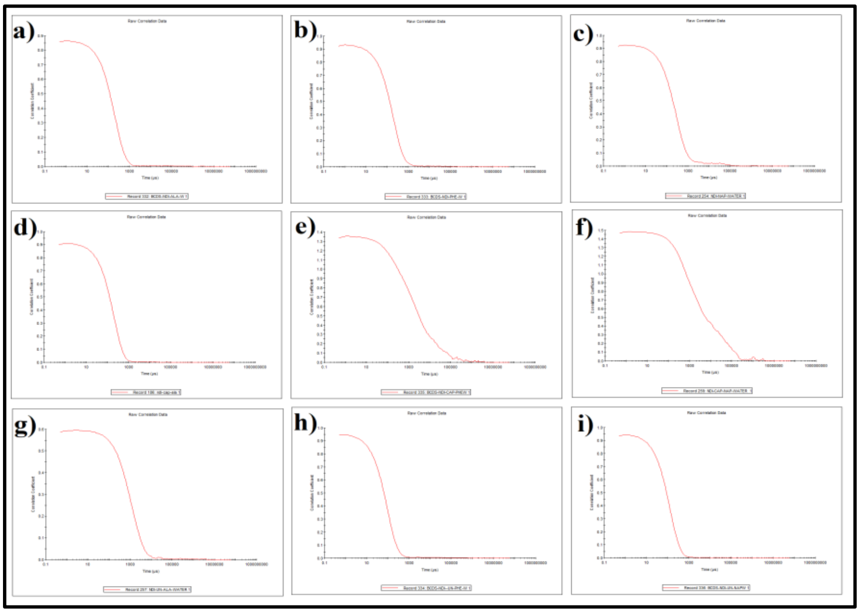

Figure 7. Correlogram of DLS plots of 20 μM of (a) **NDI-1**, (b) **NDI-2**, (c) **NDI-3**, (d) **NDI-4**, (e) **NDI-5**, (f) **NDI-6**, (g) **NDI-7**, (h) **NDI-8** and (i) **NDI-9** in 1:99 (v/v) DMSO-water binary solvent mixture.

Moreover, **NDI-1-3**, (20 μM, 99 vol% in MCH in $CHCl_3$) showed self-aggregated organic nanoparticles of ~50 nm in the corresponding TEM and FESEM images having D_h with number average diameter of ~73, 64 and 61 nm, respectively (Figure 8a-c, 9a-c, 10a-c). For **NDI-5** (20 μM, f_w = 99 vol% in DMF), organic nanoparticles of dimension ~50 nm was found in both TEM and FESEM images as well as in the corresponding DLS study (Figure 8d, 9d, 10d). Similarly, organic nanoparticles derived from **NDI-8** (20 μM) in 99 vol% in MCH in $CHCl_3$ displayed dimension of ~50 nm in TEM and SEM images with number average diameter of ~53 nm in DLS study (Figure 8e, 9e, 10e).

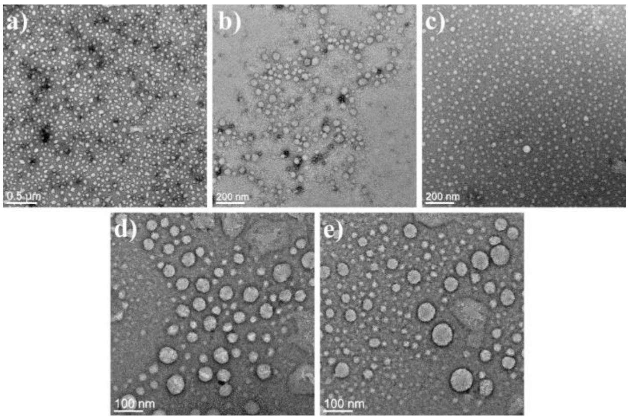

Figure 8. Negatively stained TEM images of 20 μM of (a) **NDI-1**, (b) **NDI-2**, (c) **NDI-3** in 1:99 (v/v) $CHCl_3$-MCH binary solvent mixture, (d) **NDI-5** in 1:99 (v/v) DMF-water binary solvent mixture and (e) **NDI-8** in 1:99 (v/v) $CHCl_3$-MCH binary solvent mixture.

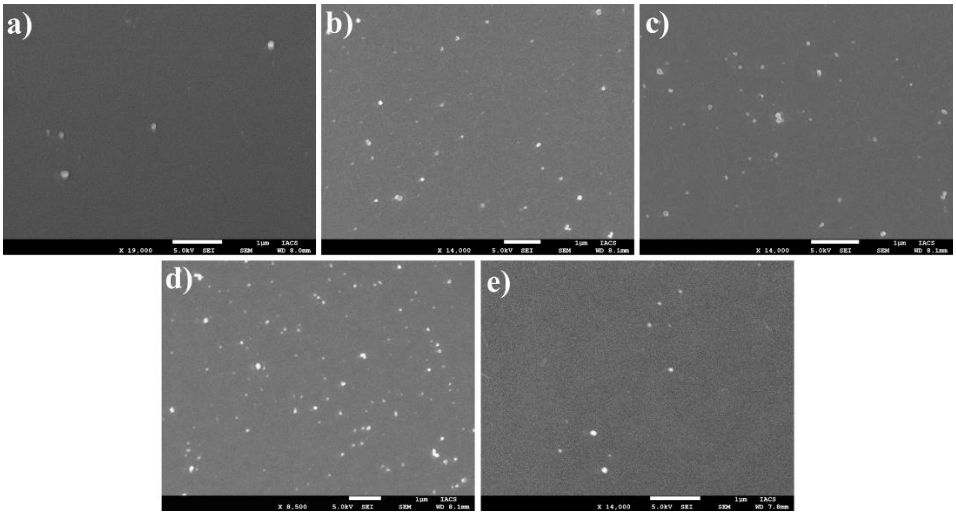

Figure 9. FESEM images of 20 µM of (a) **NDI-1**, (b) **NDI-2**, (c) **NDI-3** in 1:99 (v/v) $CHCl_3$-MCH binary solvent mixture, (d) **NDI-5** in 1:99 (v/v) DMF-water binary solvent mixture and (e) **NDI-8** in 1:99 (v/v) $CHCl_3$-MCH binary solvent mixture.

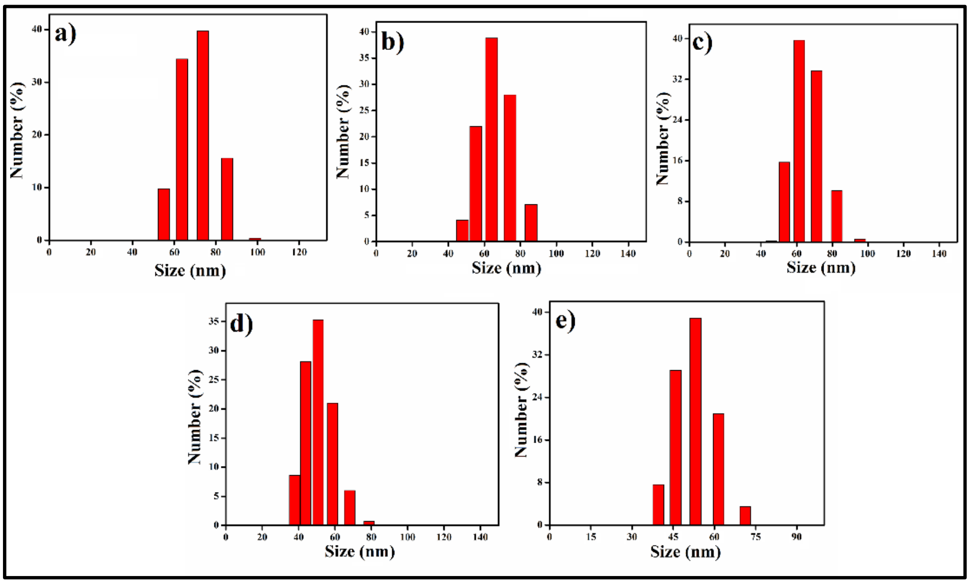

Figure 10. DLS plot of particles size distribution of 20 µM of (a) **NDI-1**, (b) **NDI-2**, (c) **NDI-3** in 1:99 (v/v) $CHCl_3$-MCH binary solvent mixture, (d) **NDI-5** in 1:99 (v/v) DMF-water binary solvent mixture and (e) **NDI-8** in 1:99 (v/v) $CHCl_3$-MCH binary solvent mixture.

Corresponding correlogram data of DLS study of **NDI-1, 2, 3** and **8** in 99 vol% MCH in $CHCl_3$ and **NDI-5** in 99 vol% water in DMF were provided in Figure 11. All these microscopic images and the corresponding DLS study of **NDI-1-9** confirmed the formation of self-aggregated organic nanoparticles in the varying compositions of investigated binary solvent systems.

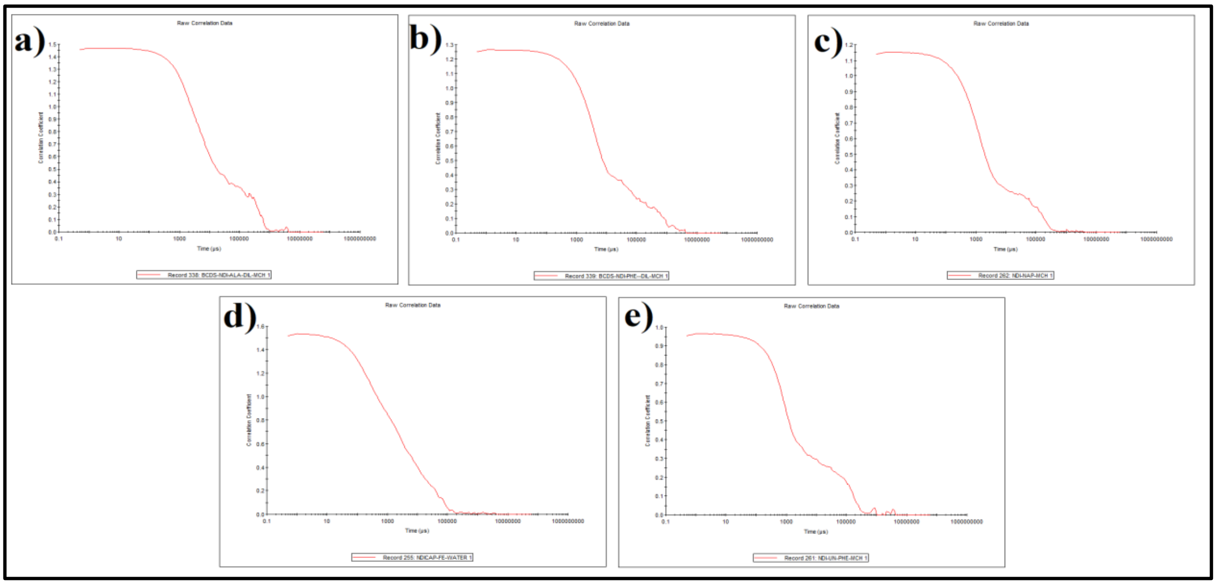

Figure 11. Correlogram of DLS plot of 20 μM of (a) **NDI-1**, (b) **NDI-2**, (c) **NDI-3** in 1:99 (v/v) $CHCl_3$-MCH binary solvent mixture, (d) **NDI-5** in 1:99 (v/v) DMF-water binary solvent mixture and (e) **NDI-8** in 1:99 (v/v) $CHCl_3$-MCH binary solvent mixture.

4.2.4. Photoluminescence property

All the NDI derivatives (250 μM) in three binary solvent systems (i.e. DMSO-water, DMF-water, $CHCl_3$-MCH) at varying compositions were irradiated under UV lamp (λ_{ex} = 365 nm). Among them, **NDI-1**, **NDI-2**, **NDI-3** and **NDI-8** in $CHCl_3$-MCH, **NDI-5** and **NDI-8** in DMF-water, **NDI-6** and **NDI-9** in DMSO-water showed fluorescence with varying emitting light (Figure 12). In case of **NDI-1**, **NDI-2**, and **NDI-3** greenish blue, bluish green and orange emission were observed respectively with increasing content of MCH in $CHCl_3$ from 60 vol% onwards. In each case the emission intensity was found to be most bright at 99 vol% of MCH (Figure 12a-c). Transparent non-fluorescent DMF solution of **NDI-5** started to exhibit green emission from f_w = 80 vol% water having brightest emission at f_w = 99 vol% water in DMF (Figure 12d). Likewise, for **NDI-8**, a greenish blue emission was noticed at 99 vol% MCH in $CHCl_3$ and 80 vol% water in DMF that became maximum at f_w = 99 vol% in respective solvent systems (Figure 12e,f). Furthermore, non-fluorescent DMSO solution of **NDI-6** and **NDI-9** showed bright yellow and orange emission from f_w = 60 vol% and f_w = 80 vol% water in DMSO and the emission intensity gets maximum at f_w = 99 vol% (Figure 12g,h). Thus, the NDI derivatives remain weakly fluorescent in molecularly dissolved state in "good" solvents while self-aggregation of the NDI based amphiphiles upon introduction of "bad" solvents results in bright fluorescence due to AIE. Intrigued by the observed photoluminescence properties of the NDI derivatives, fluorescence microscopic images of **NDI-1**, **NDI-2**, **NDI-3** and **NDI-8** (20 μM) in 99 vol% MCH in $CHCl_3$, **NDI-5** (20 μM) in f_w = 99 vol% in DMF, **NDI-6** and **NDI-9** (20 μM) in f_w = 99 vol% in DMSO were captured. Bright green fluorescent dots were observed for **NDI-1**, **NDI-2**, **NDI-5** and **NDI-8** while bright orange fluorescence dots were noted in case of **NDI-3**, **NDI-6** and **NDI-9** organic nanoparticles as a further proof of their emissive nature (Figure 13). The observed variation in the emission colour (upon UV radiation at λ_{ex} = 365 nm) from bluish green to orange might have been originating from the alteration in the molecular structure of the basic building block of the self-aggregated organic nanoparticles. Hence, these findings instigate us to explore the path of self-aggregation of the NDI-based amphiphiles by means of spectroscopy.

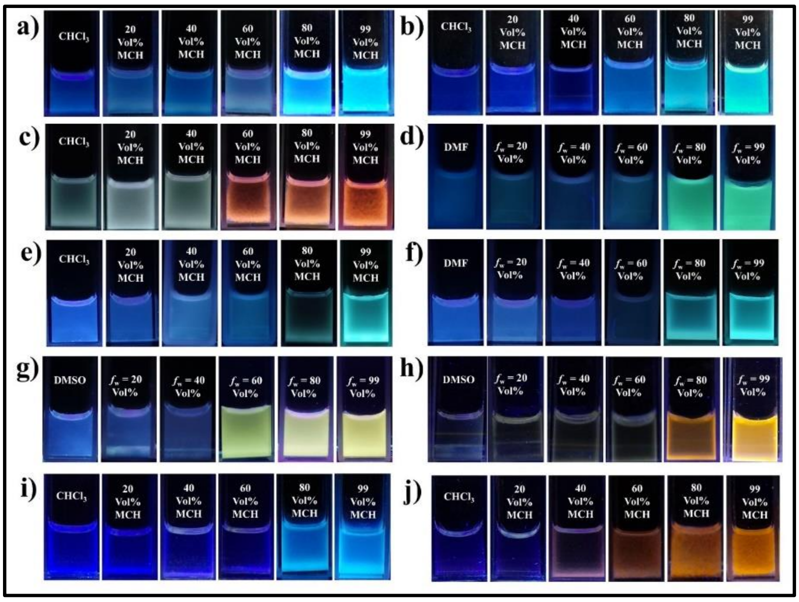

Figure 12. Photographs of change in emission colour of NDI derivatives (250 μM) with increasing MCH content in $CHCl_3$ for (a) **NDI-1**, (b) **NDI-2**, (c) **NDI-3**; (d) water content in DMF for **NDI-5**; (e) MCH content in $CHCl_3$ for **NDI-8**; (f) water content in DMF for **NDI-8**; water content in DMSO for (g) **NDI-6** and (h) **NDI-9** and MCH content in $CHCl_3$ for (i) **NDI-2a**, (j) **NDI-2b** upon UV-light irradiation (λ_{ex} = 365 nm).

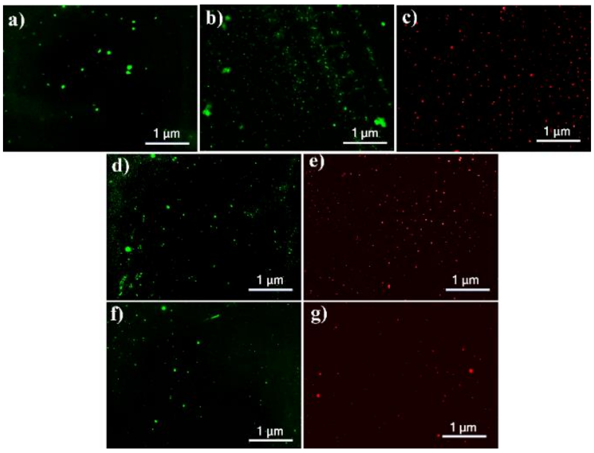

Figure 13. Fluorescence microscopic images of 20 μM of (a) **NDI-1**, (b) **NDI-2**, (c) **NDI-3** in 1:99 (v/v) $CHCl_3$-MCH solvent mixture, (d) **NDI-5** in 1:99 (v/v) DMF-water solvent mixture, (e) **NDI-6** in 1:99 (v/v) DMSO-water solvent mixture, (f) **NDI-8** in 1:99 (v/v) $CHCl_3$-MCH solvent mixture and (g) **NDI-9** in 1:99 (v/v) DMSO-water solvent mixture.

4.2.5. Spectroscopic investigation of self-aggregation

The nature of self-assembly of NDI derivatives in varying solvent systems was examined by UV-visible spectroscopy to understand the pathway of forming organic nanoparticles. Accordingly, UV spectra of all the NDI derivatives taken in pure DMSO represented their characteristic absorbance peaks in the molecularly dissolved state. Subsequently, the spectra were recorded in DMSO-water binary solvent systems of different composition to understand the deviation of the absorbance peaks and its nature compared to that of monomeric state. DMSO solution of **NDI-1-9** showed a characteristic absorbance band in the range 330-400 nm denoting the π-π* transition of the chromophore (Figure 14).[46] In the non-aggregated state (DMSO), the solutions of NDI derivatives (50 μM) showed absorbance maxima (λ_{max}) at 383 nm, 360 nm, 381 nm, 383 nm, 382 nm, 362 nm, 381 nm, 357 nm and 383 nm, respectively for **NDI-1** to **NDI-9** (Figure 14). With gradual increase in the water content, steady red shifting of the absorbance maxima took place in each of the amphiphile and at highest water amount (f_w = 99 vol%), the λ_{max} was observed at 387 nm, 363 nm, 385 nm, 390 nm, 386 nm, 365 nm, 384 nm, 362 nm and 388 nm, respectively in the same order from **NDI-1** to **NDI-9** (Figure 14). In general, the sharp monomeric peak got broadened along with an average shift of 4 nm with the increase in the amount of water in the DMSO solution of the NDI derivatives. These bathochromic shifts of absorbance maxima represented the formation of self-assembled organic nanoparticles possibly via *J*-aggregation (head-to-tail arrangement).

Additionally, UV-spectroscopic investigation of **NDI-1**, **NDI-2**, **NDI-3**, **NDI-5** and **NDI-8** was also carried out in the solvent compositions where emissive nature of organic particles was observed upon UV irradiation. Accordingly, UV-vis spectra were recorded for 50 μM of **NDI-1**, **NDI-2**, **NDI-3** and **NDI-8** in $CHCl_3$-MCH and that of **NDI-5** in DMF-water solvent systems (Figure 15a,b, e-g). Similar to the corresponding DMSO solutions, **NDI-1**, **NDI-2**, **NDI-3** and **NDI-8** dissolved in $CHCl_3$ and **NDI-5** dissolved in DMF exhibited a characteristic UV-vis band in the range 330-400 nm signifying the π-π* transition of the chromophoric units having absorbance maxima (λ_{max}) at 380 nm, 381 nm, 379 nm, 355 nm and 381 nm, respectively (Figure 15a,b, e-g). With gradual addition of MCH in chloroform solution of **NDI-1**, **NDI-2**, **NDI-3** and **NDI-8** and water in case of DMF solution of **NDI-5**, distinct red shifting of the absorbance maxima was noted. At 99 vol% MCH in $CHCl_3$ for **NDI-1**, **NDI-2**, **NDI-3** and **NDI-8** and f_w = 99 vol% water in DMF for **NDI-5** red shifted λ_{max} was obtained at 386 nm, 387 nm, 385 nm, 360 nm and 385 nm along with decrease in optical density and flattening of the nature of spectra (Figure 15a,b, e-g). These findings further led to the conclusion that self-assembly of the NDI derivatives took place via *J*-type aggregation.

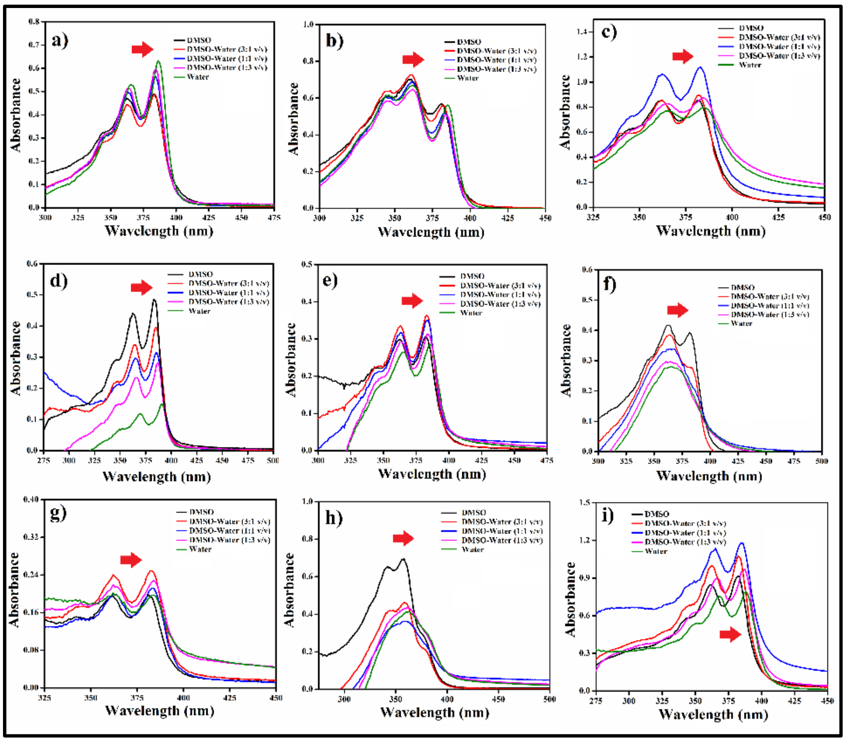

Figure 14. UV-Visible spectra of 50 μM of (a) **NDI-1**, (b) **NDI-2**, (c) **NDI-3**, (d) **NDI-4**, (e) **NDI-5**, (f) **NDI-6**, (g) **NDI-7**, (h) **NDI-8** and (i) **NDI-9** in DMSO-water solvent system.

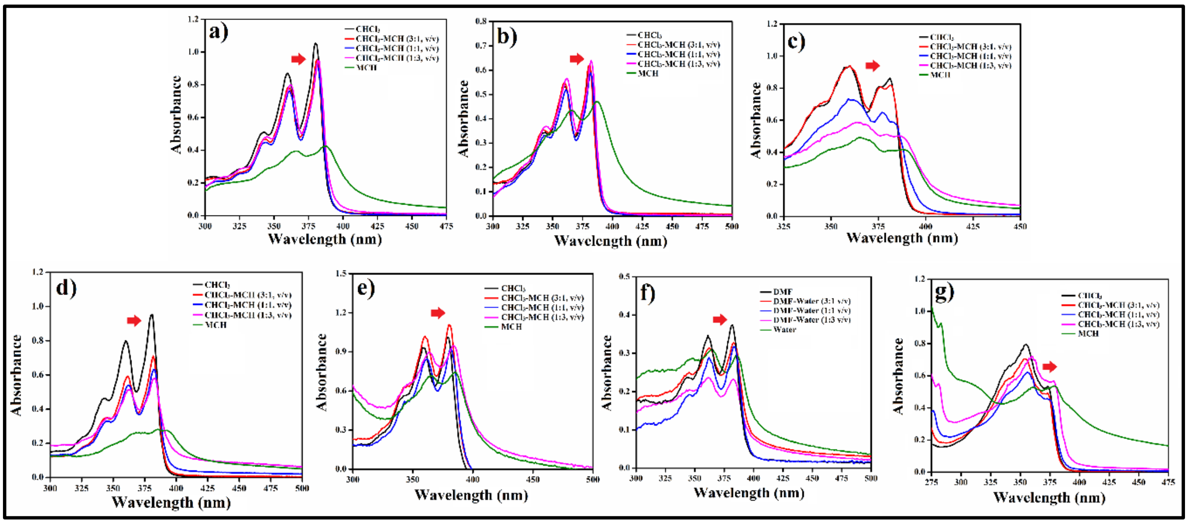

Figure 15. UV-visible spectra of 50 μM of (a) **NDI-1**, (b) **NDI-2**, (c) **NDI-2a**, (d) **NDI-2b**, (e) **NDI-3** in $CHCl_3$-MCH binary solvent mixture, (f) **NDI-5** in DMF-water binary solvent mixture and (g) **NDI-8** in $CHCl_3$-MCH binary solvent mixture.

Manifestation of supramolecular self-assembly lies upon the involvement of diverse non-covalent forces. To this end, solvent dependent ^{1}H-NMR spectra of NDI based amphiphiles were recorded in varying compositions of DMSO-d_6-D_2O solvent system to investigate the participation of hydrophobic and π-π stacking interactions during self-aggregation (Figure 16). The aromatic protons of **NDI-1** in its molecular state in DMSO-d_6 displayed sharp NMR signal in the region δ = 8.68 ppm due to the NDI aromatic core protons (Figure 16a). With increasing the amount of D_2O from 0 vol% to 33 vol% and subsequently to 50 vol%, the NMR peaks got shifted to δ = 8.61 ppm and δ = 8.46 ppm, respectively. Similarly, for **NDI-2**, ^{1}H-NMR peak corresponding to NDI core got shifted from δ = 8.62 to δ = 8.56 and to finally δ = 8.46 with increasing the D_2O content indicating the commencement of self-aggregation (Figure 16b). Additionally, NMR signals correspond to aromatic protons of phenyl moiety got broadened and shifted from δ = 7.26-7.31 in DMSO-d_6 (the non-self-assembled state) to δ = 6.96-7.09 at 33 vol% and δ = 6.89-6.97 at 50 vol% D_2O in DMSO-d_6 (Figure 16b). In case of **NDI-3**, similarly aromatic protons of both NDI core and naphthyl unit exhibited broadening an up field shifting of NMR peaks from δ = 8.58 (NDI core), δ = 7.94, 7.61-7.76 and 7.31-7.39 (naphthyl part) in non-self-assembling solvent DMSO-d_6 to δ = 8.49 (NDI core), δ = 7.82, 7.60-7.42 and 7.19-7.26 (naphthyl part) in 2:1, (v/v) DMSO-d_6- D_2O and finally to δ = 8.32 (NDI core), δ = 7.70, 7.26-7.50 and 7.04-7.17 (naphthyl part) in 1:1, (v/v) DMSO-d_6-D_2O binary solvent system (Figure 16c). Solvent dependent ^{1}H-NMR spectra of **NDI-5** and **NDI-8** were also taken by varying the solvent composition of DMSO-d_6-D_2O from pure DMSO-d_6 where the amphiphile remains in molecular state to 2:1, v/v DMSO-d_6-D_2O and 1:1, v/v DMSO-d_6-D_2O (self-aggregate state). For **NDI-5**, NMR signals corresponding to aromatic protons of NDI core (δ = 8.64) and phenyl moiety (δ = 7.10-7.59) in DMSO-d_6 got broadened and shifted to δ = 8.50, δ = 6.92-7.32 at 2:1, v/v DMSO-d_6-D_2O and δ = 8.39 and δ = 6.88-7.16 at 1:1, v/v DMSO-d_6-D_2O, respectively (Figure 16d). Likewise, **NDI-8** showed ^{1}H-NMR signal at δ = 8.67 (NDI core) and δ = 7.12-7.27 (phenyl residue) in DMSO-d_6, at δ = 8.49-8.52 (NDI core) and δ = 7.05-7.2 (phenyl residue) at 33 vol% D_2O in DMSO-d_6 and at δ = 8.4-8.46 (NDI core) and δ = 6.93 (phenyl residue) at 50 vol% D_2O in DMSO-d_6 (Figure 16e). In all the above cases, π-π stacking between the chromophoric units and the phenyl and naphthyl moieties of the amino acids is initiated with the introduction of D_2O that led to the upfield shift in the ^1H-NMR signals demonstrating the development of self-assembled structures in presence of increasing content of water in DMSO.

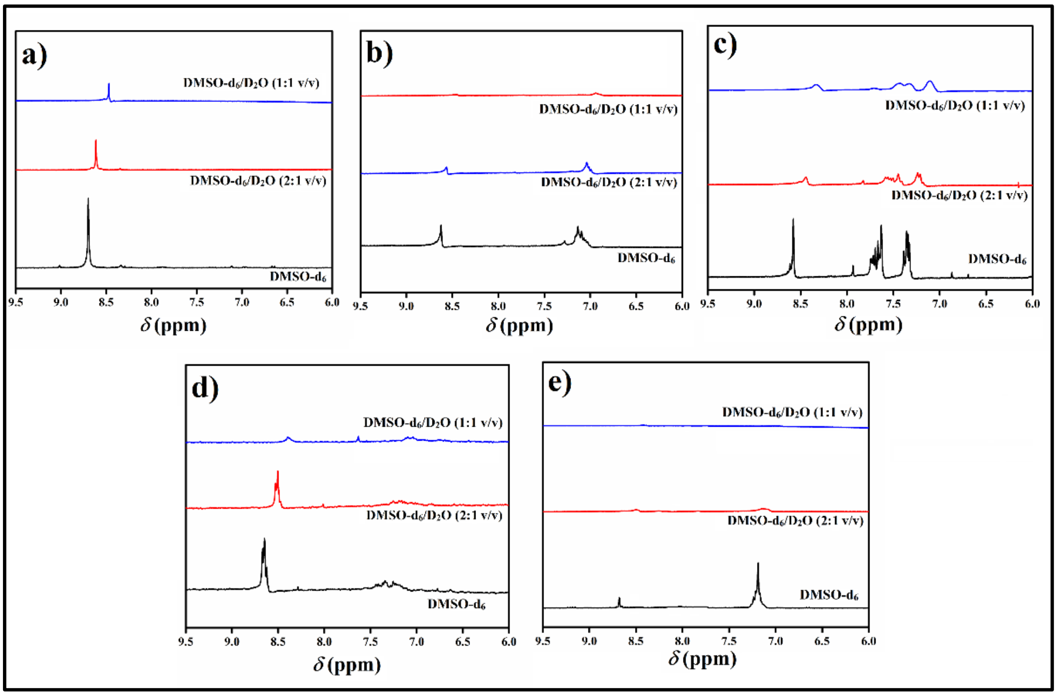

Figure 16. Solvent dependent ^{1}H-NMR spectra of 1 mM of (a) **NDI-1**, (b) **NDI-2**, (c) **NDI-3**, (d) **NDI-5** and (e) **NDI-8**.

4.2.6. Fluorescence spectroscopy

The observed varying range of emissions of the NDI derivatives upon irradiation (Figure 12) under UV lamp (λ_{ex} = 365 nm) instigated us to investigate the fluorescence spectroscopic behaviour of the emitting NDI based amphiphiles in the respective solvent systems. Fluorescence spectra of 50 µM of **NDI-1**, **NDI-2**, and **NDI-3** in $CHCl_3$ showed respective emission maxima (λ_{em}) at 406 nm, 393 nm and 420 nm upon excitation (λ_{ex}) at 350 nm (Figure 17a-c). With gradual addition of MCH, the fluorescence intensity of these peaks got steadily reduced. At 80 vol % of MCH in $CHCl_3$, an excimer peak was found to be appeared having λ_{em} at 484 nm for **NDI-1** (Figure 17a). Further addition of MCH led to the enhancement in the emission intensity being maximum at 99 vol% MCH in $CHCl_3$ (Figure 17a). Amphiphiles started to assemble seemingly through the stacking of the chromophoric units with rise in MCH content which is evident from the newly generated excimer peak at 484 nm on account of AIE. Similar trends were observed for the other two NDI derivatives (**NDI-2** and **NDI-3**). Excimer peaks were observed with λ_{em} at 495 nm and 590 nm for **NDI-2** and **NDI-3** from 80 vol% and 60 vol% MCH in $CHCl_3$, respectively (Figure 17b,c). In both cases, the emission intensities were maximum at 99 vol% MCH in $CHCl_3$. These findings were in concurrence with the preceding observation of UV irradiated (λ_{ex} = 365 nm) organic nanoparticles where **NDI-1**, **NDI-2**, and **NDI-3** showed greenish blue, bluish green, and orange emission, respectively

(Figure 12a-c). Enhancement in the π-electron cloud density (from L-alanine to L-phenylalanine to naphthyl-L-alanine) in the side chain of naphthalenediimide core possibly facilitated the electron transfer at a lesser energy to the electron deficient NDI core that resulted in increased wavelength of emission maxima.[47,48] From **NDI-1** to **NDI-2**, inclusion of one phenyl ring at each side of NDI led to 11 nm red shifting of λ_{em} from 484 to 495 nm. Notably, introduction of additional phenyl ring in the form of naphthyl moiety in each side of NDI from phenylalanine to naphthylalanine (**NDI-2** to **NDI-3**) resulted in significant (95 nm) red shift of λ_{em} from 495 to 590 nm. Overall, 106 nm red shifting in λ_{em} was observed with increasing π-electron density upon variation of the terminal unit of NDI from alanine to naphthylalanine. Relative fluorescence quantum yield of **NDI-1**, **NDI-2** and **NDI-3** at 99 vol% MCH in $CHCl_3$ was calculated to be 0.54%, 0.72% and 0.60%, respectively (with respect to quinine sulfate hydrate).

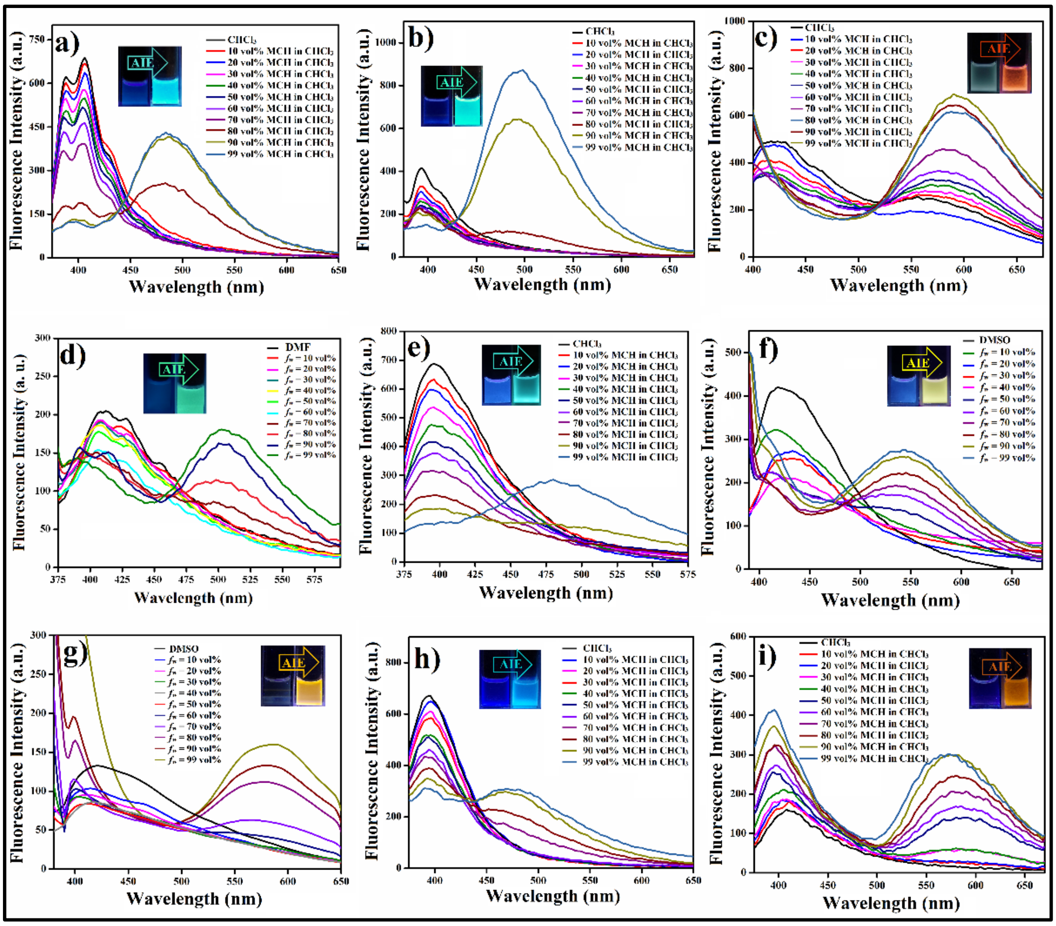

Figure 17. Fluorescence spectra (λ_{ex} = 350 nm) of 50 μM of (a) **NDI-1**, (b) **NDI-2**, (c) **NDI-3** in $CHCl_3$-MCH binary solvent mixture, (d) **NDI-5** in DMF-water binary solvent mixture, (e) **NDI-8** in $CHCl_3$-MCH binary solvent mixture, (f) **NDI-6**, (g) **NDI-9** in DMSO-water binary solvent mixture and (h) **NDI-2a**, (i) **NDI-2b** in $CHCl_3$-MCH binary solvent mixture.

Next, we investigated the emission spectra of **NDI-5** and **NDI-8** (50 μM) to analyze the influence of alkyl spacer (C-6 for **NDI-5** and C-11 for **NDI-8**) between electron deficient NDI core and π electron containing L-phenylalanine terminal. **NDI-5** in molecular dissolved state in DMF showed λ_{em} at 410 nm (Figure 17d). With increasing amount of water, intensity of this monomeric peak kept on reducing while at and above f_w = 70 vol%, an excimer appeared at 505 nm due to AIE. Fluorescence intensity got gradually escalated with further increase in water and reached its maximum at 1: 99 (v/v), DMF-water (Figure 17d). Likewise, λ_{em} for monomeric **NDI-8** was observed at 400 nm and 410 nm in $CHCl_3$ and in DMF (Figure 17e, Figure 18). Here too, formation of excimer peak was observed at 480 nm at 90 vol% MCH in $CHCl_3$ and 80 vol% water in DMF. As expected, the emission intensity was maximum at 99 vol% MCH in $CHCl_3$ and f_w = 99 vol% in both cases (Figure 17e, Figure 18). These results were in agreement with the previously observed UV irradiated (λ_{ex} = 365 nm) samples of **NDI-5** and **NDI-8** that displayed green and greenish blue emission at f_w = 99 vol% in respective solvent systems (Figure 12d-f). Relative fluorescence quantum yield of **NDI-5** and **NDI-8** at 99 vol% water in DMF and 99 vol% MCH in $CHCl_3$ is calculated to be 0.4% and 0.29%, respectively (with respect to quinine sulfate hydrate) which are ~1.8 fold and ~2.5 fold lower compared to that of **NDI-2** where L-phenylalanine is directly linked to electron deficient NDI core without any spacer. Thus, increase in spacer length between π-electron donating terminal unit and the NDI core might have slightly impeded the electron transfer in the aggregated organic nanoparticle that affected the corresponding quantum yield.

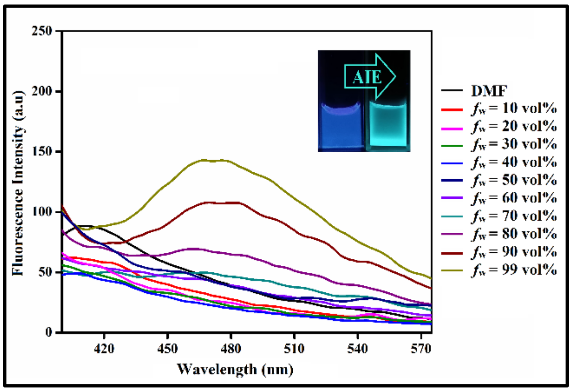

Figure 18. Fluorescence spectra (λ_{ex} = 350 nm) of **NDI-8** [50 μM] in DMF-water binary solvent mixture.

To further ascertain the influence of spacer length on AIE, fluorescence properties of **NDI-6** and **NDI-9** (50 μM) were investigated in DMSO-water binary solvent system (Figure 17f,g). In pure DMSO, **NDI-6** and **NDI-9** showed monomeric λ_{em} at 420 nm which decreased gradually with increment of water. At and above f_w = 50 vol% for **NDI-6** and f_w = 70 vol% for **NDI-9**, excimer peak was observed at λ_{em} = 545 nm and 585 nm, respectively. Emission intensity got increased with gradual increase in water up to 99 vol% in DMSO (Figure 17f,g). Such emissive nature also supports the UV irradiated **NDI-6** and **NDI-9** samples at f_w = 99 vol% that showed bright yellow and orange emission (Figure 12g,h). Relative fluorescence quantum yield of **NDI-6** and **NDI-9** at f_w = 99 vol% is estimated to be 0.34% and 0.31% respectively (with respect to quinine sulfate hydrate) which are ~1.77-fold and ~1.94-fold lower compared to that of **NDI-3** which has no spacer between NDI core and naphthyl alanine residue. Thus, the observed trend of the influence of spacer length on AIE in case of naphthyl alanine appended NDI amphiphiles (**NDI-3**, **NDI-6** and **NDI-9**) is analogous to that of L-phenylalanine containing NDI derivatives (**NDI-2**, **NDI-5** and **NDI-8**). Hence, it is evident that when the terminal amino acid residue is directly linked with the NDI core (**NDI-1**, **NDI-2** and **NDI-3**), the quantum yields were notably higher than that of the amphiphiles where donor and accepter part are separated by C-6 (6-amino caproic acid in **NDI-5** and **NDI-6**) and C-11 (11-amino undecanoic acid in **NDI-8** and **NDI-9**) spacer. Augmented distance between π-electron donating amino acid and electron deficient NDI core presumably played a key role by means of inducing relaxation in the restricted intermolecular rotation in presence of flexible alkyl chain that plummeted the quantum yield of FONPs.

Next, we compared the fluorescence properties of **NDI-4**, **NDI-5** and **NDI-6**. The key role of π-electron density at the terminal moiety of NDI amphiphiles got also affirmed from the varying emission maxima of the AIE in respective organic nanoparticles. **NDI-5** and **NDI-6** showed λ_{em} at 505 nm and 545 nm in f_w = 99 vol% water in DMF and DMSO, respectively (Figure 17d,f). In contrast, **NDI-4** showed no photoluminescence in those solvent systems. The reason behind non-fluorescent **NDI-4** organic nanoparticle was perhaps due to the absence of π-electron containing aromatic rings in the alanine residue as well as the distance (C-6) between donor (alanine) and accepter (NDI core) part. However, in case of L-phenylalanine containing NDI-amphiphile with C-6 spacer, distinct AIE was observed with λ_{em} at 505 nm. Moreover, a red shift of 40 nm was noted upon moving from **NDI-5** to **NDI-6** possibly due to the increasing π-electron density at the terminal moiety from phenylalanine to naphthyl alanine. Similarly, in case of **NDI-7**, **NDI-8** and **NDI-9**, no emission was observed for **NDI-7** (due to lack of aromatic residue in donor unit and increased distance (C-11) between donor and acceptor) while prominent AIE was seen for both **NDI-8** (λ_{em} = 480 nm) to **NDI-9** (λ_{em} = 585 nm). Notably, a red shift of 105 nm in the emission maxima was observed from **NDI-8** to **NDI-9** (Figure 17e,g, 18) because of increased π electron density in the molecular backbone. Hence it is further established that prevalence of more π-electron cloud in the side chain of naphthalenediimide unit resulted in increased wavelength of emission maxima for the AIE of FONPs possibly due to smooth transfer of electron to the electron deficient NDI core.

To establish further the crucial role of π-electron cloud in modulating the AIE, we synthesized two more NDI based amphiphiles having nitro (-NO_2) and methoxy (-OMe) substituted L-phenylalanine (**NDI-2a** and **NDI-2b**) directly linked with NDI core (Figure 1). The electron withdrawing (-NO_2) and electron donating (-OMe) groups were included in the side chain substitution in order to draw a comparison with the unsubstituted counterpart, **NDI-2**. Both **NDI-2a** and **NDI-2b** were completely soluble in $CHCl_3$. MCH solvent was added gradually to the $CHCl_3$ solutions of these two amphiphiles and these mixed solutions (250 μM) were irradiated under UV lamp (λ_{ex} = 365 nm). Greenish blue and orange emission were observed for **NDI-2a** and **NDI-2b** along with prominent translucency at and above 80 vol% and 60 vol% MCH in $CHCl_3$, respectively (Figure 3c,d, Figure 12i,j). Their aggregation pattern was investigated by solvent dependent UV-vis spectroscopy with increasing content of MCH in $CHCl_3$. Red shifted absorbance maxima were observed where monomeric peaks at 358 nm and 381 nm got shifted to 364 nm and 386 nm respectively for **NDI-2a** (50 μM) and **NDI-2b** (50 μM) at aggregated state (99 vol% MCH in $CHCl_3$) indicating *J*-type aggregation similar to that of other NDI derivatives (Figure 15c,d,). Subsequently, in the corresponding fluorescence spectra (λ_{ex} = 350 nm), **NDI-2a** and **2b** (50 μM) in molecularly dissolved state showed λ_{em} at 394 nm and 408 nm in $CHCl_3$, respectively (Figure 17h,i). With gradual addition of MCH, the fluorescence intensity of the monomeric peaks of **NDI-2a** steadily decreased with the emergence of an excimer peak due to AIE from 70 vol% at 475 nm. Expectedly, the emission intensity of this peak reached maximum at 99 vol% MCH in $CHCl_3$ (Figure 17h). Similarly, in case of **NDI-2b**, excimer peak was found to appear from 50 vol% MCH in $CHCl_3$ having maximum intensity at 99 vol% with λ_{em} at 570 nm (Figure 17i). Therefore, in comparison to the emission maxima of unsubstituted **NDI-2** (λ_{em} = 495 nm), introduction of electron withdrawing group -NO_2 in the **NDI-2** backbone led to a blue shift of ~20 nm in λ_{em} (475 nm) for **NDI-2a** most possibly due to decline in π-electron density in the side chain of NDI. On the other hand, incorporation of electron donating group -OMe resulted in a red shift of ~75 nm in λ_{em} (570 nm) for **NDI-2b** due to enhanced availability of π-electron in the side chain of NDI. This observation further ascertained that fluorescence property due to AIE of organic nanoparticle gets modulated depending on the presence of transferrable π-electron to the NDI core. Overall, this signifies the influence of electronic structure of the substituents in tuning the emission maxima of NDI derivatives causing multi colour luminescence (Figure 19).

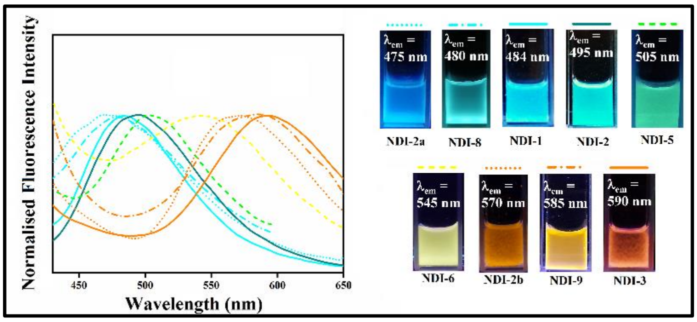

Figure 19. Tuneable emission maxima (with normalised emission intensity) of substituent-modified NDI derivatives (**NDI-1, 2, 2a, 2b, 3, 5, 6, 8** and **9** (λ_{ex} = 350 nm)) along with corresponding photographs of multicolour emission of the NDI derivatives irradiated with a UV-lamp (λ_{ex} = 365 nm).

Furthermore, concentration-dependent fluorescence spectra of **NDI-1**, **2**, **2a, 2b**, **3**, **5**, **6**, **8** and **9** in varying binary solvent mixtures were recorded within concentration range of 5-300 µM (Figure 20). With increase in concentration of NDI derivatives, the emission intensity of the corresponding excimer bands at the respective emission maxima steadily improved and became saturated at and above 150 µM, 150 µM, 200 µM, 100 µM, 100 µM, 200 µM, 200 µM, 200 µM and 50 µM for **NDI-1**, **2**, **2a, 2b**, **3**, **5**, **6**, **8** and **9**, respectively (Figure 20). This reflects that with increase in the NDI concentration, improvement in the AIE was observed perhaps due to the participation of higher number of amphiphilic units in the development of self-aggregated organic nanoparticles.

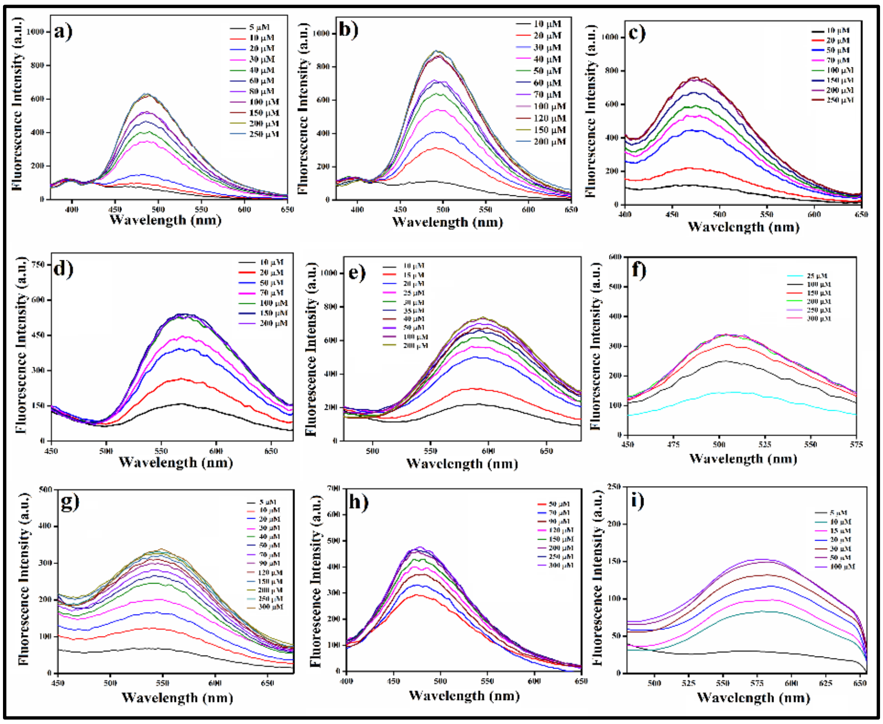

Figure 20. Concentration-dependent emission spectra of (a) **NDI-1**, (b) **NDI-2**, (c) **NDI-2a**, (d) **NDI-2b**, (e) **NDI-3** in 1:99 (v/v) $CHCl_3$-MCH solvent mixture, (f) **NDI-5** in 1:99 (v/v) DMF-water solvent mixture, (g) **NDI-6** in 1:99 (v/v) DMSO-water solvent mixture, (h) **NDI-8** in 1:99 (v/v) $CHCl_3$-MCH solvent mixture and (i) **NDI-9** in 1:99 (v/v) DMSO-water solvent mixture.

4.2.7. Time-resolved study

In continuation with the preceding observations, fluorescence lifetime was measured by TCSPC for an elaborate comprehension of the AIE phenomenon of these NDI derivatives. Corresponding investigations were carried out with picosecond excitation at 375 nm for all the emitting NDI derivatives (50 µM) in pure and binary solvent systems at monomeric and self-aggregated state. In all cases, triexponentially fitted decay curves were obtained (Figure 21). For **NDI-1**, **NDI-2**, **NDI-3** dissolved in $CHCl_3$, the fluorescence was monitored at λ_{mon} = 406 nm, 393 nm and 420 nm, respectively and their average lifetime was found to be 0.03 ns, 0.10 ns and 0.37 ns (Table 1). Emission of their respective aggregated FONPs was monitored at λ_{mon} = 484 nm, 495 nm and 590 nm in 80 vol%, 80 vol% and 60 vol% MCH in $CHCl_3$ and also in 99 vol% MCH in $CHCl_3$ (Figure 21a-c). The average lifetime values were 0.31 ns and 0.55 ns; 0.61 ns and 1.24 ns; and 1.24 ns and 1.48 ns for **NDI-1**, **NDI-2**, and **NDI-3**, respectively at 80 or 60 vol% and 99 vol% MCH in $CHCl_3$ (Table 1). In all the cases, pre-associated excimer in the AIE resulted in the long decay lifetime at higher content of MCH. The average lifetime value of **NDI-5** was calculated to be 0.88 ns, 1.38 ns and 1.54 ns in DMF (λ_{mon} = 410 nm), f_w = 70 and 99 vol% water (λ_{mon} = 505 nm) in DMF, respectively (Table 1, Figure 21d). For **NDI-6**, in DMSO (λ_{mon} = 420 nm), f_w = 50 and 99 vol% (λ_{mon} = 545 nm) water in DMSO, the average lifetime was estimated to be 1.07 ns, 1.36 ns and 1.77 ns, respectively (Table 1, Figure 21e). In both cases, longer decay time was observed at higher percentage of water for the aggregated organic nanoparticles. Similarly, **NDI-8** had a longer decay time of 1.08 ns at 99 vol% MCH in $CHCl_3$ (λ_{mon} = 480 nm) compared to that at 90 vol% (0.89 ns; λ_{mon} = 480 nm) and that in only $CHCl_3$ (0.11 ns; λ_{mon} = 400 nm) (Table 1, Figure 21f). In the same way, a relatively longer decay time of 1.10 ns was observed for **NDI-9** in 99 vol% water in DMSO (λ_{mon} = 585 nm) whereas it had average lifetime of 0.10 ns and 0.17 ns in 0 vol% (λ_{mon} = 420 nm) and 70 vol% water in DMSO (λ_{mon} = 585 nm) (Table 1, Figure 21g). A longer decay time of 0.74 ns and 0.18 ns was observed for **NDI-2a** and **NDI-2b** in 99 vol% MCH in $CHCl_3$ (λ_{mon} = 475 nm and 570 nm, respectively) compared to average lifetimes of their $CHCl_3$ solutions and solutions with lower percentage of MCH in $CHCl_3$ (Table 1, Figure 21h,i). The average lifetime of **NDI-2a** in $CHCl_3$ and 70 vol% MCH in $CHCl_3$ was 0.03 ns (λ_{mon} = 394 nm) and 0.09 ns (λ_{mon} = 475 nm) while for **NDI-2b**, it was 0.02 ns (λ_{mon} = 408 nm) and 0.17 ns (λ_{mon} = 570 nm) at $CHCl_3$ and 50 vol% MCH in $CHCl_3$ (Table 1, Figure 21h,i). Hence, higher decay time was noted for all the self-aggregated organic nanoparticles primarily owing to the aggregation-induced emission.

Table 1. Lifetime values of NDI derivatives in the presence of different fractions of MCH in $CHCl_3$, water in DMSO and water in DMF (λ_{ex} = 375 nm).

NDI	solvent	λ_{mon} (nm)	τ_1 (ns) (a_1)	τ_2 (ns) (a_2)	τ_3 (ns) (a_3)	Average lifetime (τ) (ns)
NDI-1	$CHCl_3$	406	0.543 (0.002)	1.205 (0.0003)	0.023 (0.997)	0.03
NDI-1	80 vol% MCH in $CHCl_3$	484	1.329 (0.070)	8.465 (0.010)	0.141 (0.920)	0.31
NDI-1	99 vol% MCH in $CHCl_3$	484	1.133 (0.184)	4.482 (0.027)	0.279 (0.789)	0.55
NDI-2	$CHCl_3$	393	0.166 (0.439)	0.382 (0.016)	0.031 (-0.545)	0.10
NDI-2	80 vol% MCH in $CHCl_3$	495	1.691 (0.113)	7.633 (0.031)	0.211 (0.856)	0.61
NDI-2	99 vol% MCH in $CHCl_3$	495	2.164 (0.213)	9.028 (0.053)	0.409 (0.734)	1.24
NDI-3	$CHCl_3$	420	1.210 (0.100)	4.466 (0.018)	0.186 (0.882)	0.37
NDI-3	60 vol% MCH in $CHCl_3$	590	1.808 (0.307)	0.393 (0.607)	5.220 (0.086)	1.24
NDI-3	99 vol% MCH in $CHCl_3$	590	1.508 (0.548)	0.494 (0.360)	5.202 (0.091)	1.48
NDI-5	DMF	410	1.056 (0.536)	0.388 (0.437)	5.259 (0.027)	0.88
NDI-5	70 vol% water in DMF	505	2.781 (0.132)	10.813 (0.036)	0.743 (0.831)	1.38
NDI-5	99 vol% water in DMF	505	2.535 (0.210)	8.678 (0.089)	0.338 (0.701)	1.54
NDI-6	DMSO	420	1.452 (0.489)	0.275 (0.479)	7.011 (0.032)	1.07
NDI-6	50 vol% water in DMSO	545	3.597 (0.136)	17.643 (0.035)	0.316 (0.830)	1.36
NDI-6	99 vol% water in DMSO	545	3.423 (0.207)	14.778 (0.045)	0.526 (0.747)	1.77
NDI-8	$CHCl_3$	400	0.336 (0.074)	0.076 (0.920)	1.793 (0.006)	0.11
NDI-8	90 vol% MCH in $CHCl_3$	480	1.810 (0.195)	7.802 (0.035)	0.339 (0.771)	0.89
NDI-8	99 vol% MCH in $CHCl_3$	480	1.739 (0.160)	9.526 (0.057)	0.330 (0.782)	1.08
NDI-9	DMSO	420	0.906 (0.031)	4.157 (0.005)	0.048 (0.964)	0.10
NDI-9	70 vol% water in DMSO	585	0.856 (0.051)	4.535 (0.009)	0.088 (0.940)	0.17
NDI-9	99 vol% water in DMSO	585	2.035 (0.206)	7.195 (0.071)	0.235 (0.723)	1.10
NDI-2a	$CHCl_3$	394	0.191 (0.013)	0.025 (0.987)	2.687 (0.0004)	0.03
NDI-2a	70 vol% MCH in $CHCl_3$	475	0.968 (0.028)	4.445 (0.004)	0.046 (0.968)	0.09
NDI-2a	99 vol% MCH in $CHCl_3$	475	1.72 (0.150)	8.218 (.033)	0.259 (0.817)	0.74
NDI-2b	$CHCl_3$	408	1.02 (0.002)	3.968 (0.0006)	0.017 (0.997)	0.02
NDI-2b	50 vol% MCH in $CHCl_3$	570	0.856 (0.051)	4.535 (0.009)	0.088 (0.94)	0.17
NDI-2b	99 vol% MCH in $CHCl_3$	570	0.754 (0.056)	3.353 (0.01)	0.099 (0.93)	0.18

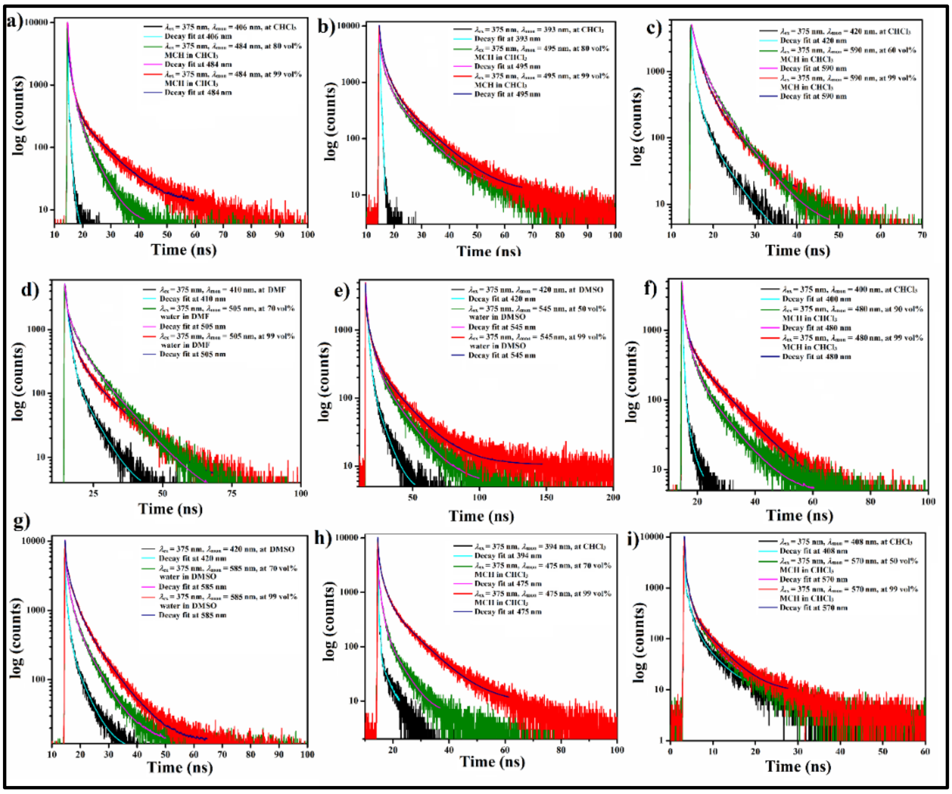

Figure 21. TCSPC decay profiles of 50 μM of (a) **NDI-1**, (b) **NDI-2**, (c) **NDI-3** in $CHCl_3$-MCH solvent mixture, (d) **NDI-5** in DMF-water solvent mixture, (e) **NDI-6** in DMSO-water solvent mixture, (f) **NDI-8** in $CHCl_3$-MCH solvent mixture and (g) **NDI-9** in DMSO-water binary solvent mixture and (h) **NDI-2a**, (i) **NDI-2b** in $CHCl_3$-MCH solvent mixture.

4.3. CONCLUSION

In this present work, NDI based amino acid appended amphiphiles with or without alkyl spacer (**NDI-1-9**) were developed that generated self-assembled organic nanoparticles via *J*-aggregation having radii of ~50 nm in varying solvent systems of DMSO/DMF-water, $CHCl_3$-MCH). All the developed organic nanoparticles (except **NDI-4** and **NDI-7**) exhibited aggregation induced emission at varying emission maxima. Red shifted emission maxima were observed (greenish blue to bluish green to orange emissions) from λ_{em} = 484 nm to 495 nm and 590 nm in case of **NDI-1-3** FONPs upon enrichment of π-electron cloud from L-alanine to L-phenylalanine to 3-(2-naphthyl)-L-alanine. Similarly, a red shift of 40 nm and 105 nm in the λ_{em} was observed moving from phenyl alanine to naphthyl alanine terminal for C-6 (**NDI-5**, λ_{em} = 505 nm to **NDI-6**, λ_{em} = 545 nm) and C-11 (**NDI-8**, λ_{em} = 480 nm to **NDI-9**, λ_{em} = 585 nm) alkyl spacer containing FONPs, respectively. Incorporation of electron withdrawing -NO_2 and donating -OMe groups at the molecular backbone (**NDI-2a**, λ_{em} = 475 nm and **NDI-2b**, λ_{em} = 570 nm**)** showed blue (20 nm) shifted and red (75 nm) shifted emission maxima compared to that of **NDI-2** (λ_{em} = 495 nm) as the electron availability was judiciously regulated. Enhancement of available π-electron in the substituted building block led to red shifting in emission from blue-green to yellow-orange array of colours in the NDI based self-assembled FONPs primarily due to the facilitated electron transfer at a lesser energy while increase in alkyl spacer length caused relatively lower quantum yield.

4.4. EXPERIMENTAL SECTION

4.4.1. Materials

1,4,5,8-Naphthalenetetracarboxylic dianhydride, O-methyl-L-tyrosine and all deuterated NMR solvents were bought from Sigma-Aldrich. L-Alanine, L-phenylalanine, 6-aminocaproic acid, 11-aminoundecanoic acid, *N*, *N*-dicyclohexylcarbodiimide (DCC), *N*-hydroxybenzotriazole (HOBT), 4-*N*, *N*-(dimethylamino) pyridine (DMAP), sodium hydroxide, thionyl chloride, trifluoroacetic acid (TFA), organic solvents, silica gel (60-120 and 100-200 mesh) were purchased from SRL, India. 3-(2-Naphthyl)-L-alanine was procured from Combi-Blocks. 4-Nitro-L-phenylalanine was purchased from TCI chemicals. Milli-Q water was used for all spectroscopic and microscopic investigations. NMR spectra were taken in an AVANCE (Bruker) spectrometer. Bruker Ultraflex MALDI mass spectrometer was used to record MALDI-TOF spectra.

4.4.2. Synthesis of NDI derivatives

All the NDI based amphiphiles were synthesized and purified by the following mentioned pathway (Scheme 1). First, 1,4,5,8-naphthalenetetracarboxylic dianhydride (1.0 equiv) and L-alanine (2.5 equiv) were heated at 110 °C for 12 h under nitrogen atmosphere in dry dimethylformamide (DMF). DMF was removed from the reaction mixture by vacuum distillation. The crude mass was then extracted in dichloromethane (DCM) followed by washing it with diluted HCl. After evaporation of DCM, the mass was purified by column chromatography (100-200 mesh silica gel; 2 % MeOH/$CHCl_3$) and followed by washed with diethyl ether to obtain **NDI-1**. Similarly, **NDI-2**, **2a**, **2b** and **NDI-3** were synthesized using L-phenylalanine, 4-nitro-L-phenylalanine, O-methyl-L-tyrosine and 3-(2-naphthyl)-L-alanine, respectively.

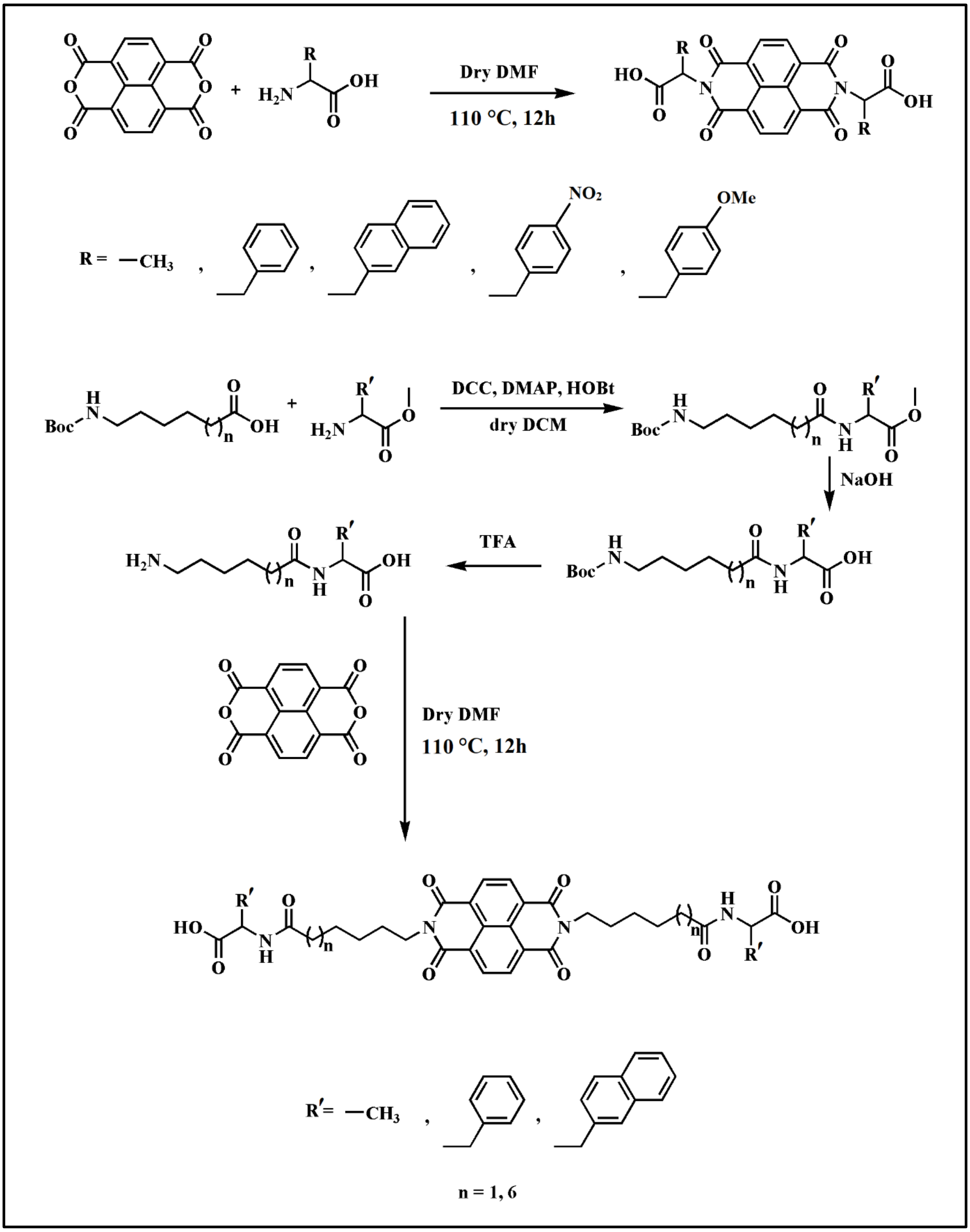

Scheme 1. Synthetic scheme of **NDI-1, 2, 2a, 2b, 3, 4, 5, 6, 7, 8** and **9**.

In case of **NDI-4**, methyl ester of L-alanine (1 equiv) and Boc protected 6-amino caproic acid (1.0 equiv) were coupled by using DCC (1.1 equiv), DMAP (1.1 equiv) and HOBT (1.1 equiv) in dry DCM under nitrogen atmosphere for 12 h. The reaction mixture was washed with 1 N HCl and dried over anhydrous sodium sulfate. The obtained mass upon solvent evaporation was purified by column chromatography using a 60-120 mesh silica gel using 1% MeOH/$CHCl_3$ eluent to obtain the coupled product. The methyl ester protected coupled product was hydrolyzed by stirring the reaction mixture in a methanolic solution of NaOH at room temperature for 12 h. After evaporation of methanol, the hydrolyzed product was taken in ethyl acetate and washed with HCl (1M) to obtain free carboxylic acid. Subsequently, the deprotection of the Boc (tertbutoxycarbonyl) group was carried out using TFA (1.5 equiv) in dry DCM for 4 h with continuous stirring. After solvent removal, the concentrated mass was dried and solubilized in EtOAc. The organic part was washed with aqueous Na_2CO_3 solution (10%) followed by water and dried over anhydrous Na_2SO_4 to obtain deprotected amine. 1,4,5,8-naphthalenetetracarboxylic dianhydride (1.0 equiv) and the just obtained amine (2.5 equiv) were heated at 110 °C under nitrogen atmosphere for 12 h in dry DMF. DMF was removed by vacuum distillation. The crude mass was extracted in DCM and washed with diluted HCl. The mass obtained upon evaporation of DCM was purified by column chromatography (100-200 mesh silica gel; 2 % MeOH/$CHCl_3$) to obtain **NDI-4**. In a similar pathway, **NDI-5** and **NDI-6** were synthesized where methyl ester of L-phenylalanine and 3-(2-naphthyl)-L-alanine were used respectively, for coupling with Boc protected 6-amino caproic acid. Likewise, the initial coupling reaction took place between Boc protected 11-amino undecanoic acid and methyl esters of L-alanine, L-phenylalanine and 3-(2-naphthyl)-L-alanine for the preparation of **NDI-7**, **NDI-8** and **NDI-9**, respectively. All the subsequent reactions were carried out in similar way as mentioned above. All the NDI derivatives (**NDI-1, 2, 2a, 2b, 3, 4, 5, 6, 7, 8, 9**) were characterized by ^1H NMR and MALDI-TOF mass spectrometry.

4.4.3. Sample preparation for spectroscopic and microscopic investigations

Stock solutions (10 mM) of all the NDI derivatives were prepared in DMSO. In addition, stock solutions (10 mM) of **NDI-1**, **NDI-2**, **NDI-2a**, **NDI-2b**, **NDI-3** and **NDI-8** were prepared in $CHCl_3$ and that of **NDI-5** and **NDI-8** were also prepared in DMF. From this stock solutions, the desired volume was added to the binary solvent systems (DMSO-water, DMF-water, $CHCl_3$-methyl cyclohexane) to achieve 5-300 μM concentrations of the synthesized NDI derivatives and those solutions were used in different spectroscopic and microscopic experiments.

4.4.4. Transmission electron microscopy (TEM)

4 μL solution of **NDI-1-9** (20 μM) in 99 vol% water in DMSO; **NDI-1**, **NDI-2**, **NDI-3** and **NDI-8** (20 μM) in 99 vol% methyl cyclohexane (MCH) in $CHCl_3$, **NDI-5** (20 μM) in 99 vol% water in DMF was placed on a carbon covered copper grid with mesh size of 300 and desiccated. Freshly prepared uranyl acetate solution (1% w/v, 1 μL) was utilized for negative staining of the sample. After keeping it for 4 h under vacuum, TEM images were captured in a JEOL JEM 2010 microscope.

4.4.5. Field-emission scanning electron microscopy (FESEM)

4 μL solution of **NDI-1-9** (20 μM) in 99 vol% water in DMSO; **NDI-1**, **NDI-2**, **NDI-3** and **NDI-8** (20 μM) in 99 vol% MCH in $CHCl_3$ and **NDI-5** (20 μM) in 99 vol% water in DMF was deposited on glass coverslips and was dried for 3 h under vacuum. Subsequently, the FESEM images were taken under a JEOL-6700F microscope.

4.4.6. Dynamic light-scattering (DLS)

The mean hydrodynamic diameter (D_h) of self-assembled structures is determined by DLS study. 1 mL solution of **NDI-1-9**, **2a**, **2b** (20 μM) in 99 vol% water in DMSO; **NDI-1**, **NDI-2**, **NDI-2a**, **NDI-2b**, **NDI-3** and **NDI-8** (20 μM) in 99 vol% MCH in $CHCl_3$ and **NDI-5** (20 μM) in 99 vol% water in DMF was used for the diameter measurement. Zen 3690 Zetasizer Nano ZS instrument (Malvern Instrument Ltd.) was used with scattering intensity at 175° angle. Obtained data were studied by a Cumulant Fit in Malvern Zetasizer software.

4.4.7. Fluorescence microscopy

Fluorescence microscopic images of **NDI-1-9** (20 μM) were captured in a IX83 inverted microscope at 20x magnification. 10 μL solution of **NDI-1**, **NDI-2**, **NDI-3** and **NDI-8** in 99 vol% MCH in $CHCl_3$, **NDI-5** in f_w = 99 vol% in DMF, **NDI-6** and **NDI-9** in f_w = 99 vol% in DMSO was drop cast on glass slides followed by air-drying before imaging.

4.4.8. UV-visible spectroscopic investigation

UV-visible spectra of all the amphiphilic compounds in different solvent systems were recorded in a Cary 50 Bio UV-Visible spectrophotometer. Solvent-dependent UV-visible spectra were also recorded for **NDI-1-9** (50 μM) in varying solvent compositions of DMSO-water (from f_w = 0% to 100%); **NDI-1**, **NDI-2**, **NDI-2a**, **NDI-2b**, **NDI-3** and **NDI-8** (50 μM) in binary solvent system of $CHCl_3$-MCH (with increasing MCH concentration from 0% to 100%) and **NDI-5** (50 μM) in 0 vol% to 100 vol% water in DMF.

4.4.9. ^{1}H-NMR study in varying solvent composition

Solvent-dependent ^{1}H-NMR spectra of **NDI-1-3** along with **NDI-5** and **NDI-8** (1 mM) in DMSO-d_6 and in DMSO-d_6-D_2O of varying ratio (1:1 (v/v) and 1:2 (v/v) DMSO-d_6-D_2O) were recorded in an Avance 300 MHz (Bruker) spectrometer.

4.4.10. Fluorescence spectroscopy

The emission spectra of **NDI-1**, **NDI-2**, **NDI-3**, **NDI-8** and **NDI-2a**, **NDI-2b** (50 μM) in $CHCl_3$-MCH solvent system (with increasing MCH concentration from 0% to 99%), **NDI-5**, **NDI-8** (50 μM) in DMF-water system (0 vol% to 99 vol% water in DMF) and **NDI-6** (50 μM), **NDI-9** (50 μM) in the mixed solvent system of DMSO-water (with increasing water content from 0 vol% to 99 vol%) were recorded in a Varian Cary Eclipse luminescence spectrometer with excitation wavelength (λ_{ex}) = 350 nm. Also, concentration dependent fluorescence spectra of all the individual amphiphiles in those mentioned solvent systems were registered within the concentration range of 5-300 μM. All the experimental concentrations were maintained by adding the desired volume of stock solutions as prepared.

4.4.11. Quantum yield (QY) measurement

QYs of the unknown fluorophores (self-aggregated FONPs derived from **NDI-1**, **NDI-2**, **NDI-3** and **NDI-8** in 99 vol% MCH in $CHCl_3$, **NDI-5** in 99 vol% water in DMF, and **NDI-6**, **NDI-9** in 99 vol% water in DMSO**)** (ϕ_u) were assessed with respect to a fluorophore of known quantum yield (ϕ_s) as the reference from the following equation,

$$\emptyset_u = \left(\frac{A_s F_u n_u^2}{A_u F_s n_s^2}\right)\emptyset_s \qquad (1)$$

Here, A_u and A_s stand for the optical density of the unknown and known sample at respective excitation wavelength. Integrated fluorescence intensities of unknown and reference samples at same wavelength are denoted as F_u and F_s, respectively. The n_u and n_s are the corresponding refractive indices of solvents belonging to the unknown and known sample. Quantum yields were measured using solutions with analogous absorbance (<0.01). In this experiment, we used Quinine sulfate in sulfuric acid (0.1 M) as the reference having QY (ϕ_s) = 54.0%.

4.4.12. Time-resolved study

Time-correlation single photon count (TCSPC) measurement was carried out with a picosecond diode laser IBH-405. All amphiphilic solutions were excited (λ_{ex}) at 375 nm and their emission was monitored at particular wavelength described as λ_{mon}. λ_{mon} for **NDI-1** (50 μM), **NDI-2** (50 μM), **NDI-2a** (50 μM), **NDI-2b** (50 μM), **NDI-3** (50 μM) and **NDI-8** (50 μM) in $CHCl_3$, **NDI-5** in DMF, and **NDI-6**, **NDI-9** in DMSO were 406 nm, 393 nm, 394 nm, 408 nm, 420 nm, 400 nm, 410 nm, 420 nm and 420 nm, respectively. Moreover, **NDI-1** (50 μM), **NDI-2** (50 μM), **NDI-2a** (50 μM), **NDI-2b** (50 μM), **NDI-3** (50 μM) and **NDI-8** (50 μM) in 99 vol% MCH in $CHCl_3$, **NDI-5** in 99 vol% water in DMF, and **NDI-6** and **NDI-9** in 99 vol% water in DMSO had λ_{mon} of 484 nm, 495 nm, 475 nm, 570 nm, 590 nm, 480 nm, 505 nm, 545 nm and 585 nm. Similarly, in case of **NDI-1** (50 μM) and **NDI-2** (50 μM) in 80 vol% MCH in $CHCl_3$, **NDI-2a** in 70 vol% MCH in $CHCl_3$, **NDI-2b** in 50 vol% MCH in $CHCl_3$, **NDI-3** (50 μM) in 60 vol% MCH in $CHCl_3$, **NDI-5** (50 μM) in 70 vol% water in DMF, **NDI-6** (50 μM) in 50 vol% water in DMSO, **NDI-8** (50 μM) in 90 vol% MCH in $CHCl_3$ and **NDI-9** in 70 vol% water in DMSO emission was monitored at λ_{mon}, 484 nm, 495 nm, 475 nm, 570 nm, 590 nm, 505 nm, 545 nm, 480 nm and 585 nm, respectively. IBH DAS6 software was employed to survey the fluorescence decay. Experimental time-resolved fluorescence decay *p(t)* was analysed by following equation 2

$$p(t) = b + \sum_{i}^{n} \alpha_i \; e^{\left(\frac{-t}{\tau_i}\right)} \tag{2}$$

Here, n = number of discrete emissive species, b = baseline correction ("dc" offset), α_i = pre-exponential factors, and τ_i = excited state fluorescence lifetimes for the i th component, respectively. For multiexponential decays, the average lifetime was calculated using equation 3

$$\langle\tau\rangle = \sum_{i=1}^{n} \alpha_i \tau_i \tag{3}$$

Here, $\alpha_i = \frac{\alpha_i}{\sum \alpha_i}$ depicts the contribution of a decay component.

4.5. CHARACTERISATION DATA

4.5.1. Characterisation of NDI-1

^{1}H-NMR (400 MHz, MeOD, 25 °C): δ/ppm: 8.764 (s, 4H, protons of naphthalenediimide core), 5.716-5.844 (m, 2H, chiral centre of L-alanine residue) 1.585-1.675 (d, 6H, methyl protons of L-alanine residue). HRMS: m/z: 411.33 $[M+H]^+$ (calculated), 411.1366 (found).

4.5.2. Characterisation of NDI-2

^{1}H-NMR (400 MHz, MeOD, 25 °C): δ/ppm: 8.613 (s, 4H, protons of naphthalenediimide core), 7.115-7.133 (m, 4H, meta protons of phenyl ring) 6.988-7.062 (m, 6H, ortho, para protons of phenyl ring), 5.957-5.996 (m, 2H, chiral centre of L-phenylalanine residue), 3.625-3.660 (m, 2H, benzyl proton), 3.472-3.521 (m, 2H, benzyl proton). HRMS: m/z: 563.53 $[M+H]^+$ (calculated), 563.0746 (found); 585.53 $[M+Na]^+$ (calculated), 585.0704 (found).

4.5.3. Characterisation of NDI-3

^{1}H-NMR (400 MHz, MeOD, 25 °C): δ/ppm: 8.506 (s, 4H, protons of naphthalenediimide core), 7.466-7.616 (m, 8H, C-1, C-4, C-5, C-8 protons of naphthyl ring), 7.225-7.304 (m, 6H, C-3, C-6, C-7 protons of naphthyl ring), 6.055-6.094 (m, 2H, chiral centre of L-naphthylalanine residue), 3.763-3.811 (m, 2H, proton adjacent to naphthyl ring), 3.583-3.644 (m, 2H, proton adjacent to naphthyl ring). HRMS: m/z: 701.64 $[M+K]^+$ (calculated), 701.840 (found).

4.5.4. Characterisation of NDI-4

^{1}H-NMR (400 MHz, MeOD, 25 °C): δ/ppm: 9.015 (s, 4H, protons of naphthalenediimide core), 4.914-5.018 (m, 2H, chiral centre of L-alanine residue), 4.117-4.135 (m, 4H, C-6 proton of caproic acid residue), 2.268-2.287 (m, 4H, C-2 protons of caproic acid residue), 2.015-2.068 (m, 8H, C-3, C-5 protons of caproic acid residue), 1.641 (m, 6H, methyl protons of L-alanine residue), 1.229-1.452 (m, 4H, C-4 protons of caproic acid residue). HRMS: m/z: 636.65 $[M]^+$ (calculated), 636.880 (found).

4.5.5. Characterisation of NDI-5

^{1}H-NMR (400 MHz, DMSO-d_6, 25 °C): δ/ppm: 8.639-8.684 (m, 4H, protons of naphthalenediimide core), 7.404-7.457 (m, 4H, meta protons of phenyl ring), 7.288-7.336 (m, 4H, ortho protons of phenyl ring), 7.204 (m, 2H, para protons of phenyl ring), 5.556-5.582 (m, 2H, chiral centre of L-phenylalanine residue), 4.049-4.118 (m, 6H, C-6 proton of caproic acid residue, benzyl proton), 2.744 (m, 2H, benzyl proton), 2.150-2.199 (m, 4H, C-2 proton of caproic acid residue), 1.689-1.730 (m, 4H, C-5 proton of caproic acid residue), 1.588-1.643 (m, 4H, C-3 proton of caproic acid residue), 1.231 (m, 4H, C-4 proton of caproic acid residue). HRMS: m/z: 788.84 $[M]^+$ (calculated), 788.413 (found).

4.5.6. Characterisation of NDI-6

^{1}H-NMR (400 MHz, $CDCl_3$, 25 °C): δ/ppm: 8.737 (s, 4H, protons of naphthalenediimide core), 7.735-7.753 (m, 2H, C-5 proton of naphthyl ring), 7.685 (m, 2H, C-8 proton of naphthyl ring), 7.597 (m, 2H, C-4 proton of naphthyl ring), 7.506-7.529 (m, 2H, C-1 proton of naphthyl ring), 7.421-7.430 (m, 2H, C-7 proton of naphthyl ring), 7.356 (m, 2H, C-6 proton of naphthyl ring), 7.295 (m, 2H, C-3 proton of naphthyl ring), 4.932 (m, 2H, chiral centre of L-naphthylalanine residue), 3.444-3.496 (m, 2H, proton adjacent to naphthyl ring), 3.384 (m, 4H, C-6 proton of caproic acid residue), 3.302 (m, 2H, proton adjacent to naphthyl ring), 2.138-2.158 (m, 4H, C-2 proton of caproic acid residue), 1.883 (m, 4H, C-5 proton of caproic acid residue), 1.722-1.739 (m, 4H, C-3 proton of caproic acid residue), 1.147-1.287 (m, 4H, C-4 proton of caproic acid residue). HRMS: m/z: 888.96 $[M]^+$ (calculated), 888.356 (found).

4.5.7. Characterisation of NDI-7

^{1}H-NMR (400 MHz, $CDCl_3$, 25 °C): δ/ppm: 8.808 (s, 4H, protons of naphthalenediimide core), 4.572-4.608 (m, 2H, chiral centre of L-alanine residue), 3.738 (m, 4H, C-11 protons of undecanoic acid residue), 2.169-2.207 (m, 4H, C-2 protons of undecanoic acid residue), 2.081 (m, 4H, C-10 protons of undecanoic acid residue), 1.912-1.963 (m, 4H, C-3 protons of undecanoic acid residue), 1.671-1.726 (m, 4H, C-9 protons of undecanoic acid residue), 1.607 (m, 4H, C-4 protons of undecanoic acid residue), 1.321-1.415 (d, 6H, methyl protons of L-alanine residue), 1.244-1.274 (d, 16H, C-5, C-6, C-7, C-8 protons of undecanoic acid residue). HRMS: m/z: 777.91 $[M+H]^+$ (calculated), 778.729 (found).

4.5.8. Characterisation of NDI-8

^{1}H-NMR (400 MHz, $CDCl_3$, 25 °C): δ/ppm: 8.733-8.760 (s, 4H, protons of naphthalenediimide core), 7.216-7.280 (m, 4H, meta protons of phenyl ring), 7.077-7.091 (m, 6H, ortho and para protons of phenyl ring), 4.877-4.910 (m, 2H, chiral centre of L-phenylalanine residue), 3.728 (m, 2H, protons adjacent to phenyl ring), 3.433-3.485 (m, 4H, C-11 protons of undecanoic acid residue), 3.061-3.177 (m, 2H, protons adjacent to phenyl ring), 2.277-2.364 (m, 4H, C-2 protons of undecanoic acid residue), 2.145-2.182 (m, 4H, C-10 protons of undecanoic acid residue), 1.922-1.952 (m, 4H, C-3 protons of undecanoic acid residue), 1.692-1.735 (m, 4H, C-9 protons of undecanoic acid residue), 1.521-1.621 (m, 4H, C-4 protons of undecanoic acid residue), 1.114-1.471(m, 16H, C-5, C-6, C-7, C-8 protons of undecanoic acid residue) HRMS: m/z: 968.11 $[M+K]^+$ (calculated), 967.72 (found).

4.5.9. Characterisation of NDI-9

^{1}H-NMR (400 MHz, $CDCl_3$, 25 °C): δ/ppm: 8.820 (s, 4H, protons of naphthalenediimide core), 8.004-8.034 (m, 4H, C-5, C-8 proton of naphthyl ring), 7.919-7.960 (m, 2H, C-4 proton of naphthyl ring), 7.752-7.772 (m, 2H, C-1 protons of naphthyl ring), 7.622 (m, 4H, C-7 protons of naphthyl ring), 7.493-7.563 (m, 4H, C-6 protons of naphthyl ring), 7.445 (m, 2H, C-3 protons of naphthyl ring), 4.967 (m, 2H, chiral centre of naphthyl alanine residue), 4.052-4.062 (m, 2H, protons adjacent to naphthyl ring), 3.627-3.645 (m, 4H, C-11 protons of undecanoic acid residue), 3.069 (m, 2H, protons adjacent to naphthyl ring), 2.283-2.430 (m, 4H, C-2 protons of undecanoic acid residue), 1.904-1.924 (m, 4H, C-10 protons of undecanoic acid residue), 1.622-1.635 (m, 4H, C-3 protons of undecanoic acid residue), 1.412-1.519 (m, 8H, C-4, C-9 protons of undecanoic acid residue), 1.253-1.281 (m, 16H, C-5, C-6, C-7, C-8 protons of undecanoic acid residue). HRMS: m/z: 1052.22 $[M+Na]^+$ (calculated), 1052.881 (found). 1068.22 $[M+K]^+$ (calculated), 1068.835 (found).

4.5.10. Characterisation of NDI-2a

^{1}H-NMR (400 MHz, DMSO-d_6, 25 °C): δ/ppm: 8.659-8.693 (s, 4H, protons of naphthalenediimide core), 8.018-8.039 (d, 4H, meta protons with respect to nitro groups), 7.505-7.526 (d, 4H, ortho protons with respect to nitro groups), 5.894-5.930 (m, 2H, chiral centre of amino acid), 4.045 (m, 2H, benzyl proton), 3.730-3.779 (m, 2H, benzyl proton). HRMS: m/z: 675.52 $[M+Na]^+$ (calculated), 676.145 (found); 691.52 $[M+K]^+$ (calculated), 692.165 (found).

4.5.11. Characterisation of NDI-2b

^{1}H-NMR (400 MHz, DMSO-d_6, 25 °C): δ/ppm: 8.592-8.649 (s, 4H, protons of naphthalenediimide core), 7.054-7.075 (d, 4H, meta protons with respect to -OMe groups), 6.653-6.674 (d, 4H, ortho protons with respect to -OMe groups), 5.776-5.812 (m, 2H, chiral centre of amino acid), 4.099 (s, 6H, methoxy protons), 3.578 (m, 2H, benzyl protons), 3.106 (m, 2H, benzyl protons). HRMS: m/z: 645.58 $[M+Na]^+$ (calculated), 646.061 (found)

4.6. SPECTRA

4.6.1. ^{1}H-NMR spectra

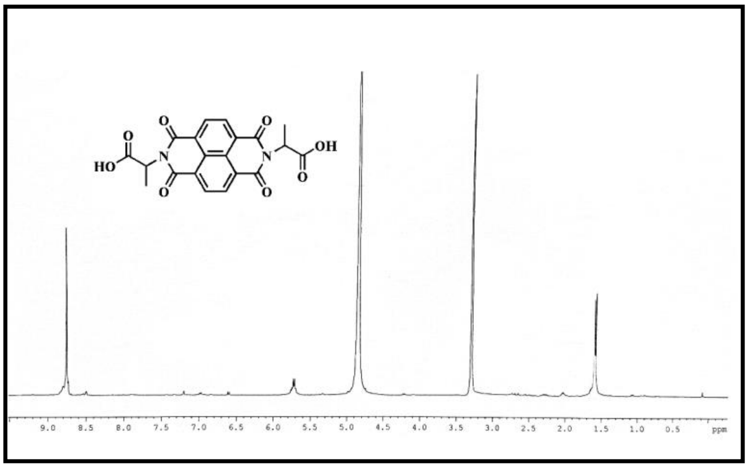

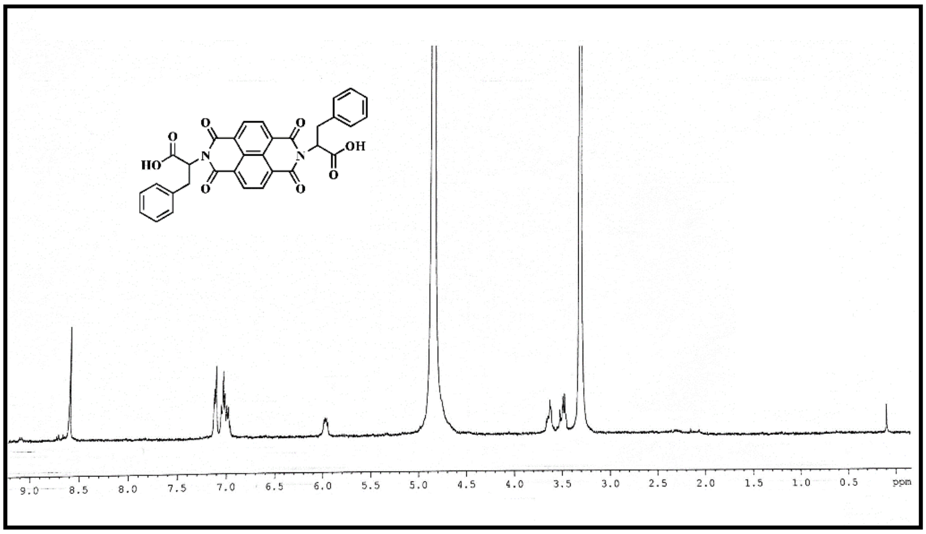
HO
OH
N
O
9.0
8.5
8.0
7.5
7.0
6.5
6.0
5.5
5.0
4.5
4.0
3.5
3.0
2.5
2.0
1.5
1.0
0.5
ppm

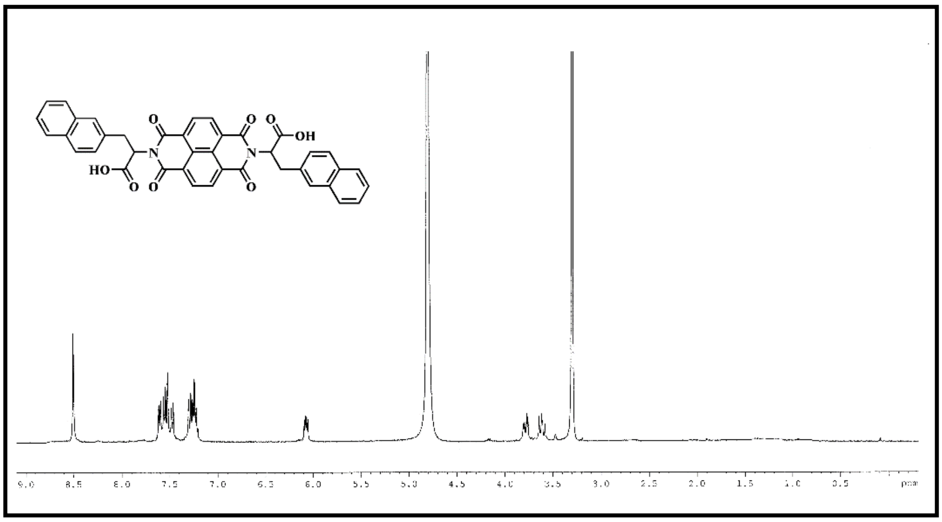
HO
OH
N
O
9.0
8.5
8.0
7.5
7.0
6.5
6.0
5.5
5.0
4.5
4.0
3.5
3.0
2.5
2.0
1.5
1.0
0.5
ppm

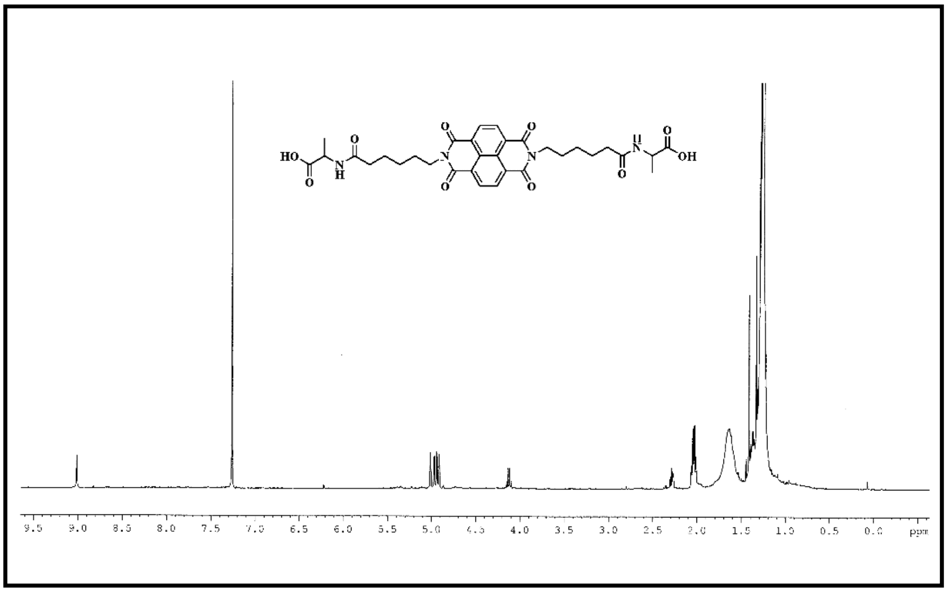
HO
OH
N
H
O
9.5
9.0
8.5
8.0
7.5
7.0
6.5
6.0
5.5
5.0
4.5
4.0
3.5
3.0
2.5
2.0
1.5
1.0
0.5
0.0
ppm

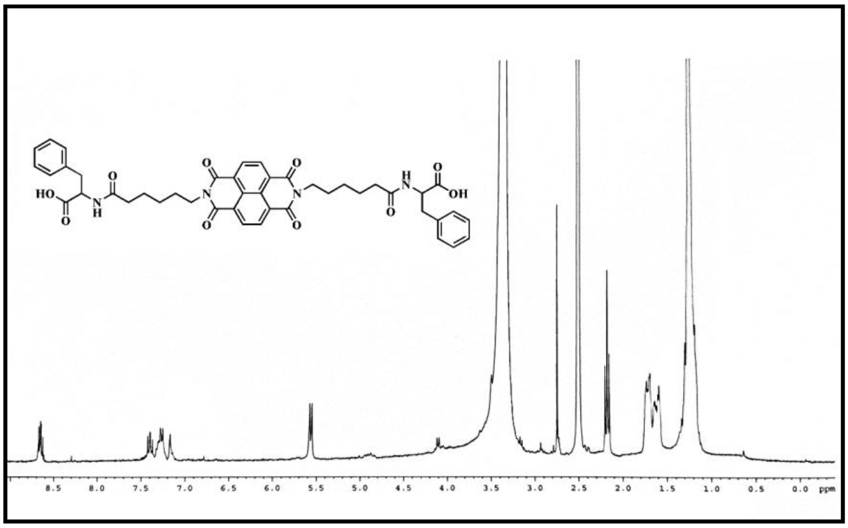
HO
O
N
H
O
N
O
O
N
O
O
O
H
N
O
OH
8.5
8.0
7.5
7.0
6.5
6.0
5.5
5.0
4.5
4.0
3.5
3.0
2.5
2.0
1.5
1.0
0.5
0.0
ppm

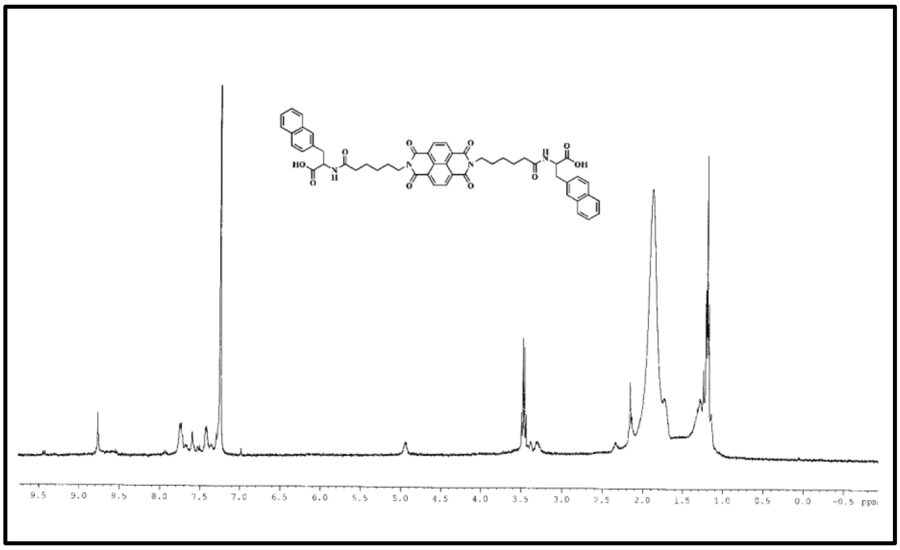
HO
O
N
H
O
N
O
O
N
O
O
O
N
H
O
OH
9.5
9.0
8.5
8.0
7.5
7.0
6.5
6.0
5.5
5.0
4.5
4.0
3.5
3.0
2.5
2.0
1.5
1.0
0.5
0.0
-0.5
ppm

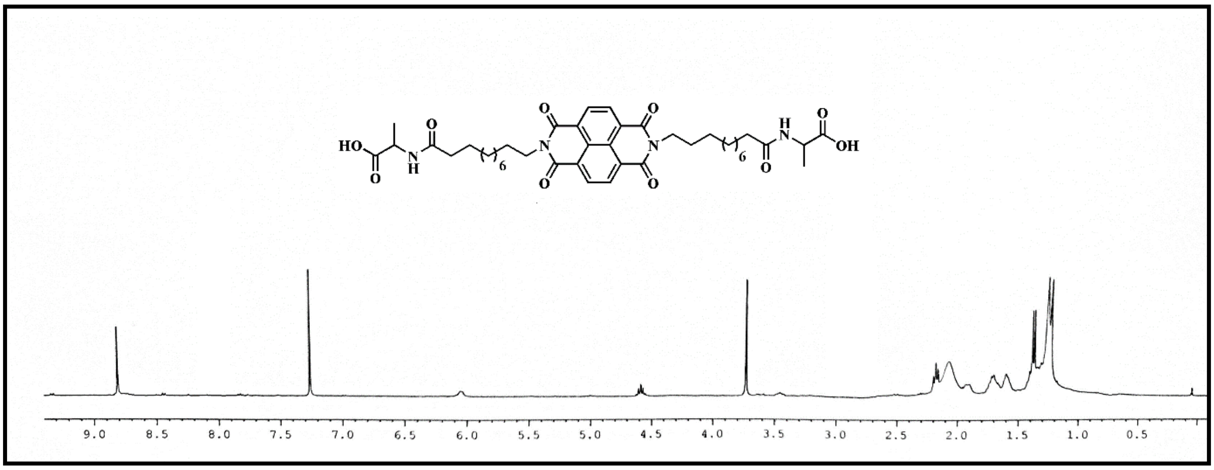
HO
O
N
H
O
6
N
O
O
N
O
O
6
O
H
N
O
OH
9.0
8.5
8.0
7.5
7.0
6.5
6.0
5.5
5.0
4.5
4.0
3.5
3.0
2.5
2.0
1.5
1.0
0.5

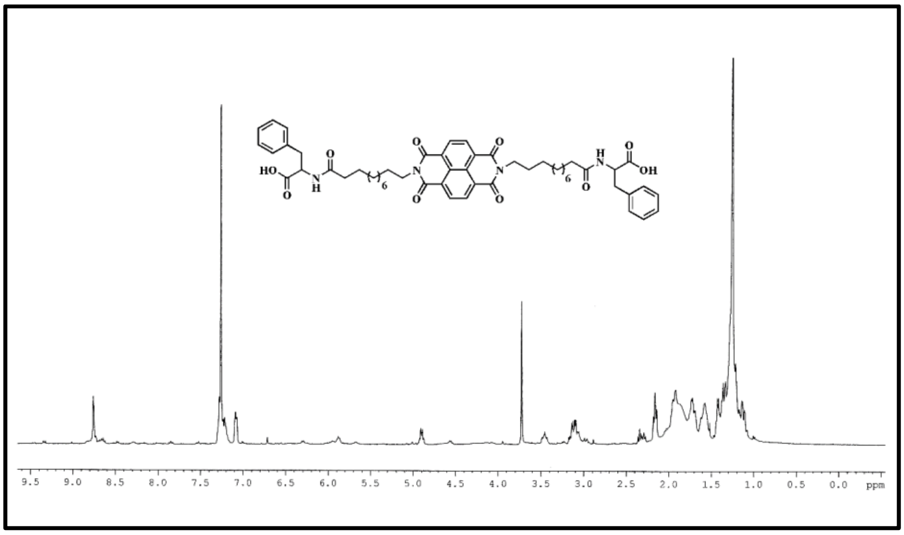
HO
O
N
H
O
6
N
O
O
O
O
N
6
O
H
N
O
OH
9.5
9.0
8.5
8.0
7.5
7.0
6.5
6.0
5.5
5.0
4.5
4.0
3.5
3.0
2.5
2.0
1.5
1.0
0.5
0.0
ppm

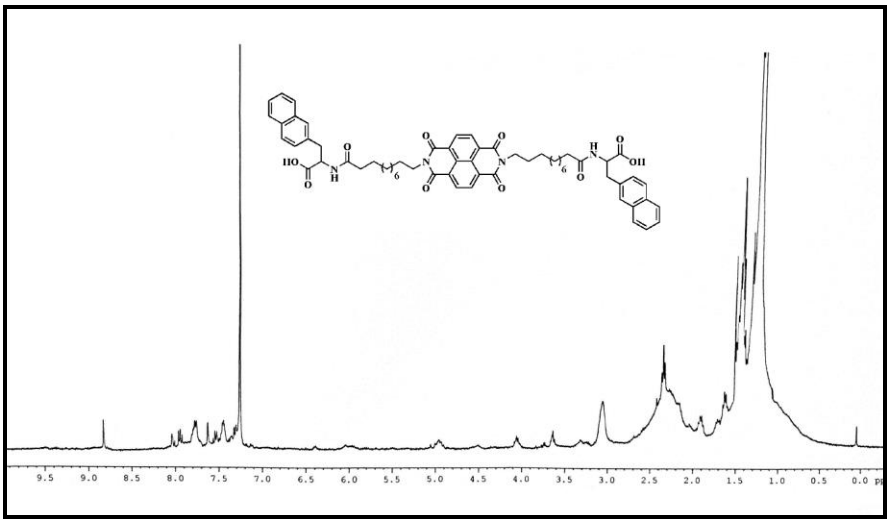
HO
O
N
H
O
6
N
O
O
O
O
N
6
O
H
N
O
OH
9.5
9.0
8.5
8.0
7.5
7.0
6.5
6.0
5.5
5.0
4.5
4.0
3.5
3.0
2.5
2.0
1.5
1.0
0.5
0.0

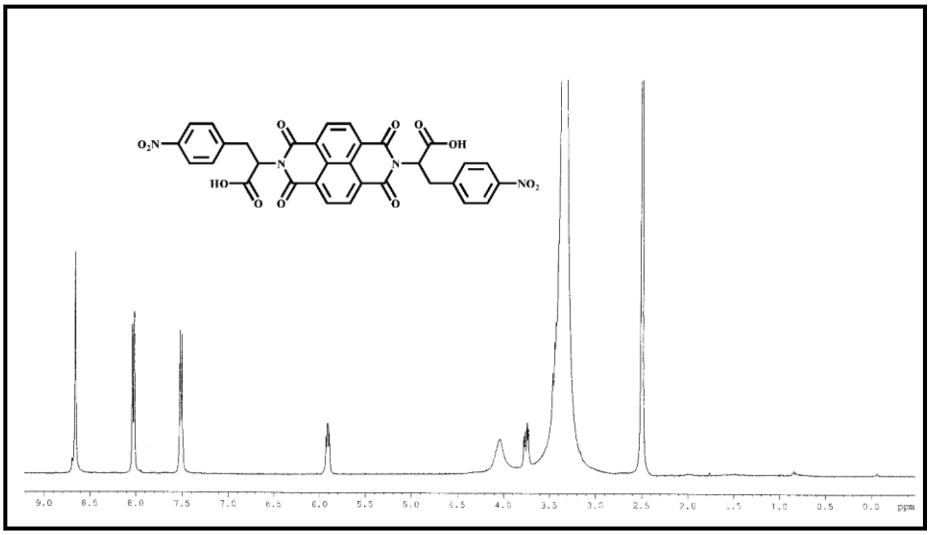
O₂N
O
O
OH
N
N
HO
O
O
O
NO₂
9.0
8.5
8.0
7.5
7.0
6.5
6.0
5.5
5.0
4.5
4.0
3.5
3.0
2.5
2.0
1.5
1.0
0.5
0.0
ppm

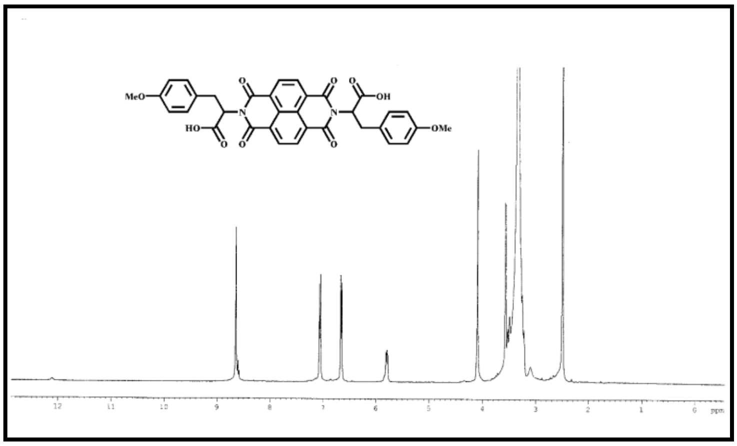

4.6.2. Mass spectra

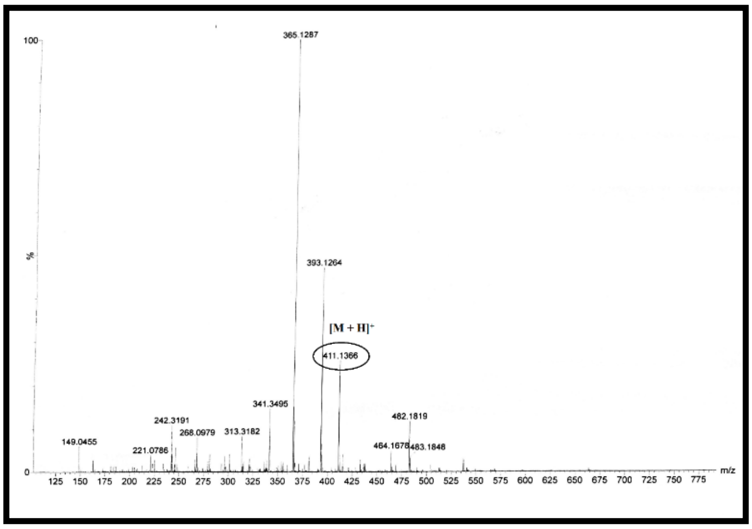

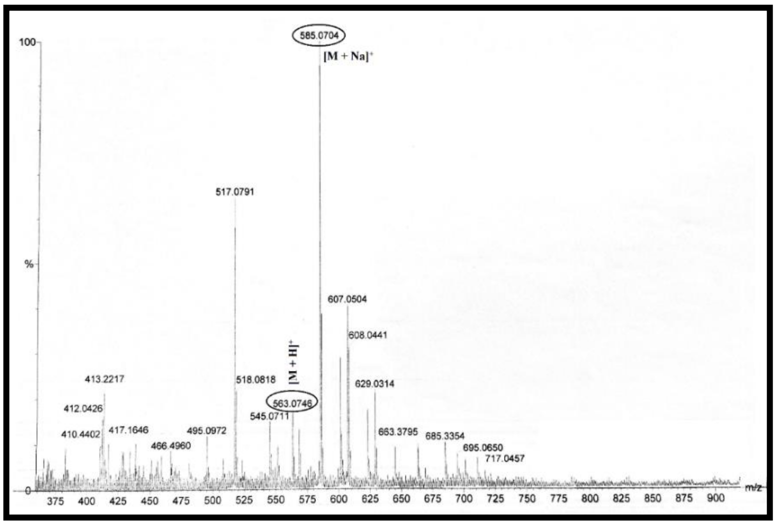

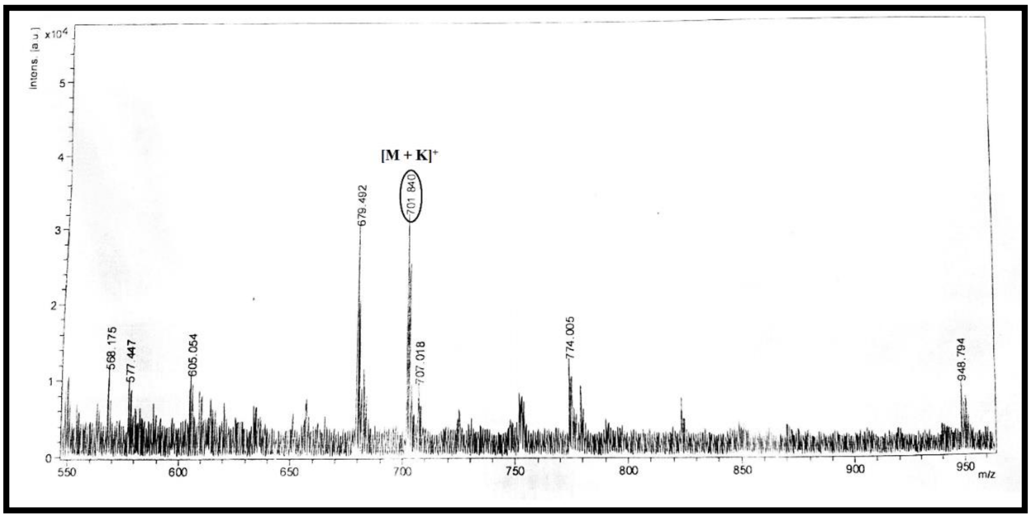
Intens. [a.u.]
x10^4
5
4
3
2
1
0
[M + K]$^+$
568.175
577.447
605.054
679.492
701.840
707.018
774.005
948.794
550
600
650
700
750
800
850
900
950
m/z

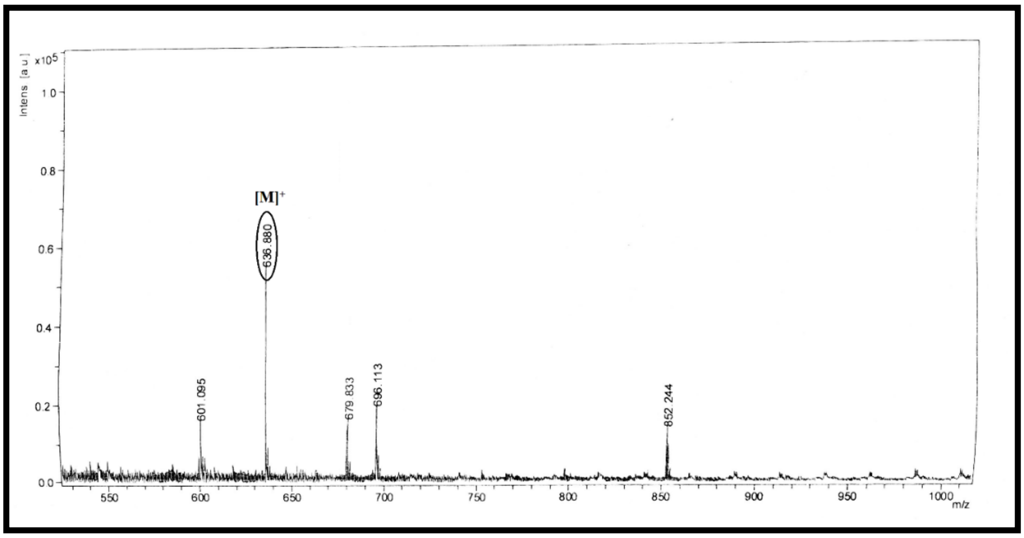
Intens. [a.u.]
x10^5
1.0
0.8
0.6
0.4
0.2
0.0
[M]$^+$
601.095
636.880
679.833
696.113
852.244
550
600
650
700
750
800
850
900
950
1000
m/z

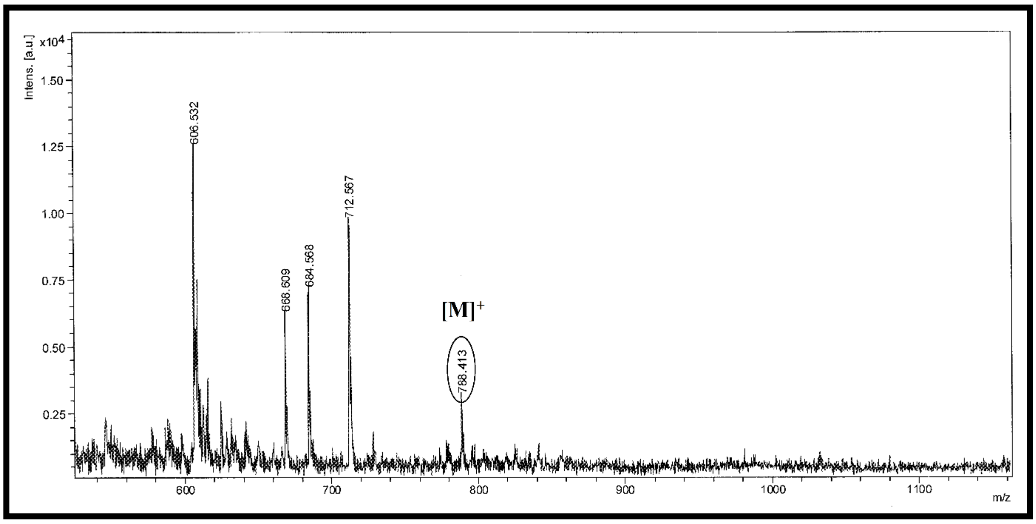
Intens. [a.u.]
x10^4
1.50
1.25
1.00
0.75
0.50
0.25
606.532
668.609
684.568
712.567
[M]$^+$
788.413
600
700
800
900
1000
1100
m/z

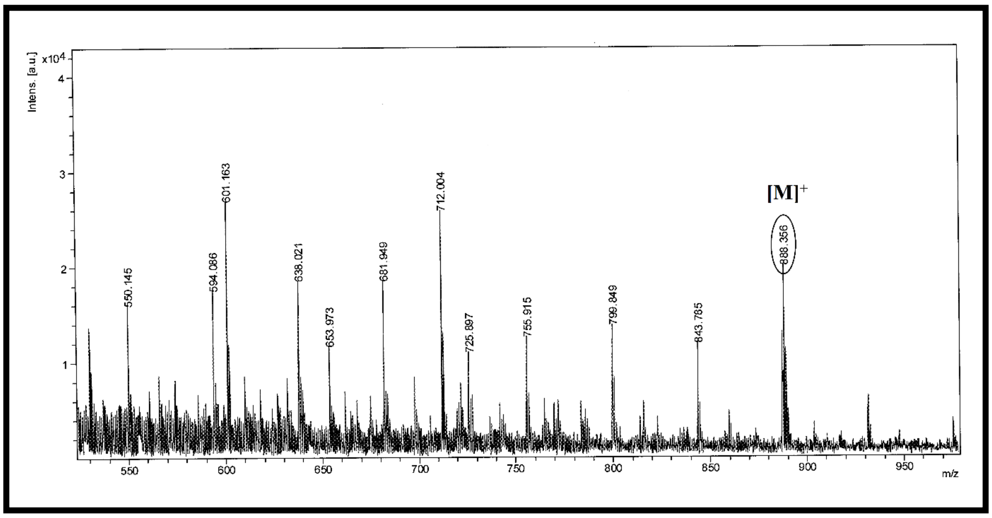
Intens. [a.u.]
x10⁴
4
3
2
1
550.145
594.086
601.163
638.021
653.973
681.949
712.004
725.897
755.915
799.849
843.785
[M]⁺
888.356
550
600
650
700
750
800
850
900
950
m/z

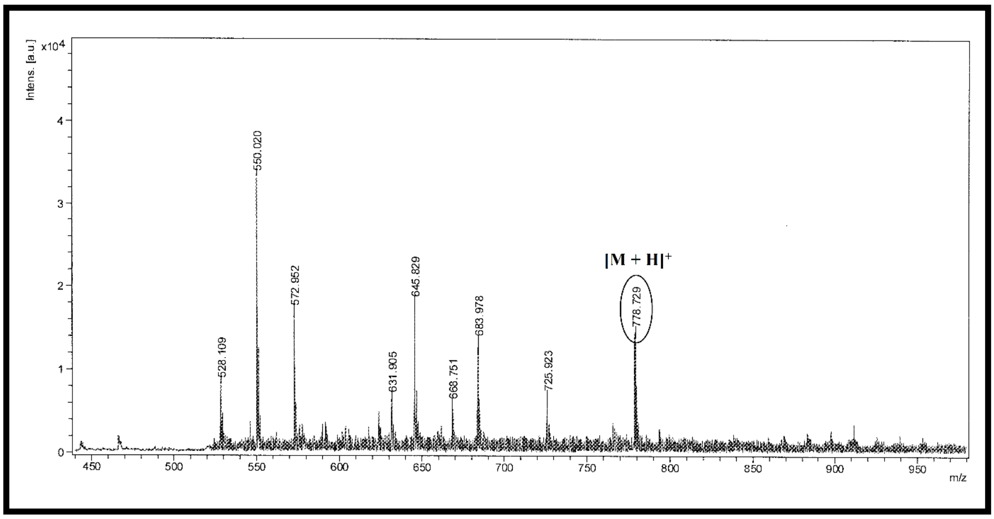
Intens. [a.u.]
x10⁴
4
3
2
1
0
528.109
550.020
572.952
631.905
645.829
668.751
683.978
725.923
[M + H]⁺
778.729
450
500
550
600
650
700
750
800
850
900
950
m/z

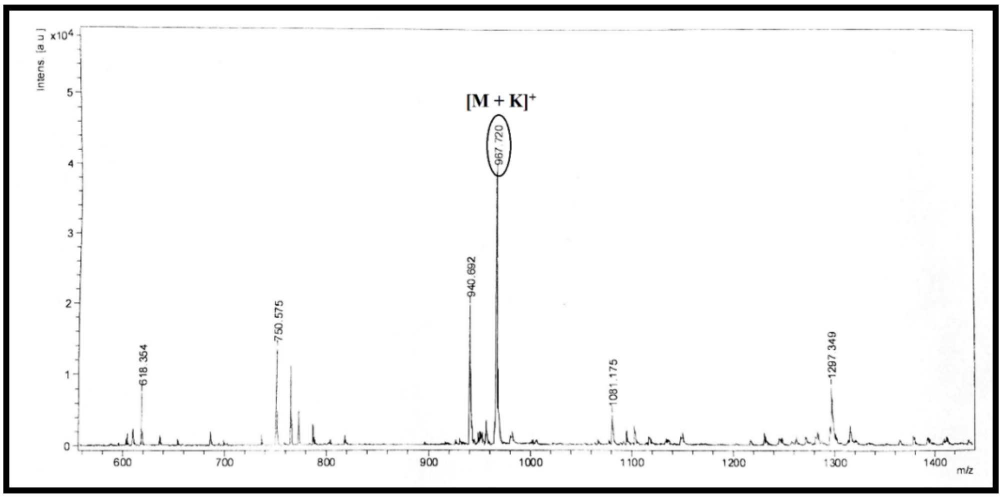
Intens. [a.u.]
x10⁴
5
4
3
2
1
0
618.354
750.575
940.692
[M + K]⁺
967.720
1081.175
1297.349
600
700
800
900
1000
1100
1200
1300
1400
m/z

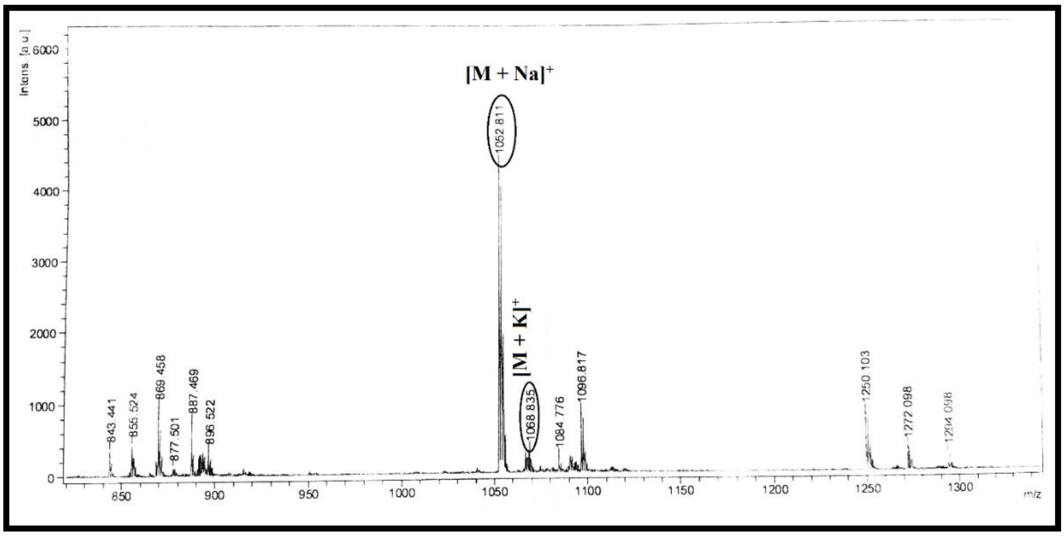
Intens. [a.u.]
6000
5000
4000
3000
2000
1000
0
[M + Na]$^+$
1052.811
[M + K]$^+$
1068.835
843.441
855.524
869.458
877.501
887.469
896.522
1084.776
1096.817
1250.103
1272.098
1294.098
850
900
950
1000
1050
1100
1150
1200
1250
1300
m/z

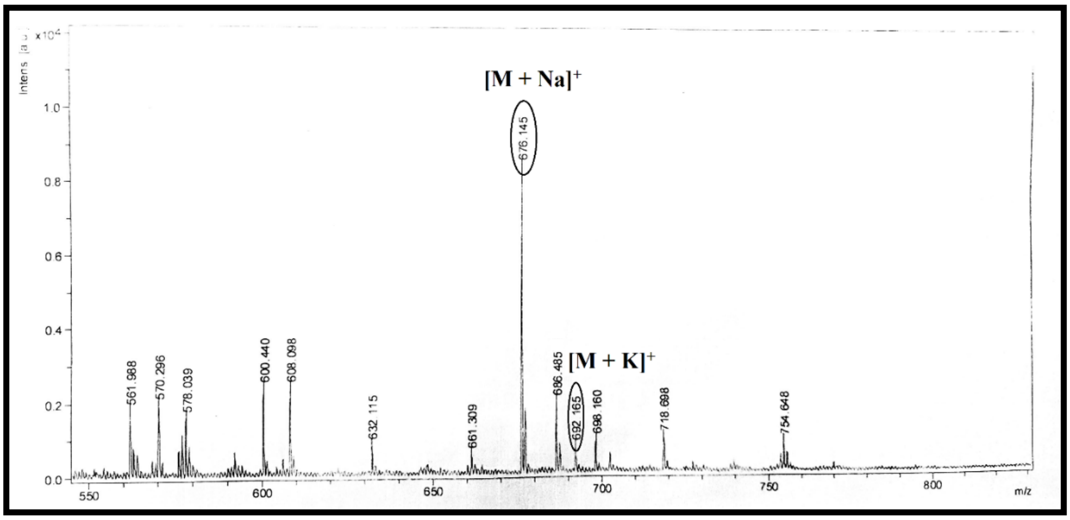
Intens. [a.u.]
x10^4
1.0
0.8
0.6
0.4
0.2
0.0
[M + Na]$^+$
676.145
[M + K]$^+$
692.165
561.988
570.296
578.039
600.440
608.098
632.115
661.309
686.485
698.160
718.698
754.648
550
600
650
700
750
800
m/z

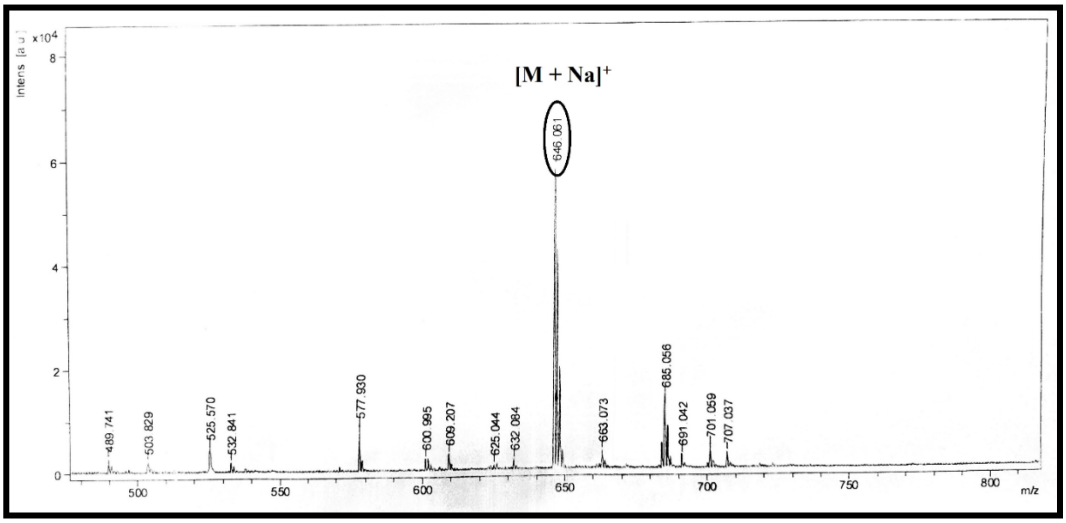
Intens. [a.u.]
x10^4
8
6
4
2
0
[M + Na]$^+$
646.061
489.741
503.829
525.570
532.841
577.930
600.995
609.207
625.044
632.084
663.073
685.056
691.042
701.059
707.037
500
550
600
650
700
750
800
m/z

4.7. REFERENCES

(1) J. M. Lehn, *Angew. Chem. Int. Ed. Engl.* **1988**, *27*, 89.

(2) J. M. Lehn, *Angew. Chem. Int. Ed.* **1990**, *29*, 1304.

(3) G. M. Whitesides, J. P. Mathias, C. T. Seto, *Science* **1991**, *254*, 1312.

(4) B. K. Das, B. Pramanik, S. Chowdhuri, O. A. Scherman, D. Das, *Chem. Commun.* **2020**, *56*, 3393.

(5) B. O. Okesola, D. K. Smith, *Chem. Soc. Rev.* **2016**, *45*, 4226.

(6) M. D. Segarra-Maset, V. J. Nebot, J. F. Miravet, B. Escuder, *Chem. Soc. Rev.* **2013**, *42*, 7086.

(7) S. Sarkar, P. Choudhury, S. Dinda, P. K. Das, *Langmuir* **2018**, *34*, 10449.

(8) D. Sarkar, M. Chowdhury, P. K. Das, *Langmuir* **2022**, *38*, 3480.

(9) K. Matsuurua, *RSC Adv.* **2014**, *4*, 2942.

(10) N. J. Sinha, M. G. Langenstein, D. J. Pochan, C. J. Kloxin, J. G. Saven, *Chem. Rev.* **2021**, *121*, 13915.

(11) F. Sheehan, D. Sementa, A. Jain, M. Kumar, M. T. Najjaran, D. Kroiss, R.V. Ulijn, *Chem. Rev.* **2021**, *121*, 13869.

(12) J. M. Fletcher, R. L. Harniman, F. R. Barnes, A. L. Boyle, A. Collins, J. Mantell, T. H. Sharp, M. Antognozzi, P. J. Booth, N. Linden, M. J. Miles, R. B. Sessions, P. Verkade, D. N. Woolfson, *Science* **2013**, *340*, 595.

(13) Zhang, S. Fabrication of novel biomaterials through molecular self-assembly. *Nat. Biotechnol.* **2003**, *21*, 1171-1178.

(14) M. J. Webber, E. A. Appel, E. W. Meijer, R. Langer, *Nat. Mater.* **2016**, *15*, 13.

(15) P. Singh, S. K. Brar, M. Bajaj, N. Narang, V. S. Mithu, O. P. Katare, N. Wangoo, R. K. Sharma, *Mater. Sci. Eng. C* **2017**, *72*, 590.

(16) S. Santoso, W. Hwang, H. Hartman, S. Zhang, *Nano Lett.* **2002**, *2*, 687.

(17) S. Vauthey, S. Santoso, H. Gong, N. Watson, S. Zhang, *Proc. Natl. Acad. Sci. U.S.A.* **2002**, *99*, 5355.

(18) H. Cui, T. Muraoka, A. G. Cheetham, S. I. Stupp, *Nano Lett.* **2009**, *9*, 945.

(19) R. C. Claussen, B. M. Rabatic, S. I. Stupp, *J. Am. Chem. Soc.* **2003**, *125,* 12680.

(20) N. Wiradharma, Y. W. Tong, Y. Y. Yang, *Biomaterials* **2009**, *30,* 3100.

(21) D. M. Ryana, B. L. Nilsson, *Polym. Chem.* **2012**, *3*, 18.

(22) F. Gelain, A. Horii, S. Zhang, *Macromol. Biosci.* **2007**, *7*, 544.

(23) C. Chen, F. Pan, S. Zhang, J. Hu, M. Cao, J. Wang, H. Xu, X. Zhao, J. R. Lu, *Biomacromolecules* **2010**, *11*, 402.

(24) L. A. Abramovich, L. Vaks, O. Carny, D. Trudler, A. Magno, A. Caflisch, D. Frenkel, E. Gazit, *Nat. Chem. Biol.* **2012**, *8*, 701.

(25) D. G. Babar, S. Sarkar, *Appl. Nanosci.* **2017**, *7*, 101.

(26) B. K. An, S. K. Kwon, S. D. Jung, S. Y. Park, *J. Am. Chem. Soc.* **2002**, *124*, 14410.

(27) M. Kumar, S. J. George, *Nanoscale* **2011**, *3*, 2130.

(28) A. Kaeser, I. Fischer, R. Abbel, P. Besenius, D. Dasgupta, M. A. J. Gillisen, G. Portale, A. L. Stevens, L. M. Herz, A. P. H. J. Schenning, *ACS Nano* **2013**, *7*, 408.

(29) X. Zhang, S. Wang, L. Xu, L. Feng, Y. Ji, L. Tao, S. Lia, Y. Wei, *Nanoscale* **2012**, *4*, 5581.

(30) Z. Wang, T. Y. Yong, J. Wan, Z. H. Li, H. Zhao, Y. Zhao, L. Gan, X. L. Yang, H. B. Xu, C. Zhang, *ACS Appl. Mater. Interfaces* **2015**, *7*, 3420.

(31) M. Ahmed, M. Faisal, A. Ihsan, M. M. Naseer, *Analyst* **2019**, *144*, 2480.

(32) J. Luo, Z. Xie, J. W. Y. Lam, L. Cheng, H. Chen, C. Qiu, H. S. Kwok, X. Zhan, Y. Liu, D. Zhu, B. Z. Tang, *Chem. Commun.* **2001**, 1740.

(33) Y. Hong, J. W. Y. Lam, B. Z. Tang, *Chem. Commun.* **2009**, 4332.

(34) Y. Hong, J. W. Y. Lam, B. Z. Tang, *Chem. Soc. Rev.* **2011**, *40*, 5361.

(35) J. Mei, N. L. C. Leung, R. T. K. Kwok, J. W. Y. Lam, B. Z. Tang, *Chem. Rev.* **2015**, *115*, 11718.

(36) M. A. Kobaisi, S. V. Bhosale, K. Latham, A. M. Raynor, S. V. Bhosale, *Chem. Rev.* **2016**, *116*, 11685.

(37) S. V. Bhosale, M. L. Kobaisi, R. W. Jadhav, P. P. Morajkar, L. A. Jones, S. J. George, *Chem. Soc. Rev.* **2021**, *50*, 9845.

(38) F. Wurthner, S. Ahmed, C. Thalacker, T. Debaerdemaeker, *Chem. Eur. J.* **2002**, *8*, 4742.

(39) P. Choudhury, S. Sarkar, P. K. Das, *Langmuir* **2018**, *34*, 14328.

(41) S. V. Bhosale, C. H. Jani, S. J. Langford, *Chem. Soc. Rev.* **2008**, *37*, 331-342.

(42) S. Maniam, H. F. Higginbotham, T. D. M. Bell, S. J. Langford, *Chem. Eur. J.* **2019**, *25*, 7044.

(43) H. Shao, J. Seifert, N. C. Romano, M. Gao, J. J. Helmus, C. P. Jaroniec, D. A. Modarelli, J. R. Parquette, *Angew. Chem. Int. Ed.* **2010**, *49*, 7688.

(44) T. W. Anderson, G. D. Pantos, J. K. M. Sanders, *Org. Biomol. Chem.* **2011**, *9*, 7547.

(45) M. Pandeeswar, H. Khare, S. Ramakumar, T. Govindaraju, *RSC Adv.* **2014**, *4*, 20154.

(46) T. D. M. Bell, S. V. Bhosale, C. M. Forsyth, D. Hayne, K. P. Ghiggino, J. A. Hutchison, C. H. Jani, S. J. Langford, M. A. P. Lee, C. P. Woodward, *Chem. Commun.* **2010**, *46*, 4881.

(47) I. B. Berlman, *Handbook of fluorescence spectra of aromatic molecules*; Academic Press, New York, 1965 (1st edition), 1971 (2nd edition).

(48) J. Mooney, P. Kambhampati, *J. Phys. Chem. Lett.* **2013**, *4*, 3316.

* * *

POSTLUDE

The realm of molecular chemistry deals with development of a wide range of very powerful procedures for synthesizing sophisticated molecules and materials from atoms that are linked by covalent bonds. Supramolecular chemistry, on the other hand, goes beyond molecular level and generates complex, functional systems from small amphiphilic units held together by intermolecular non-covalent interactions.

The “bottom-up” strategy of constructing nano-architectures based on supramolecular self-assembly has been drawing notable attraction for the past forty years. Self-assembly relies on the spontaneous organization of molecular tectons producing patterns or ordered structures at any scale. Nature of interaction is dependent of structural and electronic properties of individual molecules that governs their shape, charge, polarizability, etc. In recent past, supramolecular self-organization of small amphiphilic molecules has grown into a most important arena of research due to its nano-dimensional artistic approach and has fast-tracked numerous prospects in physics, chemistry and biology. One of the most advantageous aspects of supramolecular self-assembly is their ability to mimic complex biological entities with simple building blocks which might as well be a stepping stone to understand the “life” and solving real-world problems. They have broadened the horizon of alternative pathways to traditional molecular chemistry by the development of environmentally benign micro/nano-reactors for the synthetic chemistry. Thousands of scientists, all over the globe, are constantly involved in exploring supramolecular self-assemblies in multidisciplinary fields.

The prime research objective of our group at IACS is to design multimodal functionalized amphiphiles that generates diverse supramolecular aggregates with task specific applications. These self-assembled soft-materials are explored in multiple domains ranging from biochemical to bio-medicinal applications. The present thesis describes stimuli responsive disassembly of self-aggregates and their application in drug release, detection of analytes by AIE based nano-dimensional bio probes and generation of Fluorescent Organic Nanoparticles with tuneable emission. The scientific work documented in this thesis is the outcome of our constant endeavour towards developing functional nanomaterials contributing to the scientific advancement and ends with a hope that it could be interpretable to the interested individuals.

LIST OF PUBLICATIONS

1. **Deblina Sarkar**, Anup Kumar Ghosh, Aftab Hossain Khan and Prasanta Kumar Das. *"Organic nanoparticles with tuneable AIE derived from amino acids appended naphthalenediimide based amphiphiles."* **2022** (Manuscript communicated).
2. **Deblina Sarkar**, Monalisa Chowdhury and Prasanta Kumar Das. *"Naphthalimide-based azo-functionalized supramolecular vesicle in hypoxia-responsive drug delivery."* ***Langmuir*** **2022**, *38*, 3480-3492.
3. **Deblina Sarkar**, Monalisa Chowdhury and Prasanta Kumar Das. *"Napthalimide based fluorescent organic nanoparticles in selective sensing of Fe^{3+} and as a diagnostic probe for Fe^{2+}/Fe^{3+} transition."* ***J. Mater. Chem. B*** **2021**, *9*, 494-507.
4. **Deblina Sarkar**, Pritam Choudhury, Soumik Dinda, and Prasanta Kumar Das. *"Vesicle formation by cholesterol based hydrazone tethered amphiphiles: stimuli responsive dissipation of self-assembly."* ***J. Colloid Interface Sci.*** **2018**, *530*, 67-77.
5. Debayan Chakraborty, **Deblina Sarkar**, Anup Kumar Ghosh and Prasanta Kumar Das. *"Lipase sensing by naphthalene diimide based fluorescent organic nanoparticles: a solvent induced manifestation of self-assembly."* ***Soft Matter*** **2021**, *17*, 2170-2180.
6. Deep Mandal, Pritam Choudhury, **Deblina Sarkar** and Prasanta Kumar Das. *"Dissipation of self-assemblies by fusion of complementary gels: an elegant strategy for programmed enzymatic reactions."* ***Chem. Commun.*** **2017**, *53*, 7844-7847.